DOCTORAL THESIS

AQUATIC SELF-PROPULSION AND ENERGY HARVESTING FROM THE CURRENTS THROUGH FLEXIBLE FLAPPING FOILS

Autopropulsión acuática y extracción de energía de las corrientes mediante perfiles flexibles oscilantes

PABLO ESTEBAN LÓPEZ-TELLO

UNIVERSIDAD DE MÁLAGA

Ph.D. Program: Mechatronic Engineering
Dpto. de Ingeniería Mecánica, Térmica y de Fluidos
Área de Mecánica de Fluidos
Escuela de Ingenierías Industriales

SUPERVISORS

Dr. D. Ramón Fernández Feria
Dr. D. Enrique Sanmiguel Rojas

Málaga, España, 2024

UNIVERSIDAD DE MÁLAGA

AUTOR: Pablo Esteban López-Tello

https://orcid.org/0000-0001-6500-262X

EDITA: Publicaciones y Divulgación Científica. Universidad de Málaga

The mind adapts and converts to its own purposes the obstacle to our acting. The impediment to action advances action. What stands in the way becomes the way.

La mente se adapta y convierte los obstáculos en sus propios propósitos. El impedimento a la acción avanza la acción. Lo que se interpone en el camino se convierte en el camino.

Marcus Aurelius

DECLARACIÓN DE AUTORÍA Y ORIGINALIDAD DE LA TESIS PRESENTADA PARA OBTENER EL TÍTULO DE DOCTOR

D./Dña PABLO ESTEBAN LÓPEZ-TELLO.

Estudiante del programa de doctorado EN INGENIERÍA MECATRÓNICA de la Universidad de Málaga, autor/a de la tesis, presentada para la obtención del título de doctor por la Universidad de Málaga, titulada: AUTOPROPULSIÓN ACUÁTICA Y EXTRACCIÓN DE ENERGÍA DE LAS CORRIENTES MEDIANTE PERFILES FLEXIBLES OSCILANTES.

Realizada bajo la tutorización de D. RAMÓN FERNÁNDEZ FERIA y dirección de D. RAMÓN FERNÁNDEZ FERIA y D. ENRIQUE SANMIGUEL ROJAS (si tuviera varios directores deberá hacer constar el nombre de todos)

DECLARO QUE:

La tesis presentada es una obra original que no infringe los derechos de propiedad intelectual ni los derechos de propiedad industrial u otros, conforme al ordenamiento jurídico vigente (Real Decreto Legislativo 1/1996, de 12 de abril, por el que se aprueba el texto refundido de la Ley de Propiedad Intelectual, regularizando, aclarando y armonizando las disposiciones legales vigentes sobre la materia), modificado por la Ley 2/2019, de 1 de marzo.

Igualmente asumo, ante a la Universidad de Málaga y ante cualquier otra instancia, la responsabilidad que pudiera derivarse en caso de plagio de contenidos en la tesis presentada, conforme al ordenamiento jurídico vigente.

En Málaga, a 01 de FEBRERO de 2024.

Fdo.: D. PABLO ESTEBAN LÓPEZ-TELLO Doctorando/a	Fdo.: D. RAMÓN FERNÁNDEZ FERIA Tutor/a
Fdo.: D. RAMÓN FERNÁNDEZ FERIA Director/es de tesis	Fdo.: D. ENRIQUE SANMIGUEL ROJAS

Autorización

El profesor Dr. Ramón Fernández Feria y el profesor Dr. Enrique Sanmiguel Rojas, ambos Catedráticos de Universidad en el departamento de Ingeniería Mecánica, Térmica y de Fluidos de la Universidad de Málaga,

CERTIFICAN:

Que D. Pablo Esteban López-Tello, alumno de la Universidad de Málaga, ha realizado bajo su dirección la presente tesis doctoral titulada *Autopropulsión acuática y extracción de energía de las corrientes mediante perfiles flexibles oscilantes*, cumpliendo con todos los requisitos necesarios para optar al grado de Doctor Internacional, por lo que AUTORIZAN SU LECTURA Y DEFENSA PÚBLICA.

Málaga, España, 2024

Dr. D. Enrique Sanmiguel Rojas

Dr. D. Ramón Fernández Feria

Declaración

El profesor Dr. Ramón Fernández Feria y el profesor Dr. Enrique Sanmiguel Rojas, ambos Catedráticos de Universidad en el departamento de Ingeniería Mecánica, Térmica y de Fluidos de la Universidad de Málaga,

INFORMAN:

Que el trabajo de investigación que se ha desarrollado durante la tesis doctoral de D. Pablo Esteban López-Tello es original y las publicaciones que avalan esta tesis no han sido utilizadas en tesis anteriores.

Málaga, España, 2024

Dr. D. Enrique Sanmiguel Rojas

Dr. D. Ramón Fernández Feria

Agradecimientos

Aún recuerdo, como si fuera ayer, aquellas primeras lecciones de Mecánica de Fluidos que tan fascinado me dejaron cuando empecé mis estudios universitarios, siempre me sorprendió que con simples ecuaciones (aunque a veces no tan simples) se pudiera modelar la realidad de una forma tan sencilla y precisa. Sin embargo, no fue sino hasta el cuarto año de carrera que pude compartir aula con el profesor D. Ramón Fernández Feria. Poco sabía aquel joven yo que pocos años más tarde tendría la oportunidad de trabajar junto a él y que finalmente sería su tutor de tesis. Es por esto que me gustaría mostrar mi más profunda gratitud hacia su persona, no solo por darme la oportunidad de aprender junto a él, sino también por ser un referente y guía, por acompañarme y ayudarme a recorrer este camino, por brindarme su confianza y apoyo a lo largo de estos años, y por todos sus esfuerzos para complementar mi formación.

Me gustaría agradecer también a mi codirector de tesis, el profesor D. Enrique Sanmiguel Rojas, por compartir su dilatada experiencia en el campo de la Mecánica de Fluidos computacional, así como su experiencia profesional fuera del ámbito académico. Es algo que valoro en gran medida.

Debo agradecer también la ayuda de Sergio Pinazo, Alberto Rodríguez y José Luis Perona, así como la del profesor D. José Velázquez, sin duda fue indispensable para completar los experimentos que lleve a cabo en el canal de agua. Los solitarios días en el laboratorio se desvanecían en cuanto ellos aparecían.

I would like to thank Professor Michel Cervantes of Luleå University of Technology, Sweden, for giving me the opportunity to collaborate with him, and for including me in his research group from the beginning. I also thank Henrik Lycksam and Joel Sundström for helping me with the LDA system. Also, I would like to thank Shahab Shiraghaee, Davy Spelthan, and Mohammad Bahrami for making my days in Luleå even greater.

Finalmente, agradezco enormemente el apoyo recibido por mi familia, padres y hermano. Por sus sabios consejos, por su amor y preocupación, gracias a ellos soy quien soy a día de hoy. Gracias por darme tanto sin nunca pedir nada a cambio. También debo agradecerme a mí mismo, por ser perseverante, por no abandonar cuando el camino se volvía difícil y por intentar siempre dar lo mejor de mí. Gracias también a todas esas personas que lamentablemente dejo sin mencionar, pero que me han ayudado a crecer no solo profesionalmente sino también como persona. Muchas gracias, de corazón.

Resumen

En esta tesis, se analizará principalmente el potencial de los vehículos acuáticos bioinspirados que se propulsan mediante perfiles batientes. En especial se utilizará un enfoque teórico basado en la teoría del movimiento fluido potencial lineal para la interacción fluido-perfil, válida en el rango de pequeñas amplitudes y altos números de Reynolds. Por otro lado, en la literatura reciente se ha observado un potencial realmente prometedor en lo referente a la obtención de energía mediante dispositivos basados en este tipo de tecnología. Así pues, se realizarán algunos estudios experimentales en esta línea durante la última parte de la tesis.

En general, la locomoción acuática involucra una complicada interacción entre el nadador y el entorno en el que se mueve. Esto se conoce en la literatura científica como interacción fluido-estructura y su estudio resulta esencial para conocer con detalle la física detrás de este tipo de fenómenos. Para abordar adecuadamente este tema, el primer capítulo de la tesis se centrará en el análisis de un modelo de autopropulsión bidimensional simple basado en un perfil batiente aislado con un movimiento de cabeceo impuesto no estacionario y un desplazamiento nulo en la dirección perpendicular al avance. El movimiento de cabeceo vendrá dado por una expresión sinusoidal en función de la frecuencia de movimiento del perfil y será actuada en el punto de pivote sobre el cual gira. La velocidad a la que se propulsa el perfil se obtendrá a partir de la segunda ley de Newton aplicada al centro de masa del mismo. Dado que en este estudio se está considerando el movimiento del perfil de forma aislada, sin estar anclado al cuerpo propulsado, será necesario considerar la fricción viscosa no estacionaria en el perfil, no siendo posible modelar dicha fricción como una constante (coeficiente de arrastre). Para modelar esta fricción viscosa se utilizarán simulaciones numéricas de alta resolución en un amplio número de Reynolds basado en la frecuencia ($10^3 \lesssim Re_\omega \lesssim 10^4$). Estas simulaciones numéricas que involucran la interacción fluido-estructura se llevarán a cabo con la ayuda del software comercial Ansys Fluent, el cual basa su resolución en el método numérico de volúmenes finitos. Concretamente se utilizará la versión 21.2. Además, el perfil será modelado mediante una lámina de espesor delgado en lugar de los comúnmente utilizados perfiles NACA. Esto posibilitará contrastar mejor los resultados, así como desarrollar un modelo viscoso más compatible con la teoría, ya que en la teoría de flujo potencial el perfil considerado es infinitamente delgado, lo que en 2D sería una línea. El punto de pivote se situará cerca del borde de ataque del perfil, ya que según la literatura es la posición que ofrece mejores resultados. Para modelar la interacción fluido-estructura se hará uso de las denominadas User Defined Functions (UDF), que básicamente se tratan de programas en C compilados en el solver de Fluent. Esta UDF contendrá el movimiento de cabeceo impuesto en el perfil, para lo cual el comando DEFINE-CG-MOTION será de gran ayuda. Además,

incluirá también la ecuación de empuje derivada de la segunda ley de Newton, que será integrada y resuelta para cada instante de tiempo. Por otro lado, el mallado estará dividido en dos regiones principales: un mallado de fondo y un mallado móvil, el cuál contendrá la lámina delgada y será el encargado de simular su locomoción. Dado que la malla móvil eventualmente colisionará con la pared del dominio, será también necesario implementar un algoritmo de capas que se encargue de destruir y reconstruir el mallado de fondo a la velocidad de movimiento del centro de masas de la lámina delgada. Por supuesto, se realizará un estudio de convergencia de malla analizando tanto el tamaño de los elementos del mallado como su convergencia temporal. Utilizando el código desarrollado en Fluent, se realizarán $5{\times}8$ simulaciones numéricas para distintas amplitudes del movimiento de cabeceo y para distintos números de Reynolds basados en la frecuencia, que permitirán extraer la información necesaria para crear el modelo de fricción viscosa no estacionaria.

Una vez cumplido este propósito, se utilizará dicho modelo viscoso en combinación con dos modelos de empuje no estacionarios distintos, los cuales se basan en la teoría de flujo potencial lineal. Concretamente, uno de los modelos de empuje proviene de los resultados obtenidos por Theodorsen [1935] y Garrick [1936], mientras que el segundo proviene de un estudio más reciente llevado acabo por Fernandez-Feria [2016], basado en la teoría del impulso de vorticidad linealizada. La ecuación diferencial ordinaria resultante para la velocidad de propulsión se adimensionalizará y se resolverá tanto numéricamente, utilizando el software comercial Matlab, como analíticamente mediante el método de perturbaciones de dos escalas. Para el método de perturbaciones se asumirá que la velocidad adimensional puede ser descompuesta en dos términos: un componente oscilatorio en la misma escala de tiempo que el resto de variables y un segundo componente correspondiente a la velocidad promedio que evoluciona en una escala de tiempo mucho más lenta. Además, se asumirá que la velocidad de propulsión adimensional es mucho menor que la unidad para que la aproximación analítica funcione. Los resultados de ambos modelos serán comparados con las simulaciones numéricas realizadas a pequeñas amplitudes y altos números de Reynolds, estableciendo el rango de validez de los modelos, así como su precisión y mejor funcionamiento en cada caso.

Una vez llevado a cabo este primer estudio preliminar, se abordará el diseño de un modelo teórico para un vehículo acuático real propulsado mediante un perfil batiente rígido, cuyo movimiento de cabeceo será directamente generado por un par impuesto de pequeña amplitud producido por un motor. Dicho par será modelado mediante una expresión sinusoidal en función de la frecuencia de movimiento y actuará en la localización del punto de pivote del perfil. Además, el propulsor estará elásticamente unido a la estructura del vehículo mediante muelles y amortiguadores longitudinales y torsionales, lo cual permitirá al perfil moverse en la dirección perpendicular a la corriente, además de mantener el movimiento de cabeceo anteriormente mencionado. El modelo teórico se basará en la teoría potencial de flujo lineal para la interacción fluido-estructura, la cual nos proporcionará los coeficientes de sustentación, momento y empuje, en combinación con la dinámica de autopropulsión propia del perfil batiente. Así pues, analizando el diagrama de cuerpo libre resultante se obtendrán las ecuaciones de gobierno en la dirección de la fuerza vertical y del momento. Mientras que la ecuación de empuje resultará de utilizar directamente la segunda ley de Newton aplicada al centro de masa del vehículo. Cabe destacar que a diferencia del caso anterior ahora el perfil batiente sí se

encuentra anclado al cuerpo propulsado y, por consiguiente, la fricción que sufre el vehículo sí puede ser modelada mediante un coeficiente de arrastre, no siendo necesario considerar la fricción viscosa no estacionaria en el perfil. El sistema de tres ecuaciones diferenciales ordinarias resultante (para el movimiento de desplazamiento en la dirección perpendicular al flujo h, el movimiento de cabeceo α y la velocidad de propulsión u) se adimensionalizará y se resolverá tanto numérica como analíticamente. Para la resolución numérica de las ecuaciones diferenciales se utilizará el software Matlab, siendo de gran ayuda el paquete *odeset* y particularmente la función *mass matrix*. Para la resolución analítica se utilizará nuevamente el método de perturbaciones de dos escalas, asumiendo la existencia de dos escalas de tiempo bien diferenciadas en las variables principales y considerando que la amplitud del par impuesto en formato adimensional será mucho menor que la unidad. Como resultado de esta suposición, se obtendrán varias expansiones asintóticas para las tres variables h, α y u. A priori los coeficientes asociados a dichas expansiones asintóticas serán desconocidos, sin embargo, estos pueden ser obtenidos tras expandir y analizar todos los términos en las correspondientes ecuaciones diferenciales. Para las variables h y α con obtener la expansión hasta el primer orden será suficiente, sin embargo, para la variable u será necesario profundizar hasta el segundo orden de la expansión si se desea recoger el comportamiento oscilatorio de la velocidad de avance del vehículo. Una vez realizado este proceso se obtendrán soluciones analíticas, válidas para pequeñas amplitudes del par adimensional, no solo de las variables mencionadas anteriormente sino también para el coeficiente de potencia, el coste de transporte, la eficiencia y el número de Strouhal. Además, se proporcionarán los mapas en los planos paramétricos de todas estas variables, tanto de su resolución analítica como numérica.

Adicionalmente, se compararán los resultados analíticos y numéricos que se obtienen de la resolución de las ecuaciones de gobierno con las simulaciones numéricas de alta resolución desarrolladas en el estudio anterior. Para ello, se realizará una pequeña modificación en la UDF para incorporar la nueva ecuación de empuje que análogamente será integrada y resuelta para cada instante de tiempo. Además, para hacer la comparación posible se seleccionará una constante del muelle longitudinal k_h muy alta, lo cual inhibirá el movimiento de desplazamiento vertical del perfil posibilitando así reutilizar el código desarrollado en Fluent. Una vez resueltas las ecuaciones de forma numérica se analizará la solución para α y se obtendrá la amplitud de su movimiento. Este dato será utilizado para realizar las simulaciones numéricas de alta resolución en Fluent, ya que el código funciona con un movimiento de cabeceo prescrito y no mediante un par impuesto. Por supuesto, las simulaciones se realizarán a altos números de Reynolds ($Re_\omega = 5000$) puesto que la teoría potencial no considera la viscosidad del fluido en la propulsión, solo en el coeficiente de arrastre del vehículo. Por otro lado, la literatura científica ha demostrado en varios estudios que la resonancia estructural del sistema sobre el que se encuentra montado el propulsor puede mejorar enormemente no solo la velocidad de propulsión del vehículo, sino también la eficiencia del mismo. Así pues, haciendo uso de los resultados numéricos obtenidos de la resolución de las ecuaciones diferenciales se estudiará la resonancia asociada a los muelles longitudinales y torsionales y cómo esta afecta a la velocidad y eficiencia del vehículo. Además, gracias a la resolución analítica obtenida con el método de perturbaciones, se facilitarán algunas expresiones simples para predecir esta región de resonancia en la que sistema funciona óptimamente. Estos resultados analíticos han sido propuestos también para una patente de vehículo de propulsión acuático.

Una vez desarrollado este primer modelo teórico de vehículo acuático, resulta interesante extenderlo para el caso de un propulsor flexible, pues la literatura refleja grandes beneficios cuando esta es considerada. Así pues, el nuevo y más completo modelo de vehículo acuático se desarrollará para permitir un movimiento de deflexión pasivo en el perfil, además de los dos considerados anteriormente en el caso rígido, todos ellos generados nuevamente por un pequeño par proveniente de un motor y la interacción fluido-estructura. El nuevo modelo teórico se basará en la teoría potencial de flujo lineal para la interacción fluido-estructura, la cual ahora nos proporcionará los coeficientes de sustentación, momento, deflexión y empuje, en combinación con la ecuación de Euler-Bernouilli para una barra. Esta nueva ecuación de Euler-Bernouilli será la encargada de modelar la dinámica de autopropulsión propia del perfil batiente, incorporando además la flexibilidad del perfil a través del módulo de Young E y del espesor del mismo γ. Para este modelo teórico se asumirá la hipótesis de que la cantidad $E\gamma^3$ será constante a lo largo de todo el perfil, simplificando así en gran medida la resolución de las ecuaciones. Así pues, se obtendrán las ecuaciones de gobierno en las direcciones de la fuerza transversal, del momento y de la deflexión del perfil. Mientras que la ecuación de empuje de nuevo resultará de aplicar la segunda ley de Newton al centro de masa del vehículo. Al igual que el caso anterior, al estar el propulsor anclado al cuerpo propulsado la fricción que sufre se modelará a través de un coeficiente de arrastre y no mediante la fricción viscosa no estacionaria en el perfil.

El sistema de cuatro ecuaciones diferenciales ordinarias resultante (para el movimiento de desplazamiento en la dirección perpendicular al flujo h, el movimiento de cabeceo α, el movimiento de deflexión del perfil d y la velocidad de propulsión u) se adimensionalizará y, de nuevo, se resolverá tanto numérica como analíticamente. La solución numérica de las ecuaciones diferenciales se obtendrá de la misma forma que en el caso anterior utilizando el paquete *odeset* de Matlab y la función *mass matrix*, siendo ahora su resolución un poco más costosa desde el punto de vista computacional al incorporar la ecuación diferencial asociada a la deflexión del perfil. Para la resolución analítica se seguirá un proceso análogo al caso rígido empleando nuevamente el método de perturbaciones de dos escalas y asumiendo que la amplitud del par impuesto en formato adimensional será mucho menor que la unidad. Como resultado se obtendrán las expansiones asintóticas para las cuatro variables h, α, d y u, determinándose sus respectivos coeficientes tras la correspondiente expansión y análisis de las ecuaciones diferenciales. Para este caso será suficiente con analizar hasta el primer orden en las expansiones de h, α y d, mientras que para la variable u se necesitará avanzar hasta el segundo orden, al igual que sucedía con el perfil rígido. Finalizado este proceso se obtendrán soluciones analíticas, válidas para pequeñas amplitudes del par adimensional, para las variables anteriores y para el coeficiente de potencia, el coste de transporte, la eficiencia y el número de Strouhal. Por otro lado, se estudiará de nuevo la resonancia del sistema para el caso del propulsor flexible y se demostrará que esta se produce para las mismas condiciones que para el caso rígido, en primera aproximación, pero mejorando la eficiencia en las regiones de esta resonancia distintas a las que generan un empuje máximo.

Para este caso se proporcionarán solamente los mapas asociados a la solución numérica, que es la de mayor interés, para las principales variables, analizando su comportamiento en función de la relación de rigidez y de los demás parámetros que son: el coeficiente del muelle

torsional, la distancia al punto de pivote y el número de Lighthill (todos ellos en formato adimensional). Además, se estudiará con detalle la evolución del número de Strouhal en función del número de Lighthill comparándola con los resultados experimentales obtenidos por Eloy [2012] para peces cuyo mecanismo de locomoción principal es la oscilación de su aleta caudal, sirviendo como validación adicional de los resultados. Se mostrará también como el rendimiento, el coste de trasporte y la velocidad de propulsión se ve afectada por la fricción, asociada a este número de Lighthill.

Finalmente, en la última parte de la tesis se realizará un estudio experimental sobre el potencial de extracción de energía de los perfiles batientes. Concretamente, se estudiará un prototipo de turbina que aprovecha la energía de una corriente incidente mediante el movimiento pasivo de un perfil rígido. Dicho prototipo está basado en el trabajo previamente realizado por Boudreau et al. [2018] pero incorporando sensores de fuerza y momento útiles para caracterizar el rendimiento del dispositivo. Básicamente, el dispositivo consiste en un perfil NACA rígido que se soporta mediante muelles torsionales y longitudinales, y que además cuenta con un amortiguador/freno magnético que afecta al movimiento del dispositivo en la dirección perpendicular al flujo. Este amortiguador magnético actúa también como sumidero de energía sirviendo para modelar la capacidad de extracción de energía del prototipo. El dispositivo se instala en un canal de agua, lo que permite controlar la velocidad de la corriente incidente. Además, se presentará la formulación del problema, donde haciendo uso del diagrama de cuerpo libre se obtendrán las ecuaciones diferenciales de gobierno en la dirección de las fuerzas transversales, las fuerzas de arrastre y el momento. Estas ecuaciones diferenciales resultantes serán similares a las obtenidas por Boudreau et al. [2018], pero estarán adaptadas a la nomenclatura de la tesis y al tratamiento de datos aplicado a las señales. Por supuesto, se aplicará la adimensionalización correspondiente de dichas ecuaciones.

El objetivo principal de este estudio será la caracterización del funcionamiento del dispositivo para un amplio rango de condiciones de operación. Concretamente se analizarán 6×8 puntos de operación variando los muelles longitudinales y la potencia del freno magnético para una única velocidad de corriente, es decir para un número de Reynolds fijo ($Re \simeq 22200$). En este caso no se utilizará ningún muelle torsional, ya que según la literatura las mejores condiciones de funcionamiento del dispositivo se consiguen con un movimiento de cabeceo completamente libre. Por otro lado, para medir y registrar el desplazamiento en la dirección perpendicular al flujo y el movimiento de cabeceo se utilizarán dos encoders giratorios, mientras que para las fuerzas y momentos que soporta el perfil en el eje de giro se utilizará un sensor capaz de medir estos esfuerzos. Todas las señales analógicas serán procesadas posteriormente con una placa de adquisición de datos y con unos códigos desarrollados con el software comercial LabVIEW. Una vez procesadas las señales temporales se suavizarán aplicando un filtro de Butterworth de séptimo orden y posteriormente se analizarán los valores promedios de las mismas para los últimos 90 ciclos de funcionamiento. Cada experimento se repetirá tres veces permitiendo así obtener un resultado promedio final más fiable y la desviación típica de cada medida. Se presentarán y discutirán las evoluciones temporales de los principales términos de las ecuaciones de gobierno, así como de los correspondientes coeficientes de potencia asociados a cada uno de estos términos. En particular se estudiarán estas evoluciones para el caso base, escogiéndose este para el punto de operación que mayor rendimiento pre-

sente con respecto a la energía que el fluido transfiere al dispositivo. Además, se presentarán y analizarán los mapas correspondientes a las siguientes magnitudes: los promedios de los movimientos de desplazamiento transversal y de cabeceo, así como sus correspondientes amplitudes, la frecuencia y desfase entre ambos movimientos, los coeficientes de sustentación, arrastre y momento, los coeficientes de potencia asociados a la energía extraída mediante el amortiguador magnético y a la energía que el fluido transfiere al dispositivo, y los rendimientos asociados a estas dos últimas variables.

Por último, para tener un mayor entendimiento de las estructuras de vórtices que se crean durante el movimiento del perfil, se realizarán algunos experimentos adicionales empleando la técnica experimental de PIV (Particle Image Velocimetry). Para ello, se utilizará un cámara de alta velocidad y un láser que iluminará el plano medio del canal de agua, donde se tomarán las medidas. El agua se alimentará con partículas de 10 μm de diámetro que reflejarán la luz del láser y permitirán visualizar las estructuras del flujo. Mientras que las imágenes serán procesadas con un código en Matlab desarrollado por el Departamento de Mecánica de Fluidos de la Universidad de Málaga. Así pues, se analizarán tres puntos de operación de interés, entre los que se incluye el caso base, y se presentarán los resultados del campo de vorticidad normalizado para varios instantes de tiempo durante un ciclo de funcionamiento del perfil.

Palabras clave: Locomoción acuática, Propulsión mediante perfiles batientes, Interacción fluido-estructura, Teoría de flujo potencial lineal, Simulaciones numéricas de alta resolución, Dispositivos de extracción de energía, Turbinas basadas en perfiles batientes totalmente pasivos, Velocimetría por imágenes de partículas.

Abstract

This thesis is mainly devoted to the study of bio-inspired aquatic vehicles that are self-propelled by a flapping hydrofoil, especially through a theoretical approach based on the linear potential-flow theory for the fluid-foil interaction, valid in the range of small amplitudes and high Reynolds numbers. The energy-harvesting potential of this kind of technology is also quite promising, so we also perform some experimental studies in that direction in the last part of the thesis.

In general, aquatic locomotion involves an intricate interaction between the swimmer and its environment. Therefore, understanding this process requires considering the Fluid-Structure Interaction (FSI) of the swimmer moving within a fluid. To appropriately address this issue, the first chapter of the thesis is focused on the study of a simple two-dimensional self-propulsion model based on an isolated flapping hydrofoil with a non-stationary imposed pitching motion and non-displacement in the perpendicular direction of the flow, i.e., no heaving motion. The pitching motion is given by a sinusoidal expression based on the frequency of the foil's motion applied at its pivot point. The propulsion velocity of the foil is then derived from Newton's second law applied to its center of mass. Moreover, as this study considers an isolated pitching foil, which is not attached to the swimmer's body, it is necessary to consider the non-stationary viscous friction on the foil, not contemplated by the potential flow model, and a constant drag cannot be used. To model this viscous friction, we use high-resolution numerical simulations over a wide range of Reynolds numbers based on frequency ($10^3 \lesssim Re_\omega \lesssim 10^4$). These numerical simulations that involve the fluid-structure interaction are conducted through the commercial software Ansys Fluent, which employs the finite volume numerical method. Specifically, version 21.2 is used. Thus, the foil is modeled as a thin plate instead of the commonly used NACA profiles, which allows us to develop a viscous model more compatible with the potential-flow theory since it considers the foil profile as infinitely thin. The pivot point is located at the leading edge (LE) of the foil. Furthermore, a User Defined Function (UDF) is employed to model the fluid-structure interaction, which consists of a C program compiled in the Fluent solver. This UDF includes the imposed pitching motion on the foil, for which the DEFINE-CG-MOTION command is really useful, and also incorporates the thrust equation derived from Newton's second law. On the other hand, the mesh is divided into two regions: a background mesh and a moving mesh containing the thin plate. Given that the moving mesh would eventually collide with the domain wall, a layering algorithm needs to be implemented. This algorithm can destroy and build up the background mesh at the velocity of the center of mass of the plate. A mesh convergence study is also conducted, analyzing both mesh element size and temporal convergence.

With this developed Fluent code, 5×8 numerical simulations are performed for various pitching motion amplitudes and Reynolds numbers based on frequency, and the information needed to create the non-stationary viscous friction model is obtained. Then, this viscous model is combined with two different non-stationary thrust models, both based on linear potential-flow theory. Specifically, one thrust model is derived from the results obtained by Theodorsen [1935] and Garrick [1936], while the second one comes from a more recent study performed by Fernandez-Feria [2016], which is based on the linearized vortical impulse theory. The resulting ordinary differential equation for the propulsion velocity is non-dimensionalized and solved both numerically using Matlab and analytically through the two-scale perturbation method. The perturbation method assumes that the non-dimensional propulsion velocity can be decomposed into two terms: an oscillatory component on the same timescale as the other variables and a second component corresponding to the mean velocity evolving on a much slower timescale. Additionally, it is assumed that the non-dimensional propulsion velocity is much smaller than unity for the analytical approximation to be valid. Both results for the two thrust models are compared with small amplitude and high Reynolds number numerical simulations. Thus, the validity range of the models are determined, and so the precision and performance of each model in the range of Reynolds numbers considered.

Once the first preliminary approach is conducted, we focus our study on the design of a theoretical model for an actual aquatic vehicle self-propelled by a rigid foil undergoing pitching oscillations. This pitching motion is directly generated by an imposed torque of small amplitudes, which would be produced by a motor. This imposed torque is given by a sinusoidal expression based on the frequency of the foil's motion applied at its pivot point. Moreover, the foil is elastically supported to the vehicle hull through translational and torsional springs and dampers, also allowing for passive heaving motion. The model is based on the linear potential-flow theory for the FSI (providing the lift, thrust, and moment coefficients), coupled with the self-propelled dynamics of that semi-passive flapping foil. Thus, analyzing the resulting free-body diagram, the governing equations for the force in the heave direction and the moment are obtained. However, the thrust equation directly results from Newton's second law applied to the center of mass of the vehicle. Notice that, in contrast to the previous case, the flapping foil is now attached to the swimmer's body, which means that the friction on the vehicle can be modeled through a drag coefficient. Therefore, we do not need to consider the non-stationary viscous friction on the foil. The resulting system of three ordinary differential equations (for the heaving h and pitching α motions, and for the swimming velocity u) is non-dimensionalized and solved both numerically using Matlab, and analytically through a perturbation method. For the numerical solution, the *odeset* package and the *mass matrix* function are particularly helpful. For the analytical solution, the two-scale perturbation method is used again, assuming two different timescales for the main variables and amplitudes of the non-dimensional imposed torque much smaller than unity. As a result, some asymptotic expansions are proposed for the h, α, and u, whose coefficients can be determined after the proper expansion and analysis of the equation terms. For h and α, the analysis up to the first order is enough, while for u, the second order is also needed. Then, analytic solutions valid for small torque amplitudes are obtained for the heaving and pitching motions, as well as for the swimming velocity, the power coefficient, the cost of transport, the efficiency, and the Strouhal number. Furthermore, some maps in the relevant

parametric planes are provided for all of these performance parameters, with both numerical and analytical results.

Additionally, the analytical and numerical results are compared with the high-resolution numerical simulations developed in the previous study. To that end, a slight modification is made to the UDF, so the new thrust equation is implemented. In order to make the comparison possible, a very high value for the longitudinal spring constant k_h is set, thus neglecting the heaving motion. Once the equations are numerically solved, the solution for α is analyzed, and the amplitude of its movement is obtained. This result is then used to perform the high-resolution numerical simulations in Fluent, as the code operates with a prescribed pitching motion rather than an imposed torque. Of course, the simulations will be conducted at a high Reynolds numbers ($Re_\omega = 5000$) since the potential-flow theory does not consider the viscosity of the fluid. On the other hand, it has been demonstrated in several studies that the structural resonance of the system on which the propulsor is mounted can significantly improve not only the propulsion force of the vehicle but also its efficiency. Therefore, using the numerical results obtained from the solution of the differential equations, the resonance associated with the longitudinal and torsional springs is studied, as well as how it affects the speed and efficiency of the vehicle. Moreover, thanks to the analytical resolution obtained with the perturbation method, some simple expressions are provided to predict this resonance region of the system. These analytical results have been used for a patent proposal of a water vehicle propeller.

Once the first theoretical model for the aquatic vehicle is well-studied, we extend it to the case of a flexible flapping foil propeller. Thus, the new and more complete model allows for a passive flexural motion of the foil in addition to the passive pitching and heaving motions of the rigid foil case, all of them generated by the actuating imposed torque and the fluid-foil interaction as in the previous case. This theoretical model is based on the linear potential-flow theory for the FSI (providing now the lift, thrust, moment, and flexural moment coefficients) in combination with the Euler-Bernoulli beam equation. This new Euler-Bernoulli equation models the self-propulsion dynamics of the flapping foil, incorporating the flexibility of the propeller through its Young's modulus E and its thickness γ. The quantity $E\gamma^3$ is assumed to be constant along the foil, significantly simplifying the resolution of the equations. Therefore, the governing equations for the force in the heave direction, the moment, and flexural deflection are obtained. The thrust equation again results from Newton's second law applied to the center of mass of the vehicle. As in the rigid case, the foil is attached to the swimmer's body. Hence, the non-stationary viscous friction does not need to be modeled, and a constant vehicle's drag coefficient can be used.

The system of four ordinary differential equations (for the heaving h, pitching α, and flexural deflection d motions, and the swimming velocity u) is then non-dimensionalized and solved both numerically and analytically. The numerical solution is obtained similarly to the rigid foil case, using the *odeset* package and the *matrix mass* function in Matlab. However, the computational cost is slightly greater now due to the additional differential equation for flexural deflection. The analytical solution is again obtained through the two-scale perturbation method following the same procedure as in the previous case, assuming that the

amplitude of the non-dimensional torque is much smaller than unity, but the perturbation analysis is now much more involved. As a result, asymptotic expansions for the four variables h, α, d, and u are proposed, and their coefficients are determined through the expansion and analysis of the equation terms. Analyzing up to the first order in the expansions for h, α, and d is found to be enough. In contrast, the variable u requires analysis up to the second order, in a similar way to the rigid foil case. Furthermore, analytical solutions valid for small torque amplitudes are obtained, not only for the variables mentioned above, but also for the power coefficients, the cost of transport, the efficiency, and the Strouhal number. Additionally, the resonance region of the system is also studied for the flexible propeller, finding the same resonant spring constants as in the rigid foil case. Now, only the maps from the numerical solution are presented for the main variables of interest, analyzing their behavior as a function of the stiffness ratio and the rest of the parameters, which are the torsional spring constant, the distance to the pivot point, and the Lighthill number (all of them in non-dimensional format). In addition, the evolutions of the Strouhal and Lighthill numbers are well studied, comparing our results with the experimental data from Eloy [2012] for fish whose primary locomotion mechanism is the oscillations of their caudal fin, serving as an additional validation of the analytical solution. The impact of the Lighthill number on the performance, cost of transport, and swimming velocity is also properly studied.

Finally, in the last part of the thesis, an experimental study on energy harvesting potential through flapping foils is conducted. Specifically, a fully-passive flapping-foil turbine is analyzed. The prototype is based on the previous work developed by Boudreau et al. [2018], but with the implementation of additional force and torque sensors to better analyze the performance of the turbine. It consists of a rigid NACA foil elastically supported by springs in heave and in pitch as well as by a magnetic damper/brake in heave. The damper is used to model the energy sink that would result from the energy conversion into electricity by an electric generator. The device is installed in a water channel so the incoming flow velocity can be controlled. The governing differential equations for the forces in the lift and drag directions, as well as the moment around the pivot axis, are also presented. This resulting system of differential equations is similar to the one obtained by Boudreau et al. [2018] but adapted to this thesis nomenclature and the data treatment applied to the signals. Non-dimensionalization of these equations is also applied. The primary objective of this study is to characterize the device's performance over a broad range of operating conditions. Specifically, 6×8 operating points are analyzed, varying the longitudinal springs and the magnetic brake power for a fixed incoming flow velocity, i.e., a fixed Reynolds number ($Re \approx 22200$). Torsional springs are not used for this study, as the literature suggests that the best performance is achieved with a completely free pitching motion.

On the other hand, to measure and record the heaving and pitching motions, two rotary encoders are used, while the forces and moment acting on the pivot axis are measured with a force/torque transducer. The analogical signals are processed using a data acquisition board and some LabVIEW codes. The processed temporal signals are also smoothed with a seventh-order Butterworth filter, and their averaged values for the last 90 operating cycles are analyzed. Furthermore, each experiment is repeated three times in order to obtain a more reliable final average result and the corresponding standard deviation for each measure. The

temporal evolutions of the main terms in the governing equations and their associated power coefficients for the baseline case are presented and properly discussed. This baseline case is selected for the best operating point based on the power transmitted from the fluid to the foil. Additionally, some maps for the main magnitudes are presented and analyzed, including the average heaving and pitching motions, their corresponding amplitudes, the frequency and phase lag, the lift, drag, and moment coefficients, the power coefficients associated with the energy harvested by the magnetic damper (effective power) and the energy that the fluid transmits to the foil, along with their corresponding efficiencies. Furthermore, for a better understanding of the vortex structures created during the foil's movement, some additional experiments are conducted using the Particle Image Velocimetry (PIV) experimental technique. A high-speed camera and a laser illuminating the midplane of the water channel are used. The water is seeded with 10 μm diameter particles that reflect the laser light, thus enabling the visualization of flow structures. The images are processed with a Matlab code developed by the Fluid Mechanics Department at the University of Málaga. Therefore, three operation points of interest, including the baseline case, are analyzed, and the normalized vorticity field results are presented for various time instants during a whole operating cycle.

Key words: Aquatic locomotion, Flapping foil propulsion, Fluid-structure interaction, Linear potential-flow theory, High-resolution numerical simulations, Energy harvesting devices, Fully-passive flapping-foil turbine, Particle image velocimetry.

Publications

ARTICLES:

R. Fernandez-Feria, E. Sanmiguel-Rojas, and P.E. Lopez-Tello. Numerical validation of simple non-stationary models for self-propelled pitching foils. *Ocean Eng. 260, 111973*. DOI: 10.1016/j.oceaneng.2022.111973, 2022.

P.E. Lopez-Tello, R. Fernandez-Feria, and E. Sanmiguel-Rojas. Efficient self-propelled locomotion by an elastically supported rigid foil actuated by a torque. *Appl. Math. Model. 116*, pp. 236-253. DOI: 10.1016/j.apm.2022.11.007, 2023.

P.E. Lopez-Tello and R. Fernandez-Feria. Effect of flexibility on the self-propelled locomotion by an elastically supported stiff foil actuated by a torque. *Phys. Rev. Fluids 8, 063102*. DOI: 10.1103/PhysRevFluids.8.063102, 2023.

CONFERENCES:

R. Fernandez-Feria, E. Sanmiguel-Rojas, and P.E. Lopez-Tello. Numerical validation of simple non-stationary models for self-propelled pitching foils. In: 1st Spanish Fluid Mechanics Conference (Cádiz, Spain). Session: Fluid-Structure Interaction I. Talk 01. June 2022.

P.E. Lopez-Tello, R. Fernandez-Feria, and E. Sanmiguel-Rojas. Efficient self-propelled locomotion by an elastically supported rigid foil actuated by a torque. In: 72nd Annual Meeting of the American Physical Society, Division of Fluid Dynamics (Indianapolis, USA). Session: High Reynolds Number Swimming I. Talk 07. November 2022.

PATENT:

Water vehicle propeller.
URL: https://umapatent.uma.es/en/patent/propulsor-para-vehiculos-acuaticos727/.
Inventors: R. Fernandez-Feria, E. Sanmiguel-Rojas, and P. E. Lopez-Tello.
Priority date (Application to the Spanish Patent Office, code P202230954): November 4th, 2022.
International application (code PCT/ES2023/070644): October 31th, 2023.
Currently with Positive State of the Art Report from the Spanish Patent Office: February 23th, 2023.

Contents

Chapter 1

Introduction

1.1 Motivation

Since the beginning of time, human beings have observed and taken inspiration from nature, which is not casual. Nature has proved its unquestionable validity through one of the hardest possible tests, the evolutionary process, where all forms of life adapt to extreme conditions or disappear in time. This simple process of trial and failure has allowed life to evolve from the first simple cell to all the diversity of beings we have today. Scientists and engineers know that very well, and for that reason, they try to understand and replicate the physics behind numerous biological processes. In this direction, one of the most attractive and fascinating research fields is the movement of animals, especially that of the swimming and flying species, since they have shown extraordinary performance in a vast majority of adverse conditions. In addition, the study of this field has taken great interest in the last century due to the evident and potential benefits derived from this method of propulsion and all the technology and devices that can be created as a result.

In this context, researchers have extensively analyzed the movement of several fishes and aquatic mammals, concluding that their way of movement can be characterized into three main categories (Webb [1975]). These categories are based on the body and fin movements, which are the following: fish that use their bodies and caudal fins, fish that use extended median or paired fins, and fish that use shorter median or paired fins. Of these three categories, the first is the most common in nature, and inside that, researchers distinguish five main modes, which are: the anguilliform mode, in which a wave passes evenly along a long slender body (e.g., eels), the subcarangiform mode in which the wave increases quickly in amplitude towards the tail (e.g., trouts), the carangiform mode in which the wave is concentrated near the tail and oscillates rapidly (e.g., remoras), the thunniform mode characterized by rapid swimming with a large powerful crescent-shaped tail (e.g., lamnid sharks), and finally the ostraciform mode with almost no oscillation except that of the tail fin (e.g., Ostraciidae).

Scientists have studied all these ways of movement (e.g., Lighthill [1969, 1970, 1971], Wu [1971a,b]), particularly to find new forms of propulsion, wondering if it is possible to replicate this behavior for aquatic vehicles and take advantage of its good performance (Triantafyllou and Triantafyllou [1995], Triantafyllou et al. [2000], Lauder et al. [2007], Wen et al. [2012],

Gibouin et al. [2018], Smits [2019], Zhu et al. [2019b], Sanchez-Rodriguez et al. [2021]). In the specific case of the carangiform group, it was found that propulsion was mainly produced by their caudal fin, so it could be relatively easy to replicate and study. Therefore, it opened a completely new and unexplored field based on what we know as flapping foils. In this sense, several aquatic technologies based on this system have been developed in the past few decades (Triantafyllou et al. [1993], Yamamoto et al. [1995], Rozhdestvensky and Ryzov [2003], Platzer et al. [2008], Augier et al. [2015], Wu et al. [2020]). These new propellers present some advantages in relation to traditional rotating propellers, such as higher maneuverability and easier control. They also perform at a lower frequency, which is more environmentally friendly than the conventional ones, have fewer cavitation problems, which can promote a longer useful life, and produce less noise.

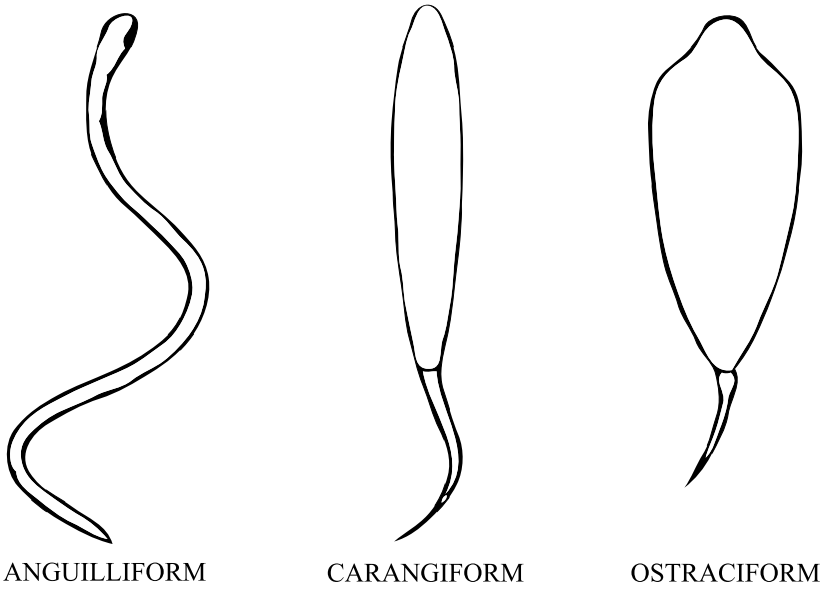

Figure 1.1: Scheme of the main modes of movement from fish that use their bodies and caudal fins in their locomotion. Figure from Webb [1975].

As it is well summarized in Wu et al. [2020], flapping foils are quite more complex than they look at first glance. Generally, the problem involving a flapping foil can be governed by around ten parameters, which is not simple at all. They can be divided into four types: environmental parameter (describing the fluid properties), geometric parameter (describing the shape of foils), kinematic parameter (describing the motion of foils), and performance parameter (describing propulsion and energy harvesting performance of foils).

The main environmental parameters considered in these studies are freestream velocity U_∞, kinematic viscosity ν of the fluid, which are summarized in the Reynolds number Re, defined as

$$Re = \frac{U_\infty L_0}{\nu}, \tag{1.1}$$

where L_0 is the characteristic length that can be represented by the chord length c, the max-

imum thickness D, or the span length s of the flapping foil. For two-dimensional (2D) cases, the common length used is the chord or the semi-chord length.

Concerning the geometric parameters, those are related to the shape of the foil, which are the chord length c (or the semi-chord length), the maximum thickness D, the span length s, the cross-section shape, and the planform for the three-dimensional cases. For the 2D foil, only c, D, and the cross-section shape are considered. The common cross-section shapes of interest are rectangles, ellipses, and teardrops (e.g., NACA profiles).

About the kinematic parameters (related to the motion of the foil), the main ones are the Strouhal number St and the reduced frequency k, both used to describe the externally imposed frequency. The Strouhal number is defined as

$$St = \frac{\tilde{f} L_0}{U_\infty}, \tag{1.2}$$

where $\tilde{f}$ is the frequency of the oscillation, and similarly to the Reynolds number case L_0 can be represented by the chord length c, the maximum thickness D, or the peak-to-peak amplitude $\tilde{A}$, which is the parameter more commonly used in the bibliography. Notice that a *tilde* is used to remark that the variable is in the dimensional form to distinguish it from its dimensionless counterpart. On the other hand, the reduced frequency is defined as

$$k = \frac{\omega c}{2U_\infty} = \frac{\pi \tilde{f} c}{2U_\infty}, \tag{1.3}$$

being ω the angular velocity of the movement. It is found that the Strouhal number based on the peak-to-peak amplitude is limited in a narrow range for fish-like swimming and flapping flight animals in nature, which is from 0.2 to 0.4 as it is well depicted in (Taylor et al. [2003], Gazzola et al. [2014], Saadat et al. [2017]). In addition, the flapping foil motion is usually designed to couple two sinusoidal motions with the same frequency. Those are defined in dimensional form as

$$\tilde{h}(\tilde{t}) = \tilde{h}_0 \sin\left(2\pi \tilde{f} \tilde{t}\right), \tag{1.4}$$

$$\tilde{\alpha}(\tilde{t}) = \tilde{\alpha}_0 \sin\left(2\pi \tilde{f} \tilde{t} + \phi\right), \tag{1.5}$$

where $\tilde{h}(\tilde{t})$ and $\tilde{\alpha}(\tilde{t})$ are the instantaneous vertical position of the foil and the instantaneous angle between the freestream velocity and the foil chord, respectively. On the other hand, $\tilde{h}_0$ and $\tilde{\alpha}_0$ are the heave and pitch amplitudes, and ϕ is the phase angle between pitch and heave. Notice that some authors named the pitching motion as $\tilde{\theta}(\tilde{t})$ to differentiate it from the angle of attack, which is usually named $\tilde{\alpha}$ when it is considered for the study. However, in this thesis, we are going to assume the general nomenclature, which is $\tilde{\alpha}(\tilde{t})$ for the pitching motion (see Figure 1.2 for more clarity). These pitch and heave are applied at the pivot point axis, located at a distance $\tilde{a}$ from the leading edge (LE), or $c - \tilde{a}$ from the trailing edge (TE) of the foil.

Finally, the performance parameters used to describe the propulsion performance include the thrust coefficient C_T, the input power coefficient C_P, and the propulsion efficiency η.

These quantities are normally used with time or cicle-average value. Thus, the mean thrust coefficient is defined as

$$\overline{C_T} = \frac{2\overline{T}}{\rho U_\infty^2 cs}, \tag{1.6}$$

where ρ is the fluid density and $\overline{T}$ is the time-averaged force in the direction of the fluid, i.e. the thrust force, which is defined as

$$\overline{T} = \frac{1}{\tau}\int_0^\tau T(\tilde{t})d\tilde{t}, \tag{1.7}$$

being $T(\tilde{t})$ the instantaneous force component in the $\tilde{x}$ direction and τ the oscillation period. The mean input power coefficient is defined as

$$\overline{C_P} = \frac{2\overline{P}}{\rho U_\infty^3 cs}, \tag{1.8}$$

where $\overline{P}$ is the mean input power, which can be calculated by

$$\overline{P} = \frac{1}{\tau}\left[\int_0^\tau L(\tilde{t})\frac{d\tilde{h}(\tilde{t})}{d\tilde{t}}d\tilde{t} + \int_0^\tau M(\tilde{t})\frac{d\tilde{\alpha}(\tilde{t})}{d\tilde{t}}d\tilde{t}\right], \tag{1.9}$$

where $L(\tilde{t})$ is the instantaneous force component in $\tilde{y}$ direction, i.e. lift force, and $M(\tilde{t})$ is the instantaneous pitching moment.

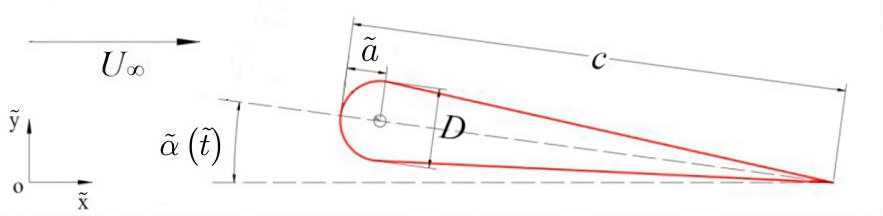

Figure 1.2: Schematic of the foil kinematic parameters. Figure adapted from Wu et al. [2020] to this thesis nomenclature.

Hence, the final propulsion efficiency is obtained by

$$\eta = \frac{\overline{C_T}}{\overline{C_P}}. \tag{1.10}$$

On the other hand, some of the most commonly used coefficients are the mean lift coefficient, defined as

$$\overline{C_L} = \frac{2\overline{L}}{\rho U_\infty^2 cs}, \tag{1.11}$$

and the mean pitching moment coefficient, which is

$$\overline{C_M} = \frac{2\overline{M}}{\rho U_\infty^2 c^2 s}. \tag{1.12}$$

In the particular case of self-propulsion of a flapping foil, the swimming velocity $\tilde{u}(\tilde{t})$ is not constant, so that we cannot use a constant free stream velocity U_∞ to non-dimensionalyze the different variables and parameters. Instead one uses ωc. Thus, the above time-average parameters can be rewritten using a *hat* as a superscript to remark that they are based on frequency ω:

$$\overline{\hat{C}_T} = \frac{8\overline{T}}{\pi\rho c^3\omega^2 s}, \quad \overline{\hat{C}_P} = \frac{16\overline{P}}{\pi\rho c^4\omega^3 s}, \quad \overline{\hat{C}_L} = \frac{8\overline{L}}{\pi\rho c^3\omega^2 s}, \quad \overline{\hat{C}_M} = \frac{8\overline{M}}{\pi\rho c^4\omega^2 s}. \tag{1.13}$$

Therefore, the efficiency η can also be defined in terms of these new parameters

$$\eta = \frac{\overline{u\hat{C}_T}}{\overline{\hat{C}_P}}. \tag{1.14}$$

Finally, there is another performance parameter that is interesting to consider in the self-propulsion case: the cost of transport. It is usually defined as the energy consumption per unit distance traveled by the vehicle

$$\widetilde{CoT} = \frac{\overline{P}}{\widetilde{U}}, \qquad CoT = \frac{\overline{\hat{C}_P}}{U}, \tag{1.15}$$

where $\widetilde{U}$ is the mean cruising velocity of the flapping foil in dimensional form. It is also important to remark that all these coefficients have been defined for a 3D flapping foil, and for the two-dimensional cases (the ones that will be covered in this thesis), the expressions are equal but with the span length s removed since the forces will have units of force per length span.

The motion of the foil can be categorized into three main modes: pitching, heaving, and flapping, which is a combination of the above (see Figure 1.3). These motions can also be classified as full-active motion, which means that both pitching and heaving motions are prescribed (imposed), semi-active motions, with commonly forced pitching and induced heaving motions (it can also be forced heaving and induced pitching), and fully-passive motions, where both movements are self-sustained.

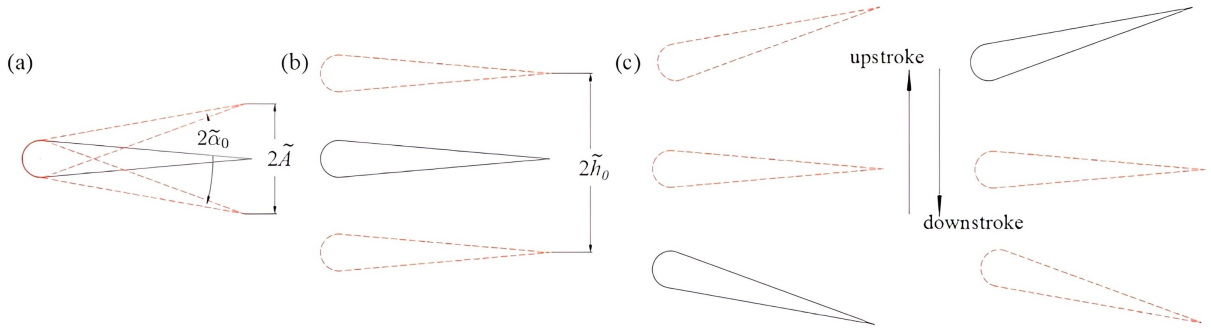

Figure 1.3: Schematics of (a) pitching motion, (b) heaving motion, and (c) flapping motion. Figure adapted from Wu et al. [2020] to this thesis nomenclature.

To sum up, flapping foil technology has been widely studied from several approaches, especially during the last two decades. From the experimental field is habitual to perform simulations in water and wind tunnels (Schnipper et al. [2009], Lua et al. [2016], Andersen et al. [2017], Dash et al. [2018]), but also exists innovative approaches using testing tanks (Anderson et al. [1998], Read et al. [2003], Hover et al. [2004], Schouveiler et al. [2005]), being the Particle Image Velocimetry (PIV) the most popular technique used to extract information in these studies. The problem can also be studied from a numerical perspective, which is becoming more and more popular as technology develops. Many research teams use complex computational codes developed by themselves, which is known as Direct numerical simulations (DNS) (e.g., Arranz et al. [2018], Gonzalo et al. [2018], Moriche et al. [2019]). In contrast, Computational fluid dynamics (CFD) are now more commonly used and implemented on some commercial or open-source codes (e.g., Fluent, CFX, OpenFOAM). Most of them are based on Finite Volume Method (FVM) and a few on Finite Element Method (FEM) and Finite Difference Method (FDM), (Medjroubi et al. [2011], Boiron et al. [2012], Medjroubi et al. [2012], Yu et al. [2012, 2013], Wu et al. [2014, 2015], Lua et al. [2016], Yu et al. [2017]).

Nevertheless, both approaches are demanding on time and challenging to perform. Also, the amount of results is frequently insufficient to extract general tendencies. For this reason, a theoretical approach to the matter can be so beneficial since it can provide plenty of information and guide the above-mentioned experiments and studies with minimal computational cost (Sanchez-Rodriguez et al. [2020]). In this direction, the linear potential-flow theory is still a powerful tool for understanding and estimating the aerodynamics involved in flapping foils when small amplitudes are involved. This theory was originally developed for two-dimensional foils undergoing an arbitrary harmonic motion by Lighthill [1970] and Wu [1961, 1971a,b]. It contained the pitching and heaving motion of a rigid foil, which was previously studied for lift and moment by Theodorsen [1935] and for thrust and propulsive efficiency by Garrick [1936]. In addition, the vortical impulse theory plays an important role when studying the unsteady aerodynamics of slender bodies at high Reynolds numbers and especially on the physics behind the aerodynamic force and moment. The first contact was performed by von Kármán and Sears [1938] to obtain the lift and moment on a rigid foil undergoing an arbitrary motion and more recently by Fernandez-Feria [2016], who included the thrust force and the propulsive efficiency for a pitching and a heaving rigid foil. This new formulation also corrects Garrick [1936] for moderate and high reduced frequencies and substantially modifies the prediction of the kinematic conditions, especially for high reduced frequencies, that optimize the propulsion efficiency of heaving and pitching rigid foils (Fernandez-Feria [2017]).

Part of this thesis is devoted to the propulsion by flexible flapping foils. For this study, it is required additional characterization of the chordwise flexural deflection of the foil (and of the spanwise deflection for 3D foils). Moreover, it is found that flexibility can affect the formation of leading edge vortex (LEV), trailing edge vortex (TEV), and tip vortex, yielding in a more significant performance when the proper values are selected in both spanwise (Heathcote et al. [2008], Cleaver et al. [2016]) and chordwise (Prempraneerach et al. [2003], Bansmer et al. [2010], Alben et al. [2012], Barannyk et al. [2012], Dai et al. [2012], Marais et al. [2012], Dewey et al. [2013], Tian et al. [2013]) directions. In this sense, a common

approach to studying a flexible foil is combining a rigid NACA foil in the head location and a flat plate of variable flexibility in the tail (Heathcote et al. [2004], Heathcote and Gursul [2007], Monnier et al. [2015], Kumar and Shin [2019]).

On the other hand, since the deformation of the foil is passive in most cases, i.e., originated by its pitching and heaving kinematics, one also has to consider the fluid-structure interaction (FSI). This interaction has to be considered also for a rigid foil when it is ellastically supported and allow for passive heaving and/or pitching motions. In this direction, research has shown a significant enhancement in the performance parameters of the foil, such as thrust generation and efficiency (Anevlavi et al. [2020], Dagenais and Aegerter [2020], Manjunathan and Bhardwaj [2020], Wang et al. [2020], Demirer et al. [2021]). Many investigations about flexible foils have attributed that to resonance, i.e., to peaks in the passive deflection amplitude when the forcing frequency of the oscillations is at, or near, the natural frequencies of the fluid–foil system (Alben et al. [2012], Dewey et al. [2013], Quinn et al. [2014], Paraz et al. [2016], Floryan and Rowley [2018]). In the case of small forcing amplitudes, the lowest frequency is the more relevant, and it is proved to be responsible for the first mode flapping (Alben [2008], Moore [2015]). As the amplitude of the oscillations increases, higher modes become more relevant, and resonance ceases to be the primary enhancement mechanism in the propulsive performance of a deformable flapping foil (Ramananarivo et al. [2011], Alben et al. [2012], Quinn et al. [2014], Floryan and Rowley [2018], Goza et al. [2020]). In this context, also linear potential-flow theory in combination with the Euler-Bernoulli beam equation can provide helpful information as it is shown in Fernandez-Feria and Alaminos-Quesada [2021a,b] (this particular approach will be covered extensively in this thesis). And especially if some CFD is performed to validate the theoretical results as it is well conducted in Fernandez-Feria and Sanmiguel-Rojas [2019] and Sanmiguel-Rojas and Fernandez-Feria [2021, 2022].

To conclude, as it was summarized above, flapping foils have significant potential, and it has motivated researchers around the world to analyze this promising technology, especially during the last decade. They do not only offer novel means of propulsion for existing aquatic vehicles but also can enhance current energy harvesting systems, particularly those relying on conventional rotary turbines. Concerning the aquatic locomotion by flapping foils, its thrust generation has been widely analyzed in recent years (Lauder [2015], Mackowski and Williamson [2015], Fernandez-Feria [2017], Smits [2019], Wu et al. [2020], Paniccia et al. [2021]), and some bio-inspired prototypes have been proposed (Gibouin et al. [2018], Zhu et al. [2019a], Sanchez-Rodriguez et al. [2021]). In addition, the effect of the chordwise flexibility of the foil, which in general can enhance the propulsion performance, has also been extensively studied (Kang et al. [2011], Marais et al. [2012], Cleaver et al. [2014], Monnier et al. [2015], David et al. [2017]). Many experimental and numerical works (for both 2D and 3D) have been conducted in this area, but most of them are for oscillating foils in a fluid stream with a fixed velocity rather than for self-propelled foils, and only a few of them for a vehicle or body propelled by a flapping foil. However, none of them, to the best of our knowledge, have analyzed the case of flapping foils that are elastically mounted on the vehicle hull through translational and torsional springs and dampers. Hence, the performance and efficiency of this novel prototype, which allows for passive heaving, pitching, and flexural

deflection (in the case of a flexible foil) motions, remains unknown. Additionally, the fluid-structure interaction that results from these kinematics may allow for the resonance of the fluid-foil system in some particular configurations, yielding a better performance. Therefore, simple models based on rigorous results are necessary, even though limited to very specific situations, that allow for easy and quick guidance in the design of such self-propelled vehicles.

Concerning the energy harvesting systems based on the flapping foil technology, many studies have been conducted in last years and several devices have been proposed (Kinsey et al. [2011], Wu et al. [2014, 2015], Deng et al. [2015], Derakhshandeh et al. [2016], Griffith et al. [2016], Sitorus et al. [2016], Teng et al. [2016], Kim et al. [2017], Xu et al. [2017], Zhan et al. [2017]). These systems primarily consist of a foil that undergoes periodic translating and rotating motions in an incoming flow. Moreover, they are particularly well-suited for shallow and wide flow channels, where their rectangular cross-sections can harvest large portions of the flow and can operate more efficiently in slower flows than the conventional rotary designs. Of particular relevance is the fully-passive flapping-foil turbine that was originally developed by Boudreau et al. [2018] based on the work of Veilleux and Dumas [2017]. This concept involves a foil that is elastically mounted in pitch and in heave. As a result, the design relies on a divergence instability to start and sustain the motion and on non-linearities in the flow (dynamic stall) to limit the amplitudes, resulting in self-sustained, limit-cycle oscillations. Additionally, some recent studies consider the dependence of its dynamic behavior on the combination of the structural parameters and provide insight into the underlying fluid–structure interaction (Duarte et al. [2019, 2021a,b]). However, to the best of our knowledge, there are still no works that experimentally analyze how the fluid exchanges energy with this promising prototype. Therefore, a first approach to this issue is required so that it can guide and propose efficient configurations for future projects.

1.2 Objectives

The principal objective of this thesis is to conduct a comprehensive analysis with the intent of gaining a profound understanding of the flapping-foil technology. Specifically, the focus is on elucidating its potential applications in the realms of bio-inspired aquatic vehicles and innovative energy harvesting devices. To that end, some precise aims are conducted in the several chapters that compounds this thesis and are summarized below.

- The first objective is to adequately comprehend the physics and fluid-structure interaction inherent in the locomotion of a foil in its most straightforward manifestation. This involves studying an isolated self-propelled rigid foil undergoing a prescribed pitching motion. To achieve that, high-resolution numerical simulations and a model for the unsteady viscous friction on the foil are very beneficial.

- Once the locomotion of the isolated pitching foil is properly understood, the subsequent goal is to assess the viability of an operational aquatic vehicle. Consequently, the second objective involves formulating a model for the aforementioned aquatic vehicle, which is characterized by a flapping foil elastically mounted on the vehicle hull through translational and torsional springs and dampers. A rigid foil is used for this

first approach. Furthermore, a comprehensive analysis of various parameters such as swimming velocity, efficiency, and cost of transport in relation to the structural parameters is conducted to identify the most efficient configuration.

- Subsequently, the third objective is to scrutinize the impact of flexibility on the foil in the proposed aquatic vehicle. Therefore, a more intricate model is required, incorporating the effects of chordwise flexural deflection of the foil. This is achieved by integrating the Euler-Bernoulli beam equation and assuming a quartic approximation for the vertical displacement of the foil. Once again, a detailed analysis of several parameters for different values of the stiffness ratio of the foil is conducted, leading to the proposal of optimal configurations.

- Lastly, the fourth objective of this thesis involves conducting an experimental investigation into the fully-passive flapping-foil turbine. This investigation is centered on characterizing the device's performance across a diverse range of operational conditions, with a specific focus on elucidating the dynamic interaction between the fluid and the flapping-foil prototype. To accomplish this, a prototype similar to the one developed by Boudreau et al. [2018] is employed, improved by the inclusion of a force/torque sensor. Subsequently, a comprehensive model is formulated, incorporating all the structural parameters alongside the measured forces and moment acting on the axis of the foil. This model facilitates the examination of power coefficients and efficiencies associated with the device. Consequently, optimal configurations are proposed, serving as a preliminary foundation for future projects. Additionally, some PIV tests are conducted for specific configurations in order to enhance our comprehension of the operational dynamics of the device.

1.3 Thesis outline

Apart from the introduction and the closure, this thesis will be organized into four main chapters. A brief description is provided below.

- In Chapter 2, we will introduce the theoretical approach for the simpler case of a self-propel pitching foil using two different models of the unsteady thrust force based on linear potential theory. Both are complemented with a new simple model developed for the unsteady viscous friction obtained from high-resolution numerical simulations.

- In Chapter 3, we will explore a new theoretical model for an aquatic vehicle self-propelled by a rigid foil undergoing pitching oscillations that are generated by a torque of small amplitude. Also, the results will be validated with high-resolution numerical simulations, and some helpful power laws for the propulsion performance will be obtained. In addition, some optimal configurations for the propulsion performance will be suggested.

- In Chapter 4, we will present a final theoretical model for the locomotion of an aquatic vehicle propelled by a flexible foil actuated by a torque of small amplitude. We will

obtain simple power laws for this model and compare them with the numerical solution of the governing equation. Again, some optimal configurations will be proposed.

- Finally, in Chapter 5 we will investigate experimentally a fully-passive flapping-foil turbine prototype. The kinematics of the device, as well as the forces and moment acting on the foil, will be analyzed for a wide range of operating conditions. Both the harvesting efficiency of the prototype and the efficiency based on the power extracted from the fluid will be studied. Additionally, some of the operating points will be analyzed with the Particle Image Velocimetry (PIV) technique, and some useful information will be provided about the dynamic stall on the foil.

Moreover, four appendices will be added at the end of the manuscript, providing complementary information for a better understanding.

- Appendix A will contain a summary of the vortical impulse theory, where the main coefficients come from, and also some parameters to obtain greater clarity in the rest of the chapters.
- Appendix B will introduce the two-scale method for solving problems using a perturbative development, which will be used in Chapter 2 and Chapter 3.
- Appendix C will explain the technique used to solve the system of ordinary differential equations numerically through the commercial solver Matlab.
- Appendix D will cover the whole parameter characterization of the flapping-foil turbine prototype studied in Chapter 5.

Chapter 2

A simple non-stationary model for a self-propelled pitching foil

2.1 Introduction

Researchers have studied natural swimmers extensively, especially those that use flapping foils and tails for their locomotion, as we mention in Chapter 1. They have performed both numerical and experimental studies generally with very fixed and control conditions and based on them several scaling laws have been obtained characterizing the aquatic locomotion, i.e. the time-averaged final swimming velocity in terms of the Strouhal and Reynolds number among other parameters (Triantafyllou et al. [2005], Eloy [2012], Gazzola et al. [2014], Floryan et al. [2017], Saadat et al. [2017], Lin et al. [2021], Das et al. [2022]). However, when we look for simple models that can provide quick and reliable information (not only for its time-averaged value) to start the designing process, the literature is scarce.

Sanchez-Rodriguez et al. [2020] considered this problem working on a novel model for the self-propulsion of a rigid pitching foil using the results of Theodorsen [1935] and Garrick [1936] from linear potential theory for the unsteady lift and thrust forces exerted by the fluid on the foil and complementing the inviscid forces with a constant drag coefficient C_D. However, this assumed constant drag is not a proper model for the final swimming velocity because skin friction drag is not constant for an oscillatory foil.

For that reason, we explore here the idea of a simple non-stationary model for a two-dimensional self-propelled pitching foil, which could provide some analytical and more accurate expressions. Thus, a model for the unsteady viscous drag coefficient $C_D(t)$ will be developed taking advantage of the full-numerical simulations of a self-propelled pitching foil, which will be presented later in the chapter, in the Reynolds number's range of interest for natural and robotic swimmers. Moreover, this new drag model will be combined with two different formulations of the thrust force from the linear potential theory from Garrick [1936] and Fernandez-Feria [2016], and some simple non-stationary models for the self-propulsion of rigid pitching foil will be obtained. Besides that, to assess the range of validity of these new simple models, their results will be compared with the high-resolution numerical simulations,

conducted here together with the numerical resolution of the model equations. The developed simple models will provide analytical results not only for the time-averaged swimming velocity but also for the amplitude, frequency, and phase of its oscillations. Furthermore, the transient time needed to reach the final cruising state will be also studied.

2.2 Formulation of the problem

We consider an underwater, self-propelled swimmer consisting of a two-dimensional hydrofoil of mass m per unit span s and chord length c. Assuming that the swimming propulsion is triggered by an imposed sinusoidal pitching motion,

$$\tilde{\alpha} = \tilde{\alpha}_0 \sin(\omega \tilde{t}), \tag{2.1}$$

applied at a given pivot axis $\tilde{a}$, where $\tilde{\alpha}_0$ is the pitching amplitude, ω the frequency and $\tilde{t}$ the dimensional time. Remember that we use a *tilde* to denote that the variable is in the dimensional form, to distinguish it from its dimensionless counterpart. In addition, to simplify the full numerical simulations presented in the next section, the center of mass $\tilde{x}_0$ coincides with the pivot point, and it is constrained to move only along the $\tilde{x}$ axis, i.e., the heaving motion of the foil is not considered. This inhibition of the heaving motion will reduce the propulsion capabilities of the swimmer (Sanchez-Rodriguez et al. [2020], Das et al. [2022]), but it will still serve for the validation purposes of the present chapter. It is important to remark that the pitching motion $\tilde{\alpha}$ is measured clockwise, as it is common in the aerodynamics literature (see Figure 2.1).

The motion of the foil is governed by Newton's second law applied to the center of mass,

$$m\dot{\tilde{u}} = -F_x, \tag{2.2}$$

where $\tilde{u}$ is the dimensional swimming velocity, F_x is the $\tilde{x}$-component of the force per unit span that the fluid exerts on the foil, and a *dot* denotes a derivative with respect to time (dimensional time in this case). To obtain F_x, one has to solve the incompressible Navier-Stokes (N-S) equations, which are

$$\begin{aligned} \nabla \cdot \widetilde{\mathbf{w}} &= 0, \\ \rho \frac{\partial \widetilde{\mathbf{w}}}{\partial \tilde{t}} + \rho \widetilde{\mathbf{w}} \cdot \nabla \widetilde{\mathbf{w}} &= -\nabla \tilde{p} + \mu \nabla^2 \widetilde{\mathbf{w}}, \end{aligned} \tag{2.3}$$

being $\widetilde{\mathbf{w}}$ the fluid velocity field, ρ the fluid density, $\tilde{p}$ the pressure field and μ the dynamic viscosity.

2.2.1 Non-dimensional formulation

Once the problem is presented, it is always more general and enlightening to work on non-dimensional variables. Thus, non-dimensional variables will be used in what follows, except specified otherwise. Lengths will be scaled with the semi-chord length $c/2$ and time with ω^{-1}. So, the main non-dimensional variables of the problem will be

$$x = \frac{\tilde{x}}{c/2}, \quad z = \frac{\tilde{z}}{c/2}, \quad \alpha = \tilde{\alpha}, \quad t = \tilde{t}\omega, \quad u = \frac{\tilde{u}}{\omega c/2}, \quad \dot{u} = \frac{\dot{\tilde{u}}}{\omega^2 c/2}. \tag{2.4}$$

Notice that the non-dimensional pitching motion does coincide with its dimensional counterpart since the parameter $\tilde{\alpha}$ is measured in radians. Therefore, the hydrofoil spans from $x' = -1$ to $x' = 1$ in the coordinates (x', z') attached to the mid-chord point of the foil (see Figure 2.1 for more clarity). The center of mass and the pivot point are at $x' = -1$, corresponding $x' = -1$ to the foil's leading edge (LE) and $x' = 1$ to its trailing edge (TE).

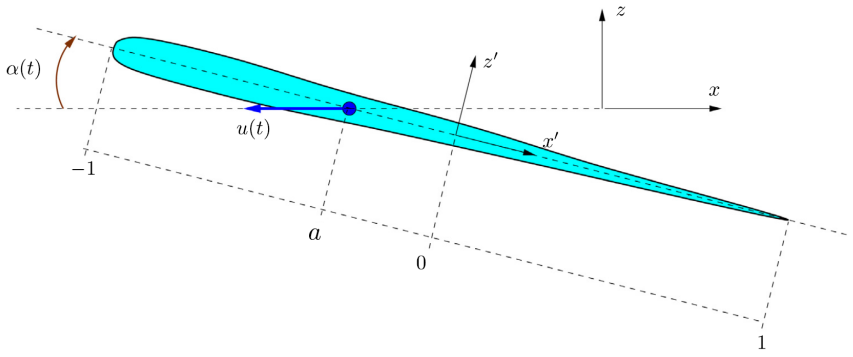

Figure 2.1: Sketch of the self-propelled foil (dimensionless quantities).

The non-dimensional swimming velocity $u(t)$, considered positive when directed towards the negative x axis of the absolute coordinates system (x, z), is in fact the inverse of the reduced frequency $k(t)$ commonly used in unsteady aerodynamics (e.g., Theodorsen [1935]), but now depending on time,

$$u(t) = \frac{\tilde{u}}{\omega c/2} = \frac{1}{k(t)}. \tag{2.5}$$

The governing equation of the motion of the foil in dimensionless format will be

$$R\dot{u} = -\hat{C}_x, \tag{2.6}$$

being

$$R = \frac{4m}{\pi\rho c^2}, \quad \hat{C}_x = \frac{8F_x}{\pi\rho c^3\omega^2} = \frac{u^2 C_x}{\pi}, \tag{2.7}$$

where R is the non-dimensional mass of the hydrofoil and $\hat{C}_x$ the non-dimensional counterpart of F_x. Also, remember that a *hat* is used to remark that this is not the standard coefficient associated with the force F_x, which would be $C_x = 2F_x/(\rho\tilde{u}^2 c)$, also included in Equation (2.7) for comparison's sake.

The incompressible Navier-stokes equations will now be in the non-dimensional format as follows

$$\begin{gathered} \nabla \cdot \mathbf{w} = 0, \\ \frac{\partial \mathbf{w}}{\partial t} + \mathbf{w} \cdot \nabla \mathbf{w} = -\nabla p + \frac{1}{Re_\omega}\nabla^2 \mathbf{w}, \end{gathered} \tag{2.8}$$

where $\mathbf{w}$ is the non-dimensional fluid velocity field (scaled with $\omega c/2$), p is the non-dimensional pressure field (scaled with $\rho\omega^2 c^2/4$), and a Reynolds number based on the frequency and the chord length has been defined

$$Re_\omega = \frac{\rho\omega c^2}{4\mu}. \tag{2.9}$$

These governing equations of the problem will be solved numerically to obtain the above-mentioned new drag model, which will be used to assess the validity range of the thrust model performed by Garrick [1936] and Fernandez-Feria [2016]. Another relevant parameter of interest for the locomotion through flapping foils is the corresponding Strouhal number (Triantafyllou et al. [1991], Taylor et al. [2003], Gazzola et al. [2014]), defined as

$$St = \frac{\tilde{f}\tilde{A}}{\widetilde{U}} = \frac{A}{2\pi U}, \tag{2.10}$$

where $\tilde{f} = \omega/(2\pi)$ is the actuation frequency in Hertz, $\widetilde{U}$ the dimensional mean forward speed, $\tilde{A}$ the dimensional beat amplitude, and U and A their non-dimensional counterparts. Notice that $\tilde{A}$ and A are taken as the maximum peak-to-peak trailing edge amplitude, i.e., $A = 2(1-a)\sin(\alpha_0)$ for the present pitching motion. Another non-dimensional parameter of interest is the Reynolds number associated with the swimming velocity, which is defined as

$$Re = \frac{\rho \widetilde{U} c}{\mu} = 2U Re_\omega. \tag{2.11}$$

2.3 Numerical method

To solve the coupled problem of fluid-structure interaction (FSI), we use the finite volume-based solver Ansys-Fluent v21.2, and to facilitate the simulations and comparison with the lineal potential theory models, the foil is considered as a thin flat plate with the pivot point (and center of mass) located at the leading edge. However, the theoretical models presented in the subsequent sections are general for any slender foil, as shown in Figure 2.1. Specifically, the fluid part is solved using both laminar flow (as in Sanmiguel-Rojas and Fernandez-Feria [2021]) and transition $k-\omega$ SST model (Sanmiguel-Rojas and Fernandez-Feria [2022]). On the other hand, to simulate the FSI, the plate is mimicked by a User Defined Function (UDF), i.e., a C program compiled in Fluent. Specifically, we use the Ansys-Fluent supplied function declaration DEFINE-CG-MOTION. Thanks to this C macro, the pitching motion defined in Equation (2.1) is imposed and, simultaneously, the motion of the foil is integrated at each time step solving Equation (2.6) computationally.

Transient, pressure-based, coupled solver with absolute velocity formulation are the settings for the solution of all simulations. The least-squares cell-based method is applied for calculating the gradients of the transport quantities on the faces of the cells. The spatial discretization methods are solved with second-order for the pressure term and second-order upwind for continuity, momentum, and turbulent quantities. The explicit relaxation factors of pressure and momentum are set at 0.75 to ensure the stability of the numerical method. The overset method is used for the moving mesh. The first-order implicit formulation is applied for discretizing the time derivatives in order to accomplish numerical stability for the dynamic mesh algorithm. At each time step, the convergence is considered reached once the absolute residuals values $5\cdot10^{-4}$, 10^{-3} and $5\cdot10^{-5}$ for continuity, turbulence, and momentum quantities are fulfilled, respectively. All simulations start from rest.

2.3.1 Computational domain and meshing

The computational domain (see Figure 2.2) is related to the chord length assuming a width of $20c$ and a length of $32c$ in all simulations. It was seen that with larger computational domains, the results have practically not changed, even in the most computationally demanding cases. The mesh consists of two different regions: a background mesh and a mesh moving as a rigid solid with the plate. This moving mesh is the one that contains the above-mentioned thin flat plate, which has a length of $c = 0.2$ m and a thickness of $0.01c$, with rounded ends (see Figure 2.5). Moreover, we assume that all the mass of the plate is concentrated at the center of mass, i.e., at the leading edge of this flat plate.

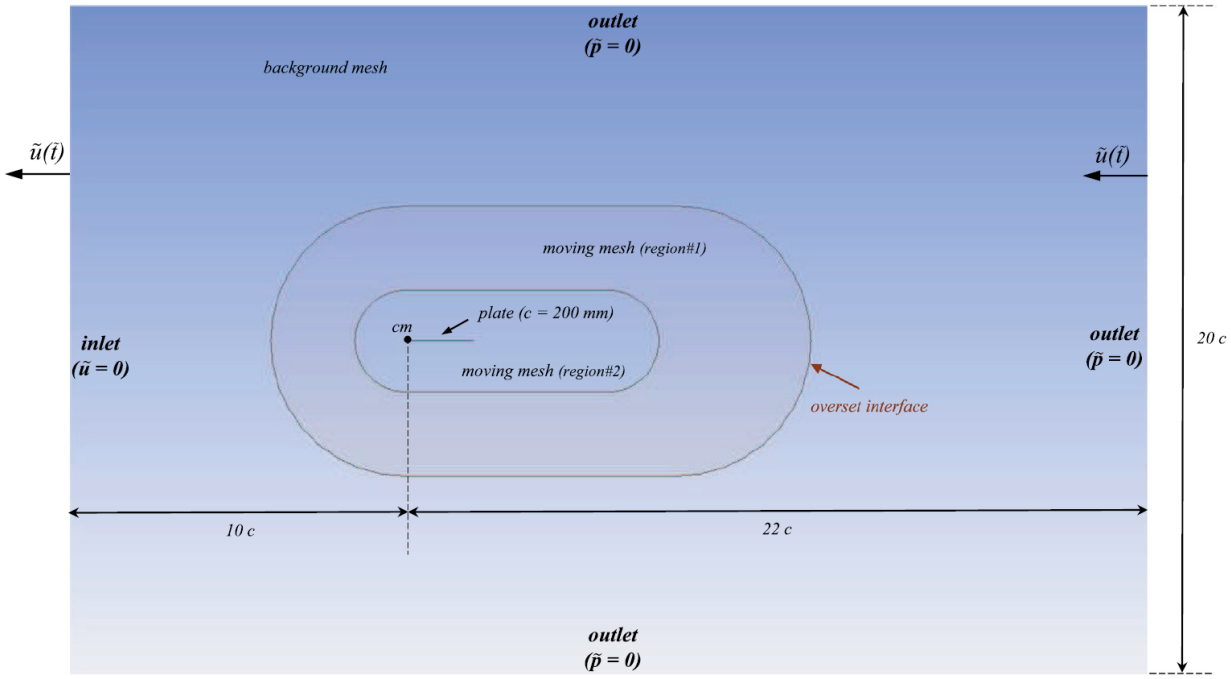

Figure 2.2: Computational domain, including subdomains, dimensions, and some indications of boundary conditions.

As the moving mesh eventually would reach the left wall and the collision would disrupt the code, we need to keep the size of the initial computational domain constant as the mesh is moving. To solve that problem, we use the layering algorithm as a dynamic mesh to destroy (on the right) and to build up (on the left) the background mesh with the velocity u of the center of mass of the plate. The moving mesh interpolates continuously over the background mesh thanks to the overset interface (see Figure 2.5). Furthermore, the moving mesh is split into two different regions to ease the meshing procedure around the plate and, at the same time, to ensure a good interpolation procedure over the background mesh at the overset interface. About the boundary conditions, which are also indicated in Figure 2.2, we set the absolute velocity to zero at the inlet, at a distance of $10c$ upstream of the plate, the non-slip wall condition on the foil, and the pressure outlet $p = 0$ on the rest of the boundaries.

Once the computational domain is established, the next step is creating the mesh. We use quad cells for that purpose since they provide higher quality solutions with fewer cells/nodes than a comparable tri mesh, and also, they reduce numerical diffusion when the mesh is aligned with the flow, which is the case. So, both background and moving meshes are designed to include only quad cells. On the other hand, to create a mesh of high quality, one has to look for some mesh metrics. In that sense, one of the most valuable parameters is the skewness factor. This value is directly related to the quality of the mesh structure. It shows how much of that mesh is close to its ideal shape or form, which is an equiangular quad. Thus, the closer the skewness of the mesh structure is to zero, the higher its mesh quality. Taking that into account, the meshes will be designed to allow a maximum skewness of 0.6. In Figure 2.3, the skewness of the elements for one of the used meshes is shown.

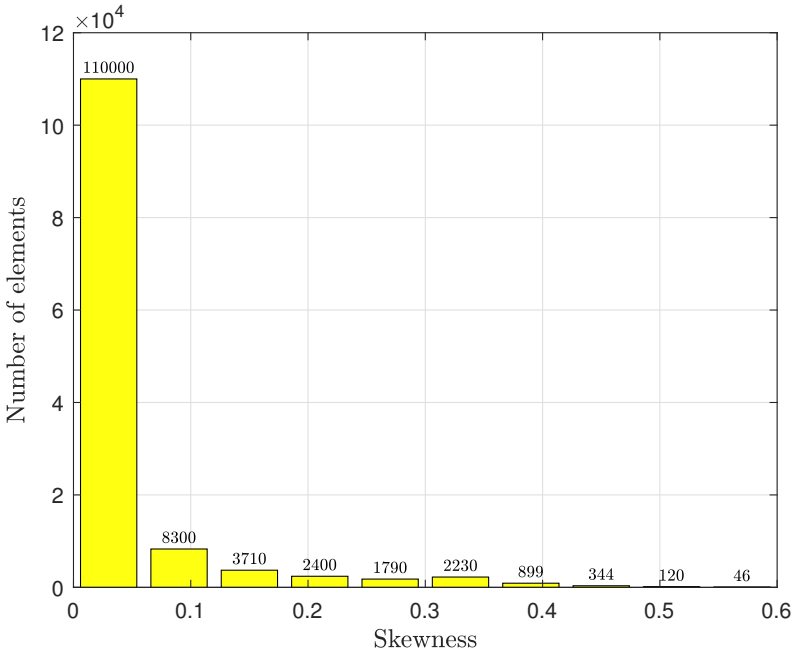

Figure 2.3: Skewness values for the elements of mesh#1.

Another critical aspect that one has to consider when creating the mesh is the boundary layer around the plate since turbulent flows are significantly affected by the presence of walls. There, the viscosity-affected regions have large gradients in the solution variables. Thus, an accurate representation of the near-wall region determines a successful prediction of wall-bounded turbulent flows.

In order to deal with this near-wall region, the dimensionless wall distance y^+ is presented. This parameter is commonly used in CFD simulations, and roughly speaking, it can be understood as a local Reynolds number, which means that its magnitude can be expected to determine the relative importance of viscous and turbulent processes. See Figure 2.4 for a better understanding of the y^+ and its relation with the inner layers. The y^+ is defined as

$$y^+ = \frac{yu_\tau}{\nu}, \tag{2.12}$$

where u_τ is the friction velocity, y the absolute distance from the wall, and ν the kinematic viscosity. Two ways are usually proposed based on this parameter.

- **Integrating the turbulence to the wall:** Some turbulence models are modified to enable the viscosity-affected region to be resolved with all the mesh down to the wall, including the viscous sublayer. When using a modified low Reynolds turbulence model to solve the near-wall region, the first cell center must be placed in the viscous sublayer (preferably $y^+ = 1$), leading to the requirement of abundant mesh cells. This system works better with low-Re models, such as the $k - \omega$ SST model. Higher computational resources are required with this strategy, but the forces on the wall are much more accurate and well-captured.

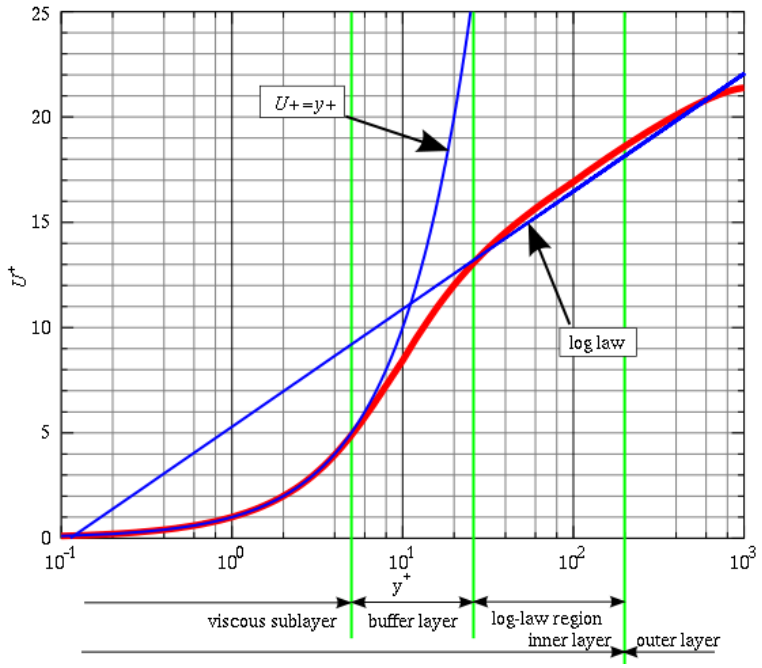

Figure 2.4: Law of the wall, horizontal velocity near the wall with mixing length model. Image from Wikimedia [2011].

- **Using the so-called wall functions:** These wall functions are equations empirically derived and used to satisfy the physics in the near wall region through a logarithmic approach. The first cell center needs to be placed in the log-law region to ensure the accuracy of the results, which is achieved with the first grid cell in the range of $30 < y^+ < 300$. Wall functions are used to bridge the inner region between the wall and the turbulence fully developed region. When using the wall functions approach, there is no need to resolve the boundary layer, causing a significant reduction of the mesh size and the computational domain. This model works better with high-Re models (such as Standard $k - \epsilon$ and RNG $k - \epsilon$). However, the forces are not well-captured on the surface, so it is used when the main interest is in the flow.

We are interested in capturing correctly the boundary layer around the plate and the forces that it experiences, so we set an inflation layer of 20 cells with a growth rate of 1.2 and the first cell thickness of size 0.007, 0.005, and 0.0035 mm for meshes #0, #1, and #2, respectively (see Figure 2.5 (b) for mesh #1). These first layer thicknesses guarantee a maximum $y^+ < 0.5$ on the foil wall, even for the most demanding case calculated with the coarse mesh#0. Therefore, the "integrating the turbulence to the wall" method is used, and the forces are well-captured around the foil.

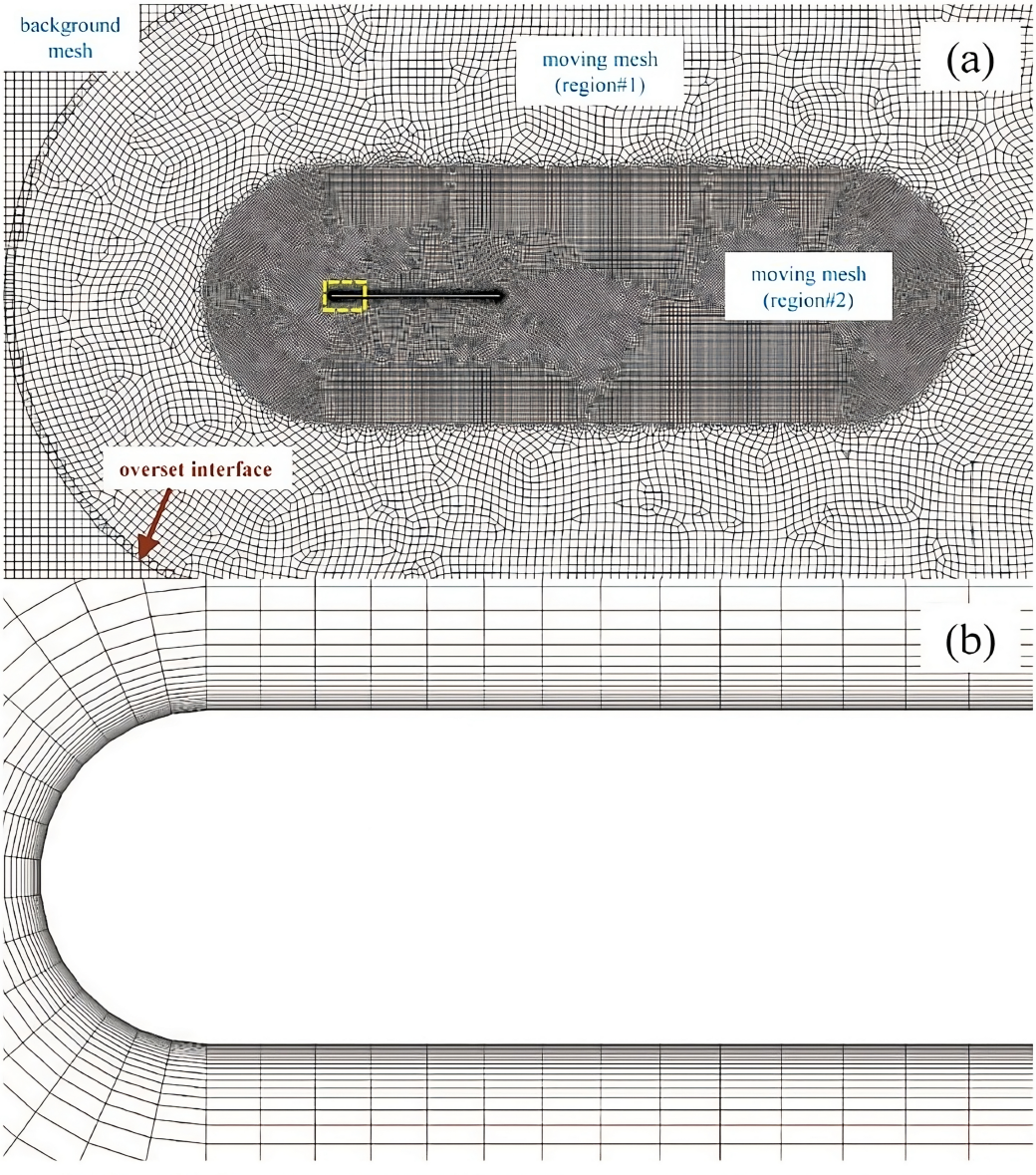

Figure 2.5: Two views of mesh#1, (b) is a zoom of the dashed rectangle in (a) containing the plate head.

A simple process to estimate the first cell thickness for a desired y^+ value is the following. For an estimated Reynolds number, we determine the skin friction coefficient, which for a flat plate is approximately

$$C_f = 0.027 Re^{-1/7}. \tag{2.13}$$

Then, the wall shear stress can be calculated by

$$\tau_\omega = \frac{1}{2} C_f \rho U_\infty^2. \tag{2.14}$$

Next, we can obtain the friction velocity

$$u_\tau = \sqrt{\frac{\tau_\omega}{\rho}}. \tag{2.15}$$

And finally, the first cell thickness through

$$y_1 = \frac{y^+ \nu}{u_\tau}. \tag{2.16}$$

This algorithm is useful to get an idea of the first cell thickness we need, but the y^+ value needs to be checked after the simulation, and a remesh might be necessary.

2.3.2 Mesh convergence study

Once both the computational domain and the mesh are created, we need to check that the mesh is appropriate. Consequently, a mesh convergence study was performed with the following three meshes: mesh#0 (coarse) with 68732 cells, 424 cells on the plate, and a time step $\Delta\tilde{t} = 5 \times 10^{-5}$ s; mesh#1 (medium) with 130103 cells, 600 on the plate and a time step $\Delta\tilde{t} = 2.5 \times 10^{-5}$ s; mesh#2 (fine) with 249549 cells, 848 on the plate and a time step $\Delta\tilde{t} = 1.25 \times 10^{-5}$ s. The time step was set to guarantee a maximum CFL of 1 in all cases.

The above-mentioned CFL is referred to as the Courant–Friedrichs–Lewy stability condition of numerical schemes. This stability condition is related to the Courant number C, which is a non-dimensional number commonly used in CFD simulations to evaluate the time step requirements of a transient simulation for a given mesh size and flow velocity. The Courant number is defined by

$$C = \frac{\widetilde{U} \Delta\tilde{t}}{\Delta\tilde{h}}, \tag{2.17}$$

where $\widetilde{U}$ indicates the flow velocity, $\Delta\tilde{t}$ is a representative time step of the simulation and $\Delta\tilde{h}$ the characteristic size of the mesh cell. In a CFD simulation, the Courant number broadly indicates how much the information travels across a computational grid cell in a unit of time. If the Courant number is greater than one, it means that the information propagates through more than one grid cell at each time step. It would make the solution inaccurate and potentially lead to nonphysical results or divergence of the solution in certain integration schemes. In Figure 2.6, we can see an example of how the Courant number and the CFL condition work.

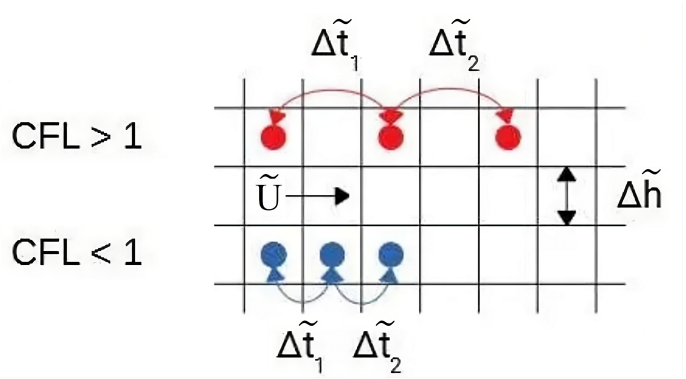

Figure 2.6: Visualisation of the Courant number and the CFL condition on a computational grid. Image from Idealsimulations [2020]

.

For that reason, the Courant number plays an important role when running a transient CFD simulation, especially if we are interested in the variations of the flow field in time as well as in space. The CFL stability condition can be expressed in terms of the Courant number as

$$C = \frac{\tilde{U}\Delta\tilde{t}}{\Delta\tilde{h}} \leq C_{max}, \tag{2.18}$$

where C_{max} varies depending on the type of time integration scheme, but it is generally equal to 1 or less (as it is considered in this work). Therefore, the CFL condition leads to $C \leq 1$.

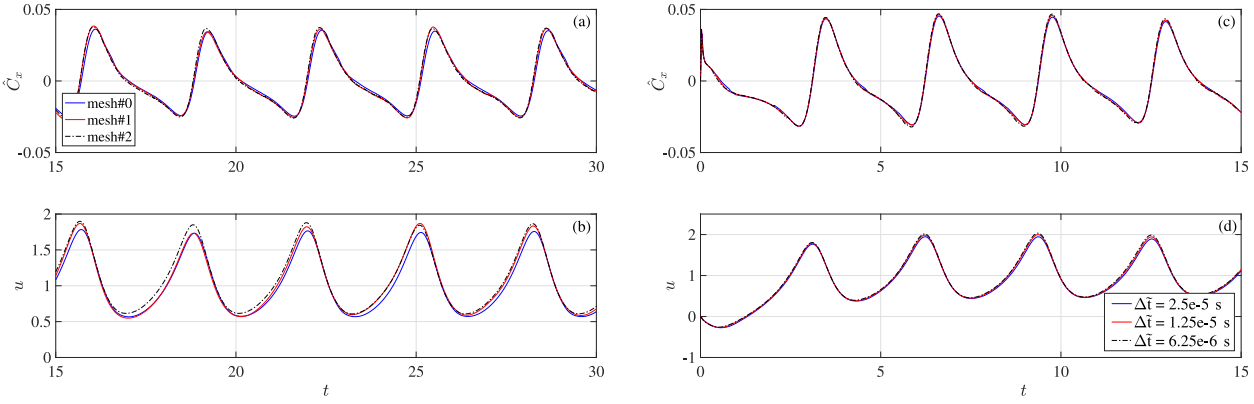

Figure 2.7: Mesh (a)–(b) and time-step (c)–(d) convergence studies in terms of the non-dimensional time evolutions of the non-dimensional force per unit span (top) and the non-dimensional swimming velocity (bottom) for $\alpha_0 = 0.2$ ($\simeq 11.46$ deg), $\tilde{f} = 2$ Hz and $R = 0.02$ in water ($Re_\omega \simeq 1.25 \times 10^5$).

In Figures 2.7 (a) and (b) are shown some of the final cycles of the x-component of the non-dimensional force per unit span and the non-dimensional velocity of the center of mass calculated with the transition turbulent model using the three meshes for one of the most unfavorable cases analyzed. It corresponds to $\alpha_0 = 0.2$ and $\tilde{f} = 2$ Hz, with $R = 0.02$ in water ($Re_\omega \simeq 1.25 \times 10^5$, resulting a time-averaged swimming velocity $U_\infty \simeq 1.06$, and $Re \simeq 2.65 \times 10^5$). We can see that the differences between the results computed with meshes

#1 and #2 are negligible, indicating that both are very close to mesh independence. Thus, all the results included in the next sections will be performed with the (medium) mesh#1, which is the one shown in Figure 2.5.

Additionally, a time-step convergence study is also performed with mesh #1 by halving the time step $\Delta\tilde{t} = 2.5 \times 10^{-5}$ s used in the mesh convergence study: $\Delta\tilde{t} = 2.5 \times 10^{-5}$ s, 1.25×10^{-5} s, and 6.25×10^{-6} s. The results are plotted in Figures 2.7 (c) and (d) being those practically indistinguishable, even for the initial cycles starting from the foil at rest where the temporal variations of u are larger than later on.

In order to check the effects of turbulence in the simulations, we take a snapshot of the non-dimensional turbulence kinetic energy at $t = 28.25$ (see Figure 2.8) for the case considered in Figure 2.7. This instant of time corresponds to a position of the plate with $\alpha = 0$, which yields a local maximum in the swimming velocity. Clearly, the effects of turbulence are manifest at these Reynolds numbers. However, when computing the force that the fluid exerts on the foil, the result does not differ much from the value obtained with the laminar simulations in the final permanent state, especially for smaller Reynolds numbers (see Figure 2.9 discussed below for $Re \simeq 45000$), demonstrating that turbulence has a negligible effect on the propulsion characteristics at the frequencies and Reynolds numbers here discussed. A similar conclusion was already reached in Sanmiguel-Rojas and Fernandez-Feria [2022] for a uniform flow at comparable Reynolds numbers past a NACA0012 airfoil, instead of the present self-propelled thin flat plate, but using quite similar numerical code and meshes to solve the fluid dynamics. In that reference, it was shown that turbulence effects are negligible if the Strouhal number is smaller than about 0.8, a value well beyond the present numerical simulations for small pitch amplitudes. Additionally, in that article, the numerical code was also validated against experimental data by Mackowski and Williamson [2015].

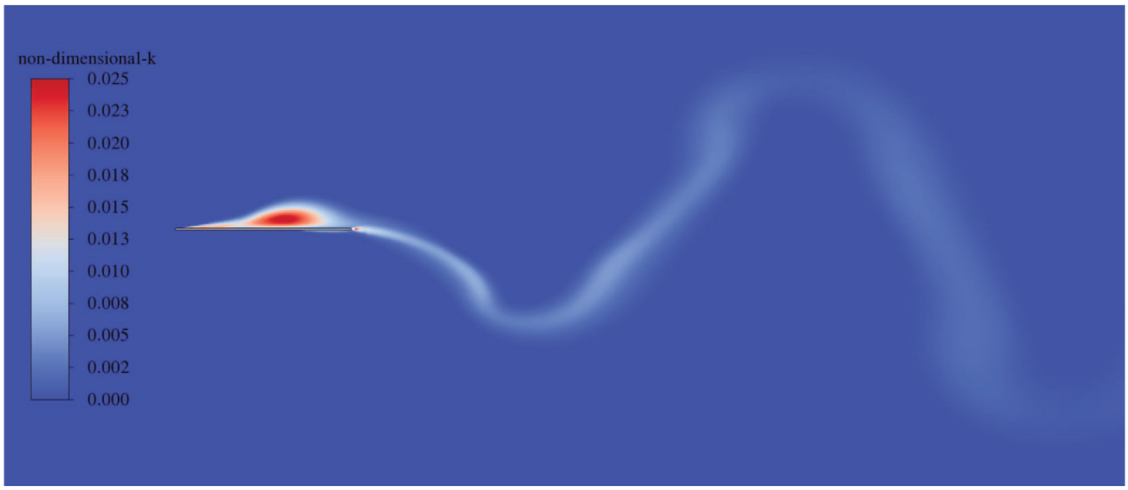

Figure 2.8: Snapshot of the non-dimensional turbulence kinetic energy at $t = 28.25$ for the case considered in Figure 2.7 computed with mesh#1.

2.3.3 Some comments about the simulations

In order to get the most complete and general information possible, we perform 5×8 numerical simulations varying the values of α_0 and Re_ω trying to cover the whole spectrum. Particularly, we take $\alpha_0 = \{0.05, 0.075, 0.1, 0.15, 0.2\}$, and we select the mass of the plate m for a given mass ratio of $R = 0.02$ in all the simulations. Moreover, we establish a fixed number of time steps $N_{ts} = 200000$ (with a maximum of 20 iterations per time step) and a fixed non-dimensional time length of $t \simeq 125$ for all the simulations. That means we need to adjust the time-step size for every case according to

$$\Delta\tilde{t} = \frac{t}{2\pi\tilde{f}N_{ts}} \simeq \frac{1}{3200\pi\tilde{f}}. \tag{2.19}$$

Thus, as the frequency is reduced, the longer the time-step size and, consequently, the final dimensional time of the simulation. That makes sense because if the foil's motion frequency is lower, the dimensional time needed to reach the final cruising state needs to be higher. On the other hand, as the time-step size is increased, we need to check in every single simulation that the CFL condition is respected since larger $\Delta\tilde{t}$ put that in compromise. Furthermore, when we reduce the frequency, the computational time needed to finish the simulation is also increased, and that happens because the number of iterations computed in each time step is larger too (e.g., the computational time needed under $\tilde{f} = 0.125$ Hz for water takes more than one week to reach the final cruising state). Consequently, we have to change some parameters in the dimensional values of the simulation in order to allow larger frequencies and lower resulting Re_ω numbers. Therefore, in the great majority of the numerical simulations, we select the fluid as water ($\rho = 998.2$ kg/m^3 and $\mu = 0.001003$ kg/ms). However, in order to achieve these lower values of Re_ω, we change the dynamic viscosity to $\mu = 0.031340$ kg/ms (see Table 2.1 below).

	$\mu = 0.001003$ kg/ms					$\mu = 0.031340$ kg/ms		
$\tilde{f}$ [Hz]	2	1	0.5	0.25	0.125	2	1	0.5
Re_ω	125062	62531	31266	15633	7816	4002	2001	1001
$\Delta\tilde{t}$ [s]	5×10^{-5}	1×10^{-4}	2×10^{-4}	4×10^{-4}	8×10^{-4}	5×10^{-5}	1×10^{-4}	2×10^{-4}
$\tilde{t}$ [s]	10	20	40	80	160	10	20	40

Table 2.1: Selected frequency and the corresponding Re_ω, $\Delta\tilde{t}$, and $\tilde{t}$ for the two dynamic viscosity values used in the numerical simulations. The fluid density in all the cases was $\rho = 998.2$ kg/m^3.

2.4 A new model for the unsteady viscous drag

Once we have performed all the numerical simulations and recollected the data, we can develop the model for the unsteady viscous drag. In that direction, the first step is analyzing the recollected data. The result of a typical numerical simulation is plotted in Figure 2.9, where we can see the non-dimensional swimming velocity $u(t)$ starting from the foil at rest and the pressure and viscous parts of the x-component force in non-dimensional form, $\hat{C}_{xp}(t)$ and $\hat{C}_{x\mu}(t)$, respectively. Notice that the sum of both components is the overall x-component force that the fluid exerts on the foil per unit span, $\hat{C}_x(t) \equiv \hat{C}_{xp}(t) + \hat{C}_{x\mu}(t)$.

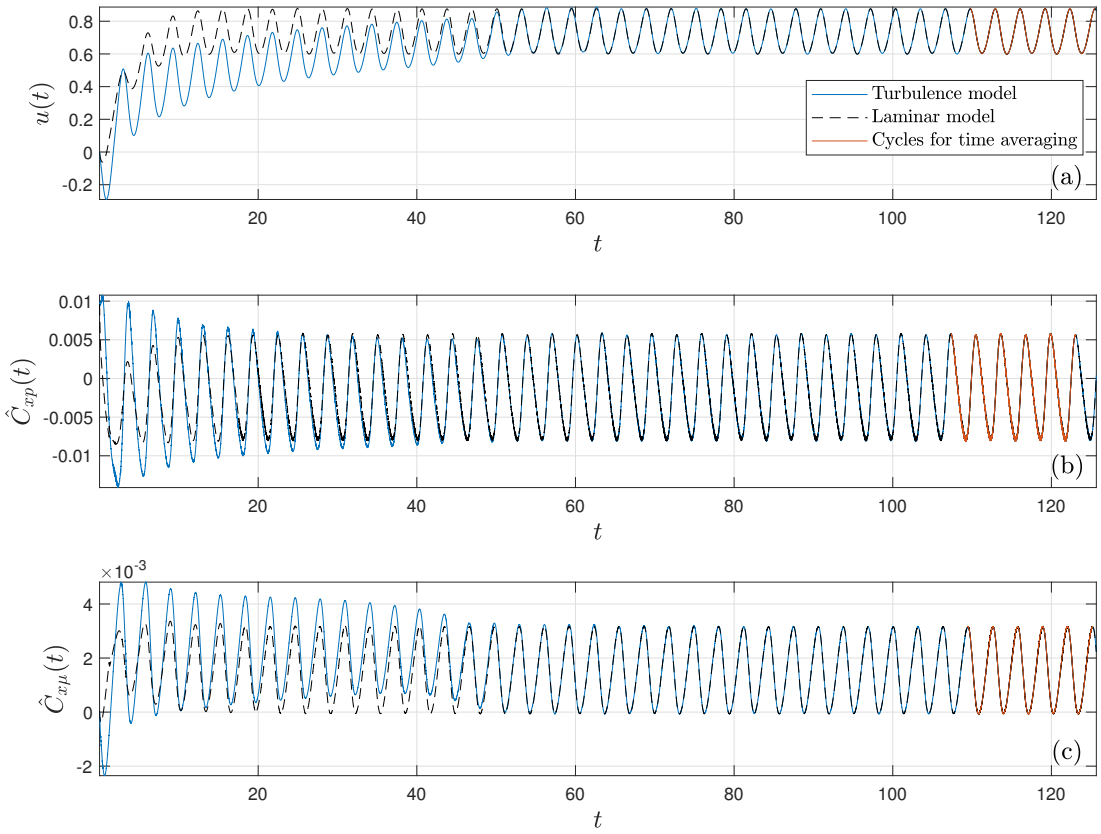

Figure 2.9: Time evolutions of the non-dimensional swimming velocity (a), non-dimensional pressure part of the x-component of the force (b), and the remaining viscous part of the force (c) for $\alpha_0 = 0.1$ ($\simeq 7.73$ deg), $R = 0.02$, $\tilde{f} = 0.5$ Hz in water ($Re_\omega \simeq 31266$), $Re \simeq 45599$. Continuous lines correspond to the results from the turbulence model, while dashed lines are obtained assuming laminar flow. The last five cycles used for time averaging are marked in red.

Moreover, the figure displays both the results assuming laminar flow and using the turbulence model. They almost coincide once the final or permanent oscillatory state has been reached but differ during the transient period towards that final state. This indicates that near-wall turbulence is more important during the transient acceleration of the foil, greatly

affecting the fluid forces. However, once the final state has been reached, the relevant turbulent regions are detached from the foil, as shown in Figure 2.8, barely affecting the fluid forces. Taking that into account, all the reported numerical results are computed with the turbulence model. On the other hand, the time average of any quantity $\phi(t)$ at the final oscillatory state is computed using the last $n = 5$ cycles (marked in red in Figure 2.9) as

$$\overline{\phi} = \frac{1}{nT_\phi} \int_t^{t+nT_\phi} \phi(t)dt, \tag{2.20}$$

where T_ϕ is the non-dimensional oscillation period of ϕ. Thus, for the case presented in Figure 2.9 the mean values are $\bar{u} \equiv U \simeq 0.7292$, $\overline{\hat{C}}_{xp} \simeq -0.0015$ and $\overline{\hat{C}}_{x\mu} \simeq 0.0015$. Notice that once the foil has reached the cruising velocity, the non-dimensional forces cancel each other, i.e., $\overline{\hat{C}}_x = \overline{\hat{C}}_{xp} + \overline{\hat{C}}_{x\mu} = 0$. On the other hand, the Reynolds number based on the velocity, in this case, is $Re \simeq 45599$ and the Strouhal number $St \simeq 0.087$.

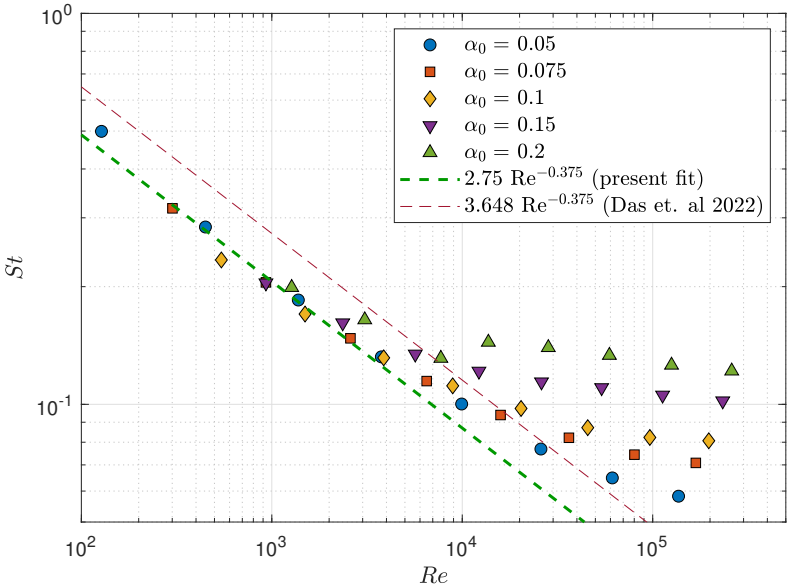

Figure 2.10: $St-Re$ relation for all the numerical results computed with $R = 0.02$ for different values of α_0 and Re_ω (symbols). The dashed thick line is a power-law fit for $Re \lesssim 2000$ while the thin one corresponds to the study conducted by Das et al. [2022].

An interesting approach is the one performed by Das et al. [2022], where the swimming velocity is characterized through the Reynolds number in a $St - Re$ chart. We adopt the same strategy in Figure 2.10 for the 5×8 numerical simulations for $R = 0.02$ with five different values of α_0 and eight different Re_ω for each α_0, that we mentioned in the previous section, and compare the trend with their results. For our data, the numerical results fit quite well the power law $St = 2.75Re^{-0.375}$ for $Re \lesssim 2000$, while their results fit a similar trend but with a different constant $St^{Das} = 3.648Re^{-0.375}$. This difference is probably due to the use of a NACA0012 airfoil in their numerical simulations instead of the present flat plate. Moreover, this power law works very well for the Reynolds range mentioned above. However, for higher Re, the results depend on the pitch amplitude, and the relationship is

more complex. Besides that, our range of Reynolds is quite different, reaching much higher values: here $100 \leqslant Re \leqslant 3 \times 10^5$ vs $10 \leqslant Re \leqslant 2000$ in Das et al. [2022]. For that reason, we use a transition turbulence model instead of the laminar one for the numerical simulations. In addition, this higher range of Re, though computationally much more demanding, is more appropriate to compare with the predictions from the inviscid linear theory that we have mentioned before.

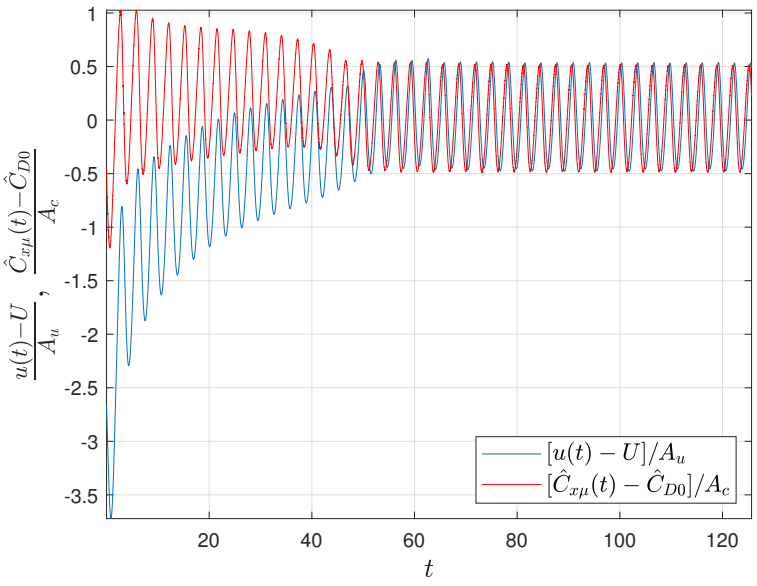

Figure 2.11: Time evolutions of $(u - U/A_u)$ and $(\hat{C}_{x\mu} - \hat{C}_{D0})/A_c$ for the same case plotted in Figure 2.9. The values for this case are $A_c \simeq 0.0032$, $A_u \simeq 0.274$, $\hat{C}_{D0} \simeq 0.0015$, $U \simeq 0.7292$.

Once we have presented the numerical data and extracted some preliminary conclusions, we can work on the new model for the unsteady viscous drag. To model this coefficient, it is convenient to compare the time evolution $u(t)$ with the corresponding $\hat{C}_{x\mu}(t)$, but normalizing them by subtracting their mean values and dividing by the corresponding amplitudes, which is made in Figure 2.11. Moreover, a representation of the last few cycles used for the time-averaging results is shown in Figure 2.12. It is observed that both normalized temporal signals almost coincide except for a phase shift. Similarly, this happens for all the computed cases; the more so, the smaller the amplitude α_0. Thus, one may write

$$\frac{\hat{C}_{x\mu}(t) - \hat{C}_{D0}}{A_c} \approx \frac{u(t-\phi) - U}{A_u}, \tag{2.21}$$

where we have named $\hat{C}_{D0} \equiv \overline{\hat{C}}_{x\mu}$ the time-averaged viscous drag coefficient, A_c and A_u are the time-averaged amplitudes of the oscillations of the viscous drag and swimming velocity, respectively, and ϕ is the phase shift, all of them functions of α_0, Re_ω and R, for given $a = -1$. Consequently, the unsteady viscous drag coefficient can be modeled as

$$\hat{C}_{x\mu}(t) \approx \hat{C}_{D0} + \hat{C}_{Du}\left[u(t-\phi) - U\right], \quad \text{with} \quad \hat{C}_{Du} = \frac{A_c}{A_u}. \tag{2.22}$$

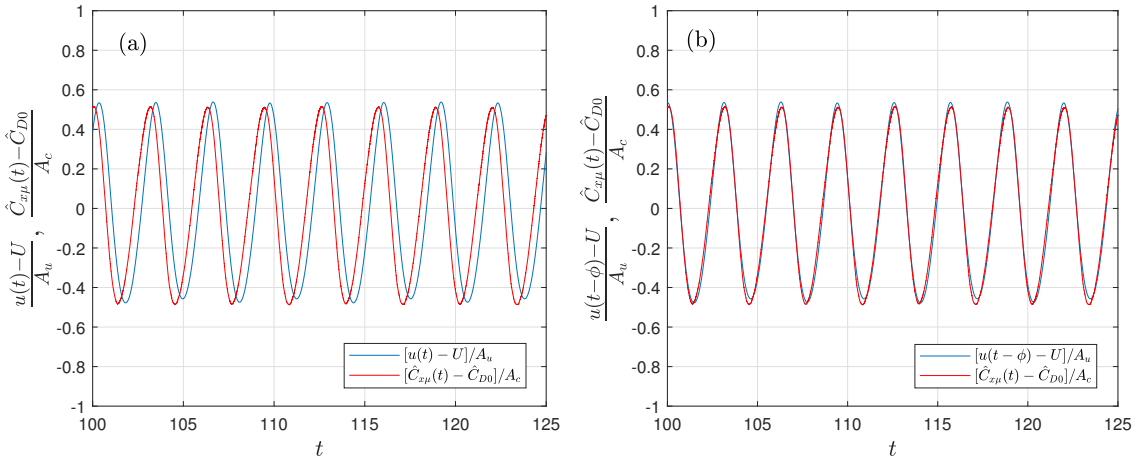

Figure 2.12: (a) Last cycles of Figure 2.11 used for time-averaging. (b) The same figure but for a phase shift $\phi \simeq 0.340$ in $u(t)$.

So, we need to characterize $\hat{C}_{D0}$, $\hat{C}_{Du}$ and ϕ in terms of the non-dimensional parameters α_0, Re_ω and R to have defined the new drag model. To that end, we use the previously mentioned 5×8 numerical simulations for $R = 0.02$ and some additional ones for $R = 0.01$ and $R = 0.04$ for selected values of α_0 and Re_ω (see Figure 2.13 for one of the computed cases varying the mass ratio R). From all these numerical data, it turns out that all the parameters, $\hat{C}_{D0}$, $\hat{C}_{Du}$, ϕ, and U, are practically independent of the mass ratio R, provided that R remains small, which is the case in flapping propulsion in water.

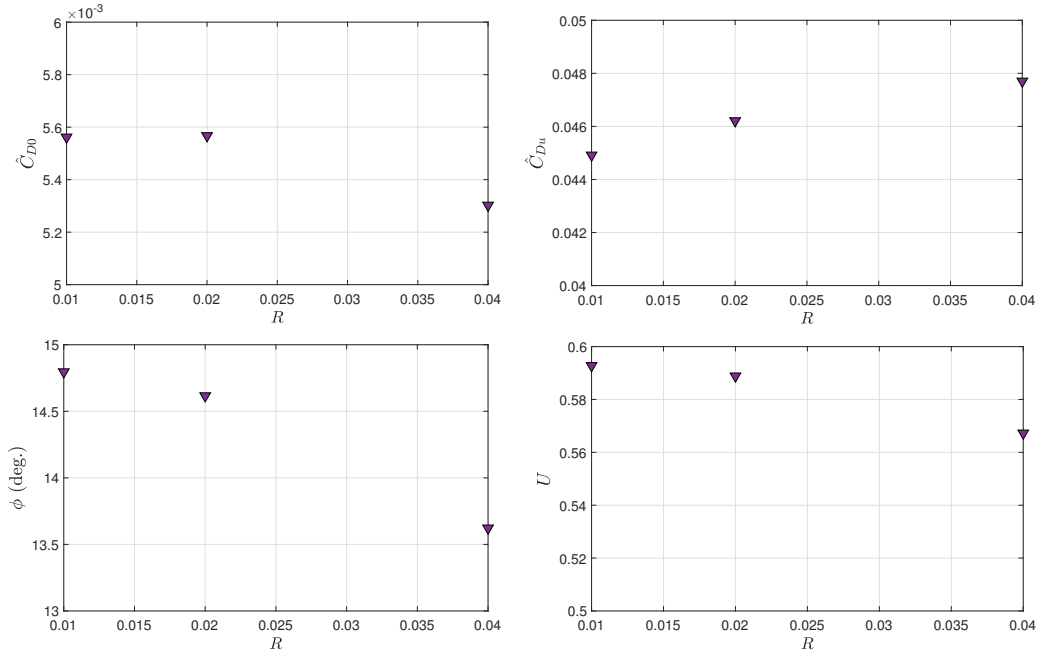

Figure 2.13: Some of the additional cases studied for $\alpha_0 = 0.15$ and $Re_\omega \simeq 2000$, showing the evolution of $\hat{C}_{D0}$, $\hat{C}_{Du}$, ϕ, and U with the mass ratio R.

On the other hand, it is found that $\hat{C}_{Du}$ is also practically independent of the pitch amplitude α_0, and besides that, it follows a power law with Re_ω in a wide range of values of Re_ω. In the case of the phase shift ϕ, it remains practically constant for all the values of α_0 and Re_ω considered. These results for $\hat{C}_{Du}$ and ϕ are displayed in Figure 2.14 and can be summarized with the following expressions:

$$\hat{C}_{Du} \approx 1.45 Re_\omega^{-0.46}, \quad \text{with } 2\times10^3 \lesssim Re_\omega \lesssim 5\times10^4, \tag{2.23}$$

$$\phi \approx 17^o, \quad \text{with } Re_\omega \lesssim 10^5. \tag{2.24}$$

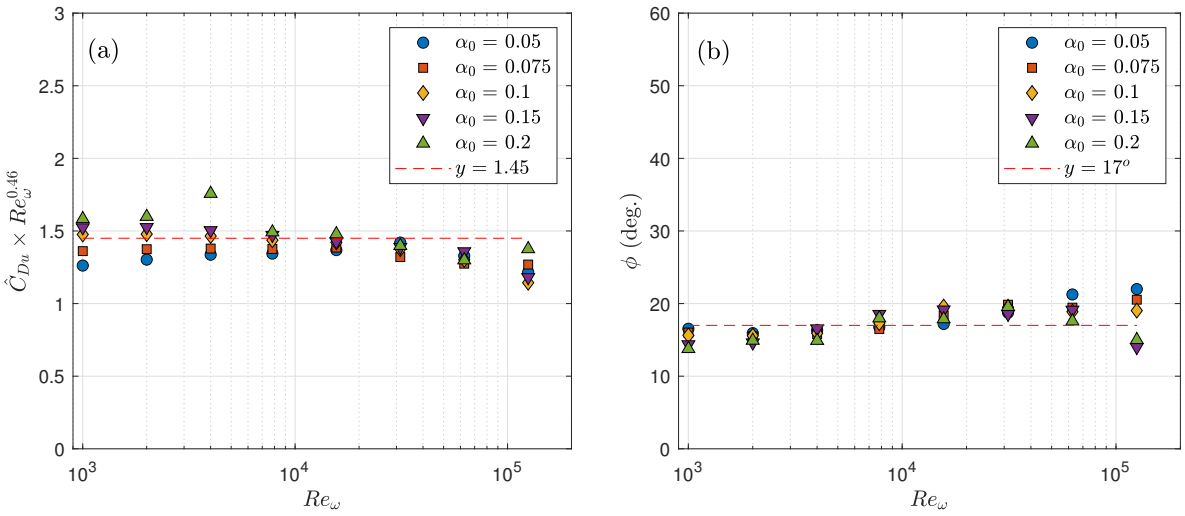

Figure 2.14: Scaled $\hat{C}_{Du}$ (a) and ϕ (b) vs Re_ω for different α_0. $R = 0.02$.

Finally, if we study the dependence of the time-averaged viscous drag $\hat{C}_{D0}$ with α_0 and Re_ω, it is found that it does not follow simple power laws as $\hat{C}_{Du}$ or ϕ. However, it does with U and, therefore, with the Reynolds number Re based on U. Especially in the case of the standard drag coefficient C_{D0}, which is related with the above-mentioned drag through $C_{D0} = \pi\hat{C}_{D0}/U^2$. In Figure 2.15 it is shown this time-averaged viscous drag coefficient and how it can be approximated by power laws of both Re and α_0 in a wide range of Reynolds numbers of interest for aquatic propulsion. Thus, it can be summarized as:

$$C_{D0} \approx 5.7 Re^{-0.71}\alpha_0^{-0.4}, \quad \text{with } 500 \lesssim Re \lesssim 2\times10^4, \tag{2.25}$$

and so, the resulting drag coefficient $\hat{C}_{D0}$ in terms of Re_ω and the rest of the parameters is

$$\hat{C}_{D0} = \frac{C_{D0}U^2}{\pi} \approx 1.11 Re_\omega^{-0.71}\alpha_0^{-0.4}U^{1.29}, \quad \text{with } 250 \lesssim URe_\omega \lesssim 1\times10^4. \tag{2.26}$$

It must be noted that the Reynolds numbers here are significantly larger than in most previous studies dealing with the skin friction on a flapping foil (Ehrenstein and Eloy [2013], Ehrenstein et al. [2014], Das et al. [2016], Gross et al. [2021], Das et al. [2022]). These computationally works for $Re \lesssim 10^3$ confirmed the Bone-Lighthill boundary layer thinning hypothesis for uniform flow past oscillatory plates, with skin friction drag coefficients proportional to $Re^{-1/2}$,

like in Blasius flat plate, but multiplied by a factor proportional to the square root of the ratio of the transverse and longitudinal velocities. Labasse et al. [2020] considered $Re = 2000$ for different α_0, finding that Blasius-type scaling is not reliable without providing any scaling law. Gross et al. [2021] also considered the range $Re \gtrsim 10^3 - 10^4$ but neglected the viscous drag for these larger Reynolds numbers, considering only a constant pressure drag coefficient.

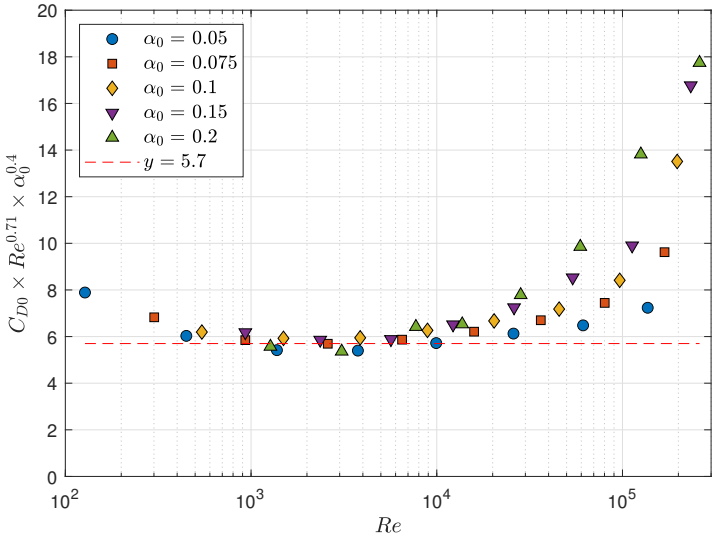

Figure 2.15: Scaled C_{D0} vs Re for different α_0. $R = 0.02$.

In this work, we use Equation (2.26) for the time-averaged viscous drag, while all the pressure forces, of any sign, are modeled with analytical expressions from linear inviscid theory. The numerical results will corroborate this choice for the pressure forces in the present Reynolds number's range, provided that α_0 is small enough, as previously found in comparison with experimental data for a pitching foil immersed in a uniform current, both for time-averaged and instantaneous thrust forces (Fernandez-Feria [2017], Fernandez-Feria and Sanmiguel-Rojas [2019], Alaminos-Quesada [2021]).

Now that we have the power laws for $\hat{C}_{D0}$, $\hat{C}_{Du}$ and ϕ, we can obtain a general expression for the new unsteady viscous drag model, which in what follows will be named as $\hat{C}_D$. So, it can be approximated by the following expression:

$$\hat{C}_D(t) \equiv \hat{C}_{x\mu}(t) \approx C_0 Re_\omega^{-a_0} \alpha_0^{-b_0} U^{c_0} + C_1 Re_\omega^{-a_1} \left[u(t-\phi) - U\right], \tag{2.27}$$

where

$$\begin{gathered} C_0 \simeq 1.11, \quad a_0 \simeq 0.71, \quad b_0 \simeq 0.4, \quad c_0 \simeq 1.29, \\ C_1 \simeq 1.45, \quad a_1 \simeq 0.46, \quad \phi \simeq 0.30. \end{gathered} \tag{2.28}$$

Notice that all the above numerical results are for a pivot point located at the leading edge $a = -1$. When it departs from the leading edge, the numerical values of the above expressions change. For that reason, Equation (2.27) will be used in the following section, in general, without specifying the numerical values of the constants. However, when we perform the comparison with the numerical results obtained for $a = -1$, the values given in Equation (2.28) will be used.

2.5 Self-propulsion models with thrust from linear potential theory

Now that we have the new model for the unsteady viscous drag coefficient $\hat{C}_D(t)$, we can take advantage of the linear inviscid theory for modeling the pressure forces and obtain a final model for the self-propelled pitching foil. To do that, we have to assume that the fluid flow is inviscid and the pitch amplitude is small ($|\alpha| \ll 1$), and so the thrust force generated by the pressure acting on the pitching foil surface can be obtained analytically. The resulting thrust coefficient $\hat{C}_T(t)$ corresponds to $-\hat{C}_x(t)$ but neglecting viscous forces, so the self-propulsion problem in this near-inviscid limit will be governed by Equation (2.6) but slightly modified into

$$R\dot{u} = \hat{C}_T - \hat{C}_D. \tag{2.29}$$

We use two alternative expressions to model this thrust coefficient. The first one is that obtained by Garrick [1936] from Theodorsen's theory (Theodorsen [1935]), which will be named as $\hat{C}_T^G(t)$, and the second one that results from the linearized vortical impulse theory obtained by Fernandez-Feria [2016], which will be known as $\hat{C}_T^F(t)$. Both contain the same term $-\alpha\hat{C}_L(t)$, where $\hat{C}_L(t)$ is Theodorsen's lift force non-dimensionalized with the present scaling, modified by Greeberg [1947] with an additional added mass term proportional to $\dot{u}(t)$ to account for the pulsating stream, and with Theodorsen's function appearing in the circulatory terms evaluated at variable $k(t) = 1/u(t)$. To have a better understanding of these coefficients and where they come from, see Appendix A. For pure pitching motion, the coefficients can be written as

$$\hat{C}_L(t) = -a\ddot{\alpha} + u\dot{\alpha} + \dot{u}\alpha + \Re[C(k)]u\Gamma_0(t), \quad \text{with} \quad \Gamma_0(t) = -2\left[\left(a - \frac{1}{2}\right)\dot{\alpha} - u\alpha\right], \tag{2.30}$$

where $C(k)$ is Theodorsen's function and $\Re$ means real part. The remaining terms of the thrust coefficient are different in both formulations:

$$\hat{C}_T^G(t) = -\alpha\hat{C}_L + \frac{1}{2}\left\{\Re[C(k)]\Gamma_0 - \dot{\alpha}\right\}^2, \tag{2.31}$$

$$\hat{C}_T^F(t) = -\alpha\hat{C}_L + \dot{\alpha}(a\dot{\alpha} - u\alpha) + \Gamma_0\left\{\Re\left[\frac{2iC_1(k)}{\pi}\right][2\alpha u + (1-a)\dot{\alpha}] - \Re[C(k)]u\alpha\right\}. \tag{2.32}$$

After substituting any of these expressions for the thrust coefficient, together with Equation (2.27) and the pitching motion, which in non-dimensional form is given by

$$\alpha(t) = \alpha_0 \sin(t), \tag{2.33}$$

into Equation (2.29), the resulting differential equation for $u(t)$ is solved numerically taking advantage of the Matlab's solver package, particularly the *dde23* solver, and starting from $u(0) = 0$. This solver allows us to solve delay differential equations (DDEs) with constant delays, which in our case is the phase shift ϕ in the velocity u that appears in our $\hat{C}_D(t)$ model.

The corresponding problem with Garrick's thrust $\hat{C}_T^G(t)$ is equivalent to the minimal self-propulsion model of Sanchez-Rodriguez et al. [2020], but with an entirely different unsteady model for the skin friction coefficient $\hat{C}_D(t)$, and somewhat simpler because the heaving motion has been inhibited to facilitate the comparison with numerical simulation from the full N–S equations. On the other hand, a note of caution should be made about the temporal approximations in the thrust and drag coefficients since $\hat{C}_T(t)$ is obtained theoretically using the pressure field from the linear potential theory for a pitching foil in a uniform flow. In contrast, $\hat{C}_D(t)$ is obtained by adjusting numerical results of the viscous forces once a final oscillatory motion with constant time-averaged swimming velocity has been reached. Nevertheless, both will be used as an approximation during all the oscillatory motion of the foil starting from rest with the local values of u and U. It means that for the transient between the initial condition and the final oscillatory state, the results of the present model will be merely qualitative. Suitable for estimating the duration of the transient and the order of magnitude of the velocity peaks, but not for the details of $u(t)$. However, the model should work quantitatively for the final oscillatory state.

2.5.1 Approximate analytical solutions

Apart from the numerical solution of the model equation, one may take advantage of the small pitch amplitude ($\alpha_0 \ll 1$) to obtain an analytical approximation for $u(t)$, which can be very useful since it will provide quick and precise information, especially for the designing process. Thus, due to the small α_0, the thrust force is small, and so the non-dimensional swimming velocity will presumably be small too ($u \ll 1$). Taking that into account, $u(t)$ may be decomposed into an oscillatory component in the time scale t and a mean part evolving in a much slower time τ. So, one may assume

$$u \approx \gamma w(t) + UW(\tau), \quad \text{with} \quad \tau = \lambda t,\ \gamma \ll 1,\ U \ll 1,\ \lambda \ll 1, \tag{2.34}$$

where w and W are order-of-unity functions of their respective arguments, $W \to 1$ for $\tau \gg 1$, the oscillatory function $w(t)$ has zero mean, and the small parameters γ, U, and λ have to be determined from the equation of motion for each thrust model. In this case, γ represents the amplitude of the oscillations of u, U the mean forward speed, and λ the transient time (all of them in non-dimensional form). On the other hand, since u is assumed small ($k = u^{-1} \gg 1$), one may use the large-k approximation of the functions $C(k)$ and $C_1(k)$ (e.g., Fernandez-Feria and Sanmiguel-Rojas [2019]), yielding to

$$\Re[C(k)] = \frac{1}{2} + O\left(k^{-2}\right), \quad \Re\left[\frac{2iC_1(k)}{\pi}\right] = \frac{1}{(4\pi k)^{1/2}} + O\left(k^{-3/2}\right), \tag{2.35}$$

and then, the thrust coefficients can be written as

$$\hat{C}_T^G(t) \sim \frac{\alpha_0^2}{4}\left[\left(a - \frac{1}{2}\right)^2 + \left(a^2 + 3a + \frac{1}{4}\right)\cos(2t)\right] + O\left(\alpha_0^2 u\right), \tag{2.36}$$

$$\hat{C}_T^F(t) \sim \alpha_0^2 a\cos(2t) + u^{1/2}\frac{\alpha_0^2}{2\sqrt{\pi}}\left(a - \frac{1}{2}\right)(a-1)\left[1 + \cos(2t)\right] + O\left(\alpha_0^2 u\right). \tag{2.37}$$

Using the drag model equation $\hat{C}_D(t)$ and any of these two thrust models, the equation of motion Equation (2.29) can then be approximated by

$$R\left(\gamma\frac{dw}{dt}+\lambda U\frac{dW}{d\tau}\right)\approx\hat{C}_T-C_0Re_\omega^{-a_0}\alpha_0^{-b_0}(UW)^{c_0}-C_1Re_\omega^{-a_1}\gamma w(t-\phi). \tag{2.38}$$

We are interested in solving this equation using both Garrick and Fernandez-Feria's thrust models and especially the solution at the lowest order in the small parameters.

Garrick's thrust model

Considering the Garrick's thrust model depicted in Equation (2.36) and substituying that into Equation (2.38), one may obtain the following two expressions

$$R\lambda U\frac{dW}{d\tau}\approx\frac{\alpha_0^2}{4}\left(a-\frac{1}{2}\right)^2-C_0Re_\omega^{-a_0}\alpha_0^{-b_0}(UW)^{c_0}, \tag{2.39}$$

$$R\gamma\frac{dw}{dt}\approx\frac{\alpha_0^2}{4}\left(a^2+3a+\frac{1}{4}\right)\cos(2t)-C_1Re_\omega^{-a_1}\gamma w(t-\phi). \tag{2.40}$$

Working first with the equation for $W(\tau)$, one may select U and λ such as

$$R\lambda U=\frac{\alpha_0^2}{4}\left(a-\frac{1}{2}\right)^2=C_0Re_\omega^{-a_0}\alpha_0^{-b_0}U^{c_0}, \tag{2.41}$$

and so these parameters need to be

$$U=\left[\frac{(a-1/2)^2\alpha_0^{2+b_0}Re_\omega^{a_0}}{4C_0}\right]^{1/c_0}\ll 1,\qquad \lambda=\frac{\alpha_0^2(a-1/2)^2}{4RU}\ll 1. \tag{2.42}$$

These requirements also limit the validity range of the present approximation in terms of the pitch amplitude α_0 and the Reynolds based on frequency Re_ω. Thus, the equation for $W(\tau)$ yields to

$$\frac{dW}{d\tau}=1-W^{c_0}. \tag{2.43}$$

This equation has to be solved with an initial condition $W(0)=W_0$ (e.g., $W_0=0$), and always satisfies $W\to 1$ as $\tau\to\infty$ if $c_0>0$ (remember that $c_0\simeq 1.29$ for $a=-1$). Thus, U given by the above expression constitutes an analytical approximation to the final (time-averaged) swimming velocity when Garrick's thrust is used. If $c_0=2$ and $W_0=0$ the solution would be simply $W=\tanh\tau$. In general, the solution satisfying $W(0)=0$ can be written in implicit form as

$$\tau=WF[1,1/c_0;1/c_0+1,W^{c_0}], \tag{2.44}$$

where F is Gauss' hypergeometric funcion (see Olver et al. [2010] for more information).

Working now with the equation for $w(t)$, one may select a value for γ such as

$$\gamma = \frac{\alpha_0^2}{4R}\left(a^2 + 3a + \frac{1}{4}\right), \quad \text{with} \ \ |\gamma| \ll 1, \tag{2.45}$$

and so the equation simplifies to

$$\frac{dw}{dt} \approx \cos(2t) - Cw(t-\phi), \quad \text{where} \ \ C = \frac{C_1 Re_\omega^{-a_1}}{R}. \tag{2.46}$$

Making the appropriate variable change $\zeta = t - \phi$, the equation results in

$$\frac{dw}{d\zeta} \approx \cos(2\zeta + 2\phi) - Cw(\zeta), \tag{2.47}$$

which can be easily solved with the initial condition $w(\zeta = 0 - \phi) = 0$, yielding to

$$w(\zeta) = \frac{1}{C^2+4}\left\{2\sin(2\zeta+2\phi) + C\left[\cos(2\zeta+2\phi) - e^{-C(\zeta+\phi)}\right]\right\}, \tag{2.48}$$

and going back to the initial variable, the solution becomes

$$w(t) = \frac{1}{C^2+4}\left\{2\sin(2t) + C\left[\cos(2t) - e^{-Ct}\right]\right\}, \tag{2.49}$$

that satisfies $w(0) = 0$. In addition, if $C \ll 1$, this solution can be approximated by $\sin(2t)/2$. Besides that, it is also observed that the oscillatory swimming velocity has a period of π in this approximation, half that of the forced pitching motion, which is a consequence of the thrust models used. Substituting the functions $w(t)$ and $W(\lambda t)$ into Equation (2.34) yields the approximate solution with Garrick's thrust, which provides directly the final, time-averaged swimming velocity U, the amplitude of the final oscillations (about $\gamma/2$), and the order of magnitude λ^{-1} of the non-dimensional transient time to reach that final state.

Fernandez-Feria's thrust model

Considering now the Fernandez-Feria's thrust model depicted in Equation (2.37) and substituying that into Equation (2.38), one may obtain the next two expressions

$$R\lambda U\frac{dW}{d\tau} \approx \frac{\alpha_0^2}{2\sqrt{\pi}}\left(a - \frac{1}{2}\right)(a-1)(UW)^{1/2} - C_0 Re_\omega^{-a_0}\alpha_0^{-b_0}(UW)^{c_0}, \tag{2.50}$$

$$R\gamma\frac{dw}{dt} \approx \alpha_0^2 a\cos(2t) + \frac{\alpha_0^2}{2\sqrt{\pi}}\left(a - \frac{1}{2}\right)(a-1)(UW)^{1/2}\cos(2t) - C_1 Re_\omega^{-a_1}\gamma w(t-\phi). \tag{2.51}$$

However, assuming that $\gamma/U \ll 1$, the second expression can be transformed in first approximation into

$$R\gamma\frac{dw}{dt} \approx \alpha_0^2 a\cos(2t) - C_1 Re_\omega^{-a_1}\gamma w(t-\phi). \tag{2.52}$$

Working with the equation for $W(\tau)$, as it was done in the previous case, one can select U and λ such as

$$R\lambda U = \frac{\alpha_0^2}{2\sqrt{\pi}}\left(a-\frac{1}{2}\right)(a-1)U^{1/2} = C_0 Re_\omega^{-a_0}\alpha_0^{-b_0}U^{c_0}, \tag{2.53}$$

and so the parameters will be

$$U = \left[\frac{(a-1/2)(a-1)\alpha_0^{2+b_0}Re_\omega^{a_0}}{2C_0\sqrt{\pi}}\right]^{1/(c_0-0.5)} \ll 1, \qquad \lambda = \frac{\alpha_0^2(a-1/2)(a-1)}{2R\sqrt{\pi U}} \ll 1. \tag{2.54}$$

Thus, in this case the equation for $W(\tau)$ yields to

$$\frac{dW}{d\tau} = W^{1/2}\left(1-W^{c_0-1/2}\right). \tag{2.55}$$

It can be seen that W always tends to unity as $\tau \to \infty$ if $c_0 > 1/2$. So, the solution of this equation that satisfies $W(0) = 0$ can formally be written in implicit form, using the Gauss' hypergeometric function F, as

$$\tau = 2\frac{W^{c_0}-W^{1/2}}{W^{c_0-1/2}-1}F\left[1, 1/(2(c_0-1/2)); 1/(2(c_0-1/2))+1, W^{c_0-1/2}\right]. \tag{2.56}$$

Working now with the equation for $w(t)$, one can select a value for γ such as

$$\gamma = \frac{\alpha_0^2 a}{R}, \quad \text{with} \quad |\gamma| \ll 1, \tag{2.57}$$

and then, the equation for w is the same in the first approximation as in Garrick's thrust case, so that the solution is also Equation (2.49). However, the amplitude γ of the oscillations of u is now slightly different, though both are proportional to α_0^2/R. In addition, the dependencies of the mean forward speed U and the transient non-dimensional time λ on α_0 and Re_ω are pretty different, though, as we shall see in the next section, the results are quantitatively very similar within the (narrow) range of validity of the approximations.

2.5.2 Assessment of the approximate analytical solutions

In order to validate the approximate analytical solutions, we compare the velocity $u(t)$ for a particular case ($\alpha_0 = 0.075$ and $Re_\omega = 2000$ with $R = 0.02$ and $a = -1$) obtained from the five approaches described in the preceding sections: full numerical solution from the simulation performed with Fluent solver, and using the two thrust models (Garrick and Fernandez-Feria), both integrating numerically Equation (2.29) through the *dde23* Matlab's solver and using their respective analytical approximate solutions Equation (2.34). This comparison is shown in Figure 2.16. We can see that the approximate solutions are in close agreement with the numerical solution of the model equations for both thrust models in this case. As expected, the transient evolutions from the models and the numerical simulation from Fluent differ substantially. However, the final mean values U are not so different in this case, especially when using $\hat{C}_T^F$ in the model. On the other hand, the oscillation amplitude of the swimming velocity is larger than that obtained with the numerical simulation.

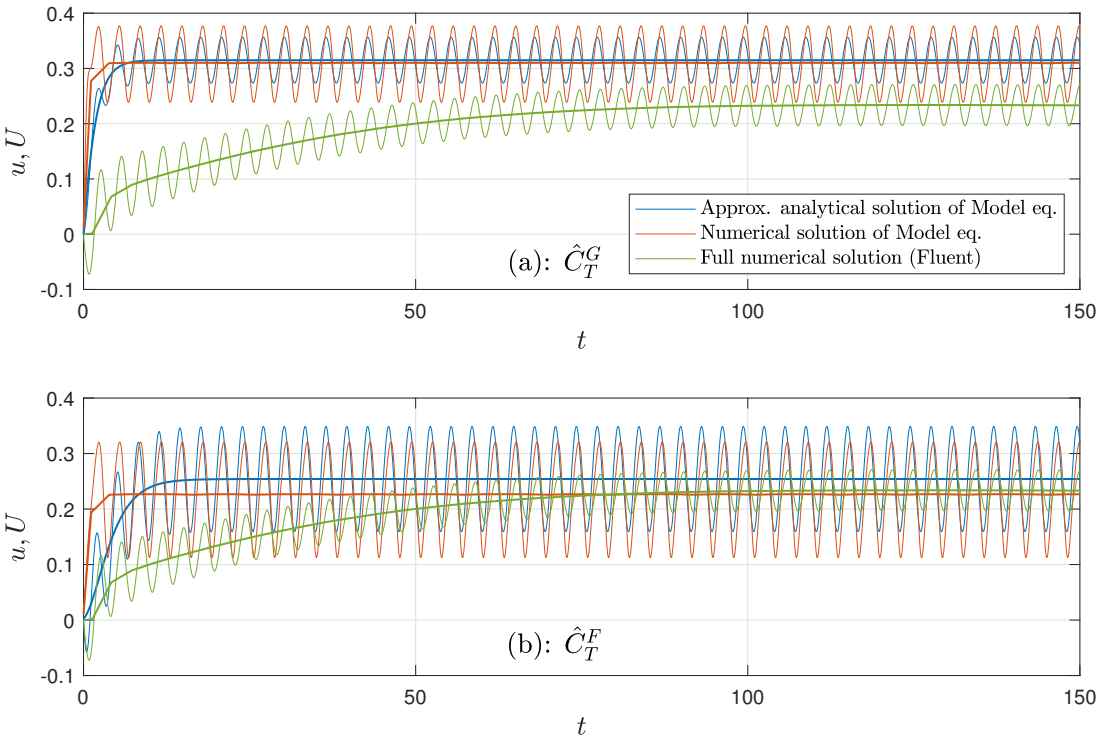

Figure 2.16: $u(t)$ computed numerically (thin green lines) and its mean U (thick green lines) compared with the model predictions using $\hat{C}_T^G$ (a) and $\hat{C}_T^F$ (b). The numerical solution of the model is plotted with red lines and the analytical approximate solution with blue lines. $\alpha_0 = 0.075$, $Re_\omega = 2000$, $R = 0.02$ and $a = -1$.

We have observed similar trends for other small values of α_0 if $Re_\omega \lesssim 10^4$ (see Figure 2.17). As expected, the best agreement for the mean swimming velocity U is found for the smallest pitch amplitude considered, which is $\alpha_0 = 0.05$, and becomes poorer as α_0 increases, especially for higher values of Re_ω. In fact, already for $\alpha_0 = 0.1$, the approximation is only acceptable for the smallest value of the Reynolds number considered ($Re_\omega = 1000$). For larger Re_ω, U from the model becomes close to, or even larger than unity, and the approximation fails. On the other hand, in most cases considered, the approximation with $\hat{C}_T^F$ works better for the smaller values of Re_ω, while the model with $\hat{C}_T^G$ is a less bad approximation for the larger values Re_ω in the range $10^3 - 10^4$. For $\alpha_0 > 0.1$ (not shown in Figure 2.17) U from the models is larger than unity for most Re_ω considered, and the approximation fails.

A glance at the strong conditions given by Equations (2.42), (2.45), (2.54) and (2.57) gives us the limited pitch amplitude range of validity of the simplified models, which have to be satisfied by the mean velocity U and the oscillation amplitude γ for each thrust model. Namely

$$\begin{aligned} \alpha_0^{2+b_0} Re_\omega^{a_0} \ll 1 \quad &\rightarrow \quad \alpha_0 \ll Re_\omega^{-a_0/(2+b_0)} \simeq Re_\omega^{-0.3}, \\ \frac{\alpha_0^2}{R} \ll 1 \quad &\rightarrow \quad \alpha_0 \ll R^{1/2}. \end{aligned} \tag{2.58}$$

These two conditions can also be presented in terms of the physical magnitudes as

$$\alpha_0 \left(\frac{\rho \omega c^2}{4\mu} \right)^{0.3} \ll 1, \qquad \alpha_0 \left(\frac{\pi \rho c^2}{4m} \right)^{0.5} \ll 1. \tag{2.59}$$

Note that the same validity conditions are obtained for both thrust approximations, in spite of the different power laws dependencies of U on α_0 and Re_ω. The first condition explains the comparison shown in Figure 2.17 between the simplified model for U and the numerical simulations, with the pitch amplitude range of validity decreasing with Re_ω. In fact, this condition predicts that for the case $\alpha_0 = 0.1$ of Figure 2.17(c) the model can only provide an approximation at the lowest Reynolds shown in the figure ($Re_\omega \sim 10^3$), while for Figure 2.17(a) the model performs for values of Re_ω well above 10^4. Furthermore, the second condition of Equation (2.58) is also partly responsible for the poorer agreement in Figure 2.17(c) for $\alpha_0 = 0.1$.

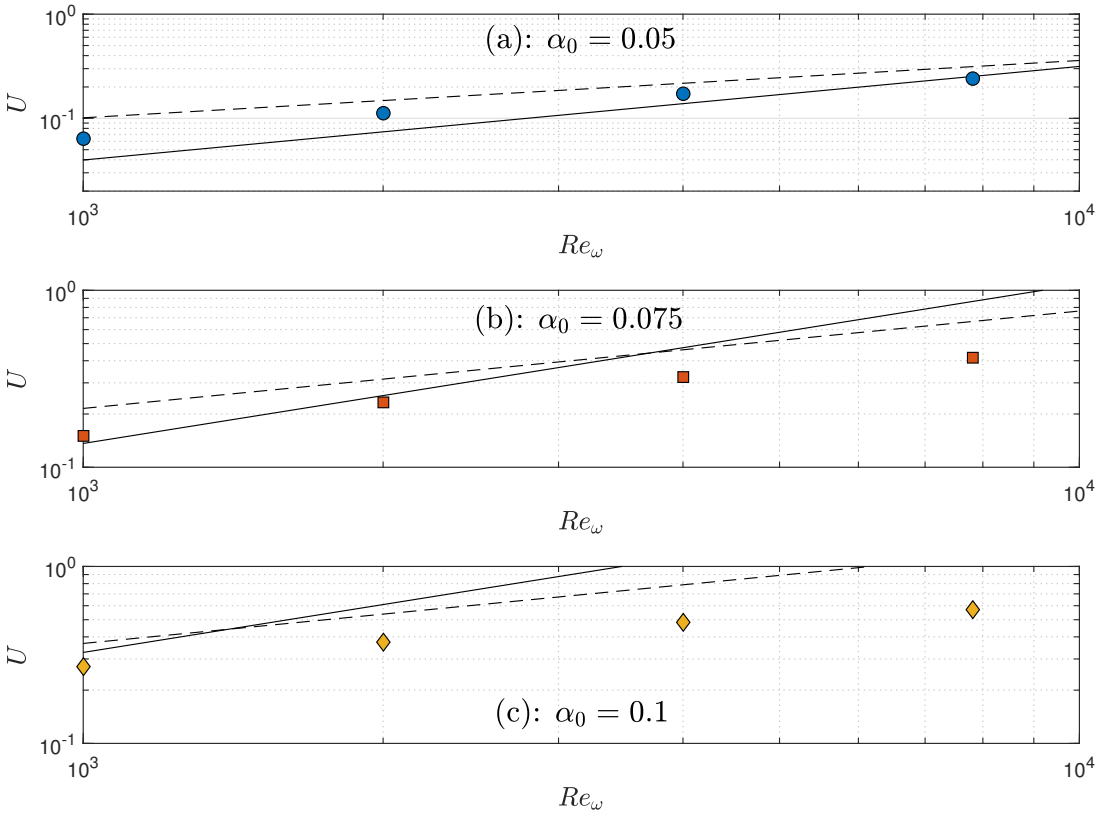

Figure 2.17: Comparison of U from the model approximations using $\hat{C}_T^G$ (dashed lines) and $\hat{C}_T^F$ (continuous lines) with numerical results for three values of α_0 and $10^3 \leq Re_\omega \leq 10^4$. $R = 0.02$ and $a = -1$.

2.6 Concluding remarks

In this chapter, we have explored the idea of a simple non-stationary model for a two-dimensional self-propelled pitching foil, obtaining some approximate analytical expressions for its non-stationary swimming velocity. These approximations have been derived using two thrust models from linear potential-flow theory, valid for a small pitch amplitude α_0, together with an unsteady viscous drag correlation obtained from high-fidelity numerical simulations (Fluent solver). In addition, these numerical simulations have also been used to assess the validity of the model approximation for the swimming velocity over a wide range of frequency-based Reynolds numbers ($10^3 \lesssim Re_\omega \lesssim 10^4$). The simplified model has been proved to be valid in a narrow range of pitch amplitudes that decreases as Re_ω increases, being negligibly small for $Re_\omega > 10^4$. In that aspect, the mass ratio R, which is usually small for flapping locomotion in water, also imposes a limitation on the pitch amplitude for the validity of the simplified model.

However, the numerical solutions of the model equations, which do not need the requirement of the small swimming velocity made for the simple approximate analytical solutions, are valid in a wider pitch amplitude range, similar to that described in Alaminos-Quesada [2021] for a pitching foil immersed in a uniform current (i.e., $St \lesssim 0.25$). Nonetheless, the approximate analytical solutions provide quick and precise information about the dependency of the swimming velocity on the different parameters, being very useful to start the design process for bioinspired underwater vehicles.

Finally, it is remarkable that although the swimming velocity predicted by the simplified expressions resulting from both thrust models considered ($\hat{C}_T^G$ and $\hat{C}_T^F$) are quantitatively similar within their common validity range, the power-law dependencies on α_0 and Re_ω are qualitatively different in each model over the Reynolds number range $10^3 \lesssim Re_\omega \lesssim 10^4$. It is also seen that the simplified model for $u(t)$ obtained with $\hat{C}_T^F$ works slightly better for very small α_0 over all the Re_ω range, and especially in the band closer to $Re_\omega = 10^3$ as α_0 increases. In contrast, the model with $\hat{C}_T^G$ works better in the band closer to $Re_\omega = 10^4$ for increasing α_0.

Chapter 3

An efficient self-propelled locomotion by a rigid foil

3.1 Introduction

In the previous chapter, we studied a simple non-stationary model for a self-propelled pitching foil, obtaining some useful analytical expressions for characterizing the swimming velocity of the foil when small pitch amplitudes are considered. Continuing with this line, in the present chapter, we want to explore the use of these new flapping propellers for locomotion through a model of a whole aquatic vehicle.

Some of the main advantages that these flapping foil propellers present in relation to their traditional rotating counterparts are higher maneuverability, easy control, low frequency, and fewer cavitation problems, among others. Those characteristics are very desirable in an aquatic vehicle, and for that reason, researchers have studied and proposed many possible configurations for a flapping propeller (Alben and Shelley [2005], Sanchez-Rodriguez et al. [2020], Lin et al. [2021], Paniccia et al. [2021], Ramos et al. [2021]). In our approach, we consider a particular one consisting of a rigid foil with a pitching motion generated by a given torque. To that end, torsional springs and dampers are considered so the pitching motion can be passively adapted to the forcing torque. Furthermore, a fully passive heaving motion of the foil is allowed since it is elastically mounted to translational springs and dampers. In relation to fully constrained configurations of rigid foils, this one allows for the possibility of resonant modes of the pitching and heaving motions that, as we shall see, may greatly enhance the thrust force and, therefore, the swimming velocity and the propulsive efficiency.

In that sense, many researchers have studied the semi-passive flapping foil configuration consisting of a forced pitching foil with passive heave, arriving to the conclusion that resonant phenomena may enhance their performance in both propulsion (Murray and Howle [2003], Mackowski and Williamson [2017], Fernandez-Feria and Alaminos-Quesada [2022]) and energy harvesting (Zhu and Peng [2009], Zhu et al. [2009], Deng et al. [2015], Su and Breuer [2019], Ma et al. [2021]) systems. However, the self-propulsion performance of a vehicle propelled by a flapping foil configuration, such as the one we have proposed before, where

its forward velocity is generated by the thrust force produced by the elastically mounted flapping foil, instead of just considering its propulsive performance in a uniform current, has not been analyzed yet. This study involves the fluid-structure interaction of the rigid foil elastically mounted to translational springs and dampers anchored to the vehicle hull. It results in a particularly complex problem that is very expensive to solve through full numerical simulations, which is probably one of the reasons for the scarce literature on this concept. Therefore, our approach to the matter will be focused on a model based on the linear potential-flow theory coupled with the dynamics of the elastically mounted rigid foil to the vehicle. In addition, this model will be validated by comparing its performance with full numerical simulations of the viscous flow in the limit of large translational spring constant so that the heaving motion of the self-propelled foil is inhibited and a comparison with the work developed in Chapter 2 can be appropriately done.

Consequently, the main goal that we pursue in this chapter is to obtain a new theoretical two-dimensional model of a more realistic aquatic vehicle propelled through that elastically mounted foil whose pitching motion is generated by a given torque applied at an arbitrary pivot axis instead of being prescribed, and coupled to a passive heaving motion. Hence, we can study the resonances arising in the elastically mounted system to select the proper spring and damper configuration that enhances the propulsion of the vehicle. To that end, we will use the linear potential-flow theory in combination with the self-propelled dynamics of the semi-passive flapping foil and, taking advantage of the small amplitude of the applied torque and the perturbative method, some simple powerlaws will be found that will serve as a valuable guide for the designing process of future aquatic vehicles prototypes.

3.2 Formulation of the problem

We consider an underwater vehicle self-propelled by a thin rigid hydrofoil through pitching and passive heaving motions (see Figure 3.1(a)). The foil has a large aspect ratio so that the flow and the fluid-foil interaction are assumed to be two-dimensional. It is actuated at a pivot point located at $\tilde{x}' = \tilde{a}$ by a sinusoidal torque per unit span $M_i(\tilde{t})$, where $\tilde{x}'$ is the coordinate along the foil centerline from the mid-chord (see Figure 3.1(b)) and $\tilde{t}$ the dimensional time. Remember that we use a *tilde* to remark that the variable is in the dimensional form to distinguish it from its dimensionless counterpart. The foil is elastically mounted to translational and torsional springs and dampers at the pivot point, with dimensional constants $\tilde{k}_h$ and $\tilde{k}_\alpha$ for the springs, and $\tilde{b}_h$ and $\tilde{b}_\alpha$ for the dampers, respectively. The corresponding force (along the transversal coordinate $\tilde{z}$) and torque exerted by these springs and dampers at the pivot point are denoted by L_o and M_o, respectively, both per unit span.

The applied sinusoidal torque induces a pitching motion $\tilde{\alpha}(\tilde{t})$ about $\tilde{x}' = \tilde{a}$, where the pivot point location may vary from $\tilde{a} = -c/2$ (leading edge) to $\tilde{a} = c/2$ (trailing edge), being c the chord length of the rigid foil. Due to the fluid-structure interaction (FSI) and to the action of the translational and torsional springs and dampers, the foil also undergoes a (passive) heaving motion along the $\tilde{z}$-direction that will be denoted by $\tilde{h}(\tilde{t})$. Both $\tilde{h}(\tilde{t})$ and $\tilde{\alpha}(\tilde{t})$ are unknowns. Additionally, the hydrofoil moves together with the vehicle while it

propels in the negative $\tilde{x}$-direction at a velocity $\tilde{u}(\tilde{t})$, also unknown.

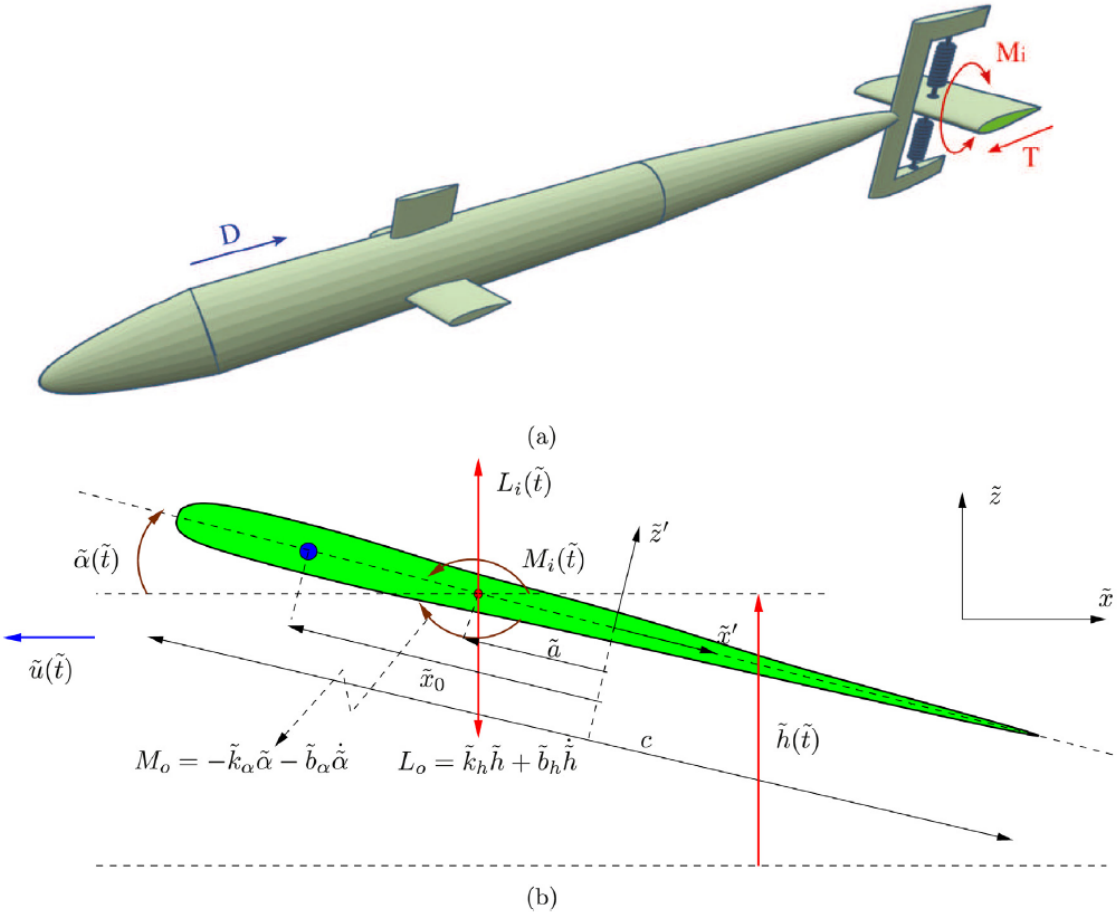

Figure 3.1: A 3D example model of the underwater vehicle (a) and a detailed sketch of the elastically supported rigid flapping foil attached to the tail of the vehicle (b). Dimensional quantities are used.

The dynamics of the rigid foil are governed by the following two equations, which result from the dynamic equation in the $\tilde{z}$-direction and the moment equation around the pivot axis, respectively.

$$m\left[\dot{\tilde{v}} + (\tilde{a} - \tilde{x}_0)\left(\ddot{\tilde{\alpha}}\cos\alpha - \dot{\tilde{\alpha}}^2\sin\alpha\right)\right] = L + L_i - L_o, \quad \text{with} \quad \tilde{v} = \dot{\tilde{h}}, \tag{3.1}$$

$$m(\tilde{x}_0 - \tilde{a})\dot{\tilde{v}}\cos\alpha - \tilde{I}_a\ddot{\tilde{\alpha}} = M + M_i - M_o, \tag{3.2}$$

where $L_o = \tilde{k}_h\tilde{h} + \tilde{b}_h\tilde{v}$ and $M_o = -\tilde{k}_\alpha\tilde{\alpha} - \tilde{b}_\alpha\dot{\tilde{\alpha}}$. In addition to the above mentioned parameters, m is the mass of the foil per unit span, $\tilde{v}$ the heave velocity, $\tilde{x}_0$ the foil's mass center, L_i an input force per unit span in the $\tilde{z}$-direction (included for completeness of the formulation so that it will be set to zero in the reported results), and L and M are the lift force and moment that the fluid exerts on the foil, both per unit span. On the other hand, $\tilde{I}_a$ is the moment of inertia and $m(\tilde{x}_0 - \tilde{a})$ the static moment about $\tilde{x} = \tilde{a}$. Notice that a *dot* denotes a derivative with respect to the dimensional time.

In relation to the equation of motion along the $\tilde{x}$-direction, we use Newton's second law applied to the vehicle center of mass

$$m'\dot{\tilde{u}} = sT - D, \tag{3.3}$$

where m' is the mass of the underwater vehicle and has units of mass in contrast to m, which has units of mass per unit span. On the other hand, T is the thrust force (per unit span s) that the fluid exerts on the hydrofoil and propels the vehicle in the opposite direction of the $\tilde{x}$ axis, and D is the drag force. Note that $\tilde{u}$ and T are assumed positive when pointing in the direction of negative $\tilde{x}$, while the drag force is positive in the opposite direction.

3.2.1 Non-dimensional formulation

Once the formulation of the problem has been presented, it is more interesting and general to work with non-dimensional variables. So, in what follows, all magnitudes are made dimensionless with the semi-chord length $c/2$, the fluid density ρ, and the frequency ω of the input torque, which in dimensionless form is given by

$$\hat{C}_{M_i} = \frac{8M_i}{\pi\rho c^4\omega^2} = \epsilon \sin t, \quad \epsilon = \frac{8A_M}{\pi\rho c^4\omega^2}, \tag{3.4}$$

where ϵ is the (known) non-dimensional torque intensity, which will be assumed small in the model, and A_M is its dimensional counterpart. The main non-dimensional variables of the problem will then be

$$\begin{gathered} x = \frac{\tilde{x}}{c/2}, \quad z = \frac{\tilde{z}}{c/2}, \quad t = \tilde{t}\omega, \quad u = \frac{\tilde{u}}{\omega c/2}, \quad \dot{u} = \frac{\dot{\tilde{u}}}{\omega^2 c/2}, \\ h = \frac{\tilde{h}}{c/2}, \quad \dot{h} = \frac{\dot{\tilde{h}}}{\omega c/2}, \quad \ddot{h} = \frac{\ddot{\tilde{h}}}{\omega^2 c/2}, \quad \alpha = \tilde{\alpha}, \quad \dot{\alpha} = \frac{\dot{\tilde{\alpha}}}{\omega}, \quad \ddot{\alpha} = \frac{\ddot{\tilde{\alpha}}}{\omega^2}. \end{gathered} \tag{3.5}$$

Notice that the non-dimensional swimming velocity $u(t)$ is in fact the inverse of the reduced frequency $k(t)$ commonly used in unsteady aerodynamics (e.g., Theodorsen [1935]), but now depending on time,

$$u(t) = \frac{\tilde{u}}{\omega c/2} = \frac{1}{k(t)}. \tag{3.6}$$

Taking all that into account, the dynamics of the rigid foil are governed by the following non-dimensional equations

$$R\left[\dot{v} + (a - x_0)\left(\ddot{\alpha}\cos\alpha - \dot{\alpha}^2 \sin\alpha\right)\right] = \hat{C}_L + \hat{C}_{L_i} - \hat{C}_{L_o}, \quad \text{with} \quad v = \dot{h}, \tag{3.7}$$

$$R\left[(x_0 - a)\dot{v}\cos\alpha - I_a\ddot{\alpha}\right] = 2(\hat{C}_M + \hat{C}_{M_i} - \hat{C}_{M_o}), \tag{3.8}$$

with $\hat{C}_{L_o} = k_h h + b_h v$ and $\hat{C}_{M_o} = -k_\alpha \alpha - b_\alpha \dot{\alpha}$, the non-dimensional force and torque exerted by the springs and dampers at the pivot point per unit span, respectively. On the other hand, $\hat{C}_L$ and $\hat{C}_M$ are the non-dimensional force component in the z-direction and the non-dimensional moment, respectively, that the fluid exerts on the foil per unit span, $\hat{C}_{L_i}$ the non-dimensional input force associated to L_i, and R the mass ratio. Note that now the *dot* denotes a derivative with respect to the dimensionless time t.

As in the previous chapter, a *hat* on all these coefficients is used to remark that they are not the usual lift and moment coefficients, C_L and C_M, scaled with $1/2\rho\tilde{u}^2 c$ and $1/2\rho\tilde{u}^2 c^2$, respectively; they are related to each other through

$$C_L = \frac{2L}{\rho\tilde{u}^2 c} = \frac{\pi\hat{C}_L}{u^2}, \qquad C_M = \frac{2M}{\rho\tilde{u}^2 c^2} = \frac{\pi\hat{C}_M}{u^2}, \tag{3.9}$$

and similarly for $\hat{C}_{L_i}$ and $\hat{C}_{M_i}$. Now, taking into consideration the foil's density and thickness distributions $\rho_s(\tilde{x}')$ and $\gamma(\tilde{x}')$, the remaining parameters in Equations (3.7) and (3.8) are

$$\begin{gathered} R = \frac{4m}{\pi\rho c^2}, \quad m = \int_{-c/2}^{c/2} \rho_s \gamma d\tilde{x}', \quad x_0 = \frac{1}{2}\int_{-1}^{1} x'\mathcal{M}dx', \\ I_a = \frac{1}{2}\int_{-1}^{1} (x'-a)^2 \mathcal{M}dx', \quad \text{with} \quad \mathcal{M} := \frac{\rho_s \gamma c}{m}. \end{gathered} \tag{3.10}$$

If the density ρ_s and the thickness γ were constants, such as $\mathcal{M} = 1$, then the center of mass would be at the mid-chord, $x_0 = 0$, and so

$$I_a = a^2 + \frac{1}{3}. \tag{3.11}$$

Also, note that we do not assume that the pivot point location coincides with the center of mass. It remains to define the spring and damper constants, related to their dimensional counterparts (per unit span) through

$$k_h = \frac{4\tilde{k}_h}{\pi\rho c^2\omega^2}, \quad b_h = \frac{4\tilde{b}_h}{\pi\rho c^2\omega}, \quad k_\alpha = \frac{8\tilde{k}_\alpha}{\pi\rho c^4\omega^2}, \quad b_\alpha = \frac{8\tilde{b}_\alpha}{\pi\rho c^4\omega}. \tag{3.12}$$

In relation to the equation of motion along the x-direction (Equation (3.3)), it can be written in dimensionless form as

$$R'\dot{u} = \hat{C}_T - Liu^2, \tag{3.13}$$

where

$$\hat{C}_T = \frac{8T}{\pi\rho c^3\omega^2} = \frac{u^2 C_T}{\pi}, \tag{3.14}$$

is the non-dimensional thrust force per unit span that the fluid exerts on the hydrofoil and propels the vehicle in the negative direction of the x axis, and Liu^2 is the vehicle's non-dimensional drag force written in terms of the Lighthill number Li, related to the drag coefficient C_D by

$$Li = \frac{A_w}{\pi cs} C_D, \qquad \text{with} \quad C_D = \frac{2D}{\rho\tilde{u}^2 A_w}, \tag{3.15}$$

being A_w the characteristic surface of the vehicle, and s the foil's span length. For simplicity, we shall assume that C_D is constant in the relevant range of Reynolds numbers for underwater propulsion (Gazzola et al. [2014], Gross et al. [2021]). Finally,

$$R' = \frac{4m'}{\pi\rho c^2 s}, \tag{3.16}$$

is the dimensionless mass ratio of the underwater vehicle. We shall not consider the vehicle's vertical motion due to the action of gravity, which, in any case, can be minimized using a neutrally buoyant vehicle.

3.2.2 Performance parameters

Looking at the above expressions, we can see that Equations (3.7), (3.8) and (3.13) constitute a set of three ordinary differential equations (ODEs) for $h(t)$, $\alpha(t)$ and $u(t)$ that can be solved for the given torque (Equation (3.4)) if the coefficients $\hat{C}_L(t)$, $\hat{C}_M(t)$ and $\hat{C}_T(t)$ coming from the FSI are known in terms of h, α and u (it will be adequately explained in subsequent sections of the chapter). But before that, it is convenient to define some relevant quantities to characterize the vehicle's self-propulsion.

One of them is the propulsive (Froude) efficiency, defined as the propulsion power divided by the power input spent to generate that propulsion. In dimensionless form, the power input is

$$\hat{C}_{P_i}(t) = \frac{16P_i(t)}{\pi\rho c^4\omega^3} = \dot{h}\hat{C}_{L_i}(t) - 2\dot{\alpha}\hat{C}_{M_i}(t) = -2\dot{\alpha}\epsilon\sin t. \tag{3.17}$$

Note that the minus sign comes from the different sign conventions for the pitch angle and the input torque; see Figure 3.1(b). In the present work, we assume $\hat{C}_{L_i} = 0$ so that the heaving motion is passive, and all the input power is associated with the input torque. On the other hand, the instantaneous propulsive power is the product of the velocity times the thrust force that generates this speed. Thus, the instantaneous propulsive efficiency is

$$H(t) = \frac{u(t)\hat{C}_T(t)}{\hat{C}_{P_i}(t)}. \tag{3.18}$$

Once the equations are solved for a given set of initial conditions, the solution will eventually reach a final permanent state consisting of an oscillatory periodic motion around a mean for each variable. Thus, for any magnitude $\phi(t)$, its time-average over n cycles (typically we take $n = 5$), once the permanent state for $t \gg 1$ has been reached, is denoted by an *overline* and given by

$$\bar{\phi} = \frac{1}{2\pi n}\int_t^{t+2\pi n} \phi(t)dt, \qquad t \gg 1. \tag{3.19}$$

Of particular relevance is the mean swimming speed $U = \bar{u}$, or mean value of u as $t \to \infty$, which in some circumstances is of interest to maximize in terms of the different parameters governing the problem. Notice that once a constant swimming velocity U has been reached, the time-average of the left-hand side of Equation (3.13) vanishes, and so does the mean of the right-hand side. Thus, the mean thrust generated by the flapping hydrofoil becomes equal to the mean drag of the whole cruising vehicle: $\overline{\hat{C}}_T = Li\overline{u^2} > 0$ for $t \to \infty$. Consequently, the propulsive efficiency is

$$\eta = \overline{H} = \frac{\overline{u\hat{C}_T}}{\overline{\hat{C}_{P_i}}} = \frac{R'\overline{u\dot{u}} + Li\overline{u^3}}{\overline{\hat{C}_{P_i}}} \simeq \frac{Li\overline{u^3}}{\overline{\hat{C}_{P_i}}}, \tag{3.20}$$

where Equation (3.13) has been used. The last expression after '$\simeq$' comes from the fact that once the final oscillatory state has been reached, u becomes an almost harmonic function of time and $u\dot{u} \simeq 0$. This expression shows that, for a given powering torque and vehicle's drag (Li), maximizing the dimensionless swimming velocity U is equivalent to maximizing η.

It is known that maximum propulsive efficiency is usually reached in a narrow range of the Strouhal number (Triantafyllou et al. [1993]), which is defined as

$$St = \frac{\omega \tilde{A}}{2\pi \widetilde{U}} = \frac{A}{2\pi U}, \tag{3.21}$$

where $\tilde{A}$ is the beat amplitude, taken as the maximum peak-to-peak flapping foil amplitude (A is its dimensionless counterpart). Thus, sometimes it is more interesting to characterize the cruising velocity U in terms of St, usually in combination with the corresponding Reynolds number (Das et al. [2022])

$$Re = \frac{\widetilde{U} c}{\nu}, \tag{3.22}$$

where ν is the kinematic viscosity. Finally, for cruising, it is sometimes preferable to use the cost of transport instead of the Froude efficiency as a measure of the self-propulsion efficiency (Gabrielli and von Kármán [1951], Paniccia et al. [2021]). It is defined as the energy consumption per unit distance traveled by the vehicle

$$\widetilde{CoT} = \frac{\overline{P_i}}{\widetilde{U}} = \frac{\pi \rho c^3 s \omega^2}{8} CoT, \qquad CoT = \frac{\overline{\hat{C}_{P_i}}}{U}, \tag{3.23}$$

where CoT is the dimensionless cost of transport that will be used in the reported results. In contrast, some authors use the non-dimensional cost of transport $\overline{P}/(W\widetilde{U})$, where W is the weight of the vehicle. However, we believe that the above CoT is more consistent with the present non-dimensionalization.

3.3 Linearized model

If the torque intensity ϵ is small enough, one may assume that the pitch and heave amplitudes are also small, $|\alpha| \ll 1$ and $|h| \ll 1$, so that one may use the expressions of $\hat{C}_L(t)$, $\hat{C}_M(t)$ and $\hat{C}_T(t)$ from the linear potential-flow theory for a harmonic foil motion, but written in a general form in terms of α, h, u and their temporal derivatives. In particular, we use Theodorsen's expressions for the lift and moment coefficient (Theodorsen [1935]), modified by Greeberg [1947] with additional terms proportional to $\dot{u}$ to account for the pulsating stream, and with Theodorsen's function appearing in the circulatory terms evaluated at variable $k(t) = 1/u(t)$, (see Section A.1 of Appendix A for more precise and detailed information about these coefficients and where they come from):

$$\hat{C}_L = \frac{8L}{\pi \rho c^3 \omega^2} = -\dot{v} - a\ddot{\alpha} + u\dot{\alpha} + \dot{u}\alpha + \Re[C(k)] u \Gamma_0(t), \tag{3.24}$$

$$\begin{aligned} \hat{C}_M = \frac{8M}{\pi \rho c^4 \omega^2} = \frac{1}{2}\left[a\dot{v} + \left(a^2 + \frac{1}{8}\right)\ddot{\alpha} + \left(\frac{1}{2} - a\right) u\dot{\alpha} - a\dot{u}\alpha \right] \\ - \frac{1}{2}\left(\frac{1}{2} + a\right) \Re[C(k)] u \Gamma_0(t), \end{aligned} \tag{3.25}$$

$$\Gamma_0(t) = -2\left[v + \left(a - \frac{1}{2}\right)\dot{\alpha} - u\alpha \right], \tag{3.26}$$

where

$$C(k) = \frac{H_1^{(2)}(k)}{iH_0^{(2)}(k) + H_1^{(2)}(k)} = \mathcal{F}(k) + i\mathcal{G}(k), \tag{3.27}$$

is Theodorsen's function and $\Re$ means real part, being $H_n^{(2)}(z) = J_n(z) - iY_n(z)$, with $n = \{0, 1\}$ the Hankel's function of the second kind and order n, related to the Bessel functions of the first and second kind $J_n(z)$ and $Y_n(z)$. These forces and moment have been widely validated against experimental data for pitching and heaving rigid foils, even for not-so-small amplitude of the oscillations (Halfman [1952], Baik et al. [2012]). So, they are used in the linearized form of Equation (3.7) and Equation (3.8)

$$R\left[\dot{v} + (a - x_0)\ddot{\alpha}\right] = \hat{C}_L + \hat{C}_{L_i} - \hat{C}_{L_o}, \quad \text{with} \quad v = \dot{h}, \tag{3.28}$$

$$R\left[(x_0 - a)\dot{v} - I_a\ddot{\alpha}\right] = 2(\hat{C}_M + \hat{C}_{M_i} - \hat{C}_{M_o}). \tag{3.29}$$

For the thrust coefficient, we use in Equation (3.13) the results from the linearized vortical impulse theory (Fernandez-Feria [2016]), which are also explained in Appendix A. These results have been validated against experimental data for small amplitude of the oscillations and sufficiently large Reynolds numbers, both for pitching and heaving foils in a uniform flow (Fernandez-Feria [2016, 2017], Fernandez-Feria and Sanmiguel-Rojas [2019], Alaminos-Quesada [2021]) and for self-propelled pitching foils in Chapter 2. In the present notation, it can be written as

$$\begin{aligned}\hat{C}_T = \frac{8T}{\pi\rho c^3\omega^2} = &- \alpha\hat{C}_L + \dot{\alpha}\left[v + a\dot{\alpha} - u\alpha\right] + \Gamma_0(t)\Bigg\{\Re\left[\frac{2iC_1(k)}{\pi}\right] \\ &\cdot\left[-v + 2\alpha u + (1 - a)\dot{\alpha}\right] - \Re[C(k)]u\alpha\Bigg\},\end{aligned} \tag{3.30}$$

where (see Appendix A)

$$C_1(k) = \frac{\frac{1}{k}e^{-ik}}{iH_0^{(2)}(k) + H_1^{(2)}(k)} = \mathcal{F}_1(k) + i\mathcal{G}_1(k). \tag{3.31}$$

Therefore, the resulting system of ODEs (Equations (3.13), (3.28) and (3.29)) can be solved numerically for $h(t)$, $\alpha(t)$, and $u(t)$, which will be covered in later sections of this chapter. On the other hand, the self-propulsion model here developed is similar to the one considered by Sanchez-Rodriguez et al. [2020] but more general and complete since we consider a more realistic torque (Equation (3.4)) in contrast to the prescribed pitching kinematic $\alpha(t) = \alpha_0 \sin t$ used in their study. Consequently, we need the additional moment of Equation (3.29), which is physically relevant since, thanks to that, we can compute the input power and, therefore, the propulsive efficiency and the cost of transport, which cannot be obtained with the simpler model of Sanchez-Rodriguez et al. [2020]. In addition, we can select the sets of parameters that produce the optimal efficiency or the optimal cost of transport. Also, additional translational and torsional springs and dampers are used here, which enriches the model and whose characteristics may be varied to improve the propulsion performance due to resonance between passive and forced motions (Fernandez-Feria and Alaminos-Quesada [2021b]). Further, the pivot axis location $x = a$ is set here independently of the center of mass of the foil $x = x_0$ so that one may explore its effect on the propulsion performance separately.

Finally, we use expression Equation (3.30) for the thrust, which corresponds to Fernandez-Feria's thrust used in Chapter 2 but now extended for allowing the passive heaving motion of the foil. This thrust yields practically the same results as Garrick's one (Garrick [1936]) used in Sanchez-Rodriguez et al. [2020] at low reduced frequencies, and also has proven to agree better with experimental data in a broader range of parameters (Fernandez-Feria [2016], Fernandez-Feria and Sanmiguel-Rojas [2019], Alaminos-Quesada [2021]). The differences are particularly relevant for highly reduced frequencies, corresponding to the small velocity limit considered in the next section's asymptotic analysis.

3.4 Approximate analytical solution from two-scales perturbation method

Alternatively to the numerical solution of the model Equations (3.13), (3.28) and (3.29), one may take advantage of the small torque intensity ϵ to obtain an analytical approximation for $h(t)$, $\alpha(t)$, and $u(t)$ using perturbation methods. In particular, from the structure of the equations, one might assume two timescales: t, associated with the period of the oscillations, and

$$\tau = B\epsilon^b t, \tag{3.32}$$

associated with the slower variations of the mean values, where the constants B and b will be determined from the scaling of the different terms in Equation (3.13). In Appendix B can be found a brief explanation of this two-scale perturbative method and a simple example to illustrate how it is properly used. Thus, the time derivatives are approximated by

$$\frac{d}{dt} = \frac{\partial}{\partial t} + B\epsilon^b \frac{\partial}{\partial \tau}, \qquad \frac{d^2}{dt^2} = \frac{\partial^2}{\partial t^2} + 2B\epsilon^b \frac{\partial^2}{\partial t \partial \tau} + B^2\epsilon^{2b} \frac{\partial^2}{\partial \tau^2}. \tag{3.33}$$

Assuming that, and according to Equations (3.28) and (3.29), the lowest-order amplitude of the pitching and heaving oscillations is of the same order ϵ as the forcing torque $\hat{C}_{M_i}$. The asymptotic expansions for h and α with the two timescales can be written as

$$h(t,\tau) \sim \epsilon h_1(t,\tau) + \epsilon^2 h_2(t,\tau) + \cdots, \qquad \alpha(t,\tau) \sim \epsilon \alpha_1(t,\tau) + \epsilon^2 \alpha_2(t,\tau) + \cdots. \tag{3.34}$$

As we shall see, only the next terms in these expansions depend on the expansion of u if, as shown below, $u \ll \epsilon$. In general, we can write the expansion for u as

$$u(t,\tau) \sim \epsilon^{n_1} u_1(t,\tau) + \epsilon^{n_2} u_2(t,\tau) + \cdots, \tag{3.35}$$

with $1 < n_1 < n_2 < \cdots$ to be determined. To perform the expansions for the force and moment coefficients, we take into account that $k = u^{-1} \gg 1$, so that one may use the large-k approximation of the functions Equations (3.27) and (3.31) (see, e.g., Fernandez-Feria and Sanmiguel-Rojas [2019])

$$\Re[C(k)] = \frac{1}{2} + O(k^{-2}), \qquad \Re\left[\frac{2i}{\pi} C_1(k)\right] = \frac{1}{(4\pi k)^{1/2}} + O(k^{-3/2}). \tag{3.36}$$

Taking that into consideration, the force and moment coefficients can be written as

$$\hat{C}_L = -\ddot{h} - a\ddot{\alpha} + \left(\frac{3}{2} - a\right) u\dot{\alpha} + \dot{u}\alpha - u\dot{h} + u^2\alpha, \tag{3.37}$$

$$\hat{C}_M = \frac{1}{2}\left[a\ddot{h} + \left(a^2 + \frac{1}{8}\right)\ddot{\alpha} + \left(\frac{1}{2} - a\right)^2 u\dot{\alpha} - a\dot{u}\alpha + \left(\frac{1}{2} + a\right)(u\dot{h} - u^2\alpha)\right], \tag{3.38}$$

$$\hat{C}_T = \alpha\ddot{h} + a\alpha\ddot{\alpha} + (2a-3)u\alpha\dot{\alpha} - \dot{u}\alpha^2 + 2u\alpha\dot{h} - 2u^2\alpha^2 + \dot{\alpha}\dot{h} + a\dot{\alpha}^2 + \frac{1}{\sqrt{\pi}}\Bigg[\sqrt{u}\dot{h}^2$$
$$-3u^{3/2}\alpha\dot{h} + \left(2a - \frac{3}{2}\right)\sqrt{u}\dot{\alpha}\dot{h} - (3a-2)u^{3/2}\alpha\dot{\alpha} + \left(a - \frac{1}{2}\right)(a-1)\sqrt{u}\dot{\alpha}^2 + 2u^{5/2}\alpha^2\Bigg]. \tag{3.39}$$

3.4.1 Expansions of the main equations

Lift Equation

Taking into consideration all the previous information, Equation (3.28) becomes

$$R[\ddot{h} + (a - x_0)\ddot{\alpha}] + b_h\dot{h} + k_h h = -\ddot{h} - a\ddot{\alpha} + \left(\frac{3}{2} - a\right)u\dot{\alpha} + \dot{u}\alpha - u\dot{h} + u^2\alpha, \tag{3.40}$$

and substituting the corresponding asymptotic expansions until the order $1 + 2n_1$

$$R\left(\epsilon\frac{\partial^2 h_1}{\partial t^2} + \epsilon^2\frac{\partial^2 h_2}{\partial t^2} + 2B\epsilon^{b+1}\frac{\partial^2 h_1}{\partial t\partial\tau} + \cdots\right) + R(a - x_0)\left(\epsilon\frac{\partial^2\alpha_1}{\partial t^2} + \epsilon^2\frac{\partial^2\alpha_2}{\partial t^2}\right.$$
$$\left.+2B\epsilon^{b+1}\frac{\partial^2\alpha_1}{\partial t\partial\tau} + \cdots\right) + b_h\left(\epsilon\frac{\partial h_1}{\partial t} + \epsilon^2\frac{\partial h_2}{\partial t} + B\epsilon^{b+1}\frac{\partial h_1}{\partial\tau} + \cdots\right) + k_h(\epsilon h_1 + \epsilon^2 h_2 + \cdots)$$
$$= -\left(\epsilon\frac{\partial^2 h_1}{\partial t^2} + \epsilon^2\frac{\partial^2 h_2}{\partial t^2} + 2B\epsilon^{b+1}\frac{\partial^2 h_1}{\partial t\partial\tau} + \cdots\right) - a\left(\epsilon\frac{\partial^2\alpha_1}{\partial t^2} + \epsilon^2\frac{\partial^2\alpha_2}{\partial t^2} + 2B\epsilon^{b+1}\frac{\partial^2\alpha_1}{\partial t\partial\tau} + \cdots\right)$$
$$+\left(\frac{3}{2} - a\right)\left(\epsilon^{1+n_1}u_1\frac{\partial\alpha_1}{\partial t} + \epsilon^{1+n_2}u_2\frac{\partial\alpha_1}{\partial t} + \cdots\right) + \left(\epsilon^{1+n_1}\alpha_1\frac{\partial u_1}{\partial t} + \epsilon^{1+n_2}\alpha_1\frac{\partial u_2}{\partial t} + \cdots\right)$$
$$-\left(\epsilon^{1+n_1}u_1\frac{\partial h_1}{\partial t} + \epsilon^{1+n_2}u_2\frac{\partial h_1}{\partial t} + \cdots\right) + (\epsilon^{1+2n_1}\alpha_1 u_1^2 + \cdots). \tag{3.41}$$

From the right-hand side of the equation, we can find a power series such as

$$\hat{C}_L = \epsilon\hat{C}_{L,1} + \epsilon^2\hat{C}_{L,2} + \epsilon^{b+1}\hat{C}_{L,b+1} + \epsilon^{1+n_1}\hat{C}_{L,1+n_1} + \epsilon^{1+n_2}\hat{C}_{L,1+n_2} + \cdots, \tag{3.42}$$

where

$$\hat{C}_{L,1} = -\frac{\partial^2 h_1}{\partial t^2} - a\frac{\partial^2\alpha_1}{\partial t^2}, \quad \hat{C}_{L,2} = -\frac{\partial^2 h_2}{\partial t^2} - a\frac{\partial^2\alpha_2}{\partial t^2}, \quad \hat{C}_{L,b+1} = -2B\frac{\partial^2 h_1}{\partial t\partial\tau} - a2B\frac{\partial^2\alpha_1}{\partial t\partial\tau},$$
$$\hat{C}_{L,1+n_1} = \left(\frac{3}{2} - a\right)u_1\frac{\partial\alpha_1}{\partial t} + \alpha_1\frac{\partial u_1}{\partial t} - u_1\frac{\partial h_1}{\partial t},$$
$$\hat{C}_{L,1+n_2} = \left(\frac{3}{2} - a\right)u_2\frac{\partial\alpha_1}{\partial t} + \alpha_1\frac{\partial u_2}{\partial t} - u_2\frac{\partial h_1}{\partial t}. \tag{3.43}$$

Moment Equation

Analogously for the moment, Equation (3.29) becomes

$$\begin{aligned} R\left[(x_0-a)\ddot{h}-I_a\ddot{\alpha}\right]-2(b_\alpha\dot{\alpha}+k_\alpha\alpha) = a\ddot{h}+\left(a^2+\frac{1}{8}\right)\ddot{\alpha}+\left(\frac{1}{2}-a\right)^2 u\dot{\alpha} \\ -a\dot{u}\alpha+\left(\frac{1}{2}+a\right)(u\dot{h}-u^2\alpha)+2\epsilon\sin t, \end{aligned} \tag{3.44}$$

and substituting the corresponding asymptotic expansions until the order $1+2n_1$

$$\begin{aligned} R(x_0-a)\left(\epsilon\frac{\partial^2 h_1}{\partial t^2}+\epsilon^2\frac{\partial^2 h_2}{\partial t^2}+2B\epsilon^{b+1}\frac{\partial^2 h_1}{\partial t\partial\tau}+\cdots\right)-RI_a\left(\epsilon\frac{\partial^2\alpha_1}{\partial t^2}+\epsilon^2\frac{\partial^2\alpha_2}{\partial t^2}\right. \\ \left.+2B\epsilon^{b+1}\frac{\partial^2\alpha_1}{\partial t\partial\tau}+\cdots\right)-2b_\alpha\left(\epsilon\frac{\partial\alpha_1}{\partial t}+\epsilon^2\frac{\partial\alpha_2}{\partial t}+B\epsilon^{b+1}\frac{\partial\alpha_1}{\partial\tau}+\cdots\right)-2k_\alpha(\epsilon\alpha_1+\epsilon^2\alpha_2+\cdots) \\ -2\epsilon\sin t = a\left(\epsilon\frac{\partial^2 h_1}{\partial t^2}+\epsilon^2\frac{\partial^2 h_2}{\partial t^2}+2B\epsilon^{b+1}\frac{\partial^2 h_1}{\partial t\partial\tau}+\cdots\right)+\left(a^2+\frac{1}{8}\right)\left(\epsilon\frac{\partial^2\alpha_1}{\partial t^2}+\epsilon^2\frac{\partial^2\alpha_2}{\partial t^2}\right. \\ \left.+2B\epsilon^{b+1}\frac{\partial^2\alpha_1}{\partial t\partial\tau}+\cdots\right)+\left(\frac{1}{2}-a\right)^2\left(\epsilon^{1+n_1}u_1\frac{\partial\alpha_1}{\partial t}+\epsilon^{1+n_2}u_2\frac{\partial\alpha_1}{\partial t}+\cdots\right) \\ -a\left(\epsilon^{1+n_1}\alpha_1\frac{\partial u_1}{\partial t}+\epsilon^{1+n_2}\alpha_1\frac{\partial u_2}{\partial t}+\cdots\right)+\left(\frac{1}{2}+a\right)\left(\epsilon^{1+n_1}u_1\frac{\partial h_1}{\partial t}+\epsilon^{1+n_2}u_2\frac{\partial h_1}{\partial t}+\cdots\right) \\ -\left(\frac{1}{2}+a\right)(\epsilon^{1+2n_1}\alpha_1 u_1^2+\cdots). \end{aligned} \tag{3.45}$$

From the right-hand side of the equation, we can find a power series such as

$$\hat{C}_M=\epsilon\hat{C}_{M,1}+\epsilon^2\hat{C}_{M,2}+\epsilon^{b+1}\hat{C}_{M,b+1}+\epsilon^{1+n_1}\hat{C}_{M,1+n_1}+\epsilon^{1+n_2}\hat{C}_{M,1+n_2}+\cdots, \tag{3.46}$$

where

$$\begin{aligned} \hat{C}_{M,1}=a\frac{\partial^2 h_1}{\partial t^2}+\left(a^2+\frac{1}{8}\right)\frac{\partial^2\alpha_1}{\partial t^2}, \quad \hat{C}_{M,2}=a\frac{\partial^2 h_2}{\partial t^2}+\left(a^2+\frac{1}{8}\right)\frac{\partial^2\alpha_2}{\partial t^2}, \\ \hat{C}_{L,b+1}=a2B\frac{\partial^2 h_1}{\partial t\partial\tau}+\left(a^2+\frac{1}{8}\right)2B\frac{\partial^2\alpha_1}{\partial t\partial\tau}, \\ \hat{C}_{M,1+n_1}=\left(\frac{1}{2}-a\right)^2 u_1\frac{\partial\alpha_1}{\partial t}-a\alpha_1\frac{\partial u_1}{\partial t}+\left(\frac{1}{2}+a\right)u_1\frac{\partial h_1}{\partial t}, \\ \hat{C}_{M,1+n_2}=\left(\frac{1}{2}-a\right)^2 u_2\frac{\partial\alpha_1}{\partial t}-a\alpha_1\frac{\partial u_2}{\partial t}+\left(\frac{1}{2}+a\right)u_2\frac{\partial h_1}{\partial t}. \end{aligned} \tag{3.47}$$

Thrust Equation

Finally, for the thrust, Equation (3.13) becomes

$$R'\dot{u} + Liu^2 = \alpha\ddot{h} + a\alpha\ddot{\alpha} + (2a-3)u\alpha\dot{\alpha} - \dot{u}\alpha^2 + 2u\alpha\dot{h} - 2u^2\alpha^2 + \dot{\alpha}\dot{h} + a\dot{\alpha}^2 + \frac{1}{\sqrt{\pi}}\left[\sqrt{u}\dot{h}^2 \right.$$
$$\left. -3u^{3/2}\alpha\dot{h} + \left(2a-\frac{3}{2}\right)\sqrt{u}\dot{\alpha}\dot{h} - (3a-2)u^{3/2}\alpha\dot{\alpha} + \left(a-\frac{1}{2}\right)(a-1)\sqrt{u}\dot{\alpha}^2 + 2u^{5/2}\alpha^2\right]. \tag{3.48}$$

Note that now, we need the expansion of $u^{1/2}$, which is

$$(\epsilon^{n_1}u_1 + \epsilon^{n_2}u_2 + \cdots)^{1/2} = \left[(\epsilon^{n_1}u_1)\left(1 + \frac{\epsilon^{n_2}}{\epsilon^{n_1}}\frac{u_2}{u_1} + \cdots\right)\right]^{1/2} \approx \epsilon^{n_1/2}u_1^{1/2}\left[1 + \frac{1}{2}(\epsilon^{n_2-n_1}u_2u_1^{-1}) + \cdots\right], \tag{3.49}$$

and similarly for the rest of the powers of u. Substituting then the corresponding asymptotic expansions until the order $2+n_2$ we obtain

$$R'\left(\epsilon^{n_1}\frac{\partial u_1}{\partial t} + \epsilon^{n_2}\frac{\partial u_2}{\partial t} + B\epsilon^{b+n_1}\frac{\partial u_1}{\partial \tau} + \cdots\right) + Li(\epsilon^{2n_1}u_1^2 + 2\epsilon^{n_1+n_2}u_1u_2 + \epsilon^{2n_2}u_2^2 + \cdots)$$
$$= \left(\epsilon^2\alpha_1\frac{\partial^2 h_1}{\partial t^2} + \cdots\right) + a\left(\epsilon^2\alpha_1\frac{\partial^2\alpha_1}{\partial t^2} + \cdots\right) + (2a-3)\left(\epsilon^{2+n_1}u_1\alpha_1\frac{\partial\alpha_1}{\partial t} + \cdots\right)$$
$$-\left(\epsilon^{2+n_1}\alpha_1^2\frac{\partial u_1}{\partial t} + \epsilon^{2+n_2}\alpha_1^2\frac{\partial u_2}{\partial t}\cdots\right) + 2\left(\epsilon^{2+n_1}u_1\alpha_1\frac{\partial h_1}{\partial t} + \epsilon^{2+n_2}u_2\alpha_1\frac{\partial h_1}{\partial t}\cdots\right)$$
$$-2(\cdots) + \left(\epsilon^2\frac{\partial\alpha_1}{\partial t}\frac{\partial h_1}{\partial t} + \cdots\right) + a\left(\epsilon^2\frac{\partial\alpha_1}{\partial t}\frac{\partial\alpha_1}{\partial t} + \cdots\right) + \frac{1}{\sqrt{\pi}}\Bigg\{$$
$$\left(\epsilon^{2+n_1/2}u_1^{1/2}\frac{\partial h_1}{\partial t}\frac{\partial h_1}{\partial t} + \cdots\right) - 3(\cdots) + \left(2a-\frac{3}{2}\right)\left(\epsilon^{2+n_1/2}u_1^{1/2}\frac{\partial\alpha_1}{\partial t}\frac{\partial h_1}{\partial t} + \cdots\right)$$
$$-(3a-2)(\cdots) + \left(a-\frac{1}{2}\right)(a-1)\left(\epsilon^{2+n_1/2}u_1^{1/2}\frac{\partial\alpha_1}{\partial t}\frac{\partial\alpha_1}{\partial t} + \cdots\right) + 2(\cdots)\Bigg\}. \tag{3.50}$$

From the right-hand side of the equation, we can find a power series such as

$$\hat{C}_T = \epsilon\hat{C}_{T,1} + \epsilon^2\hat{C}_{T,2} + \epsilon^{2+n_1/2}\hat{C}_{T,2+n_1/2} + \cdots, \tag{3.51}$$

where

$$\hat{C}_{T,1} = 0, \quad \hat{C}_{T,2} = \alpha_1\frac{\partial^2 h_1}{\partial t^2} + a\alpha_1\frac{\partial^2\alpha_1}{\partial t^2} + \frac{\partial\alpha_1}{\partial t}\frac{\partial h_1}{\partial t} + a\left(\frac{\partial\alpha_1}{\partial t}\right)^2,$$
$$\hat{C}_{T,2+n_1/2} = \frac{u_1^{1/2}}{\sqrt{\pi}}\left[\left(\frac{\partial h_1}{\partial t}\right)^2 + \left(2a-\frac{3}{2}\right)\frac{\partial\alpha_1}{\partial t}\frac{\partial h_1}{\partial t} + \left(a-\frac{1}{2}\right)(a-1)\left(\frac{\partial\alpha_1}{\partial t}\right)^2\right]. \tag{3.52}$$

Once we have all the expansions performed, if we look at the permanent final state, we can see that the leading drag term (i.e., Liu^2) must balance the leading thrust term. Since the $O(\epsilon^2)$ thrust term only depends on t, the drag term must balance the next order in the expansion of $\hat{C}_T$. Thus

$$\begin{aligned} 2n_1 = 2 + n_1/2 \rightarrow n_1 = 4/3, \\ n_1 + n_2 = 2 + n_1 \rightarrow n_2 = 2, \\ n_1 + n_3 = 2 + n_2 \rightarrow n_3 = 8/3. \end{aligned} \tag{3.53}$$

In addition, these terms must also balance the leading term containing derivatives with the slow time τ, i.e.,

$$b + n_1 = 2n_1 \rightarrow b = n_1 = 4/3. \tag{3.54}$$

Consequently, the expansion for u is

$$u(t,\tau) = \epsilon^{4/3}u_1(t,\tau) + \epsilon^2 u_2(t,\tau) + \epsilon^{8/3}u_3(t,\tau) + \cdots, \tag{3.55}$$

and the timescale τ associated with the slower variations of the mean values is

$$\tau = B\epsilon^{4/3}t. \tag{3.56}$$

Resulting equations

Gathering all the terms in the main expressions, we can obtain the following resulting equations. From the Lift Equation, we get

$$\begin{aligned} O(\epsilon) &: R\frac{\partial^2 h_1}{\partial t^2} + R(a-x_0)\frac{\partial^2 \alpha_1}{\partial t^2} + b_h\frac{\partial h_1}{\partial t} + k_h h_1 = \hat{C}_{L,1}, \\ O(\epsilon^2) &: R\frac{\partial^2 h_2}{\partial t^2} + R(a-x_0)\frac{\partial^2 \alpha_2}{\partial t^2} + b_h\frac{\partial h_2}{\partial t} + k_h h_2 = \hat{C}_{L,2}, \\ O(\epsilon^{7/3}) &: R2B\frac{\partial^2 h_1}{\partial t\partial \tau} + R(a-x_0)2B\frac{\partial^2 \alpha_1}{\partial t\partial \tau} + b_h B\frac{\partial h_1}{\partial \tau} = \hat{C}_{L,b+1} + \hat{C}_{L,1+n_1} = \hat{C}_{L,7/3}. \end{aligned} \tag{3.57}$$

From the Moment Equation

$$\begin{aligned} O(\epsilon) &: R(x_0-a)\frac{\partial^2 h_1}{\partial t^2} - RI_a\frac{\partial^2 \alpha_1}{\partial t^2} - 2b_\alpha\frac{\partial \alpha_1}{\partial t} - 2k_\alpha\alpha_1 - 2\sin t = \hat{C}_{M,1}, \\ O(\epsilon^2) &: R(x_0-a)\frac{\partial^2 h_2}{\partial t^2} - RI_a\frac{\partial^2 \alpha_2}{\partial t^2} - 2b_\alpha\frac{\partial \alpha_2}{\partial t} - 2k_\alpha\alpha_2 = \hat{C}_{M,2}, \\ O(\epsilon^{7/3}) &: R(x_0-a)2B\frac{\partial^2 h_1}{\partial t\partial \tau} - RI_a 2B\frac{\partial^2 \alpha_1}{\partial t\partial \tau} - 2b_\alpha B\frac{\partial \alpha_1}{\partial \tau} = \hat{C}_{M,b+1} + \hat{C}_{M,1+n_1} = \hat{C}_{M,7/3}. \end{aligned} \tag{3.58}$$

Finally, from the Thrust Equation

$$\begin{aligned} O(\epsilon^{4/3}) &: R'\frac{\partial u_1}{\partial t} = \hat{C}_{T,1} = 0 \rightarrow u_1 = u_1(\tau), \\ O(\epsilon^2) &: R'\frac{\partial u_2}{\partial t} = \hat{C}_{T,2}, \\ O(\epsilon^{8/3}) &: R'\left(\frac{\partial u_3}{\partial t} + B\frac{\partial u_1}{\partial \tau}\right) + Liu_1^2 = \hat{C}_{T,2+n_1/2} = \hat{C}_{T,8/3}. \end{aligned} \tag{3.59}$$

3.4.2 Analysis of the lowest order in the lift and moment equations

Analyzing the lowest order in the lift and moment equations, one gets the two following expressions, which are independent of u

$$\begin{cases} (R+1)\dfrac{\partial^2 h_1}{\partial t^2} + [R(a-x_0)+a]\dfrac{\partial^2 \alpha_1}{\partial t^2} + b_h \dfrac{\partial h_1}{\partial t} + k_h h_1 = 0, \\ [R(x_0-a)-a]\dfrac{\partial^2 h_1}{\partial t^2} - \left[RI_a + \left(a^2+\dfrac{1}{8}\right)\right]\dfrac{\partial^2 \alpha_1}{\partial t^2} - 2b_\alpha \dfrac{\partial \alpha_1}{\partial t} - 2k_\alpha \alpha_1 = 2\sin t. \end{cases} \tag{3.60}$$

This system of two linear equations for h_1 and α_1 has a homogeneous solution that contains transient terms of the form $e^{\lambda_1 t}$ and a particular solution for the term $2e^{it}$, such as $h_1 = h_{1H} + h_{1P}$ and $\alpha_1 = \alpha_{1H} + \alpha_{1P}$.

Homogeneous solution

One can get the homogeneous solution knowing that it has to be of the form $h_{1H} = \hat{h}_1 e^{\lambda_1 t}$, $\alpha_{1H} = \hat{\alpha}_1 e^{\lambda_1 t}$. By substituting into the System of Equations (3.60), the following equations are obtained for $\hat{h}_1$ and $\hat{\alpha}_1$

$$\begin{pmatrix} (R+1)\lambda_1^2 + b_h\lambda_1 + k_h & [R(a-x_0)+a]\lambda_1^2 \\ [R(x_0-a)-a]\,\lambda_1^2 & -[RI_a + (a^2+1/8)]\lambda_1^2 - 2b_\alpha\lambda_1 - 2k_\alpha \end{pmatrix} \begin{pmatrix} \hat{h}_1 \\ \hat{\alpha}_1 \end{pmatrix} = \begin{pmatrix} 0 \\ 0 \end{pmatrix}. \tag{3.61}$$

The determinant of this matrix system must be null in order to obtain the not trivial solution for $\hat{h}_1$ and $\hat{\alpha}_1$, thus

$$\begin{vmatrix} (R+1)\lambda_1^2 + b_h\lambda_1 + k_h & [R(a-x_0)+a]\lambda_1^2 \\ [R(x_0-a)-a]\,\lambda_1^2 & -[RI_a + (a^2+1/8)]\lambda_1^2 - 2b_\alpha\lambda_1 - 2k_\alpha \end{vmatrix} = 0. \tag{3.62}$$

Analyzing this determinant for $x_0 = 0$ and any positive values of the dampers constants b_h and b_α, $\Re(\lambda_1)$ is found to be negative for the four possible solutions of λ_1, which means that the exponential terms $e^{\lambda_1 t}$ decays very fast to zero making the system stable for any value of k_h and of k_α and for all physically relevant values of R and a. As an example, Figure 3.2 shows the results in the plane (k_α, k_h) of the maximum of $\Re(\lambda_1)$ for $b_h = b_\alpha = 0.05$, $R = 0.02$ and two values of a. Similar results are found for $-1 \le a \le x_0 = 0$ (i.e., pitching axis upstream of the center foil, which is the center of mass) and any value of R. Actually, the system becomes more stable as R increases.

In addition, if we eliminate the dampers $b_h = b_\alpha = 0$ and take $x_0 = 0$, the solution of the resulting determinant has no real part, and the system is always neutrally stable, with the following solution for the eigenvalues

$$\lambda_1 = \pm i \left(\frac{2k_\alpha(R+1) + k_h(RI_a + a^2 + 1/8)}{R^2/3 + 11R/24 + 1/8} \right)^{1/2}. \tag{3.63}$$

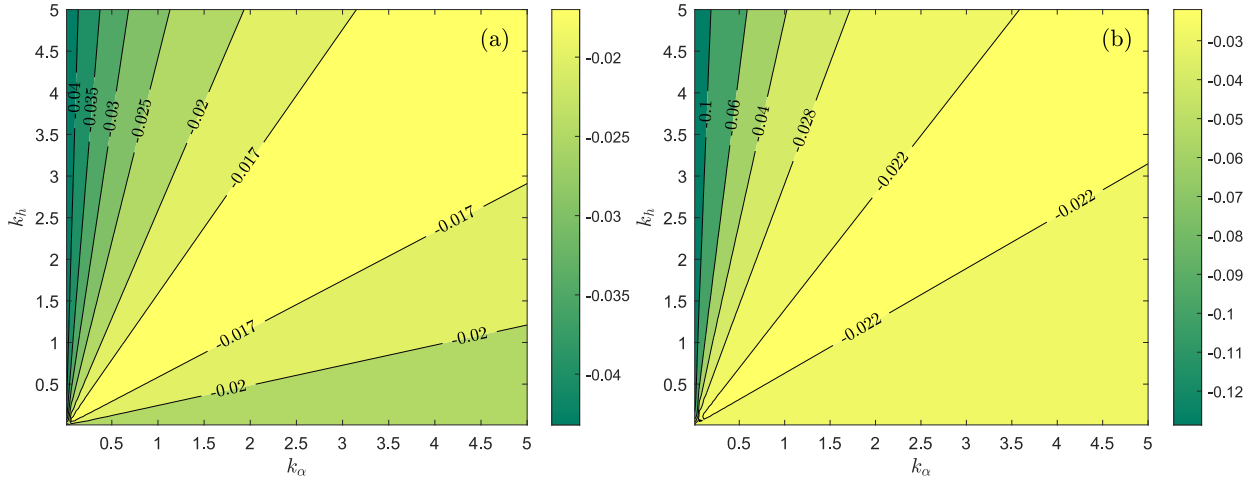

Figure 3.2: Contour plots in the $k_\alpha - k_h$ plane of $\max[\Re(\lambda_1)]$ for $R = 0.02$, $x_0 = 0$, and $b_h = b_\alpha = 0.05$, and for $a = -1$ (a) and $a = -0.5$ (b).

Particular solution

For the particular or permanent solution, it will be of the kind

$$\begin{aligned} h_{1P} &= C_1 \sin t + C_2 \cos t = H_1 \sin(t + \phi_{h1}), \\ \alpha_{1P} &= C_3 \sin t + C_4 \cos t = A_1 \sin(t + \phi_{a1}). \end{aligned} \tag{3.64}$$

This particular solution can be written in a complex format, which is easier to manipulate. Thus

$$\begin{aligned} h_{1P} &= H_1 e^{i(t+\phi_{h1})} = H_1 e^{i\phi_{h1}} e^{it} = \mathcal{H}_1 e^{it}, \\ \alpha_{1P} &= A_1 e^{i(t+\phi_{a1})} = A_1 e^{i\phi_{a1}} e^{it} = \mathcal{A}_1 e^{it}. \end{aligned} \tag{3.65}$$

Substituting this particular solution into the System of Equations (3.60), one can get the following system of linear equations for the complex parameters $\mathcal{H}_1$ and $\mathcal{A}_1$:

$$\mathbf{A} \begin{pmatrix} \mathcal{H}_1 \\ \mathcal{A}_1 \end{pmatrix} \equiv \begin{pmatrix} -(R+1) + b_h i + k_h & -[R(a-x_0)+a] \\ R(a-x_0)+a & [RI_a + (a^2+1/8)] - 2b_\alpha i - 2k_\alpha \end{pmatrix} \begin{pmatrix} \mathcal{H}_1 \\ \mathcal{A}_1 \end{pmatrix} = \begin{pmatrix} 0 \\ 2 \end{pmatrix}. \tag{3.66}$$

Once $\mathcal{H}_1$ and $\mathcal{A}_1$ are known, the values of H_1, ϕ_{h1}, A_1, and ϕ_{a1} are obtained from

$$\begin{aligned} H_1 &= \sqrt{\Re(\mathcal{H}_1)^2 + \Im(\mathcal{H}_1)^2}, \quad \phi_{h1} = \arctan\left(\frac{\Im(\mathcal{H}_1)}{\Re(\mathcal{H}_1)}\right), \\ A_1 &= \sqrt{\Re(\mathcal{A}_1)^2 + \Im(\mathcal{A}_1)^2}, \quad \phi_{a1} = \arctan\left(\frac{\Im(\mathcal{A}_1)}{\Re(\mathcal{A}_1)}\right), \end{aligned} \tag{3.67}$$

where $\Im$ means the imaginary part. The general solution coincides in practice with the particular one since, as it was shown, the real part of the eigenvalues is always negative, and so the exponential terms $e^{\lambda_1 t}$ decay very fast to zero. Thus

$$\begin{aligned} h_1 &= h_{1H} + h_{1P} \simeq h_{1P} = H_1 \sin(t + \phi_{h1}), \\ \alpha_1 &= \alpha_{1H} + \alpha_{1P} \simeq \alpha_{1P} = A_1 \sin(t + \phi_{a1}). \end{aligned} \tag{3.68}$$

Similarly, one may obtain the solution for the next order (ϵ^2) of both α and h, which is also independent of the swimming velocity u. However, it will not be given here because we are only interested in the lowest-order solution. Therefore, the final analytical expressions we obtain for h and α are

$$\begin{aligned} h(t,\tau) &\sim \epsilon h_1(t) + \cdots \sim \epsilon H_1 \sin(t + \phi_{h1}) + \cdots, \\ \alpha(t,\tau) &\sim \epsilon \alpha_1(t) + \cdots \sim \epsilon A_1 \sin(t + \phi_{a1}) + \cdots. \end{aligned} \tag{3.69}$$

with H_1, ϕ_{h1}, A_1, and ϕ_{a1} given by the mathematical expressions appearing in the Set of Equations (3.67).

Resonant values

Of particular interest are the values of the spring constants k_h and k_α that maximize the heaving and pitching amplitudes since the thrust force and, consequently, the swimming velocity U will be enhanced. These values, denoted here by k_{hr} and $k_{\alpha r}$, are obtained by minimizing $|\det(\mathbf{A})|$, where $\mathbf{A}$ is the 2×2 matrix in Equation (3.66), and physically correspond to particular resonant frequencies for given dimensional constants $\tilde{k}_h$ and $\tilde{k}_\alpha$. A good approximation for the resonant value of k_h when the damping constants b_h and b_α are small is the value of k_h for which $|\det(\mathbf{A})|$ actually vanishes when $b_h = b_\alpha = 0$. Thus,

$$k_{hr0} = 1 + R - \frac{[R(a - x_0) + a]^2}{RI_a + a^2 + 1/8 - 2k_\alpha}. \tag{3.70}$$

Note that $k_{hr0} \to \infty$ for

$$k_\alpha = \frac{1}{2}\left(RI_a + a^2 + \frac{1}{8}\right) \equiv k_{\alpha\infty}. \tag{3.71}$$

It is interesting to remark that, with the present lowest-order solution, the optimal propulsion conditions might be approximately predicted by just minimizing a relatively simple algebraic expression such as $|\det(\mathbf{A})|$.

3.4.3 Analysis of the first orders in the thrust equation

Once we have the analytical values for h_1 and α_1, we can pay attention to the thrust equation and analyze the different orders to obtain an analytical expression for u following a similar process as the one described for the lowest order of h and α.

Analysis of the order ϵ^2

The resulting expression for the order ϵ^2 in the thrust equation is

$$R'\frac{\partial u_2}{\partial t} = \alpha_1\frac{\partial^2 h_1}{\partial t^2} + a\frac{\partial^2 \alpha_1}{\partial t^2} + \frac{\partial \alpha_1}{\partial t}\frac{\partial h_1}{\partial t} + a\left(\frac{\partial \alpha_1}{\partial t}\right)^2. \tag{3.72}$$

Substituting the values of h_1 and α_1 and their respective derivatives, one can get

$$R'\frac{\partial u_2}{\partial t} = A_1\{H_1\cos(2t+\phi_{h1}+\phi_{a1}) + aA_1\cos[2(t+\phi_{a1})]\}, \tag{3.73}$$

and by integrating, one obtains the oscillatory part of the swimming velocity

$$u_2(t,\tau) = \frac{A_1}{2R'}\{H_1\sin(2t+\phi_{h1}+\phi_{a1}) + aA_1\sin[2(t+\phi_{a1})]\} + U_2(\tau), \quad \text{with } U_2(0)=0. \tag{3.74}$$

The function $U_2(\tau)$ has to be obtained from the order $\epsilon^{10/3}$, but we are only interested in the lowest-order dependence of the swimming velocity on τ, $u_1(\tau)$, to which $U_2(\tau)$ is a minor correction.

Analysis of the order $\epsilon^{8/3}$

The resulting expression for the order $\epsilon^{8/3}$ in the thrust equation is

$$R'\left(\frac{\partial u_3}{\partial t} + B\frac{\partial u_1}{\partial \tau}\right) + Liu_1^2 = \frac{u_1^{1/2}}{\sqrt{\pi}}\left[\left(\frac{\partial h_1}{\partial t}\right)^2 + \left(2a-\frac{3}{2}\right)\frac{\partial \alpha_1}{\partial t}\frac{\partial h_1}{\partial t} + \left(a-\frac{1}{2}\right)(a-1)\left(\frac{\partial \alpha_1}{\partial t}\right)^2\right]. \tag{3.75}$$

Substituting the values of h_1 and α_1 and their respective derivatives

$$\begin{aligned} R'\left(\frac{\partial u_3}{\partial t} + B\frac{\partial u_1}{\partial \tau}\right) + Liu_1^2 = \frac{u_1^{1/2}}{\sqrt{\pi}}\Bigg\{C + \frac{H_1^2}{2}\cos[2(t+\phi_{h1})] \\ + \left(a-\frac{3}{4}\right)A_1H_1\cos(2t+\phi_{h1}+\phi_{a1}) + \left(a-\frac{1}{2}\right)(a-1)\frac{A_1^2}{2}\cos[2(t+\phi_{a1})]\Bigg\}, \end{aligned} \tag{3.76}$$

where

$$C = \frac{H_1^2}{2} + \left(a-\frac{3}{4}\right)A_1H_1\cos(\phi_{a1}-\phi_{h1}) + \left(a-\frac{1}{2}\right)(a-1)\frac{A_1^2}{2}. \tag{3.77}$$

To avoid secular terms in the timescale t, we have the freedom within the two-scales perturbation method (Kevorkian and Cole [1981]) to select the equation for $u_1(\tau)$ that cancels the non-oscillatory terms. Therefore, we select

$$R'B\frac{\partial u_1}{\partial \tau} = \frac{C}{\sqrt{\pi}}u_1^{1/2} - Liu_1^2, \tag{3.78}$$

$$R'\frac{\partial u_3}{\partial t} = \frac{u_1^{1/2}}{\sqrt{\pi}}\left\{\frac{H_1^2}{2}\cos[2(t+\phi_{h1})] + \left(a-\frac{3}{4}\right)A_1H_1\cos(2t+\phi_{h1}+\phi_{a1}) + \left(a-\frac{1}{2}\right)(a-1)\frac{A_1^2}{2}\cos[2(t+\phi_{a1})]\right\}. \tag{3.79}$$

One may obtain an analytical expression for $u_1(\tau)$ from Equation (3.78). To do that, it is useful to define $u_1(\tau) = U_1 w_1(\tau)$ and substitute that into the equation. Thus, we get

$$R'BU_1\frac{\partial w_1}{\partial \tau} = \frac{C}{\sqrt{\pi}}U_1 w_1^{1/2} - LiU_1^2 w_1^2, \tag{3.80}$$

then selecting $B = \dfrac{LiU_1}{R'}$, we obtain the non-dimensional equation for the first order of the velocity

$$\frac{\partial w_1}{\partial \tau} = w_1^{1/2} - w_1^2, \tag{3.81}$$

being $U_1 = \left(\dfrac{C}{\sqrt{\pi}Li}\right)^{2/3}$. It turns out that w_1 always tends to unity as $\tau \to \infty$, and so the lowest-order (time-averaged) final swimming velocity is

$$U \sim \epsilon^{4/3}\bar{u}_1 = \epsilon^{4/3}U_1. \tag{3.82}$$

The solution of Equation (3.81) that satifies $w_1(0) = 0$ can be formally written in implicit form as

$$\tau = 2\frac{w_1^2 - w_1^{1/2}}{w_1^{3/2} - 1}F\left[1, 1/3; 4/3, w_1^{3/2}\right], \tag{3.83}$$

where F is Gauss' hypergeometric function (Olver et al. [2010]). Working with Equation (3.79), one may obtain the third order of the expansion of u. However, we are only interested in the first two terms since they provide the greater part of the information.

3.4.4 Self-propulsion characteristics from the lowest-order asymptotic solution

Summing up the results of the previous section, the lowest-order swimming velocity can be written as

$$u(t,\tau) \sim \epsilon^{4/3}U_1 w_1(\tau) + \epsilon^2\frac{A_1}{2R'}\{H_1\sin(2t+\phi_{h1}+\phi_{a1}) + aA_1\sin[2(t+\phi_{a1})]\} + \cdots, \quad \text{with} \quad \tau = \epsilon^{4/3}Bt, \tag{3.84}$$

where the constants are

$$U_1 = \left(\frac{C}{\sqrt{\pi}Li}\right)^{2/3}, \qquad B = \frac{LiU_1}{R'}, \tag{3.85}$$

and the function $w_1(\tau)$ is given by Equation (3.83). On the other hand, the lowest-order heaving and pitching motions are

$$h(t) \sim \epsilon H_1 \sin(t + \phi_{h1}) + \cdots, \quad \alpha(t) \sim \epsilon A_1 \sin(t + \phi_{a1}) + \cdots, \tag{3.86}$$

with H_1, A_1, ϕ_{h1} and ϕ_{a1} given by the Set of Equations (3.67). It is observed that the dimensionless time-averaged swimming velocity is proportional to $\epsilon^{4/3}U_1$ and, because of the definition we adopt for U_1, it means that the velocity is also proportional to $\epsilon^{4/3}[\max(A_1, H_1)^2]^{2/3}/Li^{2/3} \sim [\epsilon \max(A_1, H_1)]^{4/3}/Li^{2/3}$. Thus, to maximize U one has to look for the highest amplitudes of the hydrofoil oscillations and to reduce as much as possible the body drag.

The maxima of A_1 and H_1 are attained at the resonant values of k_h and k_α for given values of the remaining parameters. Actually, these amplitudes become infinity for vanishing dampers constants when $k_h = k_{hr0}$ given by Equation (3.70) in terms of k_α. Thus, in order to approach the best performance, we shall consider small values of b_h and b_α to account for any mechanical friction: $b_h = b_\alpha = 0.05$, say. For these small values, the resonance curve in the $k_\alpha - k_h$ plane at which both A_1 and H_1 reach their maxima is very close to k_{hr0}, as shown in Figure 3.3 for specific values of the remaining parameters. In particular, we select $R = 0.02$, typical for a hydrofoil in water, a pitch axis at the leading edge ($a = -1$) and a center of mass coinciding with the center of the foil ($x_0 = 0$). These values, which are physically justified in the next section, will be used in all the reported results except otherwise specified.

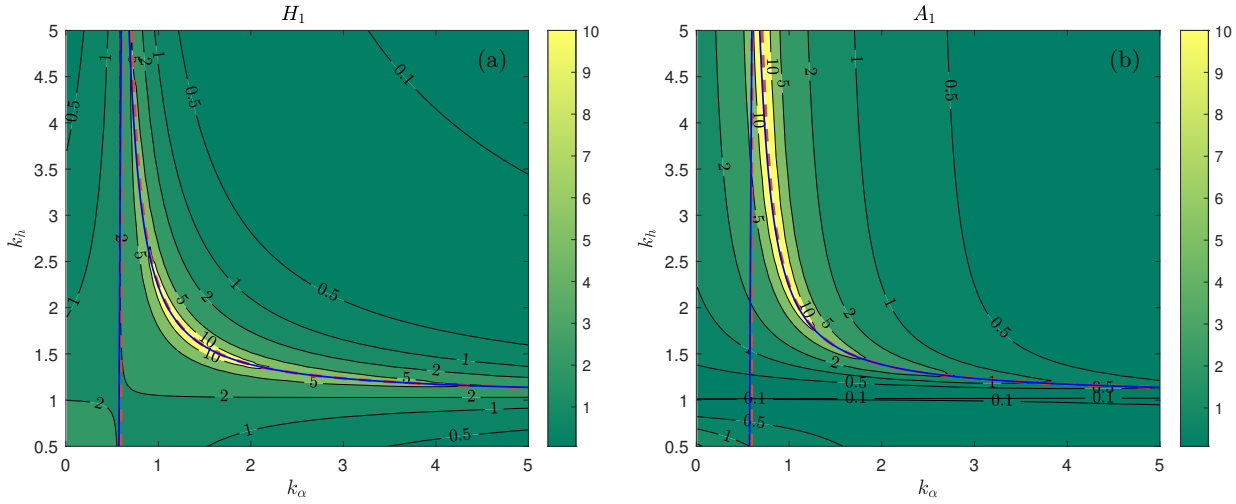

Figure 3.3: Contour plots in the $k_\alpha - k_h$ plane of H_1 (a) and A_1 (b) for $a = -1$, $R = 0.02$, $x_0 = 0$, and $b_h = b_\alpha = 0.05$. The thick blue line corresponds to the minimum of $|\det(\mathbf{A})|$, while the dashed red one to k_{hr0} given by Equation 3.70, being the vertical branch $k_{\alpha\infty}$ from Equation 3.71.

As expected, the maxima of the swimming velocity are also reached for $k_h = k_{hr} \simeq k_{hr0}$ as k_α is varied when b_h and b_α are small, as shown in Figure 3.4(a) for the same values of the parameters used in Figure 3.3. The quantity $U_1 Li^{2/3} = (C/\sqrt{\pi})^{2/3}$ plotted in this figure is the lowest-order swimming velocity scaled with $Li^{2/3}/\epsilon^{4/3}$, which is independent of the

Lighthill number and the torque amplitude ϵ. Clearly, the perturbation solution ceases to be valid as one approaches the resonant curve $k_{hr}(k_\alpha)$ since U_1 becomes so large that the small swimming velocity requirement Equation (3.35) cannot be satisfied even for very small ϵ. It will be discussed further in the following sections, where the lowest-order asymptotic solution will be compared with the numerical solution of the model Equations (3.13), (3.28) and (3.29), and also with the numerical solutions from the full Navier-Stokes equations in some particular cases.

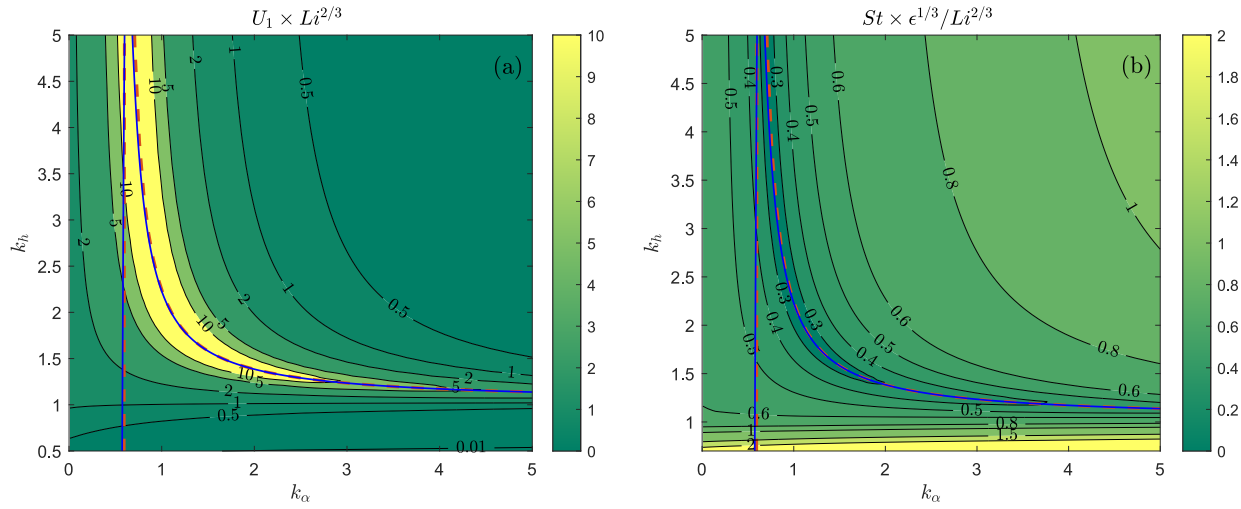

Figure 3.4: As in Figure 3.3, but for the contours of the scaled lowest-order swimming velocity, $ULi^{2/3}/\epsilon^{4/3} \sim U_1 Li^{2/3}$ (a), and the scaled lowest-order Strouhal number, $St\epsilon^{1/3}/Li^{2/3}$ (b).

Another interesting result is that the Strouhal number (Equation (3.21)), which at the lowest order of the asymptotic solution, is given by

$$St \sim \frac{2\epsilon[H_1 + (1+|a|)A_1]}{2\pi U} = \frac{Li^{2/3}}{\epsilon^{1/3}} \frac{H_1 + (1+|a|)A_1}{(\pi C)^{2/3}}, \tag{3.87}$$

reaches its minima around the resonant values of $k_h = k_{hr}(k_\alpha)$, as it is shown in Figure 3.4(b), where the maxima of the velocity are located. In addition, one is interested in the efficiency and the cost of transport derived from the lowest-order asymptotic solution. To that end, one has to compute first the power coefficient (Equation (3.17)), which, from the above lowest-order solution for $\alpha(t)$, is

$$\hat{C}_{Pi} \sim \hat{C}_{Pi1} = -2\epsilon^2 A_1 \cos(t + \phi_{a1}) \sin t, \tag{3.88}$$

and its time average,

$$\overline{\hat{C}_{Pi1}} = \frac{1}{2\pi} \int_0^{2\pi} -2\epsilon^2 A_1 \cos(t' + \phi_{a1}) \sin t' dt' = \epsilon^2 A_1 \sin \phi_{a1}. \tag{3.89}$$

With this quantity, one may compute the cost of transport (Equation (3.23)), which at the lowest order is given by

$$CoT \sim \frac{\overline{\hat{C}_{Pi1}}}{U} = \frac{\epsilon^2 A_1 \sin \phi_{a1}}{\epsilon^{4/3} U_1} = \frac{\epsilon^{2/3} \pi^{1/3} Li^{2/3} A_1 \sin \phi_{a1}}{C^{2/3}}. \tag{3.90}$$

Finally, the efficiency (Equation (3.20)) at this lowest order of the asymptotic solution can be written as

$$\eta \sim \frac{LiU^3}{\overline{\hat{C}_{Pi1}}} = \frac{Li\epsilon^4 U_1^3}{\epsilon^2 A_1 \sin\phi_{a1}} = \frac{\epsilon^2 C^2}{\pi A_1 \sin\phi_{a1} Li}. \tag{3.91}$$

These two alternative efficiencies, CoT and η, are plotted in Figure 3.5, scaled in such a way that they are independent of both Li and ϵ, as in the previous figures of this section. The high-efficiency pattern around the resonant values $k_h = k_{hr}(k_\alpha)$ almost coincides with that of the maxima of the swimming velocity, as afore-commented, and with that of local maxima of the cost of transport. This result, where the cost of transport behaves inversely to the propulsive efficiency, is analogous to that previously found by Akoz and Moored [2018] by forcing a constant self-propelled swimming velocity for a defined body via a change of frequency, and in the numerical simulations for a self-propelled fishlike body by Paniccia et al. [2021]. Hence, one has to select different values of the spring constants in order to optimize either the Froude efficiency and the swimming velocity or the cost of transport. This issue will be discussed in more detail below, but using numerical results of the model, not just the present analytical approximation.

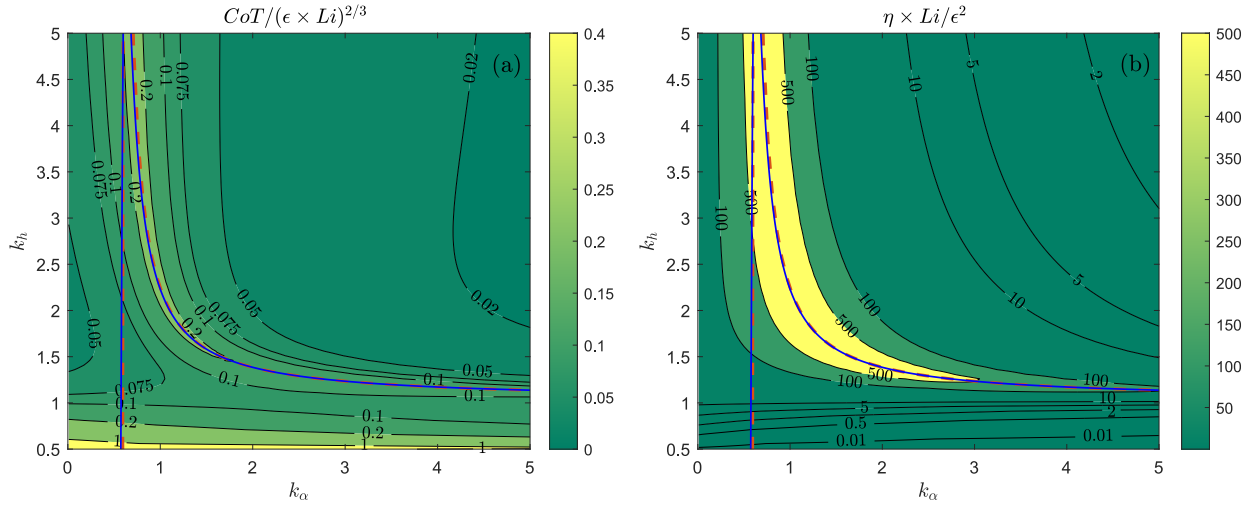

Figure 3.5: As in Figure 3.3, but for the contours of the scaled lowest-order cost of transport, $CoT/(\epsilon Li)^{2/3}$ (a), and the scaled efficiency, $\eta Li/\epsilon^2$ (b).

3.5 Assessment and numerical results from the model equations

Numerical results of the model Equations (3.13), (3.28) and (3.29) are presented in this section. They are solved using Matlab's solver *ode45*, starting from the initial conditions $\alpha(0) = 0$, $h(0) = 0$ and $u(0) = 0.01$, see Appendix C to find more information about the numerical resolution process. In addition, these results are compared with the lowest-order asymptotic solution obtained in the previous section. Nevertheless, before that, a validation of the model is presented.

3.5.1 Validation of the model from full numerical simulations

It is worth mentioning that the non-stationary thrust force (Equation (3.30)), on which the present self-propulsion model is based, has already been validated comparing with viscous numerical results and experimental data when the pitching foil is immersed into a uniform current (Alaminos-Quesada [2021]). Moreover, its performance was validated in Chapter 2 and in Fernandez-Feria and Alaminos-Quesada [2022] with full viscous numerical results of the self-propelled foil for a prescribed pitching motion, provided that the pitch amplitude is sufficiently small and the Reynolds number is larger than about 10^3. In relation to the previous chapter, in the present one, the hydrofoil undergoes an additional passive heaving motion generated by Theodorsen's lift force (Equation (3.24)) and moment (Equation (3.25)), which have been widely validated against experimental data for pitching and heaving rigid foils even for not so small amplitude of the oscillations when the Reynolds number is large enough (Halfman [1952], Baik et al. [2012]).

Nonetheless, to reinforce this validation for the present problem, which includes a self-propelled vehicle characterized by a constant drag and a mass through the non-dimensional parameters Li and R', Figure 3.6 shows a comparison of the numerical results of the model equations with those from full viscous numerical simulations for a vehicle with $Li = 0.1$ and $R' = 0.2$ (typical values for a small vehicle with a size of about 1 m) self-propelled by a purely pitching foil with pitch amplitude $\alpha_0 = 0.042$ (small enough for the present model be valid). The numerical code used for this comparison is the same as the one presented in Chapter 2, but slightly modified since now we use the more complete Equation (3.13) for the movement of the whole vehicle and not only for that one of the hydrofoil. Therefore, the code provides the thrust coefficient $\hat{C}_T(t)$ at each instant of time by solving the full Navier-Stokes (N-S) equations for the instantaneous position of the pitching foil, which follows the same dynamical Equation (3.13) of the model, but now with $\hat{C}_T(t)$ computed numerically form the exact N-S equations instead of the model Equation (3.30). In both cases, we use for the hydrofoil $R = 0.02$, $a = -1$, and $x_0 = 0$, as in the analytical results reported above. The frequency Reynolds number selected is $Re_\omega = \omega c^2/(4\nu) = 5000$. The model equations are solved with the translational spring constant $k_h = 100$ so that the heaving motion is negligible, thus matching the problem solved numerically for a pure pitching foil, together with $b_h = 0.05$, $k_\alpha = 0.05$ and $b_\alpha = 1$. This last value is selected to reduce as much as possible the transient in $\alpha(t)$ when generated by the torque (Equation (3.4)) so that it rapidly approaches the pure pitching motion used as an input in the N-S simulations. As

observed in Figure 3.6(b), the pitch $\alpha(t)$ from the model equations with torque intensity $\epsilon = 0.05$ rapidly evolves to the value $\alpha = 0.042 \sin t$ used in the N-S simulations. Also note that the corresponding lowest-order pitch amplitude in the asymptotic solution is almost the same, $\epsilon A_1 \simeq 0.044$.

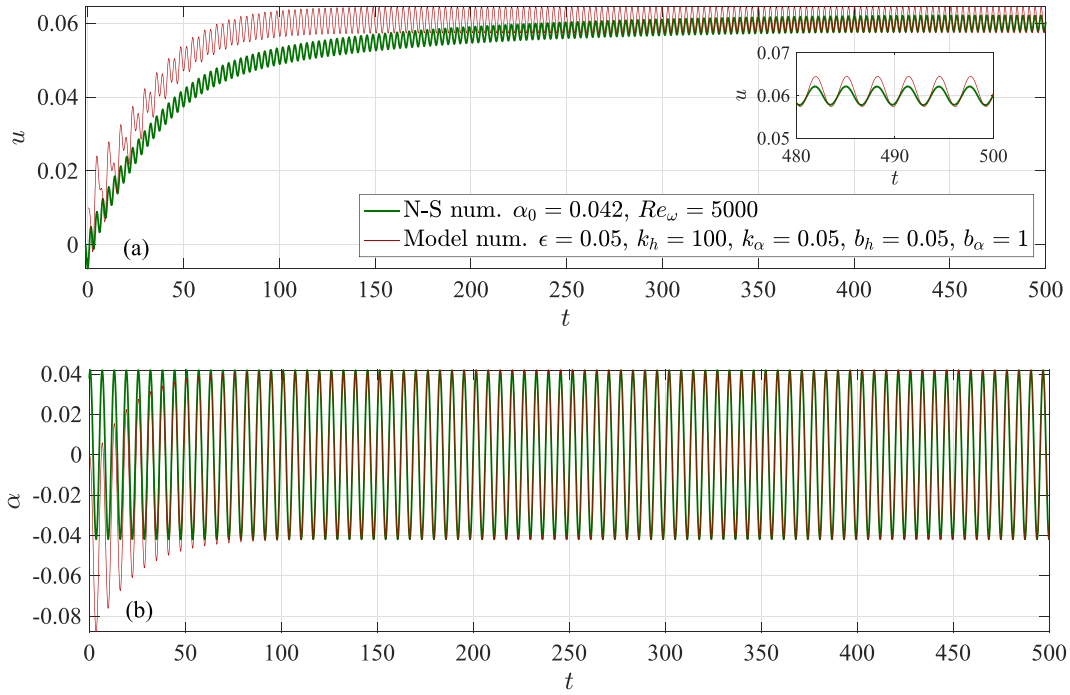

Figure 3.6: (a): Comparison between $u(t)$ obtained with $\hat{C}_T$ from full Navier-Stokes numerical simulations (N-S num.) for the pitching motion $\alpha(t) = 0.042 \sin t$ given by the green line in (b), with $u(t)$ from the numerical solution of the model equations for $\epsilon = 0.05$, $R' = 0.2$, $Li = 0.1$, $R = 0.02$, $a = -1$, $x_0 = 0$, $b_h = 0.05$, $b_\alpha = 1$, $k_h = 100$, and $k_\alpha = 0.05$. (b): $\alpha(t)$ from the model equations generated by the input torque $\hat{C}_{M_i} = \epsilon \sin t$ (red) compared to the input pitch in the N-S simulations (green). The inset in (a) is a detail of the last cycles.

From Figure 3.6, it is observed that, despite the differences in the transient of the pitch $\alpha(t)$, which in the model equations is generated by a sinusoidal torque of given intensity ϵ instead of being imposed as in the N-S simulations, the numerical results reached for the swimming velocity $u(t)$ from both approaches are very close, yielding almost the same time-averaged swimming speed U and phase, though with larger oscillations when the model is used. Similar results are obtained for other (small) values of α_0 and Re_ω between about 10^3 and 10^4.

3.5.2 Comparison between analytical and numerical results

Once the validation with the full numerical simulations is properly done, we can compare the analytical asymptotic solution of the previous sections with the numerical solution of the model equations. As mentioned before, the perturbation solution ceases to be valid as the resonant curve $k_{hr}(k_\alpha)$ is approached since U_1 becomes too large (infinite if $b_h = 0$). This is shown in Figures 3.7 and 3.8 for $k_h = 2.5$ when k_α decreases from 3 to 1.5.

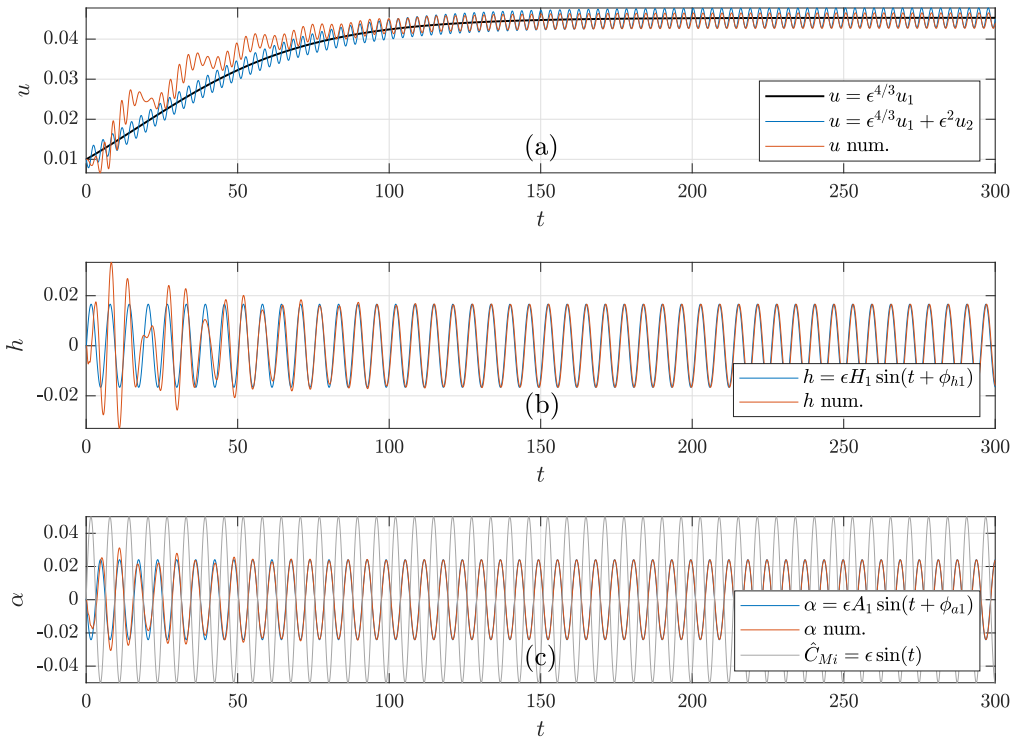

Figure 3.7: Comparison between $u(t)$ (a), $h(t)$ (b), and $\alpha(t)$ (c) computed numerically from the model equations and their analytical lowest-order solutions. The parameters are $\epsilon = 0.05$, $R' = 0.2$, $Li = 0.1$, $R = 0.02$, $a = -1$, $x_0 = 0$, $b_h = b_\alpha = 0.05$, $k_h = 2.5$ and $k_\alpha = 3$.

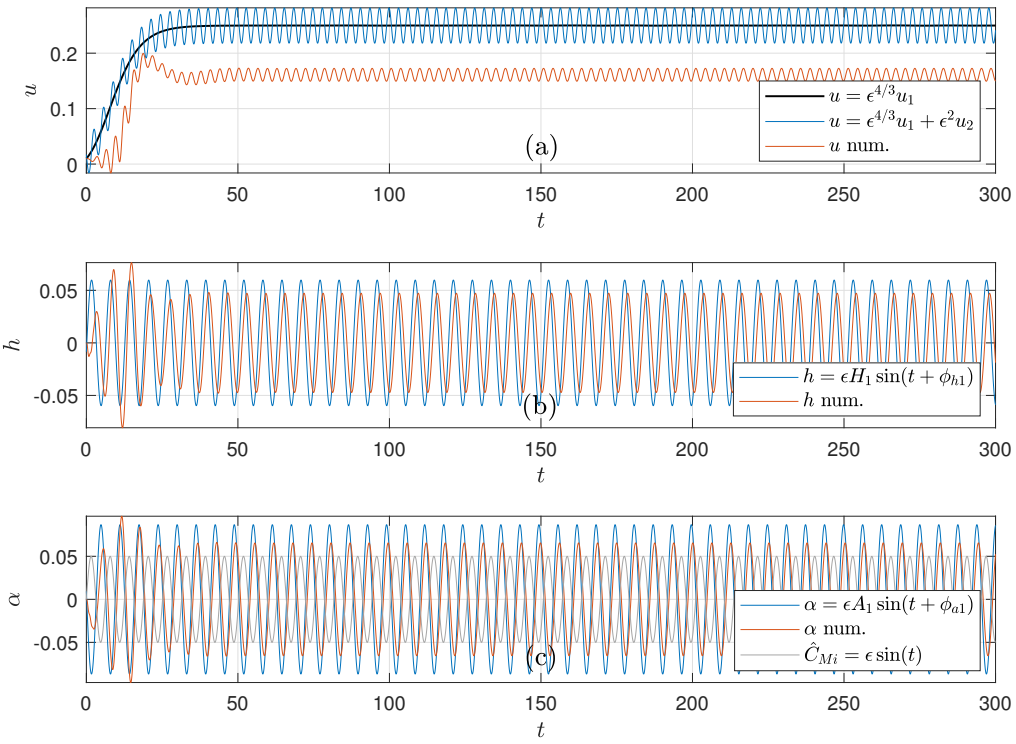

Figure 3.8: As in Figure 3.7, but for $k_\alpha = 1.5$.

By approaching the resonant curve from the right in the $k_\alpha - k_h$ plane, it is observed that the excellent agreement between the numerical and analytical solutions for $k_\alpha = 3$ in Figure 3.7, particularly for the large time oscillatory motion, disappears for $k = 1.5$ in Figure 3.8, especially for $u(t)$. This disagreement becomes more pronounced as k_α approaches $k_{hr}(k_\alpha)$ ($\simeq 0.92$ for $k_h = 2.5$), which is better appreciated in Figure 3.9. This figure shows the swimming velocity U and the Strouhal number St as k_α is varied for two values of k_h ($k_h = 2.5$ and $k_h = 100$), comparing the numerical solution of the model equations with the lowest-order analytical solution. With both approaches, U and St reach their extrema at the corresponding resonant value of k_α for each k_h. Close to this resonance, the perturbation solution ceases to be valid and departs from the numerical one, with peaks (or troughs) much more pronounced than those obtained numerically. Similarly happens for other values of k_h as k_α is varied.

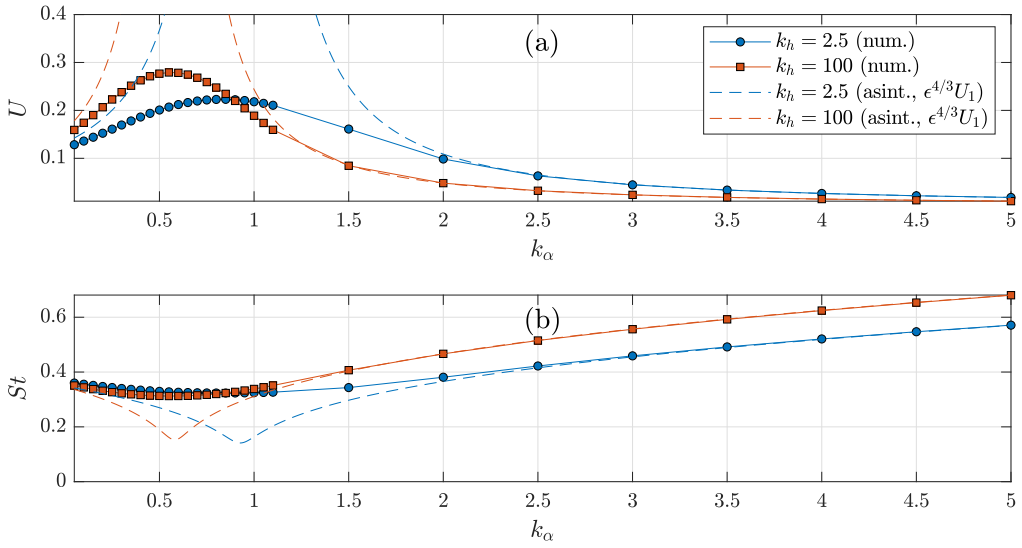

Figure 3.9: Comparison between the swimming velocity U (a) and the Strouhal number St (b) computed numerically from the model equations (continuous lines) and their analytical lowest-order perturbation solutions (dashed lines) as a function of k_α for two values of k_h, 2.5 and 100. The rest of the parameters are set to $\epsilon = 0.05$, $R' = 0.2$, $Li = 0.1$, $R = 0.02$, $a = -1$, $x_0 = 0$, and $b_h = b_\alpha = 0.05$.

3.5.3 Results from the numerical solution of the model equations

It is seen that the contour plots obtained from the asymptotic approach in the previous section are reliable except close to the resonant curve, where the extremum values of the different variables are much less pronounced. To analyze the real behavior of the different parameters around the resonant zones, we need to solve the model Equations (3.13), (3.28) and (3.29) numerically and study the resultant contours plots in the $k_\alpha - k_h$ plane. This is done in the left panels of Figures 3.10 to 3.13, where contour plots in the $k_\alpha - k_h$ plane of U, St, CoT and η, respectively, are plotted for the same small value of the torsional damper constant ($b_\alpha = 0.05$) used in Figures 3.3 to 3.5. On the other hand, as b_α is increased ($b_\alpha = 1$ in the right panels of Figures 3.10 to 3.13), the maxima of U and η decrease and displace towards smaller values of

k_h, but always near the corresponding resonant values of k_α, marked with thick lines in the figures. The minima of St and CoT evolve oppositely since they are increased when b_α grows.

Note that in these figures, the different magnitudes are not scaled with ϵ and Li as in the contour plots of the approximate analytical solutions in Figures 3.3 to 3.5. The torque intensity $\epsilon = 0.05$ and the same typical values of the remaining non-dimensional parameters used in the above comparison with the numerical solution of the full N-S equations have been selected.

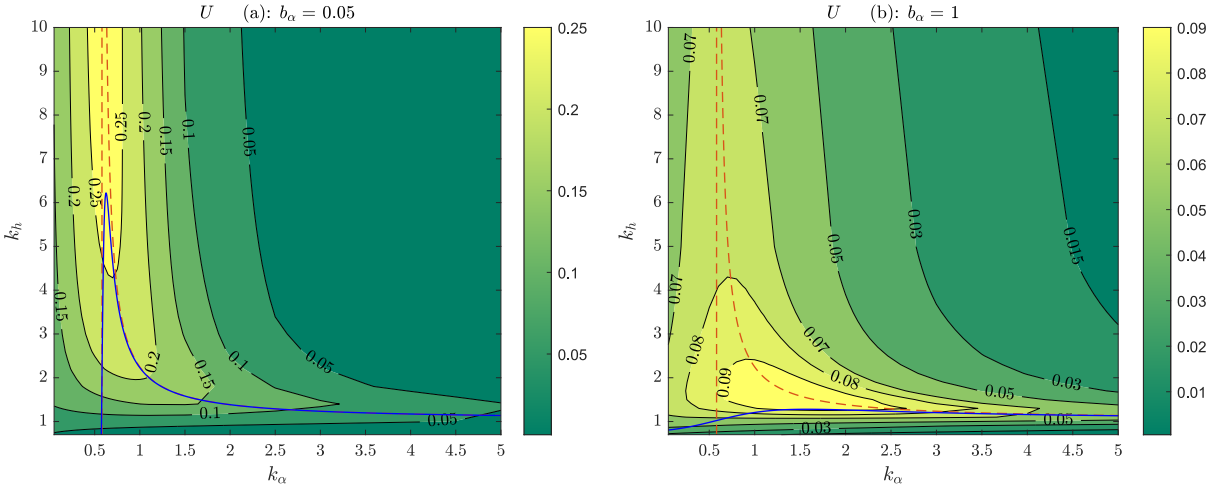

Figure 3.10: Contour plots in the $k_\alpha - k_h$ plane of U computed numerically from the model equations for $b_\alpha = 0.05$ (a) and $b_\alpha = 1$ (b), with $\epsilon = 0.05$, $R' = 0.2$, $Li = 0.1$, $R = 0.02$, $a = -1$, $x_0 = 0$, and $b_h = 0.05$. The thick blue line corresponds to the minimum of $|\det(\mathbf{A})|$, while the dashed red one to k_{hr0} given by Equation 3.70, being the vertical branch $k_{\alpha\infty}$ from Equation 3.71.

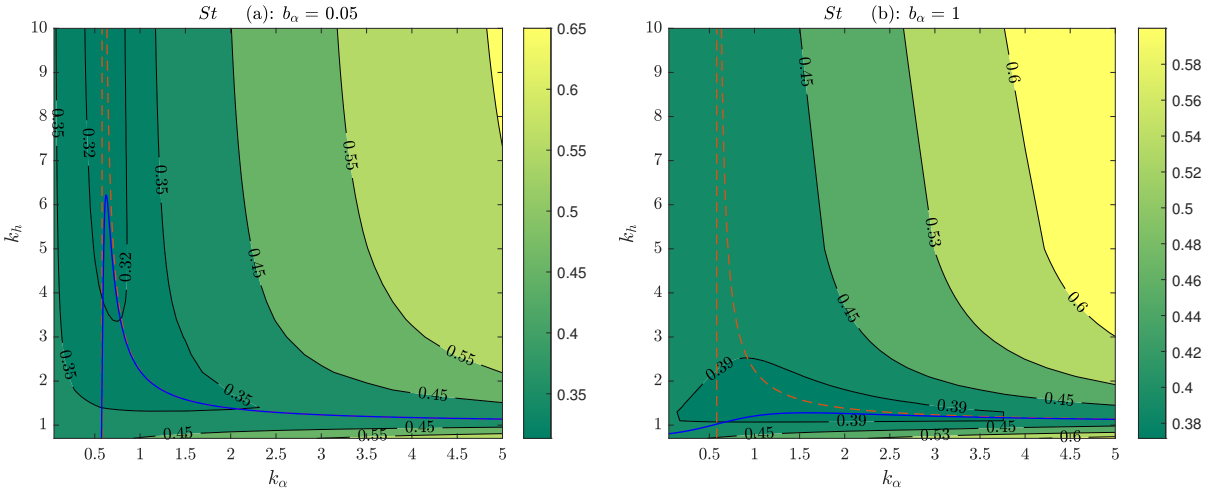

Figure 3.11: As in Figure 3.10 but for the contours of St.

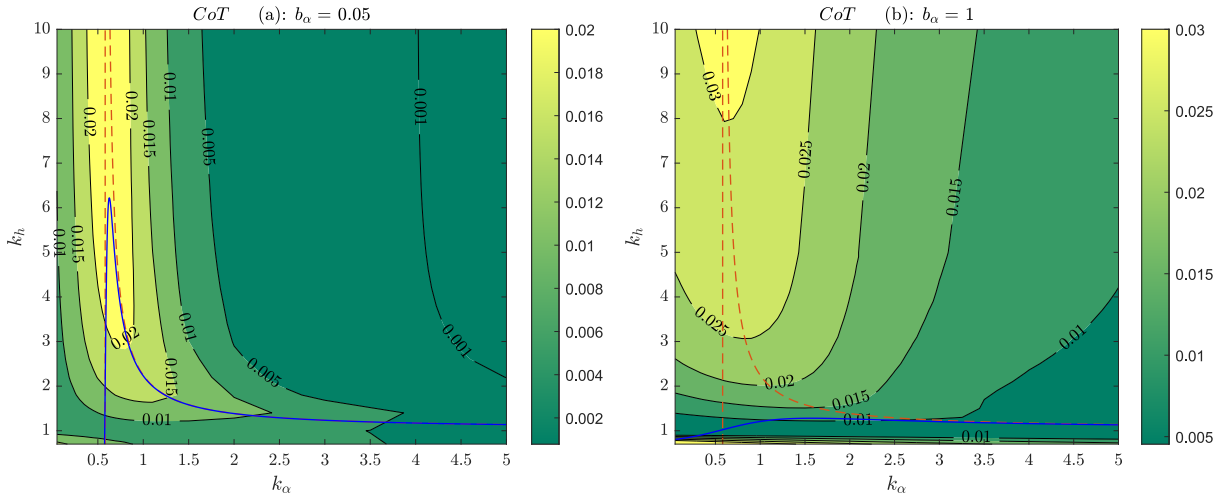

Figure 3.12: As in Figure 3.10 but for the contours of CoT.

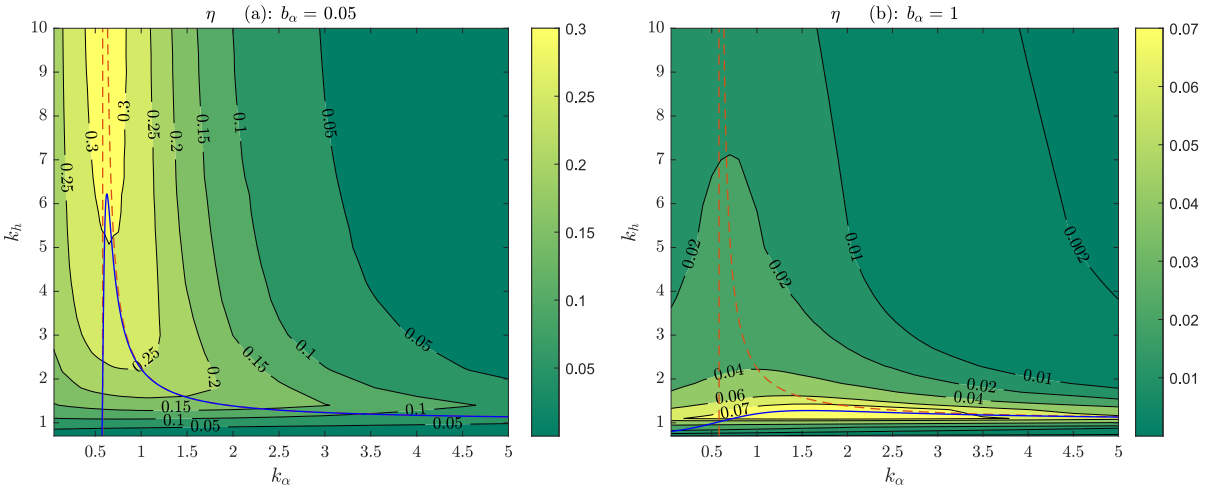

Figure 3.13: As in Figure 3.10 but for the contours of η.

It is noticeable that the maxima of U and η are located close to the values of k_h and k_α where the resonant curve $k_{hr}(k_\alpha)$ has a maximum, decreasing both U and η as the torsional damper constant b_α increases. Thus, the maximum efficiency for $b_\alpha = 0.05$ is 31.47% when $k_\alpha \simeq k_{\alpha\infty} \simeq 0.6$ and $k_h \gtrsim 6$, while, for $b_\alpha = 1$, the maximum η decreases to just above 7% when $k_\alpha \simeq k_h \simeq 1.5$. In the regions with the highest efficiency for each value of b_α, the Strouhal number remains practically constant, below 0.32 for $b_h = 0.05$ and about 0.39 for $b_h = 1$. The first value for the largest efficiency is within the range of Strouhal numbers where many swimming and flying animals in many scales cruise propelled by flapping fins and wings (Triantafyllou et al. [1993]). On the other hand, the maxima of CoT practically coincide with the maxima of U and η for $b_\alpha = 0.05$, while for $b_h = 1$ the highest values of U and η, which are significantly smaller than for $b_\alpha = 0.05$, are achieved with much lower CoT.

The above-presented contour plots are for a small value of the translational damper constant, $b_h = 0.05$, but the behavior as b_h increases remains qualitatively the same, only with U and η decreasing slightly, the more so the larger b_α. To better appreciate this, Figure 3.14 shows the different magnitudes U, St, CoT and η as functions of b_α for two values of b_h when k_h and k_α are selected to maximize η. The corresponding values of k_h and k_α are also shown. The parameters are set to $\epsilon = 0.05$, $R' = 0.2$, $Li = 0.1$, $R = 0.02$, $a = -1$, and $x_0 = 0$, as in the previous reported results. The figure shows that the maximum value of the efficiency is about 31.47% as $b_\alpha \to 0$, being almost independent of b_h in this limit. This optimal efficiency is found for the resonant values of the non-dimensional spring constants, particularly in the range of large k_h (limited to 10 in the optimization process) where $k_\alpha = k_{\alpha\infty}$ given by Equation (3.71) ($\simeq 0.6$ in the present case). For these conditions, the non-dimensional swimming velocity also reaches its maximum, close to 0.3, and the Strouhal number has a minimum of about 0.31. However, CoT is about four times larger than its minimal value, which is found to be around 0.007, also for $b_h \to 0$, but now with b_α of order unity or larger, for which the resonant values of k_α (where η reaches its maximum) are larger than $k_{\alpha\infty}$, and k_{hr} is slightly larger than $1 + R$ [see Equation (3.70) and, for instance, Figure 3.13(b)]. For these conditions, the passive heave amplitude is much larger than the pitch amplitude, and both U and η are the smallest. The corresponding Strouhal number is larger, about 0.4.

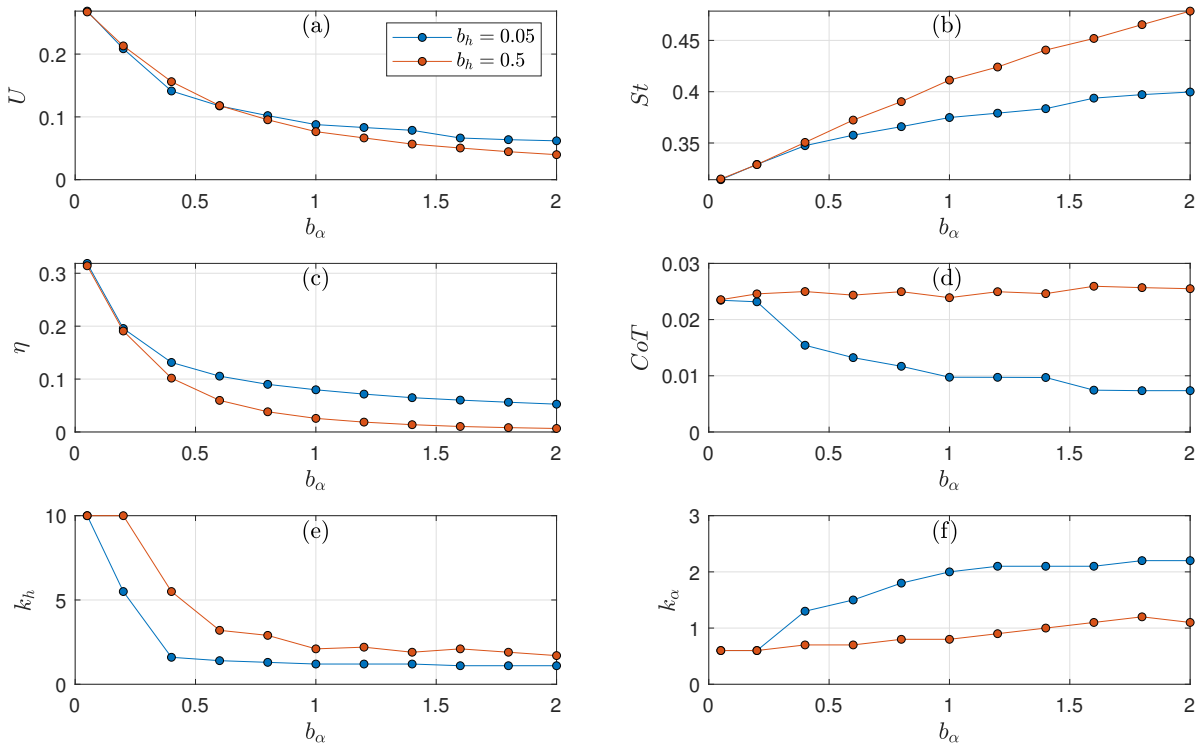

Figure 3.14: Evolutions of U (a), St (b), η (c), and CoT (d) in function of b_α for two selected values of b_h (0.05 and 0.5) at the optimal conditions of k_h (e) and k_α (f) where η reaches a maximum value when $0.05 \leq k_h \leq 10$ and $0.05 \leq k_\alpha \leq 5$. The rest of the parameters are set to $\epsilon = 0.05$, $R' = 0.2$, $Li = 0.1$, $R = 0.02$, $a = -1$, and $x_0 = 0$.

3.6 Concluding remarks

In this chapter, we have developed a simple model of an aquatic vehicle self-propelled by a rigid hydrofoil elastically mounted to translational and torsional springs and dampers that allow for passive heave when the pitching motion is generated by a given sinusoidal torque. The results of the model are obtained by just integrating a set of three ODEs, which are validated with full numerical simulations of the Navier-Stokes equations for sufficiently small pitching amplitudes and frequency Reynolds numbers between about 10^3 and 10^4. In addition, an analytical solution is also obtained, yielding relevant information about the propulsive performance through simple algebraic expressions in terms of the non-dimensional torque amplitude ϵ, the Lighthill number Li, and the remaining dimensionless parameters. Thus, it is found that

$$\begin{gathered} U \propto \epsilon^{4/3} Li^{-2/3} \rightarrow \widetilde{U} \propto (M_i/\rho)^{4/3}\, \omega^{-5/3} c^{-13/3} Li^{-2/3}, \\ \eta \propto \epsilon^2 Li^{-1} \rightarrow \eta \propto (M_i/\rho)^2\, \omega^{-4} c^{-8} Li^{-1}, \\ CoT \propto (\epsilon Li)^{2/3} \rightarrow \widetilde{CoT} \propto (M_i \omega Li)^{2/3} (\rho c)^{1/3}. \end{gathered} \tag{3.92}$$

Further, the maxima of the swimming velocity and efficiency are found for the resonant values of the non-dimensional spring constants k_h and k_α, whose expression k_{hr} as a function of k_α and the remaining non-dimensional parameters is provided with a simple algebraic equation. Particularly, for typical values of the remaining dimensionless parameters and dimensionless torque intensity $\epsilon = 0.05$, the highest efficiency found is near 32%, with the highest non-dimensional swimming velocity U close to 0.3, achieved in the absence of dampers ($b_h \simeq b_\alpha \simeq 0$) and negligible heaving motion ($k_h \gg 1$), so it corresponds to an almost purely pitching motion, and for the corresponding resonant value of the torsional spring constant, $k_\alpha = k_{\alpha\infty} = [R(a^2 + 1/3) + a^2 + 1/8]/2$, where R is the mass ratio of the foil and a the pivot axis where the torque is applied to the foil. Larger values of ϵ would yield higher values of both η and U as they grow as ϵ^2 and $\epsilon^{4/3}$, respectively, but it has to remain small for the present linear approximation be valid. This configuration with maxima of η and U does not correspond, however, to the minima of CoT, which are also achieved at the resonant values of k_h with negligible translational damper ($b_h \simeq 0$), but now for torsional damper and spring constants larger than unity, corresponding to an almost purely heaving motion, with the resonant value of the translational spring constant k_{hr} slightly larger than $1 + R$. In this limit, U and η are close to their minima.

The values of the parameters used in the reported results (other than spring and dampers constants, which are varied in a wide range) are for a typical underwater vehicle (or animal) of a size of the order of the meter with a hydrofoil of chord length about ten times smaller. To better illustrate that, we show a practical example here, taking $c = 0.3$ m, $s = 1$ m, $\rho_s = 2\rho$, and $R = 0.02$ in water, which corresponds to a foil thickness $\gamma \simeq 2.4$ mm, assumed constant so that $x_0 = 0$. The pivot axis is selected at the leading edge ($a = -1$) since it is known to maximize the propulsive performance of a pitching and heaving foil (Tuncer and Kaya [2005]). With these values, the selected $R' = 0.2$ corresponds to a small vehicle's mass of about 14 kg, and $Li = 0.1$ to a vehicle's surface $A_w \simeq 0.094/C_D$ m^2. The value $\epsilon = 0.05$ has been selected small for the model to be valid, but this does not limit the input torque M_i since it is proportional to the square of the flapping frequency according to Equation (3.4).

Thus, with the above foil dimensions in water, the results of Table 3.1 can be obtained for two different frequencies selecting the values for the optimal propulsive efficiency analyzed in this chapter, which are $k_\alpha \simeq k_{\alpha\infty} \simeq 0.6$, $k_h = 10$, and $b_h \simeq b_\alpha \simeq 0$.

$\tilde{f}$ [Hz]	A_M [Nm]	$\tilde{k}_\alpha$ [Nm]	$\tilde{k}_h$ [KN/m]	$\tilde{b}_\alpha$ [Nms]	$\tilde{b}_h$ [Ns/m]	η [%]	$\widetilde{U}$ [m/s]	$\widetilde{CoT}$ [KJ/km]
1	6.26	75	28	$\simeq 0$	$\simeq 0$	31.47	0.25	10
2	25	300	112	$\simeq 0$	$\simeq 0$	31.47	0.51	40

Table 3.1: Practical example for the designing parameters of an efficient self-propelled aquatic vehicle. Using $c = 0.3$ m, $s = 1$ m, $\rho_s = 2\rho$, $R = 0.02$, $x_0 = 0$, $a = -1$, $R' = 0.2$ ($m' \simeq 14$ kg), $Li = 0.1$, and $\epsilon = 0.05$.

Remember that the dimensional velocity increases linearly with $\tilde{f}$ but at the cost of rapidly increasing the spring constants and the input torque, which are quadratic with $\tilde{f}$. Also, notice that the cost of transport may be reduced by a factor of about 4 by selecting $k_h \simeq 1 + R \simeq 1$ and $k_\alpha \simeq 2$, but reducing the swimming velocity and the efficiency more than four times. Also, the corresponding Strouhal number, about 0.4, is larger than that for maximum efficiency, which is about 0.3.

The above results are in qualitative agreement with recent numerical results, both inviscid and viscous, by Paniccia et al. [2021] for a fishlike body propelled by an oscillating tail. These authors also find that peak efficiencies are reached for smaller values of the Strouhal number than those where the cost of transport is the lowest, being $\widetilde{CoT}$ higher when η is large, and the efficiency poor when the cost of transport is optimally low. The largest efficiencies found by these authors are higher than the present ones because the amplitudes of the tail oscillations in their simulations are not small, as is assumed in the present theory. However, their reported optimal values of $\widetilde{CoT}$ are pretty similar to those found here. On the other hand, since the model uses potential-flow theory, it cannot be applied to situations where the aquatic vehicle is propelled by large amplitude oscillations of the flapping foil, where flow separation, and particularly the leading edge vortex, plays an important role. In nature, these situations are usual in fishes for maneuvering and when very high thrust is needed, regardless of its efficiency. Nevertheless, for high cruising efficiency, the effective angle of attack of the foil has to be reduced, with weak, or even absence of, vortex formation at the leading edge (Anderson et al. [1998], Tuncer and Kaya [2005]). For these flapping conditions with weak or no flow separation, for which the present theoretical model is intended, the lift and thrust forces given by the potential-flow theory agree quite well with experimental data of pitching and heaving foils, surprisingly even for not-so-small amplitude of the oscillations (Halfman [1952], Baik et al. [2012], Fernandez-Feria [2017], Alaminos-Quesada [2021]). The present results, especially the numerical results of the model equations, which are not as limited in amplitude as the analytical asymptotic results, would be applicable for modeling the efficient cruising of actual aquatic vehicles propelled by a biomimetic flapping foil. It is supported by the fact that St numbers found for optimal efficiency conditions at resonance are always within the range where many swimming and flying animals, of many scales, cruise propelled by flapping fins and wings (Triantafyllou et al. [1993], Taylor et al. [2003]).

Chapter 4

The effect of flexibility on the self-propelled locomotion by a foil

4.1 Introduction

In Chapter 3, we studied the use of a rigid flapping foil for the locomotion of an aquatic vehicle, especially focusing the work on finding the optimal configuration of translational and torsional springs and dampers that elastically supports the foil. It was found that the optimal propulsive configuration corresponds to the resonance of the system. Simple power laws were also proposed as a part of the analysis. Continuing with this line, in the present chapter, we are interested in exploring the effect that foil's flexibility roles on this self-propelled aquatic vehicle when this foil is elastically supported and anchored to the vehicle hull, as in the previous chapter.

In recent years, researchers have been very interested in studying the flapping foil systems to propel bioinspired aquatic vehicles because of the numerous advantages they show in contrast to traditional rotatory propellers. In particular, the effect of chordwise flexibility of the foil has been shown to enhance the propulsion performance in terms of thrust, efficiency, and cruising velocity (Prempraneerach et al. [2003], Triantafyllou et al. [2004], Beal et al. [2006], Lauder et al. [2007], Heathcote and Gursul [2007], Kang et al. [2011], Marais et al. [2012], Cleaver et al. [2014], Monnier et al. [2015], David et al. [2017], Sanmiguel-Rojas and Fernandez-Feria [2021]), and also the efficiency of flapping-foil energy harvesting devices (Liu et al. [2013], Le and Ko [2015], Wu et al. [2015], Liu et al. [2016], Jeanmonod and Olivier [2017], Zhu et al. [2019a], Fernandez-Feria and Alaminos-Quesada [2021b, 2022]).

On the other hand, it is beneficial to dispose of analytical solutions characterizing the fluid-structure interaction of flexible flapping foils for the design and improvement of bioinspired swimming robotic models. These analytical approximations have to be searched within the framework of the two-dimensional and linearized inviscid flow theory for small deformations of the foil, pioneered by Wu [1961], who considered a flapping plate that incorporated flexibility, allowing it to deform according to the fluid and elastic forces it experiences. Therefore, passive flexibility changes the thrust that a flapping plate generates and, consequently, its

propulsive efficiency and its cruising speed if self-propelled. It has generally been found from these inviscid flow theories that flexibility produces greater thrust when actuated near a fluid-structure natural frequency but less otherwise, with larger propulsive efficiency than that of a rigid foil over a broad range of stiffnesses and frequencies (Katz and Weihs [1978], Alben [2008], Michelin and Smith [2009], Alben et al. [2012], Floryan and Rowley [2018, 2020], Fernandez-Feria and Alaminos-Quesada [2021a]). However, when viscous flow with non-linearities associated with flow separation is considered, optimal performance can be achieved off the structural resonance conditions (Dewey et al. [2013], Goza et al. [2020], D'Adamo et al. [2022]). In any case, structural resonance always plays a relevant role in enhancing the propulsion performance if the mass ratio of the foil is not too large (Zhang et al. [2017]), as is the case in fish-like swimming.

Taking that into account, in this chapter, we consider the locomotion of an aquatic vehicle propelled by an elastically mounted foil actuated by an oscillatory torque and analyze the effect of chordwise flexibility on the propulsion performance. Due to the driving torque applied to a given pivot axis, at which the foil is attached to longitudinal and torsional springs and dampers, the foil undergoes passive pitching, heaving, and flexural deflection motions. We use a model for the fluid-foil interaction based on the Euler-Bernoulli beam equation coupled to the results from linear potential-flow theory (Fernandez-Feria and Alaminos-Quesada [2021a]), valid for small pitching, heaving, and flexural deflection amplitudes, together with a constant drag coefficient for the vehicle of a given mass. In Chapter 3 we have considered this model for the case of the vehicle propelled by a rigid foil elastically supported, finding that the optimal propulsive performance, i.e., maximum cruising velocity and maximum propulsive efficiency, is reached for particular resonant combinations of the torsional and longitudinal springs constants for an oscillatory torque with a given frequency actuating at, or close to, the foil's leading edge. It was shown that the propulsion enhancement due to this resonant behavior, which was approximately characterized by simple analytical expressions, is quite significative, diminishing more than twice both the swimming velocity and the propulsive efficiency by just moving the torsional spring constant a few percent from its resonant value. The model for the rigid-foil flapper was validated with high Reynolds numerical simulations of a self-propelled pitching foil, and by the fact that the Strouhal number for optimal propulsion was in agreement with that found experimentally in nature for optimal cruise propelled by flapping fins or wings.

When chordwise flexibility of the foil is taken into account, the model is substantially more complicated because so it is the fluid-structure interaction of the propeller. However, using the analytical results of Alaminos-Quesada and Fernandez-Feria [2020] and Fernandez-Feria and Alaminos-Quesada [2021a] for this interaction, assuming a quartic polynomial for the flexural deflection of the foil, the resulting model is governed by four ordinary differential equations, just one more equation than for the rigid-foil counterpart. In addition to the results from the numerical integration of these equations, which is straightforward and almost instantaneous compared with numerical computations of the full viscous problem, we also derive simple analytical expression in the limit of very small non-dimensional swimming velocity, which, contrary to the flapping amplitudes, is not limited in the numerical solutions of the model equations. The resulting approximate analytical expressions provide simple scaling

laws for the non-dimensional performance parameters, such as cruising velocity, propulsive efficiency, cost of transport, and Strouhal number, in terms of the non-dimensional driving torque amplitude, vehicle's drag, characterized by the Lighthill number, and mass ratio, among others.

The literature on the propulsive performance of flexible flapping foils is vast. Most of the works are for oscillating foils in a fluid stream with fixed velocity rather than for self-propelled flexible foils, a few of them for a vehicle or body propelled by a flexible flapping foil, and none of them, to the best of our knowledge, for the present configuration of a flexible foil elastically mounted on the vehicle hull through translational and torsional springs and dampers that allows for passive heaving, pitching, and flexural deflection motions. As aforementioned, numerous theoretical, computational, and experimental studies on flexible flapping foils with prescribed pitching and/or heaving motions and passive flexural deflection immersed in a constant velocity stream show that structural resonance may play a relevant role in their propulsive performance, generally enhancing the thrust generation and/or the propulsive efficiency when actuated at, or near, structural resonance frequencies, depending on the prescribed kinematics, the flow regime, and the relative inertia of the foil (Katz and Weihs [1978], Alben [2008], Michelin and Smith [2009], Quinn et al. [2014], Yeh and Alexeev [2014], Zhang et al. [2017], Floryan and Rowley [2018, 2020], Fernandez-Feria and Alaminos-Quesada [2021a], Sanmiguel-Rojas and Fernandez-Feria [2021]). Another kind of structural resonance that may enhance the propulsive performance of rigid foils oscillating in a fluid stream with fixed velocity appears when the foil, actuated with forced pitching or heaving motion, is elastically mounted to translational or torsional springs and dampers, so that the heaving or the pitching motion is also passive (Murray and Howle [2003], Moore [2014], Mackowski and Williamson [2017], Asselin and Williamson [2019]). The new structural resonances, associated to the supporting springs and dampers and with natural frequencies quite different from those associated to the flexural deflection in the case of flexible foils, may enhance the propulsive performance even more than the resonantlike response without springs and dampers (Moore [2014, 2015], Fernandez-Feria and Alaminos-Quesada [2021a, 2022]). In any case, these flexible foils elastically mounted may be actuated in a greater variety of coupled natural frequencies to improve their propulsive performance.

When the flexible oscillating foil is not immersed in a constant velocity fluid stream but moves freely self-propelled by itself, or propelling an animal or a vehicle, the problem is quite different because the velocity of the foil relative to the flow, i.e., the free-swimming velocity, is no longer an independent control parameter, nor is it constant, but it is time dependent and resulting from the fluid-structure interaction, and therefore a function of the kinematics and structural properties of the foil. Alben et al. [2012] found resonance peaks in the inviscid free-swimming velocity of an elastic oscillating plate, similar to those found for a flexible foil immersed in a fluid stream with fixed velocity (Alben [2008]). However, only some general results for a foil in a fixed-velocity stream can be roughly extrapolated, in certain circumstances, to the time-averaged performance of these freely moving foils when using the time-averaged swimming velocity (Alben et al. [2012], Olivier and Dumas [2016], Van Buren et al. [2018]). For consistent and accurate results one has to solve the complex fluid-structure interaction problem of the freely moving body. Olivier and Dumas [2016]

considered numerically the self-propelled locomotion at low flapping Reynolds numbers of a flexible plate with imposed pitching and heaving motion about its leading edge and with a drag model, finding that increasing the flexibility decreases the time-averaged swimming velocity. This result is in contradiction with similar low Reynolds number numerical results but with only heaving motion imposed at the leading edge of the foil, where moderate flexibility usually implies a significant increase of the averaged swimming velocity near the first resonant frequency (Yeh and Alexeev [2014], Yeh et al. [2017]) or at much lower frequencies (Hua et al. [2013], Zhu et al. [2014]). In particular, Yeh and Alexeev [2014] found that elastic propulsors can be operated at a regime of maximum propulsion near the first resonant frequency, or maximum efficiency when operated away from the resonance. Hoover et al. [2018] further confirmed these results with three-dimensional simulations, giving additional insight about the role of resonance in swimming performance. More efficient aquatic locomotion (higher cruising speed and efficiency) has been found for an elastic plate actuated at resonance by combined external and internal actuation, with heaving motion at the leading edge and distributed internal bending moment (Demirer et al. [2021]), or using an optimal stiffness distribution of the heaving flexible plate (Wang et al. [2020]). However, neither of these works considered the mass nor the form of the aquatic vehicle propelled by the flexible foil, and therefore the vehicle's inertia and drag as independent parameters that affect to its locomotion. We show in the present chapter that the relevant structural resonances optimizing the locomotion through elastically mounted flexible foils with high enough stiffness are associated to the stiffness of the supporting springs, which are quite different from the aforementioned flexural resonances. Also, that these spring resonances eclipse the structural resonances associated to the chordwise deflection of the foil, qualitatively in agreement with previous theoretical works for oscillating foils in a fluid stream with fixed velocity (Moore [2015], Fernandez-Feria and Alaminos-Quesada [2021a, 2022]). Unfortunately, to the best of our knowledge, no numerical nor experimental results on the locomotion through elastically mounted flexible foils are available to compare with.

To sum up, this work may be considered as a valuable guide, offering insights and recommendations for the optimal design of novel aquatic vehicles, which are self-propelled by a flapping foil elastically mounted to the vehicle's hull. The emphasis lies in integrating the foil's flexibility to enhance the performance of the propeller, thereby contributing to advancements in the field.

4.2 Formulation of the problem

We consider an aquatic vehicle self-propelled by a flexible hydrofoil, similar to the one shown in Figure 4.1(a), of chord length c and large aspect ratio s/c, where s is the foil span, so that the flow around it may be considered two-dimensional in the plane $(\tilde{x}, \tilde{z})$ shown in Figure 4.1(b). The foil is elastically mounted to translational and torsional springs and dampers at a given pivot axis $\tilde{a}$ and actuated at the same pivot with a known torque M_i, per unit span, to generate the pitching motion that, together with the induced passive heaving and flexural deflection motions of the foil, propels the vehicle. In particular, a harmonic torque with frequency ω,

$$M_i = A_M \sin(\omega \tilde{t}), \tag{4.1}$$

will be assumed, with the amplitude A_M sufficiently small for the amplitudes of all the foil's motions to be small compared to c.

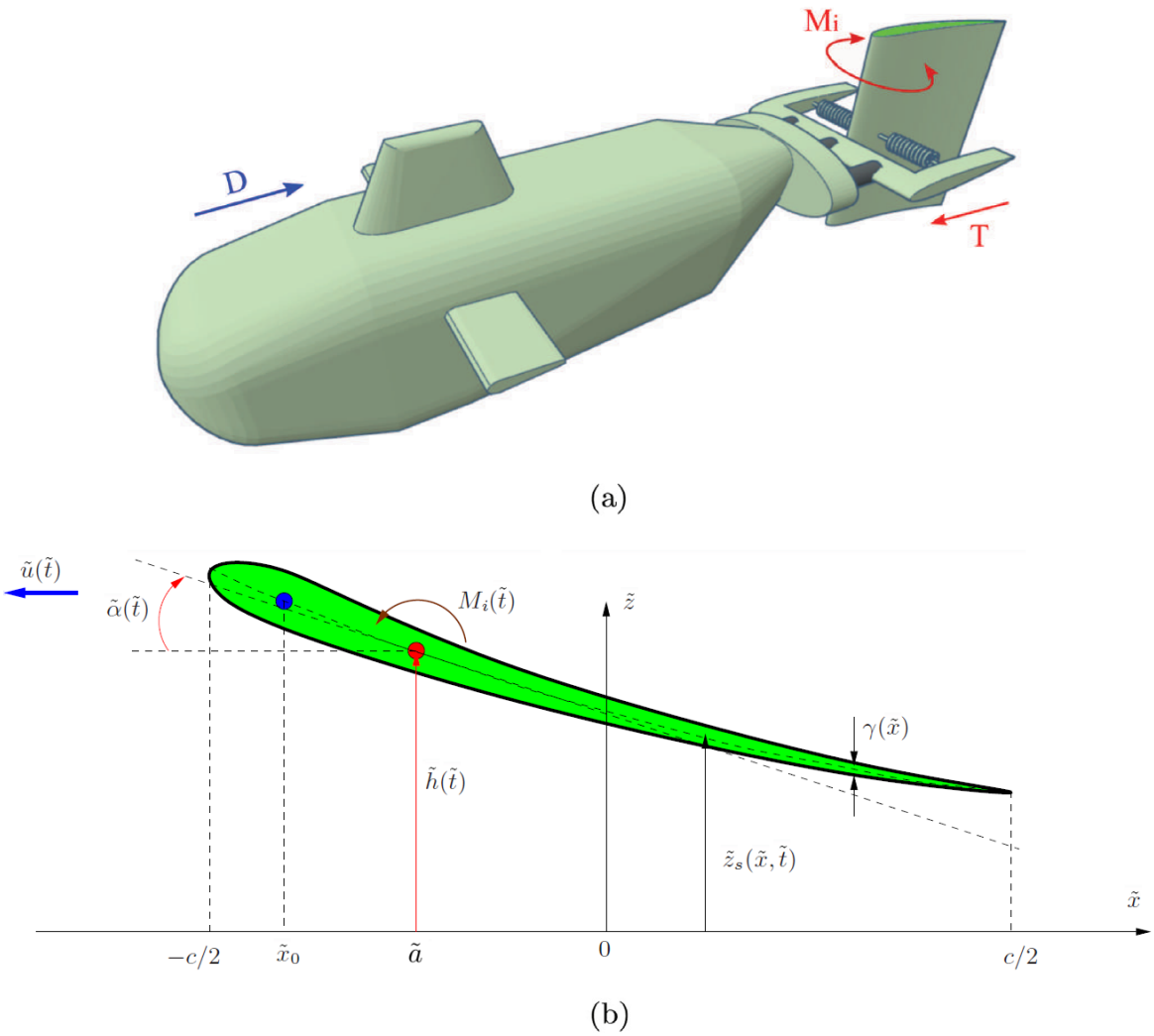

Figure 4.1: A 3D model of the underwater vehicle (a) and a detailed sketch of the elastically supported flexible foil that propels it (b). Both of them are in dimensional quantities.

Thus, one may use Euler-Bernoulli's beam equation to describe the motion of the foil centerline $\tilde{z}_s(\tilde{x},\tilde{t})$ as is conducted in Fernandez-Feria and Alaminos-Quesada [2021a].

$$\rho_s\gamma\frac{\partial^2\tilde{z}_s}{\partial\tilde{t}^2}+\frac{\partial^2}{\partial\tilde{x}^2}\left(\frac{E\gamma^3}{12}\frac{\partial^2\tilde{z}_s}{\partial\tilde{x}^2}\right)+L_o\delta(\tilde{x}-\tilde{a})-M_o\delta'(\tilde{x}-\tilde{a})=\Delta p-M_i\delta'(\tilde{x}-\tilde{a}), \tag{4.2}$$

for $-c/2\leq\tilde{x}\leq c/2$. In this equation, ρ_s, γ, and E are the density, thickness, and elastic modulus of the foil, respectively. In addition, $\delta(\tilde{x}-\tilde{a})$ is Dirac's delta function centered at $\tilde{x}=\tilde{a}$ and δ' its derivative. Those functions are quite convenient for modeling localized force and torque at the pivot point location since they satisfy the properties

$$\int_{-\infty}^{\infty}\delta(\tilde{x}-\tilde{a})F(\tilde{x})d\tilde{x}=F(\tilde{a}),\quad \int_{-\infty}^{\infty}\delta'(\tilde{x}-\tilde{a})F(\tilde{x})d\tilde{x}=-F'(\tilde{a}). \tag{4.3}$$

On the other hand,

$$L_o=\tilde{k}_h\tilde{h}+\tilde{b}_h\frac{d\tilde{h}}{d\tilde{t}},\quad M_o=-\tilde{k}_\alpha\tilde{\alpha}-\tilde{b}_\alpha\frac{d\tilde{\alpha}}{d\tilde{t}}, \tag{4.4}$$

are the force and moment per unit span exerted by the foil on the translational and torsional springs and dampers at the pivot axis, where $\tilde{h}(\tilde{t})$ and $\tilde{\alpha}(\tilde{t})$ characterize its heaving and pitching motions, respectively, and $\tilde{k}_h$, $\tilde{k}_\alpha$, $\tilde{b}_h$, and $\tilde{b}_\alpha$ are the respective constants of the springs and dampers. Note that $\tilde{\alpha}$ is taken positive clockwise following the usual convention in aerodynamics, while the moments M_o and M_i are positive counterclockwise. Also, remember that we use a *tilde* to remark that the variable is in the dimensional form to distinguish it from its dimensionless counterpart. Finally, $\Delta p=p^--p^+$ is the pressure difference between the lower and upper sides of the foil, which is the only force (per unit area) that the fluid exerts on the foil considered in the present inviscid model, valid for sufficiently high Reynolds numbers. Actually, we shall use the results from linear potential-flow theory for the pressure and, therefore, for the resulting fluid force and moment, because of the aforementioned additional assumption of small-amplitude foil motion (see below for more details). Thus, following Fernandez-Feria and Alaminos-Quesada [2021a], a quartic approximation is used for $\tilde{z}_s$,

$$\tilde{z}_s\left(\tilde{x},\tilde{t}\right)=\tilde{h}(\tilde{t})-(\tilde{x}-\tilde{a})\,\tilde{\alpha}(\tilde{t})+(\tilde{x}-\tilde{a})^2\,\tilde{d}(\tilde{t})-(\tilde{x}-\tilde{a})^3\,\frac{2\tilde{d}(\tilde{t})}{3\,(c/2-\tilde{a})}+(\tilde{x}-\tilde{a})^4\,\frac{\tilde{d}(\tilde{t})}{6\,(c/2-\tilde{a})^2}, \tag{4.5}$$

which accounts for the (passive) heaving and pitching motions, $\tilde{h}(\tilde{t})$ and $\tilde{\alpha}(\tilde{t})$, respectively, at $\tilde{x}=\tilde{a}$, and for a free trailing edge, $\partial^2\tilde{z}_s/\partial\tilde{x}^2=\partial^3\tilde{z}_s/\partial\tilde{x}^3=0$ at $\tilde{x}=c/2$.

Assuming that $E\gamma^3$ does not depend on $\tilde{x}$ and substituting Equation (4.5) into Equation (4.2), one can get

$$\begin{aligned}\rho_s\gamma\left[\frac{\partial^2\tilde{h}}{\partial\tilde{t}^2}-(\tilde{x}-\tilde{a})\frac{\partial^2\tilde{\alpha}}{\partial\tilde{t}^2}+\frac{\partial^2\tilde{d}}{\partial\tilde{t}^2}\left((\tilde{x}-\tilde{a})^2-\frac{2}{3}\frac{(\tilde{x}-\tilde{a})^3}{(c/2-\tilde{a})}+\frac{(\tilde{x}-\tilde{a})^4}{6(c/2-\tilde{a})}\right)\right]\\ +\frac{E\gamma^3\tilde{d}(\tilde{t})}{3(c/2-\tilde{a})^2}+L_o\delta(\tilde{x}-\tilde{a})-M_o\delta'(\tilde{x}-\tilde{a})=\Delta p-M_i\delta'(\tilde{x}-\tilde{a}).\end{aligned} \tag{4.6}$$

Then, integrating this expression, the equations of lift, moment, and flexural deflection can be obtained. The first one is obtained by performing the integration along the foil's chord length, the second one when multiplying Equation (4.6) by $(\tilde{x}-\tilde{a})$ and integrating, and the last one multiplying Equation (4.6) by $(\tilde{x}-\tilde{a})^2$ and again integrating along the chord length. Resulting in the following expressions (Fernandez-Feria and Alaminos-Quesada [2021a]):

$$m\dot{\tilde{v}} + m(\tilde{a}-\tilde{x}_0)\ddot{\tilde{\alpha}} + \tilde{J}_a\ddot{\tilde{d}} = L - L_o, \tag{4.7}$$

$$m(\tilde{x}_0-\tilde{a})\dot{\tilde{v}} - \tilde{I}_a\ddot{\tilde{\alpha}} + \tilde{J}_d\ddot{\tilde{d}} = M + M_i - M_o, \tag{4.8}$$

$$\tilde{I}_a\dot{\tilde{v}} - \tilde{I}_d\ddot{\tilde{\alpha}} + \tilde{K}_d\ddot{\tilde{d}} + \left(\tilde{a}^2c + \frac{c^3}{12}\right)\frac{E\gamma^3\tilde{d}}{3(c/2-\tilde{a})^2} = F, \tag{4.9}$$

where $\tilde{v} = d\tilde{h}/d\tilde{t}$ is the velocity in the $\tilde{z}$-direction, m is the mass of the foil per unit span, $\tilde{x}_0$ the foil's center of mass, and $\tilde{I}_a$ the moment of inertia. These parameters and the rest of the constants presented in these equations are defined and explained in Appendix A. Also, a *dot* denotes a derivative with respect to the dimensional time. On the other hand, the terms corresponding to the pressure force that the fluid exerts on the foil are

$$L = \int_{-c/2}^{c/2}\Delta p d\tilde{x}, \quad M = \int_{-c/2}^{c/2}(\tilde{x}-\tilde{a})\Delta p d\tilde{x}, \quad F = \int_{-c/2}^{c/2}(\tilde{x}-\tilde{a})^2\Delta p d\tilde{x}, \tag{4.10}$$

where L is the lift force, M is the moment around the pivot axis, and F is a new term associated with the defection of the foil.

The other fundamental equation of the model is Newton's equation in the $\tilde{x}$-direction applied to the vehicle center of mass,

$$m'\frac{d\tilde{u}}{d\tilde{t}} = sT - D, \tag{4.11}$$

where m' is the vehicle's mass, $\tilde{u}$ the velocity component of its center of mass in the $-\tilde{x}$ direction, D the drag force exerted by the fluid on the whole vehicle, which will be modeled below through a constant drag coefficient, and T the thrust force (per unit span s) generated by the oscillating foil through its interaction with the fluid. This force will also be modeled below using the results from linear, two-dimensional potential-flow theory.

4.2.1 Non-dimensional formulation

Once the formulation of the problem has been presented, it is more convenient and general to work on non-dimensional variables, as was done in the previous chapters. So, in what follows, all magnitudes are made dimensionless with the semi-chord length $c/2$, the fluid density ρ, and the frequency ω of the input torque, which in dimensionless form is given by

$$\hat{C}_{M_i} = \frac{8M_i}{\pi\rho c^4\omega^2} = \epsilon\sin t, \quad \epsilon = \frac{8A_M}{\pi\rho c^4\omega^2}, \tag{4.12}$$

where ϵ is the (known) non-dimensional torque intensity, which is assumed sufficiently small to generate the small amplitude foil motion required by the present model. The main non-dimensional variables of the problem will then be

$$\begin{gathered} x=\frac{\tilde{x}}{c/2}, \quad z=\frac{\tilde{z}}{c/2}, \quad t=\tilde{t}\omega, \quad u=\frac{\tilde{u}}{\omega c/2}, \quad \dot{u}=\frac{\dot{\tilde{u}}}{\omega^2 c/2}, \\ h=\frac{\tilde{h}}{c/2}, \quad \dot{h}=\frac{\dot{\tilde{h}}}{\omega c/2}, \quad \ddot{h}=\frac{\ddot{\tilde{h}}}{\omega^2 c/2}, \quad \alpha=\tilde{\alpha}, \quad \dot{\alpha}=\frac{\dot{\tilde{\alpha}}}{\omega}, \quad \ddot{\alpha}=\frac{\ddot{\tilde{\alpha}}}{\omega^2}, \\ d=\tilde{d}c/2, \quad \dot{d}=\frac{\dot{\tilde{d}}c/2}{\omega}, \quad \ddot{d}=\frac{\ddot{\tilde{d}}c/2}{\omega^2}. \end{gathered} \tag{4.13}$$

As in Chapter 3, the non-dimensional swimming velocity $u(t)$ is the inverse of the reduced frequency $k(t)$ commonly used in unsteady aerodynamics, now depending on time,

$$u(t)=\frac{\tilde{u}}{\omega c/2}=\frac{1}{k(t)}. \tag{4.14}$$

This unsteady reduced frequency will be used in the models for the dimensionless force and moment.

Taking all that into account, the non-dimensional version of Equations (4.7) to (4.9) are:

$$R\left[\ddot{h}+(a-x_0)\ddot{\alpha}+J_a\ddot{d}\right]=\hat{C}_L-\hat{C}_{L_o}, \tag{4.15}$$

$$R\left[(x_0-a)\ddot{h}-I_a\ddot{\alpha}+J_d\ddot{d}\right]=2(\hat{C}_M+\hat{C}_{M_i}-\hat{C}_{M_o}), \tag{4.16}$$

$$R\left[I_a\ddot{h}-I_d\ddot{\alpha}+K_d\ddot{d}\right]+\frac{a^2+1/3}{3(1-a)^2}Sd=\hat{C}_F, \tag{4.17}$$

where now the *dot* denotes a derivative with respect to the dimensionless time t. The terms corresponding to the pressure force that the fluid exerts on the foil are

$$\hat{C}_L=\frac{8L}{\pi\rho c^3\omega^2}=\frac{u^2C_L}{\pi}, \quad \hat{C}_M=\frac{8M}{\pi\rho c^4\omega^2}=\frac{u^2C_M}{\pi}, \quad \hat{C}_F=\frac{32F}{\pi\rho c^5\omega^2}=\frac{u^2C_F}{\pi}, \tag{4.18}$$

where, as in the previous chapters, a *hat* is used to remark that it is not the standard form of the coefficients, which is scaled with $\rho c\tilde{u}^2/2$, also included in the above relations for reference sake. The expressions of these coefficients obtained in Alaminos-Quesada and Fernandez-Feria [2020] and Fernandez-Feria and Alaminos-Quesada [2021a] from the linear potential-flow theory are also given in Appendix A. Similarly, the coefficients associated with Equation (4.4), corresponding to the translational and torsional springs and dampers, are defined as

$$\hat{C}_{L_o}=\frac{8L_o}{\pi\rho c^3\omega^2}=k_hh+b_h\dot{h}, \quad \hat{C}_{M_o}=\frac{8M_o}{\pi\rho c^4\omega^2}=-k_\alpha\alpha-b_\alpha\dot{\alpha}, \tag{4.19}$$

where

$$k_h=\frac{4\tilde{k}_h}{\pi\rho c^2\omega^2}, \quad b_h=\frac{4\tilde{b}_h}{\pi\rho c^2\omega}, \quad k_\alpha=\frac{8\tilde{k}_\alpha}{\pi\rho c^4\omega^2}, \quad b_\alpha=\frac{8\tilde{b}_\alpha}{\pi\rho c^4\omega}. \tag{4.20}$$

The remaining non-dimensional parameters in Equations (4.15) to (4.17) are the mass and stiffness ratios of the foil,

$$R = \frac{4m}{\pi\rho c^2}, \qquad S = \frac{64E\gamma^3}{\pi\rho c^5\omega^2}, \tag{4.21}$$

respectively. On the other hand, $a = 2\tilde{a}/c$ is the dimensionless pivot axis location, $a = -1$ corresponding to the leading edge and $a = 1$ to the trailing edge, and the coefficients J_a, I_a, J_d, I_d and K_d are functions of a given in Appendix A for the simplest case of constant ρ_s and γ; i.e., when $m = \rho_s c\gamma$ and $x_0 = 0$.

Working now with the dimensionless counterpart of Newton's second law (Equation (4.11)), it can be written as

$$R'\dot{u} = \hat{C}_T - Liu^2, \tag{4.22}$$

where

$$R' = \frac{4m'}{\pi\rho c^2 s}, \quad Li = \frac{A_w}{\pi c s}C_D, \quad C_D = \frac{2D}{\rho A_w \tilde{u}^2}, \tag{4.23}$$

are the dimensionless vehicle's mass and Lighthill's number based on a constant drag coefficient C_D, respectively, with A_w the characteristic surface for the vehicle's drag. The thrust coefficient of the hydrofoil,

$$\hat{C}_T = \frac{8T}{\pi\rho c^3\omega^2} = \frac{u^2 C_T}{\pi} = \frac{C_T}{\pi k^2}, \tag{4.24}$$

was obtained in Alaminos-Quesada and Fernandez-Feria [2020] from linear potential-flow theory for a flexible foil moving according to Equation (4.5) with harmonic functions $h(t)$, $\alpha(t)$ and $d(t)$ (see Appendix A for more details).

4.2.2 Performance parameters

Once equations Equations (4.15) to (4.17) and (4.22) are solved, either numerically or analytically for small u, one is interested in different non-dimensional quantities, in addition to the swimming velocity $u(t)$ itself, that provide relevant information about the self-propelled vehicle's performance.

One of them is the efficiency, defined as the propulsion power, $u(t)\hat{C}_T(t)$ in dimensionless form, divided by the power input spent to generate that propulsion, which in dimensionless form is

$$\hat{C}_{P_i}(t) = \frac{16P_i(t)}{\pi\rho c^4\omega^3} = -2\dot{\alpha}\hat{C}_{M_i}(t) = -2\dot{\alpha}\epsilon\sin t. \tag{4.25}$$

Note that the minus sign comes from the different sign conventions for the pitch angle and the input torque; see Figure 4.1(b). The instantaneous propulsive efficiency is

$$H(t) = \frac{u(t)\hat{C}_T(t)}{\hat{C}_{P_i}(t)}. \tag{4.26}$$

Since the forcing torque is a periodic function of time, one expects that so will be the long-time solutions of Equations (4.15) to (4.17) and (4.22), at least approximately. Of particular

interest are thus some time-averaged quantities. Once the permanent state for $t \gg 1$ has been reached for any magnitude $\phi(t)$, its time-average over n cycles (typically, we take $n = 5$) is denoted by an overline and given by

$$\bar{\phi} = \frac{1}{2\pi n} \int_t^{t+2\pi n} \phi(t) dt, \qquad t \gg 1. \tag{4.27}$$

The most relevant time-averaged quantities are the mean swimming speed, $U = \bar{u}$, and the propulsive (Froude) efficiency

$$\eta = \overline{H} = \frac{\overline{\hat{C}_T u}}{\overline{\hat{C}_{P_i}}} = \frac{R'\overline{u\dot{u}} + Li\overline{u^3}}{\overline{\hat{C}_{P_i}}} \simeq \frac{Li\overline{u^3}}{\overline{\hat{C}_{P_i}}}, \tag{4.28}$$

where Equation (4.22) has been used in the last expression, taking into account that $u\dot{u} \simeq 0$ if a nearly harmonic swimming velocity $u(t)$ has been reached for $t \gg 1$.

Instead of the swimming velocity U, sometimes it is more interesting to use its associated Strouhal number since it usually remains in a narrow range for efficient flapping propulsion (Triantafyllou et al. [1993], Taylor et al. [2003]). It is defined as

$$St = \frac{\omega \tilde{A}}{2\pi \widetilde{U}} = \frac{A}{2\pi U}, \tag{4.29}$$

where $\tilde{A}$ is the beat amplitude, taken as the maximum peak-to-peak flapping foil amplitude (A is its dimensionless counterpart). If the pivot axis is upstream of the mid-chord ($a < 0$), the maximum amplitude is presumably reached at the trailing edge, whose z-coordinate is $z_t(t) = z_s(1, t) = h(t) - (1 - a)\alpha(t) + (1 - a)2d(t)/2$, and $A = \overline{\max(z_t) - \min(z_t)}$. It is also interesting to know the Reynolds number associated with the motion of the foil, which is given by

$$Re = \frac{\widetilde{U} c}{\nu}, \tag{4.30}$$

where ν is the kinematic viscosity. Finally, for cruising, it is also widely used the cost of transport, instead of, or together with, the Froude efficiency, as a measure of the self-propulsion efficiency (Gabrielli and von Kármán [1951], Paniccia et al. [2021]). It is defined as the energy consumption per unit distance traveled by the vehicle. Although a dimensional form of this quantity is commonly used (e.g., with units of J/km), here we use the dimensionless version presented in Chapter 3.

$$CoT = \frac{\overline{\hat{C}_{P_i}}}{U}. \tag{4.31}$$

4.3 Numerical solution of the model equations

The system of ordinary differential equations (ODEs) Equations (4.15) to (4.17) and (4.22) for $h(t)$, $\alpha(t)$, $d(t)$, and $u(t)$ is solved numerically using Matlab's solver *ode45* starting from vanishing initial conditions, see Appendix C to find more information about the numerical resolution process. This ODE system is solved together with the expressions of $\hat{C}_L(t)$, $\hat{C}_M(t)$, $\hat{C}_F(t)$, and $\hat{C}_T(t)$ from the linear potential-flow theory for a harmonic foil motion. These expressions are given in Section A.2 of Appendix A, but for clarity purposes, we will show them here again. Therefore, the coefficients are

$$\hat{C}_L = \frac{8L}{\pi\rho c^3\omega^2} = -\dot{v} - a\ddot{\alpha} + u\dot{\alpha} + \dot{u}\alpha + A_{l2}(a)\ddot{d} + A_{l1}(a)(u\dot{d} + \dot{u}d) + \Re[C(k)]u\Gamma_0(t), \tag{4.32}$$

$$\begin{aligned}\hat{C}_M = \frac{8M}{\pi\rho c^4\omega^2} = \frac{1}{2}\Bigg[a\dot{v} + \left(a^2 + \frac{1}{8}\right)\ddot{\alpha} + \left(\frac{1}{2} - a\right)u\dot{\alpha} - a\dot{u}\alpha + A_{m2}(a)\ddot{d} + A_{m1}(a)u\dot{d} \\ + A_{m0}(a)u^2 d\Bigg] - \frac{1}{2}\left(\frac{1}{2} + a\right)\Re[C(k)]u\Gamma_0(t),\end{aligned} \tag{4.33}$$

$$\begin{aligned}\hat{C}_F = \frac{32F}{\pi\rho c^5\omega^2} = -\left(a^2 + \frac{1}{4}\right)\dot{v} - a\left(a^2 + \frac{1}{2}\right)\ddot{\alpha} + a(a-1)u\dot{\alpha} + A_{f2}(a)\ddot{d} + A_{f1}(a)u\dot{d} \\ + A_{f0}(a)u^2 d + \left(\frac{1}{2} + a + a^2\right)\Re[C(k)]u\Gamma_0(t),\end{aligned} \tag{4.34}$$

$$\begin{aligned}\hat{C}_T = \frac{8T}{\pi\rho c^3\omega^2} &= -(\alpha + 2ad)\hat{C}_L + \frac{d}{2}\left(\frac{\ddot{\alpha}}{2} + a\ddot{d} - u\dot{d}\right) + \frac{\dot{d}}{2}\left(\frac{\dot{\alpha}}{2} + a\dot{d} - ud\right) + (\dot{\alpha} + 2a\dot{d}) \\ &\cdot\left\{v + a\dot{\alpha} + \left(a^2 + \frac{1}{4}\right)\dot{d} - u(\alpha + 2ad) + \Gamma_0(t)\Re\left[\frac{i}{k}C(k) + \left(\frac{1+ik}{k}\right)\frac{2}{\pi}C_1(k)\right]\right\} \\ &- \left[v + a\dot{\alpha} - u(\alpha + 2ad) + a^2\dot{d}\right]\Gamma_0(t)\Re\left[\frac{2i}{\pi}C_1(k)\right] \\ &- d\Gamma_0(t)\Re\left[iC_2(k) + 2\left(\frac{1+ik}{k}\right)\frac{2}{\pi}C_1(k)\right] \\ &+ \dot{d}\Gamma_0(t)\Re\left[\left(\frac{2i}{k^2} - \frac{2+ik}{k}\right)\frac{2}{\pi}C_1(k) - \frac{C_2(k)}{k}\right],\end{aligned} \tag{4.35}$$

where $\hat{C}_T(t)$ is obtained from the linearized vortical impulse theory, and $\Re$ means real part. A new and extended-expression for $\Gamma_0(t)$ is then used

$$\Gamma_0(t) = -2\left[v + \left(a - \frac{1}{2}\right)\dot{\alpha} - u\alpha + A_{g1}(a)\dot{d} + A_{g0}(a)ud\right], \tag{4.36}$$

with the functions

$$C(k) = \frac{H_1^{(2)}(k)}{iH_0^{(2)}(k) + H_1^{(2)}(k)} = \mathcal{F}(k) + i\mathcal{G}(k), \tag{4.37}$$

$$C_1(k) = \frac{\frac{1}{k}e^{-ik}}{iH_0^{(2)}(k) + H_1^{(2)}(k)} = \mathcal{F}_1(k) + i\mathcal{G}_1(k), \tag{4.38}$$

$$C_2(k) = \frac{H_2^{(2)}(k)}{iH_0^{(2)}(k) + H_1^{(2)}(k)} = \mathcal{F}_2(k) + i\mathcal{G}_2(k), \tag{4.39}$$

being $H_n^{(2)}(z) = J_n(z) - iY_n(z)$, with $n = \{0, 1\}$ the Hankel's function of the second kind and order n, related to the Bessel functions of the first and second kind $J_n(z)$ and $Y_n(z)$.

In Figure 4.2, it is presented some numerical solutions for decreasing values of the stiffness parameter S using the typical values of the remaining non-dimensional parameters, which were discussed in Chapter 3 for a rigid foil. In all cases, the solutions for all the variables consist of a transient phase much longer than the oscillating period that eventually reaches a permanent state with almost periodic oscillations around a constant mean. The mean is practically zero for $h(t)$, $\alpha(t)$, and $d(t)$, while $\bar{u} \to U > 0$. Notice that, for the selected set of values of the parameters, $h(t)$, $\alpha(t)$, and $d(t)$ remain small and, therefore, within the validity range of the model equations.

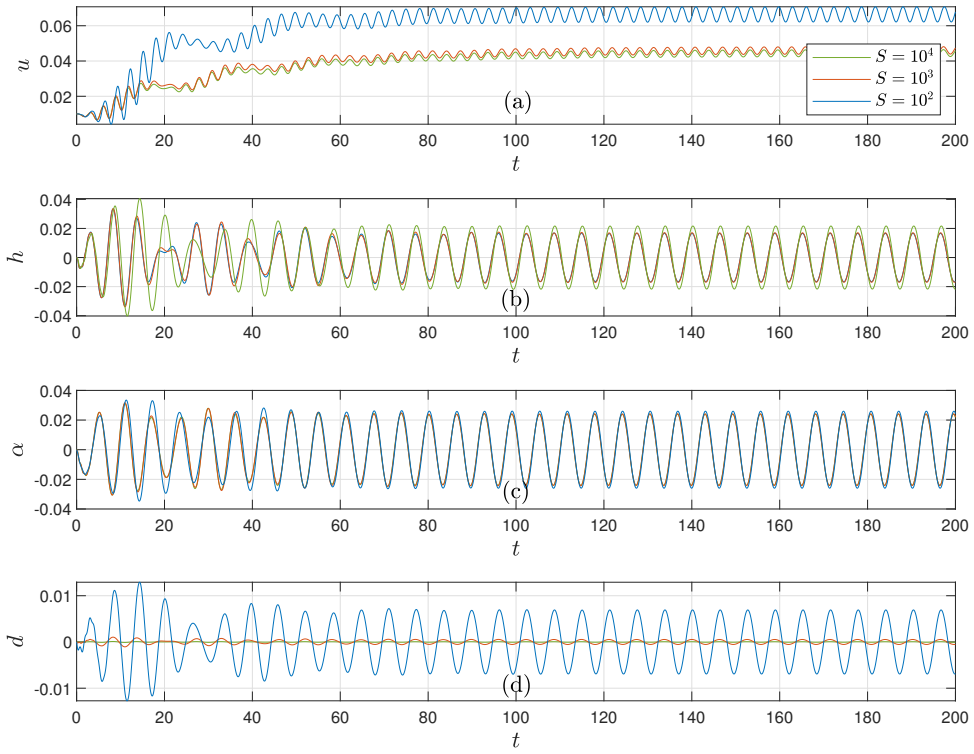

Figure 4.2: Evolutions of $u(t)$ (a), $h(t)$ (b), $\alpha(t)$ (c), and $d(t)$ (d) for $R = 0.02$, $R' = 0.2$, $a = -1$, $x_0 = 0$, $k_h = 2.5$, $k_\alpha = 3$, $b_h = b_\alpha = 0.05$, $Li = 0.1$, $\epsilon = 0.05$ and three values of S indicated in (a).

It can be observed that for very large S (10^4 and 10^3 in the figure), the foil behaves as a rigid foil, with $d(t)$ negligible and time evolutions of $u(t)$, $h(t)$, and $\alpha(t)$ almost indistinguishable for $S = 10^3$ and $S = 10^4$. As S decreases to $S = 100$, $d(t)$ becomes noticeable. The swimming velocity U increases substantially, showing that, for the present set of values of the parameters, foil flexibility improves the propulsion performance in terms of swimming speed when all the rest of the vehicle and foil characteristics remain the same. Another feature of the solutions that will be manifest later in the perturbation analytical solution is that contrary to $u(t)$, both $h(t)$ and $\alpha(t)$ remain almost unaltered in the permanent state for $S = 100$ when $d(t)$ is no longer negligible. Thus, flexibility barely affects the passive heaving and pitching motions of the foil, but it significantly affects its propulsive performance.

4.4 Approximate analytical solution from two-scales perturbation method

Although the numerical solution of the system of ODEs is straightforward, much insight into the propulsion performance may be gained by taking advantage of the small torque intensity ϵ and the large stiffness ratio S to obtain analytical approximate solutions for $h(t)$, $\alpha(t)$, $d(t)$ and $u(t)$ using perturbation methods. It will also be assumed that $u = 1/k \ll 1$, which constitutes an additional limitation of the asymptotic solution in relation to the numerical solution of the model equations for small ϵ and large S.

From the structure of the numerical solution, and similarly to the perturbation approach conducted in Chapter 3, one may assume two-time scales: a fast time t, associated with the period of the torque oscillations, and a slower time

$$\tau = B\epsilon^b t, \tag{4.40}$$

associated to the transient towards the permanent oscillatory state with constant mean, where the constants B and b have to be determined from the scaling of the different terms in the equations. In addition, since we are considering the small deflection approximation, we assume that $S \gg 1$. Therefore, the time derivatives are approximated by

$$\frac{d}{dt} = \frac{\partial}{\partial t} + B\epsilon^b \frac{\partial}{\partial \tau}, \qquad \frac{d^2}{dt^2} = \frac{\partial^2}{\partial t^2} + 2B\epsilon^b \frac{\partial^2}{\partial t \partial \tau} + B^2\epsilon^{2b} \frac{\partial^2}{\partial \tau^2}. \tag{4.41}$$

Assuming that, according to Equations (4.15) and (4.16), the lowest-order amplitude of the pitching and heaving oscillations is of the same order ϵ as the forcing torque $\hat{C}_{M_i}$. So, the asymptotic expansions for h and α with the two timescales can be written as

$$h(t,\tau) \sim \epsilon h_1(t,\tau) + \epsilon^{m_1} h_2(t,\tau) + \epsilon^{m_2} h_3(t,\tau) + \cdots, \tag{4.42}$$

$$\alpha(t,\tau) \sim \epsilon \alpha_1(t,\tau) + \epsilon^{m_1} \alpha_2(t,\tau) + \epsilon^{m_2} \alpha_3(t,\tau) + \cdots, \tag{4.43}$$

while d needs to have a different expansion in order to match the second term in Equation (4.17) with the first main order of the equations (remember that $S \gg 1$). Thus,

$$d(t,\tau) \sim \epsilon^{m_1} d_1(t,\tau) + \epsilon^{m_2} d_2(t,\tau) + \cdots. \tag{4.44}$$

This means that $Sd \sim \epsilon$, where S has to be of the order

$$S \sim \epsilon^{1-m_1} S_1, \tag{4.45}$$

to match both orders, where S_1 is a constant of order unity. Finally, the expansion of u can be written as

$$u(t,\tau) \sim \epsilon^{n_1} u_1(t,\tau) + \epsilon^{n_2} u_2(t,\tau) + \cdots, \tag{4.46}$$

with $1 < n_1 < n_2 < \cdots$ and $1 < m_1 < m_2 < \cdots$ to be determined. To perform the expansions for the force and moment coefficients we take into account that $k = u^{-1} \gg 1$, so that one may use the large$-k$ approximation of the functions appearing in Equations (4.37) to (4.39) (see, e.g., Fernandez-Feria and Sanmiguel-Rojas [2019], for more details).

$$\begin{gathered}
\Re[C(k)] = \frac{1}{2} + O(k^{-2}), \\
\Re\left[\frac{i}{k}C(k) + \left(\frac{1+ik}{k}\right)\frac{2}{\pi}C_1(k)\right] = \Re\left[\frac{2i}{\pi}C_1(k)\right] = \frac{1}{(4\pi k)^{1/2}} + O(k^{-3/2}), \\
\Re\left[iC_2(k) + 2\left(\frac{1+ik}{k}\right)\frac{2}{\pi}C_1(k)\right] = -\frac{1}{2} + O(k^{-1/2}), \\
\Re\left[\left(\frac{2i}{k^2} - \frac{2+ik}{k}\right)\frac{2}{\pi}C_1(k) - \frac{C_2(k)}{k}\right] = \frac{1}{(4\pi k)^{1/2}} + O(k^{-3/2}).
\end{gathered} \tag{4.47}$$

Taking that into account, the coefficient terms yield to

$$\begin{aligned}
\hat{C}_L = &-\ddot{h} - a\ddot{\alpha} + \left(\frac{3}{2} - a\right)u\dot{\alpha} + \dot{u}\alpha + A_{l2}\ddot{d} + (A_{l1} - A_{g1})u\dot{d} \\
&+ A_{l1}\dot{u}d - [u\dot{h} - u^2\alpha + A_{g0}u^2 d],
\end{aligned} \tag{4.48}$$

$$\begin{aligned}
\hat{C}_M = \frac{1}{2}\Bigg\{ &a\ddot{h} + \left(a^2 + \frac{1}{8}\right)\ddot{\alpha} + \left(\frac{1}{2} - a\right)^2 u\dot{\alpha} - a\dot{u}\alpha + A_{m2}\ddot{d} + \left[A_{m1} + \left(\frac{1}{2} + a\right)A_{g1}\right]u\dot{d} \\
&+ \left[A_{m0} + \left(\frac{1}{2} + a\right)A_{g0}\right]u^2 d + \left(\frac{1}{2} + a\right)[u\dot{h} - u^2\alpha]\Bigg\},
\end{aligned} \tag{4.49}$$

$$\begin{aligned}
\hat{C}_F = &-\left(a^2 + \frac{1}{4}\right)\ddot{h} - a\left(a^2 + \frac{1}{2}\right)\ddot{\alpha} + \left(-a^3 + \frac{a^2}{2} - a + \frac{1}{4}\right)u\dot{\alpha} + A_{f2}\ddot{d} \\
&+ \left[A_{f1} - \left(\frac{1}{2} + a + a^2\right)A_{g1}\right]u\dot{d} + \left[A_{f0} - \left(\frac{1}{2} + a + a^2\right)A_{g0}\right]u^2 d \\
&- \left(\frac{1}{2} + a + a^2\right)[u\dot{h} - u^2\alpha],
\end{aligned} \tag{4.50}$$

$$\begin{aligned}\hat{C}_T = {} & \alpha\ddot{h} + 2ad\ddot{h} + a\alpha\ddot{\alpha} + \left(2a^2 + \frac{1}{4}\right) d\ddot{\alpha} - A_{l2}\alpha\ddot{d} + a\left(\frac{1}{2} - 2A_{l2}\right) d\ddot{d} + \frac{1}{\sqrt{\pi}} u^{1/2}\dot{h}^2 \\ & + \frac{1}{\sqrt{\pi}}\left(2a - \frac{3}{2}\right) u^{1/2}\dot{h}\dot{\alpha} + \dot{h}\dot{\alpha} + \frac{1}{\sqrt{\pi}}(a^2 - 2a - 1 + A_{g1}) u^{1/2}\dot{h}\dot{d} + 2a\dot{h}\dot{d} + \alpha u\dot{h} - \frac{2}{\sqrt{\pi}} u^{3/2}\alpha\dot{h} \\ & - \frac{1}{\sqrt{\pi}}(2a - A_{g0}) u^{3/2} d\dot{h} + 2aud\dot{h} - \dot{h}d + \frac{1}{\sqrt{\pi}}\left(a^2 - \frac{3a}{2} + \frac{1}{2}\right) u^{1/2}\dot{\alpha}^2 + a\dot{\alpha}^2 \\ & + \frac{1}{\sqrt{\pi}}\left(a^3 - \frac{5a^2}{2} + aA_{g1} + \frac{1}{2} - A_{g1}\right) u^{1/2}\dot{\alpha}\dot{d} + \left(3a^2 + \frac{1}{2}\right)\dot{\alpha}\dot{d} - \frac{1}{\sqrt{\pi}}\left(2a - \frac{3}{2}\right) u^{3/2}\alpha\dot{\alpha} \\ & + \left(a - \frac{5}{2}\right) u\alpha\dot{\alpha} - \frac{1}{\sqrt{\pi}}\left(2a^2 - a(1 + A_{g0}) + A_{g0}\right) u^{3/2} d\dot{\alpha} + a(2a - 5) ud\dot{\alpha} + \left(\frac{1}{2} - a\right) d\dot{\alpha} \\ & + \frac{1}{\sqrt{\pi}} A_{g1}(a^2 - 2a - 1) u^{1/2}\dot{d}^2 + a(2a^2 + 1)\dot{d}^2 - \frac{1}{\sqrt{\pi}}(a^2 - 2a - 1 + A_{g1}) u^{3/2}\alpha\dot{d} \\ & - (2a + A_{l1} - A_{g1}) u\alpha\dot{d} + \frac{1}{\sqrt{\pi}}\left[A_{g0}(a^2 - 2a - 1) - 2aA_{g1}\right] u^{3/2} d\dot{d} \\ & - [4a^2 + 2a(A_{l1} - A_{g1}) + 1] ud\dot{d} - A_{g1} d\dot{d} - \alpha^2\dot{u} - (2a + A_{l1})\alpha d\dot{u} - 2aA_{l1} d^2\dot{u} \\ & + \frac{1}{\sqrt{\pi}}\alpha^2 u^{5/2} - \alpha^2 u^2 + \frac{1}{\sqrt{\pi}}(2a - A_{g0}) u^{5/2}\alpha d - (2a - A_{g0}) u^2\alpha d + u\alpha d \\ & - \frac{1}{\sqrt{\pi}}(2aA_{g0}) u^{5/2} d^2 + 2aA_{g0} u^2 d^2 - A_{g0} ud^2. \end{aligned} \tag{4.51}$$

4.4.1 Expansions of the main equations

Lift Equation

Taking into consideration all the previous information, Equation (4.15) becomes

$$\begin{aligned} R\left[\ddot{h} + (a - x_0)\ddot{\alpha} + J_a\ddot{d}\right] + b_h\dot{h} + k_h h = {} & -\ddot{h} - a\ddot{\alpha} + \left(\frac{3}{2} - a\right) u\dot{\alpha} + \dot{u}\alpha + A_{l2}\ddot{d} \\ & + (A_{l1} - A_{g1}) u\dot{d} + A_{l1}\dot{u}d - [u\dot{h} - u^2\alpha + A_{g0} u^2 d], \end{aligned} \tag{4.52}$$

and substituting the corresponding asymptotic expansions until the order $1 + n_1$

$$\begin{aligned} & R\left(\epsilon\frac{\partial^2 h_1}{\partial t^2} + \epsilon^{m_1}\frac{\partial^2 h_2}{\partial t^2} + \epsilon^{m_2}\frac{\partial^2 h_3}{\partial t^2} + 2B\epsilon^{b+1}\frac{\partial^2 h_1}{\partial t\partial\tau} + \cdots\right) + R(a - x_0)\left(\epsilon\frac{\partial^2\alpha_1}{\partial t^2} + \epsilon^{m_1}\frac{\partial^2\alpha_2}{\partial t^2}\right. \\ & \left. + \epsilon^{m_2}\frac{\partial^2\alpha_3}{\partial t^2} + 2B\epsilon^{b+1}\frac{\partial^2\alpha_1}{\partial t\partial\tau} + \cdots\right) + RJ_a\left(\epsilon^{m_1}\frac{\partial^2 d_1}{\partial t^2} + \epsilon^{m_2}\frac{\partial^2 d_2}{\partial t^2} + \cdots\right) \\ & + b_h\left(\epsilon\frac{\partial h_1}{\partial t} + \epsilon^{m_1}\frac{\partial h_2}{\partial t} + \epsilon^{m_2}\frac{\partial^2 h_3}{\partial t^2} + B\epsilon^{b+1}\frac{\partial h_1}{\partial\tau} + \cdots\right) + k_h(\epsilon h_1 + \epsilon^{m_1} h_2 + \epsilon^{m_2} h_3 + \cdots) \\ & = \hat{C}_L = \epsilon\hat{C}_{L,1} + \epsilon^{m_1}\hat{C}_{L,m_1} + \epsilon^{m_2}\hat{C}_{L,m_2} + \epsilon^{b+1}\hat{C}_{L,b+1} + \epsilon^{1+n_1}\hat{C}_{L,1+n_1} + \cdots, \end{aligned} \tag{4.53}$$

where an analogous process as the one presented in Section 3.4.1 of Chapter 3 has been conducted. However, as the procedure is the same, we will only show some of the term expansions in order to make the text more clear and easy to follow. Therefore, the orders m_2, $b+1$, and $1+n_1$ need to match in order to avoid singularities in the solution. Thus,

$$\begin{aligned}\hat{C}_{L,1} &= -\frac{\partial^2 h_1}{\partial t^2} - a\frac{\partial^2 \alpha_1}{\partial t^2}, \quad \hat{C}_{L,m_1} = -\frac{\partial^2 h_2}{\partial t^2} - a\frac{\partial^2 \alpha_2}{\partial t^2} + A_{l2}\frac{\partial^2 d_1}{\partial t^2},\\ \hat{C}_{L,m_2,b+1,1+n_1} &= -\frac{\partial^2 h_3}{\partial t^2} - a\frac{\partial^2 \alpha_3}{\partial t^2} + A_{l2}\frac{\partial^2 d_2}{\partial t^2} - 2B\frac{\partial^2 h_1}{\partial t\partial\tau} - a2B\frac{\partial^2 \alpha_1}{\partial t\partial\tau}\\ &\quad + \left(\frac{3}{2} - a\right) u_1\frac{\partial \alpha_1}{\partial t} + \alpha_1\frac{\partial u_1}{\partial t} - u_1\frac{\partial h_1}{\partial t}.\end{aligned} \tag{4.54}$$

Moment Equation

Analogously for the moment, Equation (4.16) becomes

$$\begin{aligned}&R\left[(x_0-a)\ddot{h} - I_a\ddot{\alpha} + J_d\ddot{d}\right] - 2(b_\alpha\dot{\alpha} + k_\alpha\alpha) = a\ddot{h} + \left(a^2+\frac{1}{8}\right)\ddot{\alpha} + \left(\frac{1}{2}-a\right)^2 u\dot{\alpha} - au\dot{\alpha} + A_{m2}\ddot{d}\\ &+\left[A_{m1} + \left(\frac{1}{2}+a\right)A_{g1}\right]u\dot{d} + \left[A_{m0} + \left(\frac{1}{2}+a\right)A_{g0}\right]u^2 d + \left(\frac{1}{2}+a\right)[u\dot{h} - u^2\alpha] + 2\epsilon\sin t,\end{aligned} \tag{4.55}$$

and substituting the corresponding asymptotic expansions until the order $1+n_1$

$$\begin{aligned}&R(x_0-a)\left(\epsilon\frac{\partial^2 h_1}{\partial t^2} + \epsilon^{m_1}\frac{\partial^2 h_2}{\partial t^2} + \epsilon^{m_2}\frac{\partial^2 h_3}{\partial t^2} + 2B\epsilon^{b+1}\frac{\partial^2 h_1}{\partial t\partial\tau} + \cdots\right) - RI_a\left(\epsilon\frac{\partial^2 \alpha_1}{\partial t^2} + \epsilon^{m_1}\frac{\partial^2 \alpha_2}{\partial t^2}\right.\\ &\left.+\epsilon^{m_2}\frac{\partial^2 \alpha_3}{\partial t^2} + 2B\epsilon^{b+1}\frac{\partial^2 \alpha_1}{\partial t\partial\tau} + \cdots\right) + RJ_d\left(\epsilon^{m_1}\frac{\partial^2 d_1}{\partial t^2} + \epsilon^{m_2}\frac{\partial^2 d_2}{\partial t^2} + \cdots\right)\\ &-2b_\alpha\left(\epsilon\frac{\partial h_1}{\partial t} + \epsilon^{m_1}\frac{\partial h_2}{\partial t} + \epsilon^{m_2}\frac{\partial^2 h_3}{\partial t^2} + B\epsilon^{b+1}\frac{\partial h_1}{\partial \tau} + \cdots\right) - 2k_h(\epsilon h_1 + \epsilon^{m_1}h_2 + \epsilon^{m_2}h_3 + \cdots)\\ &-2\epsilon\sin t = \hat{C}_M = \epsilon\hat{C}_{M,1} + \epsilon^{m_1}\hat{C}_{M,m_1} + \epsilon^{m_2}\hat{C}_{M,m_2} + \epsilon^{b+1}\hat{C}_{M,b+1} + \epsilon^{1+n_1}\hat{C}_{M,1+n_1} + \cdots,\end{aligned} \tag{4.56}$$

where

$$\begin{aligned}\hat{C}_{M,1} &= a\frac{\partial^2 h_1}{\partial t^2} + \left(a^2+\frac{1}{8}\right)\frac{\partial^2 \alpha_1}{\partial t^2}, \quad \hat{C}_{M,m_1} = a\frac{\partial^2 h_2}{\partial t^2} + \left(a^2+\frac{1}{8}\right)\frac{\partial^2 \alpha_2}{\partial t^2} + A_{m2}\frac{\partial^2 d_1}{\partial t^2},\\ \hat{C}_{M,m_2,b+1,1+n_1} &= a\frac{\partial^2 h_3}{\partial t^2} + \left(a^2+\frac{1}{8}\right)\frac{\partial^2 \alpha_3}{\partial t^2} + A_{m2}\frac{\partial^2 d_2}{\partial t^2} + a2B\frac{\partial^2 h_1}{\partial t\partial\tau} + \left(a^2+\frac{1}{8}\right)2B\frac{\partial^2 \alpha_1}{\partial t\partial\tau}\\ &\quad + \left(\frac{1}{2}-a\right)^2 u_1\frac{\partial \alpha_1}{\partial t} - a\alpha_1\frac{\partial u_1}{\partial t} + \left(\frac{1}{2}+a\right)u_1\frac{\partial h_1}{\partial t}.\end{aligned} \tag{4.57}$$

Flexural deflection Equation

For the flexural deflection, Equation (4.17) becomes

$$\begin{aligned} R\left[I_a\ddot{h}-I_d\ddot{\alpha}+K_d\ddot{d}\right]+\frac{a^2+1/3}{3(1-a)^2}Sd &= -\left(a^2+\frac{1}{4}\right)\ddot{h}-a\left(a^2+\frac{1}{2}\right)\ddot{\alpha} \\ &+\left(-a^3+\frac{a^2}{2}-a+\frac{1}{4}\right)u\dot{\alpha}+A_{f2}\ddot{d}+\left[A_{f1}-\left(\frac{1}{2}+a+a^2\right)A_{g1}\right]u\dot{d} \\ &+\left[A_{f0}-\left(\frac{1}{2}+a+a^2\right)A_{g0}\right]u^2d-\left(\frac{1}{2}+a+a^2\right)[u\dot{h}-u^2\alpha], \end{aligned} \tag{4.58}$$

and substituting the corresponding asymptotic expansions until the order $1+n_1$

$$\begin{aligned} &RI_a\left(\epsilon\frac{\partial^2 h_1}{\partial t^2}+\epsilon^{m_1}\frac{\partial^2 h_2}{\partial t^2}+\epsilon^{m_2}\frac{\partial^2 h_3}{\partial t^2}+2B\epsilon^{b+1}\frac{\partial^2 h_1}{\partial t\partial\tau}+\cdots\right)-RI_d\left(\epsilon\frac{\partial^2\alpha_1}{\partial t^2}+\epsilon^{m_1}\frac{\partial^2\alpha_2}{\partial t^2}\right. \\ &\left.+\epsilon^{m_2}\frac{\partial^2\alpha_3}{\partial t^2}+2B\epsilon^{b+1}\frac{\partial^2\alpha_1}{\partial t\partial\tau}+\cdots\right)+RK_d\left(\epsilon^{m_1}\frac{\partial^2 d_1}{\partial t^2}+\epsilon^{m_2}\frac{\partial^2 d_2}{\partial t^2}+\cdots\right) \\ &+\frac{a^2+1/3}{3(1-a)^2}S_1\epsilon^{1-m_1}(\epsilon^{m_1}d_1+\epsilon^{m_2}d_2+\epsilon^{m_3}d_3+\cdots)=\hat{C}_F \\ &=\epsilon\hat{C}_{F,1}+\epsilon^{m_1}\hat{C}_{F,m_1}+\epsilon^{m_2}\hat{C}_{F,m_2}+\epsilon^{b+1}\hat{C}_{F,b+1}+\epsilon^{1+n_1}\hat{C}_{F,1+n_1}+\cdots, \end{aligned} \tag{4.59}$$

where

$$\begin{aligned} \hat{C}_{F,1} &= -\left(a^2+\frac{1}{4}\right)\frac{\partial^2 h_1}{\partial t^2}-a\left(a^2+\frac{1}{2}\right)\frac{\partial^2\alpha_1}{\partial t^2}, \\ \hat{C}_{F,m_1} &= -\left(a^2+\frac{1}{4}\right)\frac{\partial^2 h_2}{\partial t^2}-a\left(a^2+\frac{1}{2}\right)\frac{\partial^2\alpha_2}{\partial t^2}+A_{f2}\frac{\partial^2 d_1}{\partial t^2}, \\ \hat{C}_{F,m_2,b+1,1+n_1} &= -\left(a^2+\frac{1}{4}\right)\frac{\partial^2 h_3}{\partial t^2}-a\left(a^2+\frac{1}{2}\right)\frac{\partial^2\alpha_3}{\partial t^2}+A_{f2}\frac{\partial^2 d_2}{\partial t^2}-\left(a^2+\frac{1}{4}\right)2B\frac{\partial^2 h_1}{\partial t\partial\tau} \\ &-a\left(a^2+\frac{1}{2}\right)2B\frac{\partial^2\alpha_1}{\partial t\partial\tau}+\left(-a^3+\frac{a^2}{2}-a+\frac{1}{4}\right)u_1\frac{\partial\alpha_1}{\partial t}-\left(\frac{1}{2}+a+a^2\right)u_1\frac{\partial h_1}{\partial t}. \end{aligned} \tag{4.60}$$

Thrust Equation

Finally, for the thrust, Equation (4.22) becomes

$$
\begin{aligned}
R'\dot{u} + Liu^2 = {} & \alpha\ddot{h} + 2ad\ddot{h} + a\alpha\ddot{\alpha} + \left(2a^2 + \frac{1}{4}\right) d\ddot{\alpha} - A_{l2}\alpha\ddot{d} + a\left(\frac{1}{2} - 2A_{l2}\right) d\ddot{d} + \frac{1}{\sqrt{\pi}} u^{1/2}\dot{h}^2 \\
& + \frac{1}{\sqrt{\pi}}\left(2a - \frac{3}{2}\right) u^{1/2}\dot{h}\dot{\alpha} + \dot{h}\dot{\alpha} + \frac{1}{\sqrt{\pi}}(a^2 - 2a - 1 + A_{g1}) u^{1/2}\dot{h}\dot{d} + 2a\dot{h}\dot{d} + \alpha u\dot{h} - \frac{2}{\sqrt{\pi}} u^{3/2}\alpha\dot{h} \\
& - \frac{1}{\sqrt{\pi}}(2a - A_{g0}) u^{3/2} d\dot{h} + 2aud\dot{h} - \dot{h}d + \frac{1}{\sqrt{\pi}}\left(a^2 - \frac{3a}{2} + \frac{1}{2}\right) u^{1/2}\dot{\alpha}^2 + a\dot{\alpha}^2 \\
& + \frac{1}{\sqrt{\pi}}\left(a^3 - \frac{5a^2}{2} + aA_{g1} + \frac{1}{2} - A_{g1}\right) u^{1/2}\dot{\alpha}\dot{d} + \left(3a^2 + \frac{1}{2}\right)\dot{\alpha}\dot{d} - \frac{1}{\sqrt{\pi}}\left(2a - \frac{3}{2}\right) u^{3/2}\alpha\dot{\alpha} \\
& + \left(a - \frac{5}{2}\right) u\alpha\dot{\alpha} - \frac{1}{\sqrt{\pi}}\left(2a^2 - a(1 + A_{g0}) + A_{g0}\right) u^{3/2} d\dot{\alpha} + a(2a - 5) ud\dot{\alpha} + \left(\frac{1}{2} - a\right) d\dot{\alpha} \\
& + \frac{1}{\sqrt{\pi}} A_{g1}(a^2 - 2a - 1) u^{1/2}\dot{d}^2 + a(2a^2 + 1)\dot{d}^2 - \frac{1}{\sqrt{\pi}}(a^2 - 2a - 1 + A_{g1}) u^{3/2}\alpha\dot{d} \\
& - (2a + A_{l1} - A_{g1}) u\alpha\dot{d} + \frac{1}{\sqrt{\pi}}\left[A_{g0}(a^2 - 2a - 1) - 2aA_{g1}\right] u^{3/2} d\dot{d} \\
& - [4a^2 + 2a(A_{l1} - A_{g1}) + 1] ud\dot{d} - A_{g1} d\dot{d} - \alpha^2\dot{u} - (2a + A_{l1})\alpha d\dot{u} - 2aA_{l1} d^2\dot{u} \\
& + \frac{1}{\sqrt{\pi}}\alpha^2 u^{5/2} - \alpha^2 u^2 + \frac{1}{\sqrt{\pi}}(2a - A_{g0}) u^{5/2}\alpha d - (2a - A_{g0}) u^2\alpha d + u\alpha d \\
& - \frac{1}{\sqrt{\pi}}(2aA_{g0}) u^{5/2} d^2 + 2aA_{g0} u^2 d^2 - A_{g0} u d^2 .
\end{aligned}
\tag{4.61}
$$

As in Chapter 3, we need the expansion of $u^{1/2}$, which is

$$
(\epsilon^{n_1} u_1 + \epsilon^{n_2} u_2 + \cdots)^{1/2} = \left[(\epsilon^{n_1} u_1)\left(1 + \frac{\epsilon^{n_2}}{\epsilon^{n_1}}\frac{u_2}{u_1} + \cdots\right)\right]^{1/2} \approx \epsilon^{n_1/2} u_1^{1/2}\left[1 + \frac{1}{2}(\epsilon^{n_2 - n_1} u_2 u_1^{-1}) + \cdots\right],
\tag{4.62}
$$

and similarly for the rest of the powers of u. Substituting the corresponding asymptotic expansions, we obtain

$$
\begin{aligned}
& R'\left(\epsilon^{n_1}\frac{\partial u_1}{\partial t} + \epsilon^{n_2}\frac{\partial u_2}{\partial t} + B\epsilon^{b+n_1}\frac{\partial u_1}{\partial \tau} + \cdots\right) + Li(\epsilon^{2n_1} u_1^2 + 2\epsilon^{n_1+n_2} u_1 u_2 + \epsilon^{2n_2} u_2^2 + \cdots) \\
& \qquad = \hat{C}_T = \epsilon\hat{C}_{T,1} + \epsilon^2\hat{C}_{T,2} + \epsilon^{1+m_1}\hat{C}_{T,1+m_1} + \epsilon^{2+n_1/2}\hat{C}_{T,2+n_1/2} + \cdots .
\end{aligned}
\tag{4.63}
$$

Here, the orders $1+m_1$ and $2+n_1/2$ need to match to avoid singularities in the solution. Thus,

$$\hat{C}_{T,1}=0,\quad \hat{C}_{T,2}=\alpha_1\frac{\partial^2 h_1}{\partial t^2}+a\alpha_1\frac{\partial^2\alpha_1}{\partial t^2}+\frac{\partial\alpha_1}{\partial t}\frac{\partial h_1}{\partial t}+a\left(\frac{\partial\alpha_1}{\partial t}\right)^2,$$

$$\begin{aligned}\hat{C}_{T,1+m_1,2+n_1/2}=\Bigg\{&\alpha_1\frac{\partial^2 h_2}{\partial t^2}+\alpha_2\frac{\partial^2 h_1}{\partial t^2}+2ad_1\frac{\partial^2 h_1}{\partial t^2}+a\alpha_1\frac{\partial^2\alpha_2}{\partial t^2}+a\alpha_2\frac{\partial^2\alpha_1}{\partial t^2}+\left(2a^2+\frac{1}{4}\right)d_1\frac{\partial^2\alpha_1}{\partial t^2}\\&-A_{l2}\alpha_1\frac{\partial^2 d_1}{\partial t^2}+\frac{\partial h_2}{\partial t}\frac{\partial\alpha_1}{\partial t}+\frac{\partial h_1}{\partial t}\frac{\partial\alpha_2}{\partial t}+2a\frac{\partial h_1}{\partial t}\frac{\partial d_1}{\partial t}-\frac{\partial h_1}{\partial t}d_1+2a\frac{\partial\alpha_1}{\partial t}\frac{\partial\alpha_2}{\partial t}\\&+\left(3a^2+\frac{1}{2}\right)\frac{\partial\alpha_1}{\partial t}\frac{\partial d_1}{\partial t}+\left(\frac{1}{2}-a\right)d_1\frac{\partial\alpha_1}{\partial t}\Bigg\}\\&+\frac{u_1^{1/2}}{\sqrt{\pi}}\left[\left(\frac{\partial h_1}{\partial t}\right)^2+\left(2a-\frac{3}{2}\right)\frac{\partial\alpha_1}{\partial t}\frac{\partial h_1}{\partial t}+\left(a-\frac{1}{2}\right)(a-1)\left(\frac{\partial\alpha_1}{\partial t}\right)^2\right].\end{aligned}\tag{4.64}$$

Similarly to Chapter 3, if we look at the permanent final state, we can see that the leading drag term Liu^2 must balance the leading thrust term. However, the $O(\epsilon^2)$ thrust term only depends on t, so the drag term must balance the next order in the expansion of $\hat{C}_T$. Thus

$$\begin{aligned}&2n_1=2+n_1/2=1+m_1\rightarrow n_1=4/3,\ m_1=5/3,\\&n_1+n_2=2+n_1=1+m_2\rightarrow n_2=2,\ m_2=7/3,\\&n_1+n_3=2+n_2=1+m_3\rightarrow n_3=8/3,\ m_3=3.\end{aligned}\tag{4.65}$$

In addition, these terms must also balance the leading term containing derivatives with the slow time τ, i.e.,

$$b+n_1=2n_1\rightarrow b=n_1=4/3.\tag{4.66}$$

Consequently, the expansions for h, α, d, and u will be

$$h(t,\tau)\sim\epsilon h_1(t,\tau)+\epsilon^{5/3}h_2(t,\tau)+\epsilon^{7/3}h_3(t,\tau)+\cdots,\tag{4.67}$$

$$\alpha(t,\tau)\sim\epsilon\alpha_1(t,\tau)+\epsilon^{5/3}\alpha_2(t,\tau)+\epsilon^{7/3}\alpha_3(t,\tau)+\cdots,\tag{4.68}$$

$$d(t,\tau)\sim\epsilon^{5/3}d_1(t,\tau)+\epsilon^{7/3}d_2(t,\tau)+\epsilon^{3}d_3(t,\tau)+\cdots,\tag{4.69}$$

$$u(t,\tau)\sim\epsilon^{4/3}u_1(t,\tau)+\epsilon^{2}u_2(t,\tau)+\epsilon^{8/3}u_3(t,\tau)+\cdots,\tag{4.70}$$

and the timescale τ associated with the slower variations of the mean values

$$\tau=B\epsilon^{4/3}t.\tag{4.71}$$

Resulting equations

We can obtain the following resulting equations by gathering all the terms in the main expressions. From the Lift Equation, we get

$$\begin{aligned}
O(\epsilon) &: R\frac{\partial^2 h_1}{\partial t^2} + R(a-x_0)\frac{\partial^2 \alpha_1}{\partial t^2} + b_h\frac{\partial h_1}{\partial t} + k_h h_1 = \hat{C}_{L,1},\\
O(\epsilon^{5/3}) &: R\frac{\partial^2 h_2}{\partial t^2} + R(a-x_0)\frac{\partial^2 \alpha_2}{\partial t^2} + RJ_a\frac{\partial^2 d_1}{\partial t^2} + b_h\frac{\partial h_2}{\partial t} + k_h h_2 = \hat{C}_{L,m_1} = \hat{C}_{L,5/3},\\
O(\epsilon^{7/3}) &: R\left(\frac{\partial^2 h_3}{\partial t^2} + 2B\frac{\partial^2 h_1}{\partial t\partial\tau}\right) + R(a-x_0)\left(\frac{\partial^2 \alpha_3}{\partial t^2} + 2B\frac{\partial^2 \alpha_1}{\partial t\partial\tau}\right) + RJ_a\frac{\partial^2 d_2}{\partial t^2}\\
&\quad + b_h\left(\frac{\partial h_3}{\partial t} + B\frac{\partial h_1}{\partial \tau}\right) + k_h h_3 = \hat{C}_{L,m_2,b+1,1+n_1} = \hat{C}_{L,7/3}.
\end{aligned} \tag{4.72}$$

From the Moment Equation

$$\begin{aligned}
O(\epsilon) &: R(x_0-a)\frac{\partial^2 h_1}{\partial t^2} - RI_a\frac{\partial^2 \alpha_1}{\partial t^2} - 2b_\alpha\frac{\partial \alpha_1}{\partial t} - 2k_\alpha\alpha_1 - 2\sin t = \hat{C}_{M,1},\\
O(\epsilon^{5/3}) &: R(x_0-a)\frac{\partial^2 h_2}{\partial t^2} - RI_a\frac{\partial^2 \alpha_2}{\partial t^2} + RJ_d\frac{\partial^2 d_1}{\partial t^2} - 2b_\alpha\frac{\partial \alpha_2}{\partial t} - 2k_\alpha\alpha_2 = \hat{C}_{M,m_1} = \hat{C}_{M,5/3},\\
O(\epsilon^{7/3}) &: R(x_0-a)\left(\frac{\partial^2 h_3}{\partial t^2} + 2B\frac{\partial^2 h_1}{\partial t\partial\tau}\right) - RI_a\left(\frac{\partial^2 \alpha_3}{\partial t^2} + 2B\frac{\partial^2 \alpha_1}{\partial t\partial\tau}\right) + RJ_d\frac{\partial^2 d_2}{\partial t^2}\\
&\quad - 2b_\alpha\left(\frac{\partial \alpha_3}{\partial t} + B\frac{\partial \alpha_1}{\partial \tau}\right) - 2k_\alpha\alpha_3 = \hat{C}_{M,m_2,b+1,1+n_1} = \hat{C}_{M,7/3}.
\end{aligned} \tag{4.73}$$

From the Flexural Deflection Equation

$$\begin{aligned}
O(\epsilon) &: RI_a\frac{\partial^2 h_1}{\partial t^2} - RI_d\frac{\partial^2 \alpha_1}{\partial t^2} + \frac{a^2+1/3}{3(1-a)^2}S_1 d_1 = \hat{C}_{F,1},\\
O(\epsilon^{5/3}) &: RI_a\frac{\partial^2 h_2}{\partial t^2} - RI_d\frac{\partial^2 \alpha_2}{\partial t^2} + RK_d\frac{\partial^2 d_1}{\partial t^2} + \frac{a^2+1/3}{3(1-a)^2}S_1 d_2 = \hat{C}_{F,m_1} = \hat{C}_{F,5/3},\\
O(\epsilon^{7/3}) &: RI_a\left(\frac{\partial^2 h_3}{\partial t^2} + 2B\frac{\partial^2 h_1}{\partial t\partial\tau}\right) - RI_d\left(\frac{\partial^2 \alpha_3}{\partial t^2} + 2B\frac{\partial^2 \alpha_1}{\partial t\partial\tau}\right) + RK_d\frac{\partial^2 d_2}{\partial t^2}\\
&\quad + \frac{a^2+1/3}{3(1-a)^2}S_1 d_3 = \hat{C}_{F,m_2,b+1,1+n_1} = \hat{C}_{F,7/3}.
\end{aligned} \tag{4.74}$$

Finally, from the Thrust Equation

$$\begin{aligned}
O(\epsilon^{4/3}) &: R'\frac{\partial u_1}{\partial t} = \hat{C}_{T,1} = 0 \to u_1 = u_1(\tau),\\
O(\epsilon^{2}) &: R'\frac{\partial u_2}{\partial t} = \hat{C}_{T,2},\\
O(\epsilon^{8/3}) &: R'\left(\frac{\partial u_3}{\partial t} + B\frac{\partial u_1}{\partial \tau}\right) + Liu_1^2 = \hat{C}_{T,1+m_1,2+n_1/2} = \hat{C}_{T,8/3}.
\end{aligned} \tag{4.75}$$

4.4.2 Analysis of the lowest order in the lift, moment, and flexural deflection equations

Analyzing the lowest order in the lift, moment, and flexural deflection equations, one gets the three following expressions, which are independent of u:

$$\begin{cases} (R+1)\dfrac{\partial^2 h_1}{\partial t^2} + [R(a-x_0)+a]\dfrac{\partial^2 \alpha_1}{\partial t^2} + b_h \dfrac{\partial h_1}{\partial t} + k_h h_1 = 0, \\ [R(x_0-a)-a]\dfrac{\partial^2 h_1}{\partial t^2} - \left[RI_a + \left(a^2+\dfrac{1}{8}\right)\right]\dfrac{\partial^2 \alpha_1}{\partial t^2} - 2b_\alpha \dfrac{\partial \alpha_1}{\partial t} - 2k_\alpha \alpha_1 = 2\sin(t), \\ \left[RI_a + \left(a^2+\dfrac{1}{4}\right)\right]\dfrac{\partial^2 h_1}{\partial t^2} + \left[a\left(a^2+\dfrac{1}{2}\right) - RI_d\right]\dfrac{\partial^2 \alpha_1}{\partial t^2} + \left(\dfrac{a^2+1/3}{3(1-a)^2}S_1\right) d_1 = 0. \end{cases} \tag{4.76}$$

This system of three linear equations for h_1, α_1, and d_1 has a homogeneous solution that contains transient terms of the form $e^{\lambda_1 t}$ and a particular solution for the term $2e^{it}$, such as $h_1 = h_{1H} + h_{1P}$, $\alpha_1 = \alpha_{1H} + \alpha_{1P}$, and $d_1 = d_{1H} + d_{1P}$. However, if we look at the flexural deflection equation, we can note that this equation can be solved independently and a solution for $d_1(t)$ can be obtained in terms of $h_1(t) = H_1 \sin(t+\phi_{h1})$ and $\alpha_1(t) = A_1 \sin(t+\phi_{a1})$. Thus,

$$d_1 = \frac{\left[RI_a + \left(a^2+\dfrac{1}{4}\right)\right] H_1 \sin(t+\phi_{h1}) + \left[a\left(a^2+\dfrac{1}{2}\right) - RI_d\right] A_1 \sin(t+\phi_{a1})}{\left(\dfrac{a^2+1/3}{3(1-a)^2}\right) S_1}. \tag{4.77}$$

Taking

$$a_h = \frac{\left[RI_a + \left(a^2+\dfrac{1}{4}\right)\right] H_1}{\left(\dfrac{a^2+1/3}{3(1-a)^2}\right) S_1}, \quad a_a = \frac{\left[a\left(a^2+\dfrac{1}{2}\right) - RI_d\right] A_1}{\left(\dfrac{a^2+1/3}{3(1-a)^2}\right) S_1}, \tag{4.78}$$

and performing some calculus, the solution for d_1 can be written as

$$d_1 = D_1 \sin(t+\phi_{d1}), \tag{4.79}$$

where

$$D_1 = \sqrt{a_h^2 + a_a^2 + 2a_h a_a \cos(\phi_{h1} - \phi_{a1})}, \quad \phi_{d1} = \arctan\left(\frac{a_h \sin\phi_{h1} + a_a \sin\phi_{a1}}{a_h \cos\phi_{h1} + a_a \cos\phi_{a1}}\right). \tag{4.80}$$

Consequently, the system in the lowest order will be reduced to only two linear equations for h_1 and α_1. This system of equations turns out to be the same as the one for the rigid foil case, which was adequately solved in Section 3.4.2 of Chapter 3.

Therefore, the final solutions for h, α, and d are

$$\begin{aligned} h(t,\tau) &\sim \epsilon H_1 \sin(t+\phi_{h1}) + \cdots, \\ \alpha(t,\tau) &\sim \epsilon A_1 \sin(t+\phi_{a1}) + \cdots, \\ d(t,\tau) &\sim \epsilon^{5/3} D_1 \sin(t+\phi_{d1}) + \cdots, \end{aligned} \tag{4.81}$$

being

$$\begin{aligned} H_1 &= \sqrt{\Re(\mathcal{H}_1)^2 + \Im(\mathcal{H}_1)^2}, \quad \phi_{h1} = \arctan\left(\frac{\Im(\mathcal{H}_1)}{\Re(\mathcal{H}_1)}\right), \\ A_1 &= \sqrt{\Re(\mathcal{A}_1)^2 + \Im(\mathcal{A}_1)^2}, \quad \phi_{a1} = \arctan\left(\frac{\Im(\mathcal{A}_1)}{\Re(\mathcal{A}_1)}\right), \end{aligned} \tag{4.82}$$

where $\Im$ means the imaginary part. On the other hand, $\mathcal{H}_1$ and $\mathcal{A}_1$ are the complex values that can be obtained by solving the matrix system resulting from the particular solution in the lowest order for the rigid foil case (see Section 3.4.2 of Chapter 3 for more details).

Resonant values

Since h and α coincide with those for a rigid foil at the lowest order, so does the resonant value of the torsional spring constant $k_{\alpha r}$ for each value of the translational spring constant k_h (see Section 3.4.2 of Chapter 3 for a more detailed explanation):

$$k_{\alpha r} = \frac{1}{2}\left\{ RI_a + a^2 + \frac{1}{8} + \frac{[R(a-x_0)+a]^2}{k_h - 1 - R} \right\}. \tag{4.83}$$

4.4.3 Analysis of the first orders in the thrust equation

Once we have the analytical values for h_1, α_1, and d_1, we can pay attention to the thrust equation and analyze the different orders to obtain an analytical expression for u.

Analysis of order ϵ^2

The resulting expression for the order ϵ^2 in the thrust equation is the same as the one from the rigid foil case, which is

$$R' \frac{\partial u_2}{\partial t} = \alpha_1 \frac{\partial^2 h_1}{\partial t^2} + a \frac{\partial^2 \alpha_1}{\partial t^2} + \frac{\partial \alpha_1}{\partial t}\frac{\partial h_1}{\partial t} + a\left(\frac{\partial \alpha_1}{\partial t}\right)^2, \tag{4.84}$$

whose solution, the oscillatory part of the swimming velocity, is

$$u_2(t,\tau) = \frac{A_1}{2R'}\{H_1 \sin(2t+\phi_{h1}+\phi_{a1}) + aA_1 \sin[2(t+\phi_{a1})]\} + U_2(\tau), \quad \text{with } U_2(0) = 0. \tag{4.85}$$

Remember that the function $U_2(\tau)$ has to be obtained from the order $\epsilon^{10/3}$. However, we are only interested in the lowest-order dependence of the swimming velocity on τ, $u_1(\tau)$, to which $U_2(\tau)$ is a small correction.

Analysis of order $\epsilon^{8/3}$

The resulting expression for the order $\epsilon^{8/3}$ in the thrust equation is

$$\begin{aligned} R'\left(\frac{\partial u_3}{\partial t}+B\frac{\partial u_1}{\partial \tau}\right)+Liu_1^2 = \Bigg\{ & C_0+H_1A_2\cos(2t+\phi_{h1}+\phi_{a2})+A_1H_2\cos(2t+\phi_{a1}+\phi_{h2}) \\ & +2aH_1D_1\cos(2t+\phi_{h1}+\phi_{d1})-\frac{H_1D_1}{2}\sin(2t+\phi_{h1}+\phi_{d1}) \\ & +\left(5a^2+\frac{3}{4}-A_{l2}\right)\frac{A_1D_1}{2}\cos(2t+\phi_{a1}+\phi_{d1})+\left(\frac{1}{2}-a\right)\frac{A_1D_1}{2}\sin(2t+\phi_{a1}+\phi_{d1}) \\ & +2aA_1A_2\cos(2t+\phi_{a1}+\phi_{a2})\Bigg\}+\frac{u^{1/2}}{\sqrt{\pi}}\Bigg\{C+\frac{H_1^2}{2}\cos[2(t+\phi_{h1})] \\ & +\left(a-\frac{1}{2}\right)(a-1)\frac{A_1^2}{2}\cos[2(t+\phi_{a1})]+\left(a-\frac{3}{4}\right)H_1A_1\cos(2t+\phi_{h1}+\phi_{a1})\Bigg\}, \end{aligned} \tag{4.86}$$

where

$$\begin{aligned} C_0 = \frac{1}{2}\Bigg\{ & A_1D_1\left[\left(a^2+\frac{1}{4}+A_{l2}\right)\cos(\phi_{a1}-\phi_{d1})+\left(a-\frac{1}{2}\right)\sin(\phi_{a1}-\phi_{d1})\right] \\ & -D_1H_1\sin(\phi_{d1}-\phi_{h1})\Bigg\}, \end{aligned} \tag{4.87}$$

$$C=\frac{H_1^2}{2}+\left(a-\frac{3}{4}\right)A_1H_1\cos(\phi_{a1}-\phi_{h1})+\left(a-\frac{1}{2}\right)(a-1)\frac{A_1^2}{2}. \tag{4.88}$$

To avoid secular terms in the timescale t, we have the freedom within the two-scales perturbation method (Kevorkian and Cole [1981]) to select the equation for $u_1(\tau)$ that cancels the non-oscillatory terms. Therefore, we select

$$R'B\frac{\partial u_1}{\partial \tau}+Liu_1^2=C_0+\frac{Cu_1^{1/2}}{\sqrt{\pi}}, \tag{4.89}$$

$$\begin{aligned} R'\frac{\partial u_3}{\partial t} = \Bigg\{ & H_1A_2\cos(2t+\phi_{h1}+\phi_{a2})+A_1H_2\cos(2t+\phi_{a1}+\phi_{h2}) \\ & +2aH_1D_1\cos(2t+\phi_{h1}+\phi_{d1})-\frac{H_1D_1}{2}\sin(2t+\phi_{h1}+\phi_{d1}) \\ & +\left(5a^2+\frac{3}{4}-A_{l2}\right)\frac{A_1D_1}{2}\cos(2t+\phi_{a1}+\phi_{d1})+\left(\frac{1}{2}-a\right)\frac{A_1D_1}{2}\sin(2t+\phi_{a1}+\phi_{d1}) \\ & +2aA_1A_2\cos(2t+\phi_{a1}+\phi_{a2})\Bigg\}+\frac{u^{1/2}}{\sqrt{\pi}}\Bigg\{\frac{H_1^2}{2}\cos[2(t+\phi_{h1})] \\ & +\left(a-\frac{1}{2}\right)(a-1)\frac{A_1^2}{2}\cos[2(t+\phi_{a1})]+\left(a-\frac{3}{4}\right)H_1A_1\cos(2t+\phi_{h1}+\phi_{a1})\Bigg\}. \end{aligned} \tag{4.90}$$

Equation (4.90) can easily be integrated to obtain explicitly u_3, except for an arbitrary function of τ. However, $u_1(\tau)$ and $u_2(t)$ would be enough since we are mostly interested in the lowest-order solution for u in terms of the slow time τ and the fast time t. Working with Equation (4.89), we can find the analytical expression for $u_1(\tau)$. To that end, it is useful to define $u_1(\tau) = U_1 w_1(\tau)$ and substitute that into the equation. Thus, we get

$$R' B U_1 \frac{\partial w_1}{\partial \tau} + LiU_1^2 w_1^2 = C_0 + \frac{C U_1^{1/2} w_1^{1/2}}{\sqrt{\pi}}, \tag{4.91}$$

and considering that $w_1(\tau \to \infty) \to 1$, we can obtain the following algebraic equation for the solution of U_1

$$LiU_1^2 - \frac{C U_1^{1/2}}{\sqrt{\pi}} - C_0 = 0. \tag{4.92}$$

Substituting this expression into the Equation (4.91) to eliminate C_0, we get

$$R' B U_1 \frac{\partial w_1}{\partial \tau} + LiU_1^2 (w_1^2 - 1) = \frac{C U_1^{1/2}}{\sqrt{\pi}} (w_1^{1/2} - 1), \tag{4.93}$$

then selecting $B = \dfrac{LiU_1}{R'}$, we obtain the non-dimensional equation for the first order of the velocity

$$\frac{\partial w_1}{\partial \tau} = C^* \left(w_1^{1/2} - 1 \right) + 1 - w_1^2, \qquad \text{with} \quad C^* = \frac{C}{\sqrt{\pi} LiU_1^{3/2}}. \tag{4.94}$$

Notice that in the rigid-foil case, U_1 is such that $C^* = 1$. On the other hand, Equation (4.94) can be easily solved numerically with some initial condition, e.g., $w_1(0) = 0$. The solution always satisfies $w_1(\infty) = 1$, so that the lowest-order non-dimensional swimming velocity is $u \sim \epsilon^{4/3} U_1$. An explicit, analytical solution of Equation (4.94) in the form $\tau = F(w_1; C^*)$ can be found, but the function F is so involved that it has no advantage whatsoever over the numerical solution. On the contrary, for the rigid-foil case (with $C^* = 1$), F was much simpler (see Chapter 3). Now, one has to solve the algebraic nonlinear Equation (4.92) numerically. To that end, it is convenient to start the iteration procedure from the first correction to the rigid-foil value when $C_0 \to 0$. The procedure is the following. We assume a seed to obtain U_1 such as $U_1 \approx U_{1r}(1 + \xi)$, where U_{1r} is the rigid-foil value of U_1 that makes $C^* = 1$ and ξ is a small parameter. Thus, from Equation (4.92), we get

$$LiU_{1r}^2 (1 + \xi)^2 - \frac{C U_{1r}^{1/2}}{\sqrt{\pi}} (1 + \xi)^{1/2} - C_0 = 0. \tag{4.95}$$

From Chapter 3, we know that $U_{1r} = \left(\dfrac{C}{\sqrt{\pi} Li} \right)^{2/3}$, so the previous equation yields to

$$(1 + \xi)^2 - (1 + \xi)^{1/2} - \frac{\sqrt{\pi} C_0}{C U_{1r}^{1/2}} = 0, \tag{4.96}$$

and developing the potential terms, it can be found that

$$\xi = \frac{2\sqrt{\pi} C_0}{3 C U_{1r}^{1/2}}. \tag{4.97}$$

Therefore, the final seed needed to obtain the value for U_1 that assures the correct physical solution of Equation (4.92), which tends to the rigid-foil solution when $S \to \infty$, is

$$U_1 \approx U_{1r}\left(1 + \frac{2\sqrt{\pi}C_0}{3CU_{1r}^{1/2}}\right), \qquad \text{with} \quad C_0 \ll CU_{1r}^{1/2}. \tag{4.98}$$

Hence, the final solution for u is

$$u(t,\tau) \sim \epsilon^{4/3}U_1\omega_1(\tau) + \frac{\epsilon^2 A_1}{2R'}\{H_1\sin(2t+\phi_{h1}+\phi_{a1}) + aA_1\sin[2(t+\phi_{a1})] + \cdots, \quad \text{with} \quad \tau = \epsilon^{4/3}Bt. \tag{4.99}$$

4.4.4 Performance parameters from lowest-order asymptotic solution

In addition to the mean swimming velocity $U \sim \epsilon^{4/3}U_1$, one can compute the other performance parameters, defined at the beginning of the chapter, at their lowest order. The power input will be

$$\hat{C}_{Pi} \sim \hat{C}_{Pi1} = -2\epsilon^2 A_1\cos(t+\phi_{a1})\sin t, \tag{4.100}$$

and its time average,

$$\overline{\hat{C}_{Pi1}} = \frac{1}{2\pi}\int_0^{2\pi} -2\epsilon^2 A_1\cos(t'+\phi_{a1})\sin t' dt' = \epsilon^2 A_1\sin\phi_{a1}. \tag{4.101}$$

The efficiency at this lowest order of the asymptotic solution can be written as

$$\eta \sim \frac{LiU^3}{\overline{\hat{C}_{Pi1}}} = \frac{Li\epsilon^4 U_1^3}{\epsilon^2 A_1\sin\phi_{a1}} = \frac{\epsilon^2 LiU_1^3}{A_1\sin\phi_{a1}}. \tag{4.102}$$

The cost of transport at the lowest order

$$CoT \sim \frac{\overline{\hat{C}_{Pi1}}}{U} = \frac{\epsilon^2 A_1\sin\phi_{a1}}{\epsilon^{4/3}U_1} = \frac{\epsilon^{2/3}A_1\sin\phi_{a1}}{U_1}. \tag{4.103}$$

Finally, the Strouhal number at the lowest order of the asymptotic solution

$$St = \frac{A}{2\pi U} \sim \frac{\epsilon^{-1/3}}{\pi U_1}\left[H_1 + (1+|a|)A_1 + \frac{1}{2}(1+|a|)^2\epsilon^{2/3}D_1\right]. \tag{4.104}$$

4.4.5 Comparison between analytical and numerical results

A comparison of the analytical lowest-order solutions for $u(t)$, $h(t)$, $\alpha(t)$, and $d(t)$ with the numerical results of the model Equations (4.15) to (4.17) and (4.22) can be seen in Figure 4.3 for the same case plotted in Figure 4.2 when $S = 1000$ and $S = 100$.

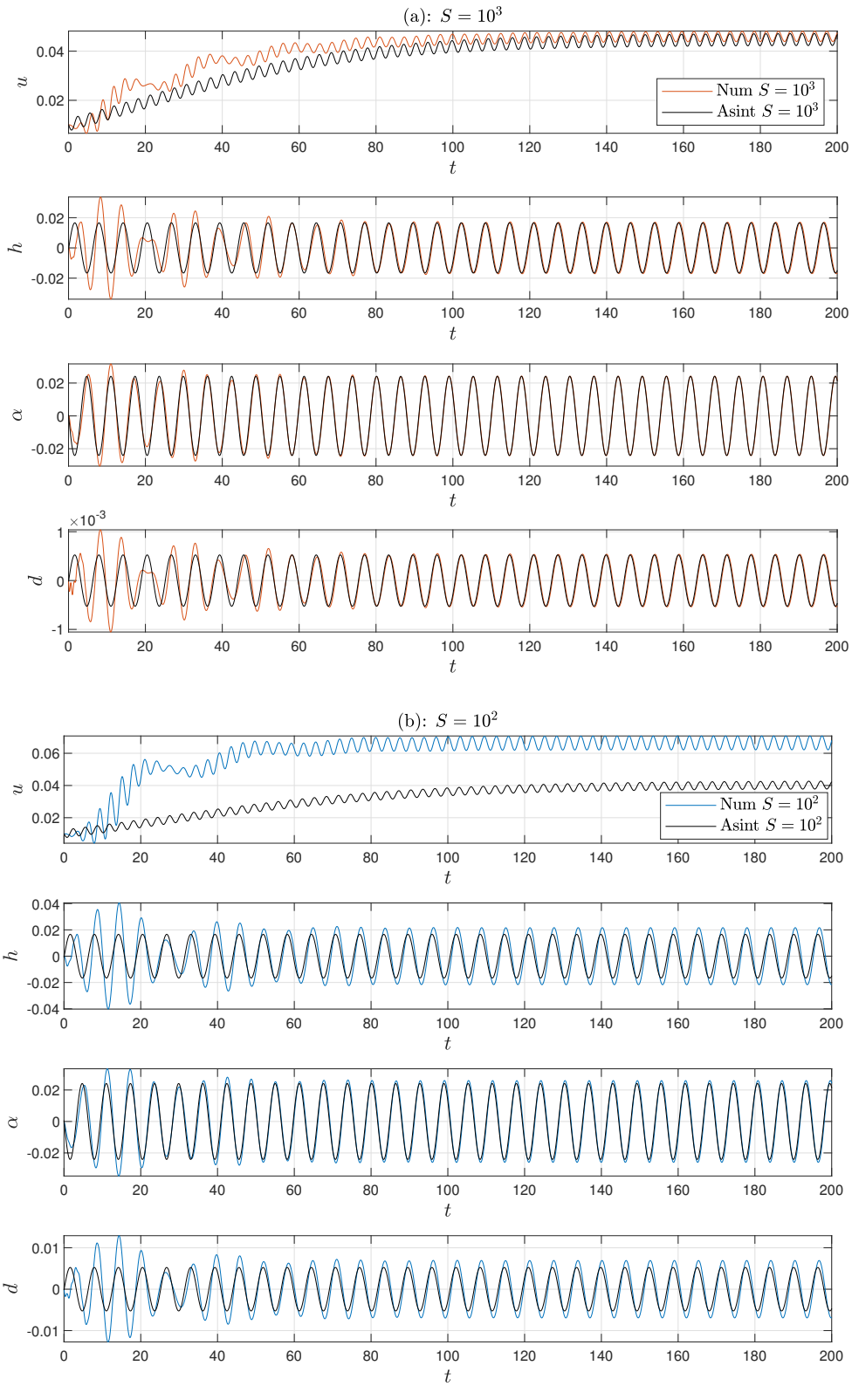

Figure 4.3: Comparison between the lowest-order asymptotic solution and the numerical solution for the same case plotted in Figure 4.2 when $S = 10^3$ (a) and $S = 10^2$ (b).

The asymptotic solution captures quite well the numerical solution for large S, becoming poorer as the stiffness ratio S decreases to 100 or below, particularly for the swimming velocity $u(t)$. It is due to the limitation of the asymptotic solution to $u \ll \epsilon$, a constraint not shared by the model equations (remember that $\epsilon = 0.05$ in the figure). However, the agreement between both solutions remains excellent for $h(t)$, $\alpha(t)$, and $d(t)$ even for $S = 100$ (and below), notably for the pitch angle α.

The disagreement for the swimming velocity increases as one approaches the resonant values of the spring constants k_h and k_α given by Equation (4.83), where the mean swimming velocity U reaches a pronounced maximum.

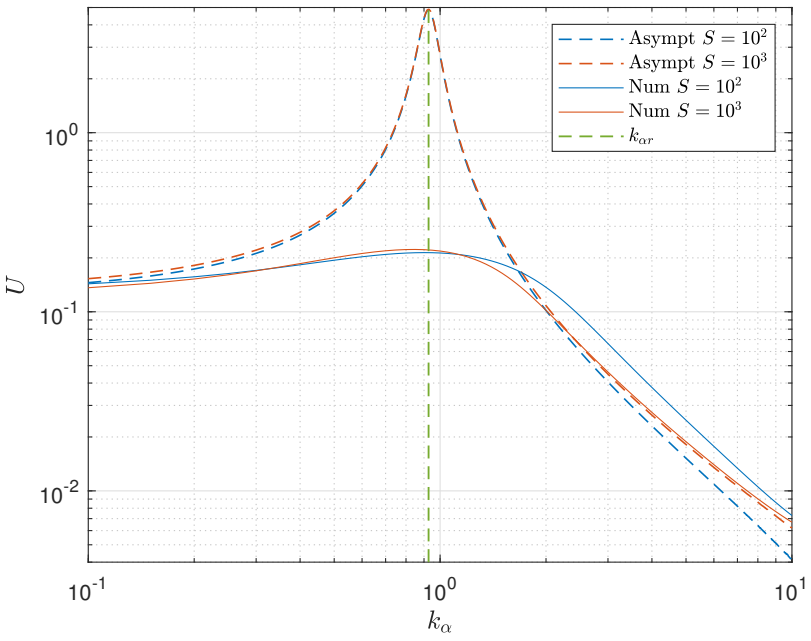

Figure 4.4: Evolution of U vs k_α for the same values of the parameters used in Figures 4.2 and 4.3, and for two values of S obtained from the lowest-order asymptotic solution (dashed lines) and the numerical solution of the model equations (continuous lines). The vertical dashed line corresponds to $k_{\alpha r}$ given by Equation 4.83.

On the other hand, Figure 4.4 compares the mean swimming velocity U obtained numerically from the model equations with the present lowest-order asymptotic solution as k_α is varied for the same values of the remaining parameters considered in Figures 4.2 and 4.3, and for stiffnesses $S = 10^3$ and $S = 10^2$. Near the resonant value ($k_{\alpha r} \simeq 0.927$ in the present case), the asymptotic solution greatly overestimates the mean swimming velocity, even for large S. Also, for $S = 100$, the velocity prediction of the asymptotic is poor even for large k_α for the reason explained above in relation to Figure 4.3. However, the lowest-order asymptotic solution correctly yields the scaling of U and, more importantly, accurately predicts the resonant values of the non-dimensional parameters for optimal propulsion performance. Thus, the present asymptotic solution will guide the search for optimal propulsion performance given in the following section, but using the numerical solution of the model equations for quantitative results close to the resonance of the system.

4.5 Optimal propulsion performance from numerical results

In this section, we look for the best propulsion performance as described by the numerical solution of the model equations and guided by the lowest-order asymptotic solution. To that end, we use a set of non-dimensional parameters appropriate for a small aquatic vehicle (or a large fish), varying mainly the stiffness parameter S, and also k_h, k_α, a, and Li. The fixed parameters are: $R = 0.02$, $R' = 0.2$, $x_0 = 0$, $b_h = b_\alpha = 0.05$, and $\epsilon = 0.05$. Note that although we select a small value of ϵ for the model assumptions to be valid, this does not restrict the analysis to a small actuating torque M_i since it is scaled with the frequency ω and the foil chord length c (see Equation (4.1)), being the actual torque also proportional to the span of the foil, so that it can be as large as desired by increasing the foil size and the actuating frequency, not being restricted to the propulsion of small aquatic vehicles.

According to the asymptotic results, the maxima of the swimming velocity are obtained for resonant values of k_α, $k_{\alpha r}(k_h, R, a, \cdots)$, which at the lowest order approximately coincide with the results for a rigid foil given by Equation (4.83). Actually, it was shown in Chapter 3 that the maximum swimming velocity for a rigid foil was reached for large k_h. In that case, according to $k_{\alpha r} \simeq (RI_a + a^2 + 1/8)/2$. Consequently, we select for these studies $k_h = 10$, large enough to reach the above asymptotic value of $k_{\alpha r}(k_h)$, and plot the performance parameters in Figure 4.5 in the $k_\alpha - S$ plane for $Li = 0.1$ and $a = -1$; i.e., for the pivot axis at the leading edge, for which $k_{\alpha r} \simeq 0.634$, shown with vertical dashed lines in Figure 4.5.

We observe in Figure 4.5(a) that the maximum swimming velocity (maximum thrust force) is reached close to this resonant value $k_{\alpha r}$ (at about $k_\alpha = 0.6$) and for a rigid foil; i.e., for $S \to \infty$. This result is in agreement with that previously found by Moore [2015], who showed that a torsional spring with a rigid foil is the optimal arrangement for thrust production in a fluid stream with fixed velocity. However, out of that resonance, for k_α larger than $k_{\alpha r}$, U increases as the stiffness S decreases, as already shown in the example of Figure 4.2. Actually, the swimming velocities reach local maxima for lower values of S corresponding to the first resonant mode S_r associated with the stiffness of the foil. For instance, for $k_\alpha = 5$, we find a local maximum of $U \simeq 0.012$ for $S_r \approx 106$, which roughly coincides with the first resonant frequency associated with the stiffness of the foil in the present non-dimensionalization (Floryan and Rowley [2018], Fernandez-Feria and Alaminos-Quesada [2021a]). In general, these local maxima of the swimming velocity are more than ten times smaller than the maxima of U for the first resonant mode associated with the torsional spring $k_\alpha = k_{\alpha r}$ when k_h is large. As found in previous models for an elastically mounted flexible foil in a fluid stream with fixed velocity, the resonances associated with the stiffness of the foil are eclipsed by the more efficient (from a thrust-producing point of view) resonance of the foil associated with its elastic support when the stiffness of the foil is high enough (Moore [2015], Fernandez-Feria and Alaminos-Quesada [2021b]).

Although the highest U is reached for a rigid foil with k_α very close to $k_{\alpha r}$, it is observed in Figure 4.5(c) that in the present self-propulsion problem, this configuration is also that

with the highest cost of transport CoT. Furthermore, the propulsive efficiency is not the maximum one, as it is shown in Figure 4.5(b). The highest propulsive efficiency is also reached close to this resonant value of the torsional spring constant $k_{\alpha r}$ but for flexible foils with S below 100. In the figure, η at $k_\alpha \simeq k_{\alpha r}$ increases from about 29.7% for $S \to \infty$ to about 35.1% for $S \approx 75$. At this value of S, the CoT is also significantly smaller than for a rigid foil (0.018 versus 0.024). Remarkably, this optimal performance around the resonant value of k_α corresponds to an almost constant value of the Strouhal number, about 0.32, in accordance with the range where many swimming and flying animals in many scales optimally cruise propelled by flapping fins and wings (Triantafyllou et al. [1993], Taylor et al. [2003]), including also fishes swimming by undulating their bodies at high enough Reynolds numbers (Eloy [2012], Gazzola et al. [2014], Saadat et al. [2017], Gross et al. [2021]), quite different from the present oscillatory swimming mode (it will be explained later in the chapter). With the present model, for $k_\alpha = k_{\alpha r}$, St in Figure 4.5(d) ranges from 0.328 as $S \to \infty$, to 0.317 for $S \approx 75$.

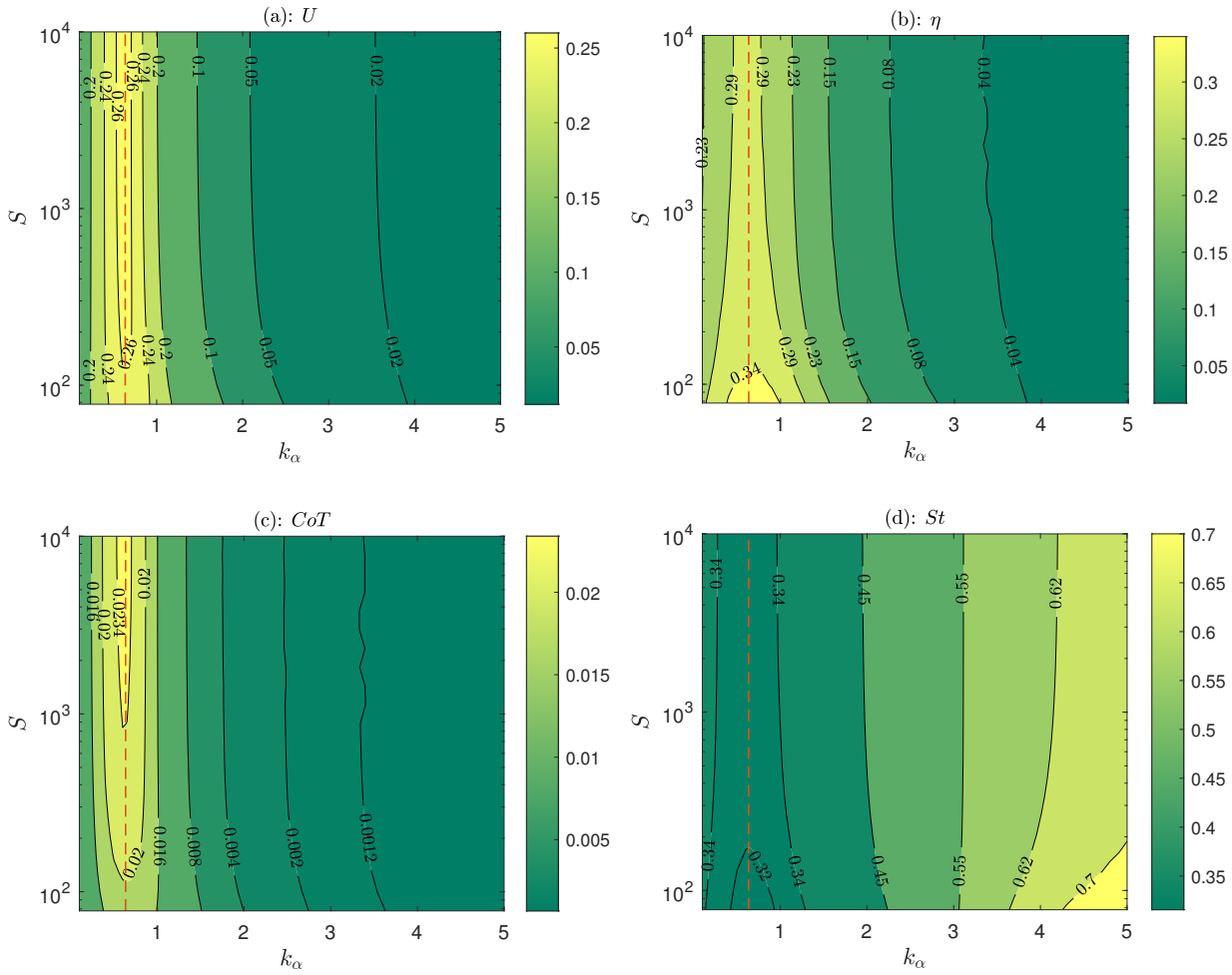

Figure 4.5: Contours of U (a), η (b), CoT (c) and St (d) in the (k_α, S) plane for $R = 0.02$, $R' = 0.2$, $x_0 = 0$, $b_h = b_\alpha = 0.05$, $\epsilon = 0.05$, $a = -1$, $Li = 0.1$ and $k_h = 10$. The vertical dashed lines correspond to $k_{\alpha r}$ given by Equation 4.83.

On the other hand, Figure 4.6 shows the propulsive performance as one moves the pivot axis downstream of the foil ($a > -1$) maintaining the resonant value $k_{\alpha r}$ (actually, Figure 4.6 is for $k_\alpha = 0.6$, where η is maximum for large S, very close to $k_{\alpha r}$). Figure 4.6(b) shows that the propulsive efficiency decreases but remains practically unchanged for the optimal efficiency case just discussed (S below 100) if $-1 \leq a \lesssim -0.9$. However, the maximum swimming velocity, with the highest cost of transport, is reached for $a \approx -0.9$ for a rigid foil, see Figure 4.6(a) and Figure 4.6(c). The Strouhal number remains practically unchanged for a near -1, as it is shown in Figure 4.6(d).

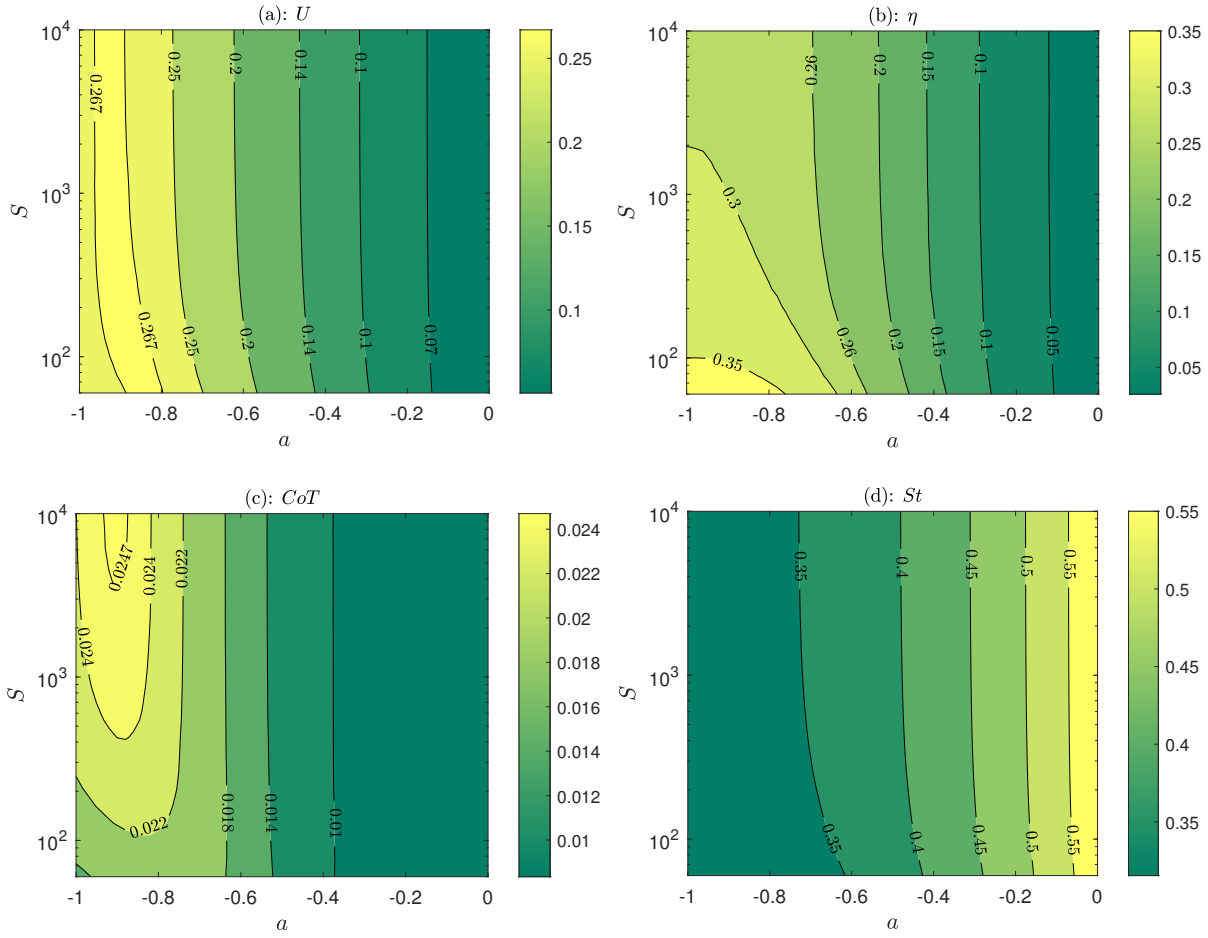

Figure 4.6: Contours of U (a), η (b), CoT (c) and St (d) in the (a, S) plane for $R = 0.02$, $R' = 0.2$, $x_0 = 0$, $b_h = b_\alpha = 0.05$, $\epsilon = 0.05$, $Li = 0.1$, $k_h = 10$ and $k_\alpha = 0.6$.

We have seen that the maximum of U is reached close to the resonant value of k_α for a rigid foil. However, this behavior depends on the vehicle's drag through Li, as shown in Figure 4.7, where contours of U divided by its rigid-foil counterpart U_{rigid} are plotted in the (Li, S) plane. In the case with $Li = 0.1$ considered in Figures 4.5 and 4.6, U/U_{rigid} decreases from unity as $S \to \infty$ about 0.95 for $S \approx 75$. However, for $Li < Li^*(S)$, where the $Li^*(S)$ contour is marked with 0 in Figure 4.7, the maximum of U at resonance increases slightly with the flexibility of the foil. Thus, for $Li = 0.005$, U/U_{rigid} increases from unity as $S \to \infty$ about 1.04 for $S \approx 75$.

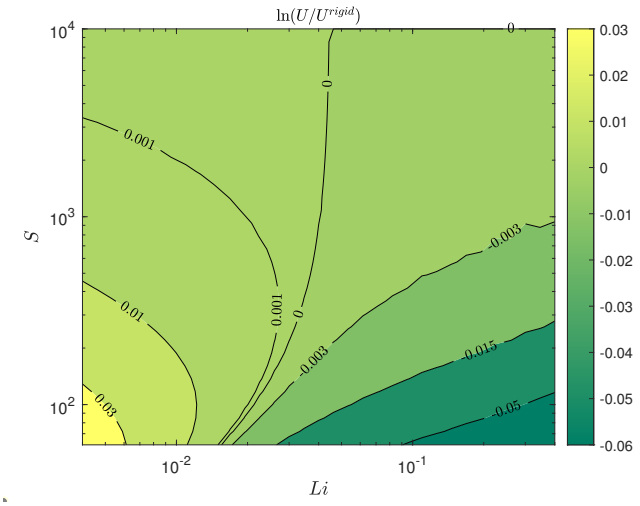

Figure 4.7: Contours of $\ln(U/U_{rigid})$ in the (Li, S) plane for $R = 0.02$, $R' = 0.2$, $x_0 = 0$, $b_h = b_\alpha = 0.05$, $\epsilon = 0.05$, $a = -1$, $k_h = 10$ and $k_\alpha = 0.6$.

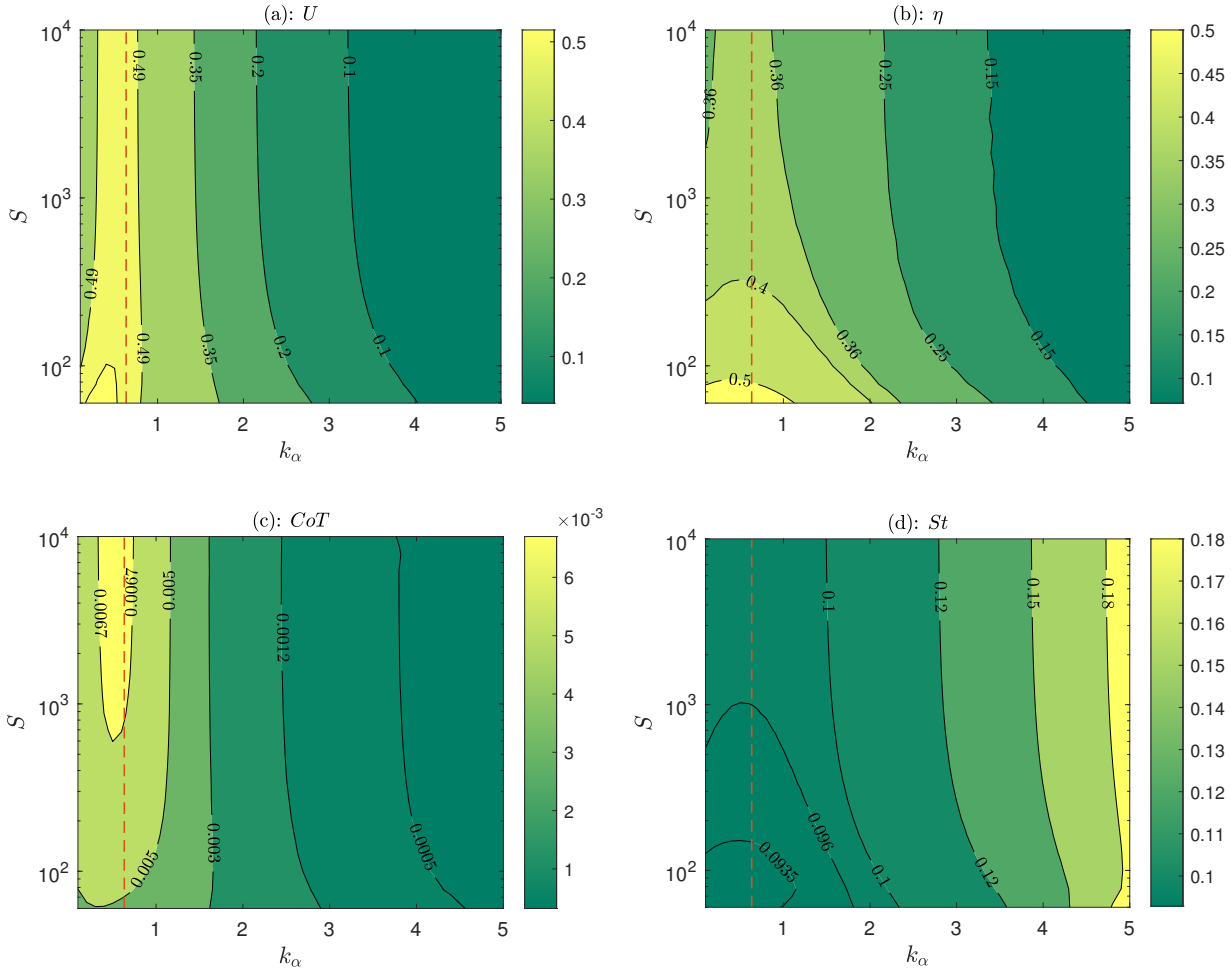

Figure 4.8: As in Figure 4.5, but for $Li = 0.01$.

To show this different behavior, Figure 4.8 reproduces the results of Figure 4.5 but for $Li = 0.01$. Now, the highest U is reached for a flexible foil with S below 10^2, see Figure 4.8(a), but still close to the resonant value $k_{\alpha r}$. For this Li, the highest efficiencies and CoT are also reached at these lower values of S when $k_\alpha \approx k_{\alpha r}$, see Figure 4.8(b) and Figure 4.8(c). However, the corresponding Strouhal numbers, shown in Figure 4.8(d), are significantly lower than those found in natural swimmers, an indication that this value of the Lighthill number is too low and difficult to achieve in nature.

4.5.1 Comparison with fish propulsion data

The expressions for the force components and moment from linearized potential-flow theory, which are coupled with the Euler-Bernoulli beam equation in the present self-propulsion model, have been amply validated against numerical simulation and experimental data in the case of rigid foils (Halfman [1952], Baik et al. [2012], Fernandez-Feria [2017], Fernandez-Feria and Sanmiguel-Rojas [2019], Alaminos-Quesada [2021]), surprisingly showing a good agreement even for not so small amplitude of the oscillations, and for flexible foils (Alaminos-Quesada and Fernandez-Feria [2020], Fernandez-Feria and Alaminos-Quesada [2021a], Sanmiguel-Rojas and Fernandez-Feria [2021]). In addition, this self-propulsion model with rigid foils has also been validated against high-fidelity numerical simulations in this thesis (see Chapters 2 and 3). However, numerical results about bodies self-propelled by flexible flapping foils elastically mounted have not been developed to our knowledge. For that reason, to assess the validity of the model, we compare in Figure 4.9 the results of the theory for the Strouhal number vs. the Lighthill number with experimental data for the swimming kinematics of several fishes compiled by Eloy [2012], and with theoretical results derived by this author.

Actually, Eloy's theoretical results, based on the elongated-body theory developed by Lighthill [1971], are for undulatory swimming, qualitatively and quantitatively very different from the oscillatory swimming mode based on oscillatory foils considered in the present model (Lighthill [1969], Smits [2019]). Consequently, we include in Figure 4.9 only the data for "scombrids" and "other fishes" compiled by Eloy [2012], which include several species of mackerels, tunas, bonitos, daces, and goldfishes, among others. These fishes are mostly propelled by the thrust produced by their caudal fin oscillatory motion, being negligible the thrust contribution by the body motion (Lighthill [1969], Smits [2019]). Incidentally, tunas are among the fastest and most efficient swimming fishes in sustained cruise (Lighthill [1969]), and precisely, they are endowed by nature with a long, almost rigid-fin tail, thus better approximating the assumptions of the present model. The other species considered in Figure 4.9, though all of them are mostly propelled by their caudal fin oscillatory motion, have more flexible caudal fins. This fact, together with the variable contribution of the body's undulatory motion to their propulsion, may explain part of the scattering in the experimental data. For the comparison in Figure 4.9, we use the Lighthill number defined by Eloy, Li^E, which is related to that defined in Equation (4.23) through $Li^E = (\pi c/s)Li$. Since the present theory is for two-dimensional foils, i.e., for large aspect ratio s/c, and it ranges from 4.5-10 in mackerels and tunas (Westneat and Wainwright [2001]), for simplicity, we have selected $s/c = 2\pi$ so that $Li^E = Li/2$. The Strouhal number defined in Equation (4.29) is the same

used by Eloy [2012].

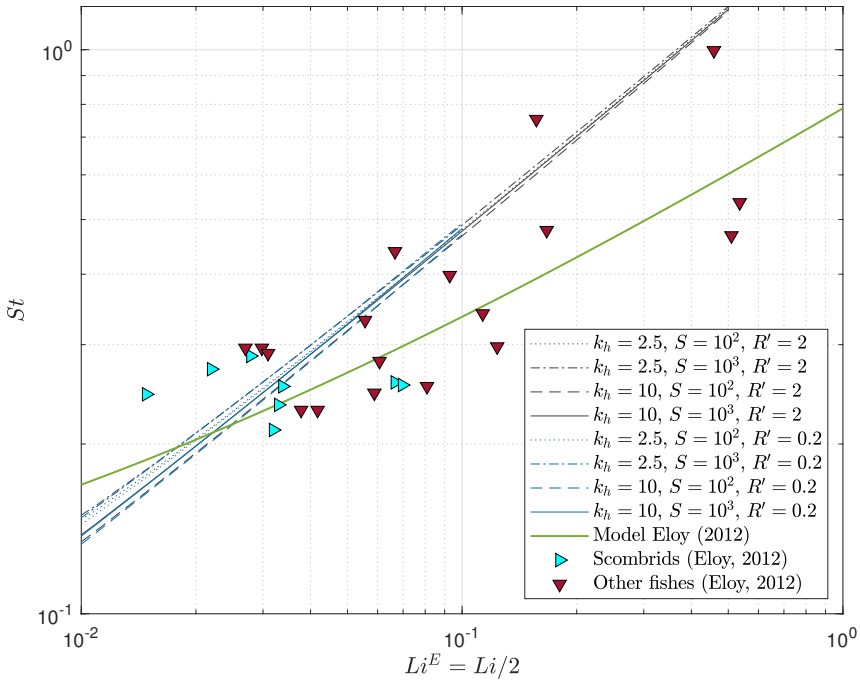

Figure 4.9: Strouhal number for maximum efficiency η as k_α is varied versus Lighthill number for several values of kh, S and R', as indicated in the legend. The green continuous line is Eloy [2012] model for undulating swimming, and the symbols are experimental data for several fishes, also presented in that study.

Therefore, we plot in Figure 4.9 the St resulting from the present model equations for translational spring constants $k_h = 2.5$ and 10, stiffness ratios $S = 10^3$ and 10^2, and vehicle's mass ratios $R' = 0.2$ and 2. Corresponding (for each value of Li) to the highest efficiency η when k_α is varied, which approximately is reached at the rigid-foil resonant value $k_{\alpha r}$, as discussed above. The remaining parameters are fixed to $R = 0.02$, $x_0 = 0$, $b_h = b_\alpha = 0.05$, $\epsilon = 0.05$, and $a = -1$. The results are almost independent of R', particularly for $Li \gtrsim 0.1$, despite the vehicle's mass disparity (note that, for $R = 0.02$, the value $R' = 0.2$ used in all previous figures roughly corresponds to a vehicle's mass ten times larger than that of its propeller, while $R' = 2$ corresponds to a vehicle about 100 times heavier than its propeller). Similar behavior is observed for the dependencies of St on k_h and S as Li is varied in such a way that for $Li \gtrsim 0.1$, the optimal Strouhal with the present oscillatory swimming model collapses to $St \approx 1.75 \left(Li^E\right)^{0.57} = 1.18 Li^{0.57}$. Consequently, this result should be compared with the power law obtained by Eloy from his undulatory swimming model, $St \approx 0.75 \left(Li^E\right)^{1/3}$, also shown in Figure 4.9. The scattering of the experimental data makes it difficult to decide which fits better, but it seems that the present model works slightly better for the thunniform swimmers, which are the scombrids in Figure 4.9 with lower Li, i.e., for typical swimmers where the primary mechanism for producing thrust is a prominent caudal fin.

Complementing last figure, Figure 4.10 shows the values of η, k_α, U, and CoT corresponding to the model curves plotted in Figure 4.9 for $R' = 2$ (for $R' = 0.2$ the results practically coincide). The optimal efficiencies are reached for k_α close to $k_{\alpha r}$, as shown in Figure 4.10(b), and obviously η increases as Li decreases, i.e., as the drag decreases. On the other hand, η may reach values higher than 50% when k_h is large (i.e., $k_h = 10$ in the figure) and $S = 100$, but for Li lower than about 0.01, too small to be achieved in nature as observed in Figure 4.9. For all values of Li, the optimal η increases, and the corresponding CoT decreases as the stiffness S decreases for a given k_h, see Figure 4.10(a) and (c). However, the swimming velocity U increases slightly with the stiffness S at these resonant values of k_α, except for very low and unrealistic values of Li as it is shown in Figure 4.10(c).

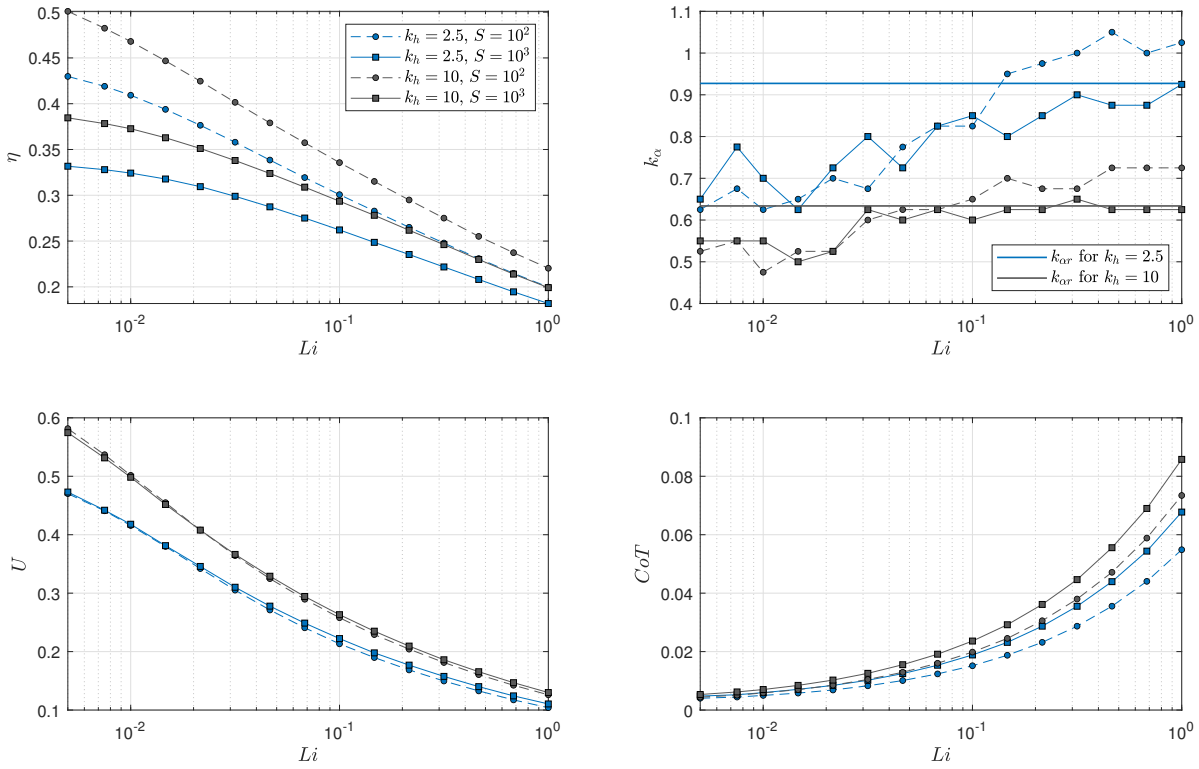

Figure 4.10: Optimal efficiencies η (a) and corresponding values of k_α (b), U (c) and CoT (d) vs Li for the $St - Li$ curves plotted in Figure 4.9 for $R' = 2$. Also shown in (b) with thicker lines are the corresponding values of $k_{\alpha r}$ for each k_h.

4.6 Concluding remarks

In this chapter, we have developed a simple model for the locomotion of an aquatic vehicle self-propelled by a flexible foil elastically supported and actuated by an oscillatory torque, which is used to gain insight into the optimal propulsion conditions. Particularly, the conditions for which the flexibility of the foil enhances the propulsive and cruising performance. The model is based on linear potential-flow theory coupled with the structural Euler-Bernoulli beam equation, valid for small amplitudes of the passive pitching, heaving, and flexural motions of the foil that propels a vehicle modeled by a constant drag coefficient and an independent mass.

An analytical perturbation solution, additionally limited to very small non-dimensional swimming velocities, guides the search for optimal propulsion solutions of the four ordinary differential equations resulting from the model as the non-dimensional parameters governing the problem are varied, for a given actuating torque amplitude non-dimensionalized with the actuating frequency, fluid density, and foil chord length. The main parameters are the stiffness and mass ratio of the foil, S and R, longitudinal and torsional springs constants, k_h and k_α, vehicle's mass ratio and Lighthill (drag) number, R' and Li, and center of mass and pivot axis locations, x_0 and a. It is found that the maxima of thrust and swimming velocity are achieved at, or very close to, a resonant combination of k_α and k_h given by a simple analytical expression in terms of R, a, and x_0 only, in the limit of a rigid foil ($S \to \infty$) for Lighthill numbers common in fishes, and when the foil is actuated at, or near, the leading edge ($a = -1$). More particularly, the maximum of the swimming velocity U occurs when k_h is sufficiently large and the resonant $k_{\alpha r}$ for $a = -1$ depends only on R. Unfortunately, this maximum of the swimming velocity is associated with a maximum of the cost of transport. However, the highest propulsive efficiencies, which are also reached for k_α close to $k_{\alpha r}$, increase as the stiffness S decreases, this being the main beneficial effect of the foil flexibility coupling with its elastic support on the propulsive performance according to the model. These results for optimal efficiency η are observed in the Lighthill number range of most fishes whose primary mechanism for producing thrust is a prominent oscillatory caudal fin, $0.02 \lesssim Li \lesssim 0.2$, almost independently of the remaining parameters, with a corresponding Strouhal number lying in a narrow range around 0.32, in agreement with many experimental data on the optimal cruise swimming of these fishes. As Li decreases, U and η increases and CoT decreases, reaching for $Li \approx 0.02$ a propulsive efficiency close to 45%. Below this Li, the swimming velocity U may become slightly larger for a flexible foil than for its rigid counterpart, and the efficiency predicted by the model becomes larger than 50%. However, so low values of Li are not reached even by the most efficient fishes in sustained cruise.

In summary, the following design guidelines follow from the present model results.

- First and obviously, for optimal cruising performance one has to minimize the Lighthill number by reducing the vehicle's drag coefficient C_D as much as possible.

- Then one has to fix a sufficiently large (non-dimensional) longitudinal spring constant k_h and a non-dimensional torsional spring constant k_α close to its resonant value $k_{\alpha r}$, which for large k_h only depends on R and a. The pivot point location has to be selected

close to the leading edge ($a \to -1$) for best performance, and R is selected from the foil geometry and density.

- Selecting the frequency of the movement ω and the foil dimensions c and s (with $s/c \gg 1$), one may obatain the dimensional counterparts of k_h and k_α, which are $\tilde{k}_h = (\pi\rho s c^2\omega^2)k_h/4$ and $\tilde{k}_\alpha = (\pi\rho s c^4\omega^2)k_\alpha/8$, and the necessary amplitude of the actuating torque, $A_M = (\pi\rho c^4\omega^2)\epsilon/8$ for any given $\epsilon \ll 1$.

- Finally, one may select the stiffness of the foil, actually the combination of Young's modulus and foil thickness $E\gamma^3$ entering in the dimensionless stiffness S, to achieve either maximum cruising speed or efficiency, or both. For relatively low values of the Lighthill number, in this study is found that maximum cruising speed U, but with high cost of transport, is achieved with a rigid foil ($S \gtrsim 10^3$, would be enough according to the present results). In contrast, maximum cruising efficiency η would be obtained for $S \lesssim 10^2$. An intermediate value of S can be fine-tuned with the model for best global performance.

To better illustrate these results, we show a practical example here as it was conducted in Chapter 3. Thus, taking $c = 0.3$ m, $s = 1$ m, $\rho_s = 2\rho$, and $R = 0.02$ in water, which corresponds to a foil thickness $\gamma \simeq 2.4$ mm, assumed constant so that $x_0 = 0$. The pivot axis is selected at the leading edge ($a = -1$) to maximize the propulsive performance. With these values, the selected $R' = 0.2$ corresponds to a small vehicle's mass of about 14 kg, and $Li = 0.1$ to a vehicle's surface $A_w \simeq 0.094/C_D$ m^2. The value $\epsilon = 0.05$ has been selected small for the model to be valid. Therefore, with the above foil dimensions in water, the results of Table 4.1 can be obtained for a chosen frequency of $\tilde{f} = 1$ Hz by selecting the values for the optimal propulsive efficiency analyzed in this chapter, which for that case are $k_\alpha \simeq 0.6$, $k_h = 10$, and $b_h \simeq b_\alpha \simeq 0$. It results in dimensional longitudinal and torsional springs of $\tilde{k}_h = 28$ KN/m and $\tilde{k}_\alpha = 75$ Nm, and an amplitude for the input torque of $A_M = 6.26$ Nm.

$\boldsymbol{S}$	η [%]	$\widetilde{U}$ [m/s]	$\widetilde{CoT}$ [KJ/km]	E [GPa]
75	36.20	0.2401	7.68	27
$\mathbf{10^3}$	30.21	0.2489	9.83	359

Table 4.1: Practical example for the designing parameters of an efficient self-propelled aquatic vehicle. Using $c = 0.3$ m, $s = 1$ m, $\rho_s = 2\rho$, $R = 0.02$, $x_0 = 0$, $a = -1$, $R' = 0.2$ ($m' \simeq 14$ kg), $Li = 0.1$, $k_\alpha = 0.6$, $k_h = 10$, $b_\alpha \simeq b_h \simeq 0$, and $\epsilon = 0.05$. A frequency of 1 Hz is used for the example.

The above results yield a difference in the maximum cruising speed of 3.54% in favor of the more rigid foil. In contrast, a difference in efficiency of 6% and a cost of transport reduction of 21.87% are obtained for the more flexible foil.

Chapter 5

An experimental investigation on the flapping-foil turbine

5.1 Introduction

Before starting this chapter, I have to greatly thank Alberto Jiménez Rodríguez since he was the first person in charge of this experimental investigation. Without his previous work, this chapter and all the results obtained here would not have been possible. Not only did he design and construct the whole turbine prototype, but he also provided me with assistance during the final investigation process. For those reasons, I would like to mention and emphasize his generous help at the beginning of this chapter.

In recent years, the use of oscillating foils for hydrokinetic energy harvesting has been greatly studied (Xiao and Zhu [2014], Young et al. [2014], Picard-Deland et al. [2019]). It has shown promising results and shortly may overcome some of the limitations of established renewable energy technologies related to cost-effectiveness and intermittency energy supply. These systems mainly consist of a foil that undergoes periodic translating and rotating motions in an incoming flow, and they have been demonstrated to reach energy extraction efficiencies that are close to or even exceed their traditional rotary counterparts (Kinsey et al. [2011], Kinsey and Dumas [2012, 2014], Xiao and Zhu [2014], Young et al. [2014]). These oscillating systems are particularly well-suited for shallow and wide flow channels since their rectangular cross-sections can harvest large portions of the flow. So, they are very interesting options for energy extraction on rivers or tidal currents.

Designers have approached the matter from several perspectives. At first, they mechanically coupled and constrained the two motions through complex mechanisms, hence making the turbine a single-degree-of-freedom (1-DOF) device (McKinney and DeLaurier [1981], Kinsey et al. [2011], Xu et al. [2017]). This approach allowed prescribing the amplitudes and the frequencies of the heaving and pitching motions as well as the phase lag between them. However, some issues could arise from this complexity, e.g., a significant amount of energy could be lost before being converted into electricity, especially due to the friction between the different moving components (Kinsey et al. [2011]). Another approach was performed

using an independent actuator for the pitching motion (Kim et al. [2017]), making the concept a two-degree-of-freedom (2-DOF) turbine. Such a 2-DOF turbine does not necessitate rigid mechanical links to couple the heaving and the pitching motions. However, it needs a dedicated actuator for the pitching motion, controllers for both degrees of freedom, and an electric generator connected to the heaving motion. Moreover, the electric generator of such a turbine may need to act as an actuator at some instants during the turbine blade cycle in order to prescribe the desired heaving motion. Therefore, this motion-constrained strategy still results in a relatively complex apparatus. Several authors proposed a simplification to the aforementioned 2-DOF version of the flapping-foil turbine by considering a free or passive heaving motion involving a blade that is elastically supported in heave instead of being connected to the turbine structure with rigid links (Shimizu et al. [2008], Zhu and Peng [2009], Zhu et al. [2009], Abiru and Yoshitake [2011, 2012], Huxham et al. [2012], Wu et al. [2014, 2015], Deng et al. [2015], Sitorus et al. [2016], Derakhshandeh et al. [2016], Griffith et al. [2016], Teng et al. [2016], Zhan et al. [2017]). However, both an actuator and a controller are still needed to prescribe the pitching motion.

More recently, a fully-passive turbine prototype was developed by Boudreau et al. [2018] based on the work of Veilleux and Dumas [2017] that was first proposed by Peng and Zhu [2009]. The concept involves a foil that is elastically mounted in pitch and heave. The design relies on a divergence instability to start and sustain the motion, and on non-linearities in the flow (dynamic stall) to limit the amplitudes, resulting in self-sustained, limit-cycle oscillations. This prototype was used as the basis of the current study. In addition, other studies also considered the dependence of the dynamic behavior of a fully-passive flapping foil on the combination of its structural parameters and provided insight into the underlying fluid–structure interactions (Duarte et al. [2019, 2021a,b]).

For all these reasons, in the final chapter of this thesis, we are interested in an experimental approach to energy extraction with this fully-passive flapping-foil turbine concept. Thus, taking as reference the work performed by Boudreau et al. [2018] and using the prototype that we already have in the Aerohydrodynamics Laboratory at the University of Málaga, we will perform our investigation.

5.2 Formulation of the problem

As we mentioned in the introduction above, in this chapter, we develop and study a fully-passive flapping-foil turbine concept as it was described in the work performed by Boudreau et al. [2018]. It consists of a rigid foil elastically supported by springs in heave and pitch as well as by a damper in heave (see Figure 5.1). This damper in heave is used to model the energy sink that would result from the energy conversion into electricity by an electric generator. The foil is free in both pitching motion $\tilde{\alpha}(\tilde{t})$ (around a pitch axis located at a distance $\tilde{a}$ from the center of the foil) and heaving motion $\tilde{h}(\tilde{t})$ (in the $\tilde{y}$-direction). The motions are restricted to these two degrees of freedom (DOF), and gravity acts in $\tilde{z}$-direction, hence playing no role in the foil dynamics.

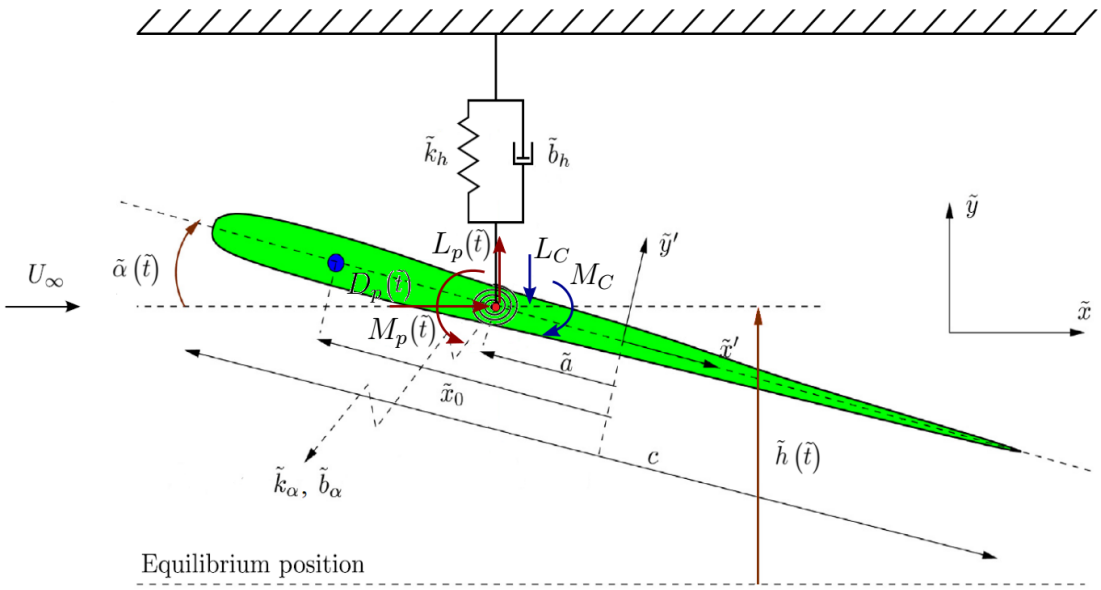

Figure 5.1: Sketch of the fully-passive flapping-foil turbine concept (dimensional quantities).

In this study, no pitch damper is explicitly used. However, due to the inherent presence of friction in a real experimental setup, some undesired viscous pitch damping is inevitably present and must be considered. It will be named as $\tilde{b}_{\alpha v}$ and represents the linear pitch damping constant of the pitch bearings. The same happens for the heaving motion, where some viscous heave damping also appears. It will be named $\tilde{b}_{hv}$ and represents the linear heave damping constant of the heave bearings. Furthermore, some Coulomb friction (dry friction) appears in both heave and pitch motions, so L_C represents the Coulomb friction force component in the heave direction and M_C the Coulomb friction moment about the pitch axis. As a result, the total linear heave damping $\tilde{b}_h$ is the sum of the linear heave damping constant of the eddy-current brake (desired energy sink) $\tilde{b}_{he}$, which corresponds to the energy that could be converted into electricity, and the viscous damping stemming from the additional undesired friction in heave $\tilde{b}_{hv}$

$$\tilde{b}_h = \tilde{b}_{he} + \tilde{b}_{hv}, \tag{5.1}$$

while the total linear pitch damping $\tilde{b}_\alpha$ simply corresponds to the undesired viscous damping in pitch

$$\tilde{b}_\alpha = \tilde{b}_{\alpha v}. \tag{5.2}$$

Thus, taking reference of the formulation depicted in Boudreau et al. [2018] and the sign conventions for $\tilde{\alpha}(\tilde{t})$ and $M(\tilde{t})$ (the moment is defined counterclockwise while $\tilde{\alpha}$ increases clockwise to follow the usual convention in aerodynamics), the motion of the rigid foil is approximately governed by 2D dynamic equations, which in dimensional form can be written as

$$\widetilde{m}_h \ddot{\tilde{h}} + \widetilde{\Omega}\left(\dot{\tilde{\alpha}}^2 \sin\tilde{\alpha} - \ddot{\tilde{\alpha}}\cos\tilde{\alpha}\right) = L - \tilde{b}_h\dot{\tilde{h}} - \tilde{k}_h\tilde{h} - L_C - L_p, \tag{5.3}$$

$$\widetilde{\Omega}\left(\dot{\tilde{\alpha}}^2 \cos\tilde{\alpha} + \ddot{\tilde{\alpha}}\sin\tilde{\alpha}\right) = D - D_p, \tag{5.4}$$

$$\widetilde{\Omega}\ddot{\tilde{h}}\cos\tilde{\alpha} - \tilde{I}_a\ddot{\tilde{\alpha}} = M + \tilde{b}_\alpha\dot{\tilde{\alpha}} + \tilde{k}_\alpha\tilde{\alpha} - M_C - M_p, \tag{5.5}$$

where $\widetilde{m}_h$ is the sum of the mass of the foil and the structure that enables its movement (heaving mass), $\widetilde{\Omega}$ is the static moment, estimated as the mass of the components only undergoing the pitching motion times the distance between the pitch axis and the center of mass of each of those components, $\tilde{I}_a$ is the moment of inertia about the pitch axis, $\tilde{k}_h$ is the heave stiffness constant, $\tilde{k}_\alpha$ is the pitch stiffness constant, L and D are the hydrodynamic force component in the $\tilde{y}$ and $\tilde{x}$ direction, respectively, and M is the hydrodynamic moment about the pitch axis. In addition, L_p is the force at the pivot axis in the $\tilde{y}$-direction that generates the heaving motion $\tilde{h}(\tilde{t})$, while D_p is the force reaction in the $\tilde{x}$-direction needed to keep the pivot axis fixed and M_p is the necessary torque to generate the pitching motion $\tilde{\alpha}(\tilde{t})$.

On the other hand, the static moment is related to other parameters through

$$\widetilde{\Omega} = \widetilde{m}_\alpha \left(\tilde{x}_0 - \tilde{a}\right), \tag{5.6}$$

where $\tilde{a}$ and $\tilde{x}_0$ are the distance to the pivot axis and the center of mass, respectively, and $\widetilde{m}_\alpha$ the mass of the components only undergoing the pitching motion. Remember that a *tilde* is used to remark that the variable is in the dimensional form to distinguish it from its dimensionless counterpart, and a *dot* denotes differentiation with respect to dimensional time.

5.2.1 Non-dimensional formulation

In order to work in non-dimensional variables, the lengths will be scaled with semi-chord length $c/2$ and the time with the freestream velocity U_∞, so the main non-dimensional variables of the problem will be

$$\begin{gathered} x = \frac{\tilde{x}}{c/2}, \quad y = \frac{\tilde{y}}{c/2}, \quad z = \frac{\tilde{z}}{c/2}, \quad t = \frac{\tilde{t}U_\infty}{c/2}, \\ h = \frac{\tilde{h}}{c/2}, \quad \dot{h} = \frac{\dot{\tilde{h}}}{U_\infty}, \quad \ddot{h} = \frac{\ddot{\tilde{h}}c/2}{U_\infty^2}, \quad \alpha = \tilde{\alpha}, \quad \dot{\alpha} = \frac{\dot{\tilde{\alpha}}c/2}{U_\infty}, \quad \ddot{\alpha} = \frac{\ddot{\tilde{\alpha}}(c/2)^2}{U_\infty^2}. \end{gathered} \tag{5.7}$$

Taking that into account, the governing equations of the problem in dimensionless format will be

$$m_h\ddot{h} + \Omega\left(\dot{\alpha}^2\sin\alpha - \ddot{\alpha}\cos\alpha\right) = C_L - b_h\dot{h} - k_h h - C_{L_C} - C_{L_p}, \tag{5.8}$$

$$\Omega\left(\ddot{\alpha}\sin\alpha + \dot{\alpha}^2\cos\alpha\right) = C_D - C_{D_p}, \tag{5.9}$$

$$\Omega\ddot{h}\cos\alpha - I_a\ddot{\alpha} = 2\left(C_M + b_\alpha\dot{\alpha} + k_\alpha\alpha - C_{M_C} - C_{M_p}\right). \tag{5.10}$$

Notice that now the *dot* is used to denote a derivative with respect to the dimensionless time t. In addition, it is important to remark that the three non-linear governing equations are coupled via the terms involving the static moment Ω. Nevertheless, the coupling terms only play a role when the static moment is not zero, i.e., when the center of mass does not coincide with the pitch axis. On the other hand, the dimensionless coefficients associated with the fluid force components and moment are

$$C_L = \frac{2L}{\rho U_\infty^2 cs}, \quad C_{L_C} = \frac{2L_C}{\rho U_\infty^2 cs}, \quad C_{L_p} = \frac{2L_p}{\rho U_\infty^2 cs},$$
$$C_D = \frac{2D}{\rho U_\infty^2 cs}, \quad C_{D_p} = \frac{2D_p}{\rho U_\infty^2 cs}, \tag{5.11}$$
$$C_M = \frac{2M}{\rho U_\infty^2 c^2 s}, \quad C_{M_C} = \frac{2M_C}{\rho U_\infty^2 c^2 s}, \quad C_{M_p} = \frac{2M_p}{\rho U_\infty^2 c^2 s},$$

where ρ is the fluid density (water in this case), and s is the length span of the foil. For a static foil, these coefficients are equal to their fluid force and moment coefficients counterparts, which are also analyzed in Section D.2.6 of Appendix D. The dimensional dry (or Coulomb) friction force and the dry friction moment, following Boudreau et al. [2018], can be written as

$$L_C = \tilde{f}_C \cdot \text{sign}(\dot{\tilde{h}}), \quad M_C = -\widetilde{m}_C \cdot \text{sign}(\dot{\tilde{\alpha}}), \tag{5.12}$$

where the dimensional constants $\tilde{f}_C$ and $\widetilde{m}_C$ for the present experimental setup are also characterized in Section D.2.2 and D.2.3 of Appendix D. The three non-dimensional parameters on the left-hand side of Equations (5.8) to (5.10) are related to their dimensional counterparts through the following equations

$$m_h = \frac{4\widetilde{m}_h}{\rho c^2 s}, \quad I_a = \frac{16\tilde{I}_a}{\rho c^4 s}, \quad \Omega = \frac{8\widetilde{\Omega}}{\rho c^3 s}. \tag{5.13}$$

Finally, the dimensionless spring and damper constants are defined as

$$k_h = \frac{\tilde{k}_h}{\rho U_\infty^2 s}, \quad b_h = \frac{2\tilde{b}_h}{\rho U_\infty cs}, \quad k_\alpha = \frac{2\tilde{k}_\alpha}{\rho U_\infty^2 c^2 s}, \quad b_\alpha = \frac{4\tilde{b}_\alpha}{\rho U_\infty c^3 s}. \tag{5.14}$$

Therefore, for a given flow, nine structural parameters determine the turbine dynamics, which are m_h, I_a, Ω, b_h, b_α, k_h, k_α, f_C, and m_C. In addition, the position of the pitch axis $a = 2\tilde{a}/c$ has to be considered for a total of ten governing structural parameters.

5.2.2 Performance parameters

In this chapter, we are mainly interested in the experimental study of the aeroelastic instability boundaries as the values of k_h and b_h are varied for given values of the remaining non-dimensional parameters. Then, for some values of these parameters, we analyze the energy-harvesting performance of the system in terms of the power transfer between the fluid and the elastically mounted foil and the vortex dynamics.

The power extraction performance is characterized by the effective power recovered through the linear damper

$$C_{P_e} = b_{he}\dot{h}^2. \tag{5.15}$$

This quantity will be compared with the total power transferred from the fluid to the pitching and heaving foil, which in dimensionless form is given by

$$C_P = \dot{h}C_L - 2\dot{\alpha}C_M. \tag{5.16}$$

To compute this last quantity from the experimental results and compare with Equation (5.15), we shall compute from experimental data every term in Equation (5.8) multiplied by $\dot{h}$, and every term in Equation (5.10) multiplied by $-\dot{\alpha}$. To simplify the formulation, we define the following additional power coefficients

$$C_{P_{hR}} = \dot{h}\left[m_h\ddot{h} + \Omega\left(\dot{\alpha}^2\sin\alpha - \ddot{\alpha}\cos\alpha\right)\right], \quad C_{P_{\alpha R}} = -\dot{\alpha}\left(\Omega\ddot{h}\cos\alpha - I_a\ddot{\alpha}\right), \tag{5.17}$$

$$C_{P_R} = C_{P_{hR}} + C_{P_{\alpha R}}, \tag{5.18}$$

$$C_{P_{hb}} = b_h\dot{h}^2 = C_{P_e} + b_{hv}\dot{h}^2, \quad C_{P_{\alpha b}} = 2b_{\alpha v}\dot{\alpha}^2, \quad C_{P_b} = C_{P_{hb}} + C_{P_{\alpha b}}, \tag{5.19}$$

$$C_{P_{hk}} = k_h\dot{h}h, \quad C_{P_{\alpha k}} = 2k_\alpha\dot{\alpha}\alpha, \quad C_{P_k} = C_{P_{hk}} + C_{P_{\alpha k}}, \tag{5.20}$$

$$C_{P_{hC}} = \dot{h}C_{L_C}, \quad C_{P_{\alpha C}} = -2\dot{\alpha}C_{M_C}, \quad C_{P_C} = C_{P_{hC}} + C_{P_{\alpha C}}, \tag{5.21}$$

$$C_{P_{hp}} = \dot{h}C_{L_p}, \quad C_{P_{\alpha p}} = -2\dot{\alpha}C_{M_p}, \quad C_{P_p} = C_{P_{hp}} + C_{P_{\alpha p}}. \tag{5.22}$$

Thus, the fluid power coefficient is given by

$$C_P = C_{P_R} + C_{P_b} + C_{P_k} + C_{P_C} + C_{P_p}, \tag{5.23}$$

where the last term C_{P_p} is the power coefficient resulting directly from the force and torque measurements at the pivot axis, C_{L_p}, and C_{M_p}. The remaining terms on the right-hand side are, respectively, the contributions from the heave and pitch inertia (subscript R), from the linear and torsional dampers (subscript b), from the linear and torsional springs (subscript k), and from the linear and rotational Coulomb frictions (subscript C). Of all these terms, the effective power extracted through the linear damper C_{P_e} is just a fraction of $C_{P_{hb}}$.

In addition to the instantaneous performance quantities, one is interested in the cycle-averaged ones. For any non-dimensional quantity $Z(t)$, we define the corresponding cycle average over the cycle number j as

$$\overline{Z}_j = f_j\int_{t_j}^{t_j+1/f_j} Z(t)dt, \tag{5.24}$$

where

$$f_j = \frac{c}{2T_jU_\infty}, \tag{5.25}$$

is the non-dimensional frequency associated to the period T_j of the j-th cycle, as defined by the measured heaving motion $h(t)$. We shall also use the related reduced frequency $k_j = 2\pi f_j$, more commonly used in unsteady aerodynamics. The global performance will be characterized by averages over a sufficiently large number N of cycles (typically, we use $N = 90$ except otherwise specified), thus for a general variable Z

$$\overline{Z} = \frac{1}{N}\sum_{j=1}^{N} Z_j. \tag{5.26}$$

On the other hand, we are also interested in the phase lag between the heaving and the pitching motions ϕ, and the amplitudes in heave h_0 and pitch α_0, all of them in non-dimensional form. These metrics are defined as

$$\phi_j = \frac{360}{T_j}\left(\tilde{t}_{\alpha_{\max,j}} - \tilde{t}_{h_{\max,j}}\right) \text{ [deg.]}, \quad h_{0,j} = \frac{\tilde{h}_{\max,j} - \tilde{h}_{\min,j}}{c/2}, \quad \alpha_{0,j} = \frac{\tilde{\alpha}_{\max,j} - \tilde{\alpha}_{\min,j}}{2}, \tag{5.27}$$

where the subscripts max and min represent the extreme positions reached during a given turbine blade oscillation for each parameter, and $\tilde{t}_{\alpha\,\max}$ and $\tilde{t}_{h\,\max}$ are the instants at which these extreme positions are reached for $\tilde{\alpha}$ and $\tilde{h}$, respectively. Of particular relevance are the mean values of the lift, drag, and momentum coefficients. Also, the energy efficiencies based on the fluid power and the effective power, defined as

$$\eta_{f,j} = \overline{C_{P,j}}\frac{c}{d_j}, \qquad \eta_{e,j} = \overline{C_{P_e,j}}\frac{c}{d_j}, \tag{5.28}$$

where d_j is the largest possible total distance swept by any portion of the foil in the j-th cycle (Kinsey and Dumas [2008]). Their averages over N cycles are denoted by $\bar{\phi}$, $\bar{h}_0$, $\bar{\alpha}_0$, $\overline{C_L}$, $\overline{C_D}$, $\overline{C_M}$, $\overline{C_{P_e}}$, $\overline{C_P}$, $\bar{\eta}_f$ and $\bar{\eta}_e$, respectively. The corresponding non-dimensional averaged frequency is denoted by $\bar{f}$ or $\bar{k} = 2\pi\bar{f}$, although the motion would not be, in general, strictly harmonic. Finally, the Reynolds number Re at which the experiments are carried out is defined by

$$Re = \frac{U_\infty c}{\nu}, \tag{5.29}$$

with ν the kinematic viscosity.

5.2.3 Harmonic motion

For a purely harmonic motion, e.g., $h(t) = h_0\cos(kt)$ and $\alpha(t) = \alpha_s + \alpha_0\cos(kt-\phi)$, it is clear that $\overline{C_{P_k}} = \overline{C_{P_{hk}}} + \overline{C_{P_{\alpha k}}} = 0$. Though not so evident, the inertial contribution also vanishes, $\overline{C_{P_R}} = \overline{C_{P_{hR}}} + \overline{C_{P_{\alpha R}}} = 0$, despite the fact that the separate contributions from heave and pitch, $\overline{C_{P_{hR}}}$ and $\overline{C_{P_{\alpha R}}}$, are not necessarily zero (Fernandez-Feria [2023]). Thus, for a general harmonic motion, the time-averaged Equation (5.23) reads

$$\overline{C_P} = \overline{C_{P_e}} + b_{hv}\overline{\dot{h}^2} + 2b_{\alpha v}\overline{\dot{\alpha}^2} + \overline{C_{P_C}} + \overline{C_{P_p}}, \tag{5.30}$$

so that the mean power transferred from the fluid to the foil is equal to the effective mean power transmitted to the linear damping $\overline{C_{P_e}}$ plus the mean power measured through the force/torque sensor $\overline{C_{P_p}}$, plus friction losses in the linear and pitch bearings and from Coulomb friction. For the above harmonic motion, these friction losses are

$$b_{hv}\overline{\dot{h}^2} + 2b_{\alpha v}\overline{\dot{\alpha}^2} + \overline{C_{P_C}} = \frac{k^2}{2}\left(b_{hv}h_0^2 + 2b_{\alpha v}\alpha_0^2\right) + 2\frac{k}{\pi}(f_C h_0 + 2m_C\alpha_0). \tag{5.31}$$

If the motion is not harmonic, there would be additional (presumably small) contributions from the springs and from the inertia of the foil. The characterization of these last contributions, which may either enhance or reduce the energy harvesting performance, is one of the objectives of the present work.

5.3 Methodology

5.3.1 Experimental setup

The experiments are conducted in the water channel at the University of Málaga Aerohydrodynamics Laboratory. This water channel has a cross-section of 0.5 m by 0.5 m and a length of 4 m. In addition, two powerful hydraulic bombs are used to provide a constant income velocity in the flow. On the other hand, the fully-passive flapping-foil turbine prototype is composed of non-moving components, i.e, the external structure that is attached to the water channel and contains the linear guided roller bearings that guide the movement of the prototype, components only undergoing the heaving motion, i.e, the carriage that holds the foil and which is moved along the bearings in the heave direction, and components undergoing both the heaving and the pitching motions, i.e., the blade and the connecting shaft which are rotating at the same time that are moving with the carriage in the heave direction. This prototype is installed in the middle of the water channel where the flow is perfectly constant. A 3D model of the turbine prototype is shown in Figure 5.2 to understand better all the parts and components involved.

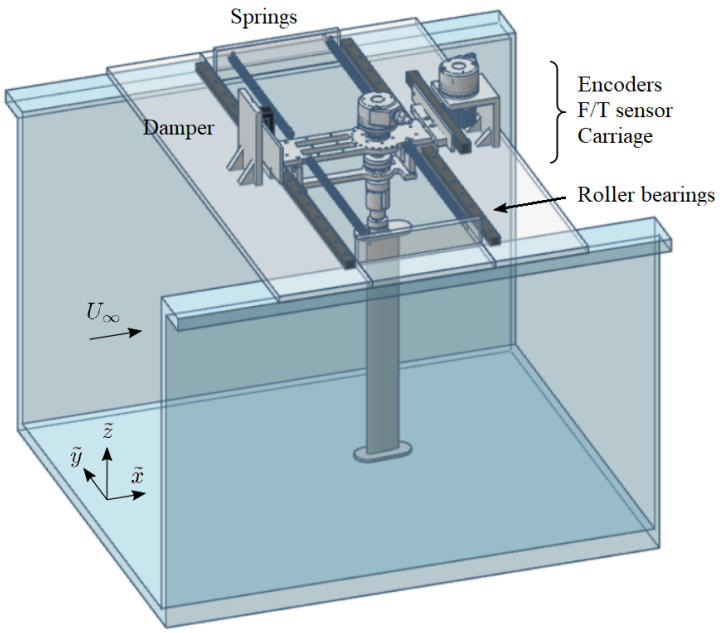

Figure 5.2: A 3D model of the turbine prototype showing all the components involved.

Moreover, the cross-section of the foil corresponds to a symmetric NACA0015 profile with a chord length of $c = 50$ mm and with the pitch axis located at a distance $\tilde{a} = -c/5$ from the center of the foil. In order to minimize the tip losses, end plates are placed at both ends of the blade, and the distance between the free extremity of the blade and the channel floor is set to a minimal gap of 5 mm. The blade span length is $s = 0.385$ m, and the water level was set to 0.43 m at rest. As a result, the blade, the end plates, and a fraction of the shaft holding the foil are submerged during the tests, while all the other components are located above water.

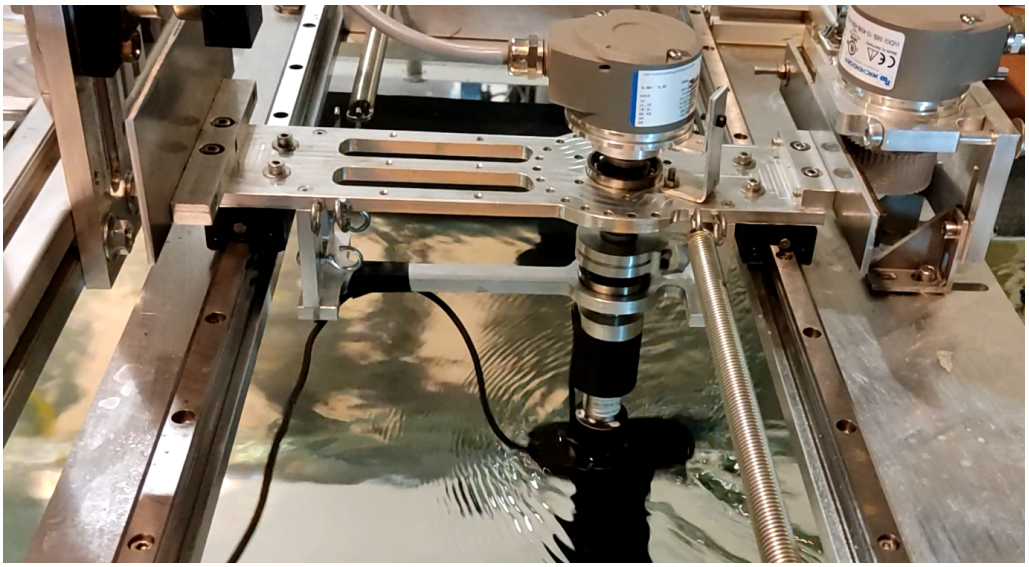

(a) $h = 0$ and $\alpha = 0^o$ (equilibrium position).

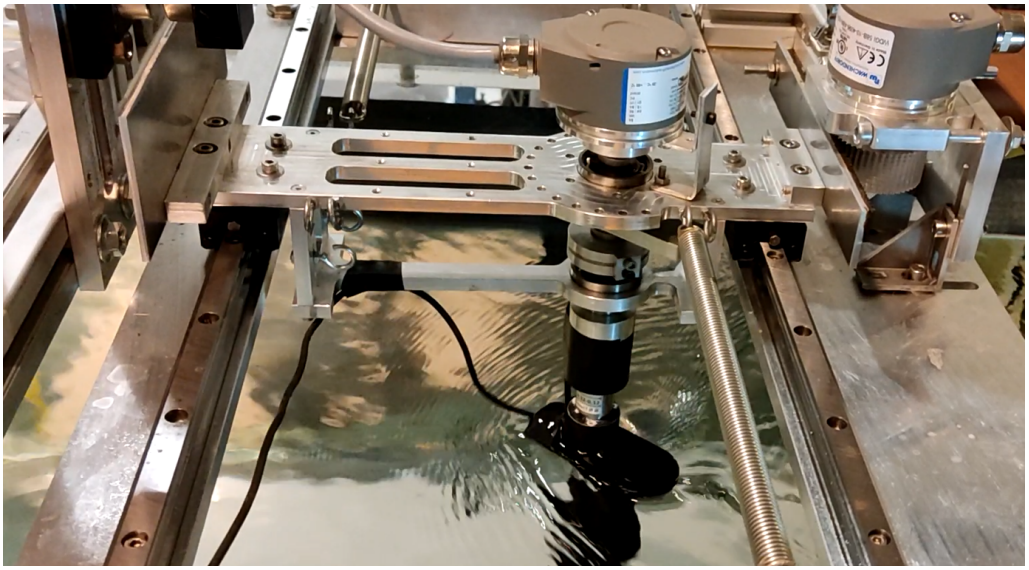

(b) $h \neq 0$ and $\alpha \neq 0^o$.

Figure 5.3: Top view of the fully-passive flapping-foil turbine prototype with the blade at two different positions during a given test in the water channel. The water is flowing from left to right in the perpendicular direction to the heaving motion.

The fully-passive flapping-foil turbine prototype presented in this chapter was designed taking as a reference the work performed by Boudreau et al. [2018] that was previously inspired by Veilleux and Dumas [2017], adapting the measurements and the components to our water channel. However, in our prototype, we are only able to vary the heave damping $\tilde{b}_{he}$ and the heave and pitch stiffness $\tilde{k}_h$ and $\tilde{k}_\alpha$, while the inertial properties, namely the heaving mass $\widetilde{m}_h$, the moment of inertia about the pitch axis $\tilde{I}_a$ and the static moment $\widetilde{\Omega}$ will remain the same for all the tests performed. As an improvement to Boudreau et al. [2018] experimental set up, we include a force/torque sensor to measure the force and moment

components synchronously with the pitch and heave motions. In Figure 5.3, we can see two images showing some positions of the developed prototype working during a test.

5.3.2 Measurements protocols

Except otherwise specified, we set a water free stream velocity $U_\infty = 0.37 \pm 0.02$ m/s in the reported results so that the Reynolds number based on the chord length is about 22200. In each experimental run, we initially hold the foil at its equilibrium position, with the blade aligned with the incoming flow. After waiting a sufficient amount of time for the flow to be stable, the foil is released. The blade positions in heave and pitch are recorded at a sampling frequency of 5000 Hz during 120 s, which allows us to record more than a hundred foil oscillations, with two rotary encoders (WachendorffWDGI 58B) generating 4096 pulses per revolution. The digital signals provided by each encoder are converted into analog signals (0-5 V) and then are sampled with a NI USB-6210 data-acquisition board connected to a computer. A LabVIEW code is also used to process the information. In order to obtain the heaving position of the blade, a timing belt pulley is fixed to the shaft of the heave encoder. It is in contact with a timing belt glued to an aluminum plate undergoing the heaving motion, as shown in Figure 5.4, which allows us to transform the registered heaving encoder information into the heaving displacement of the foil. The foil velocity and acceleration components in heave and pitch are computed using second-order central difference schemes.

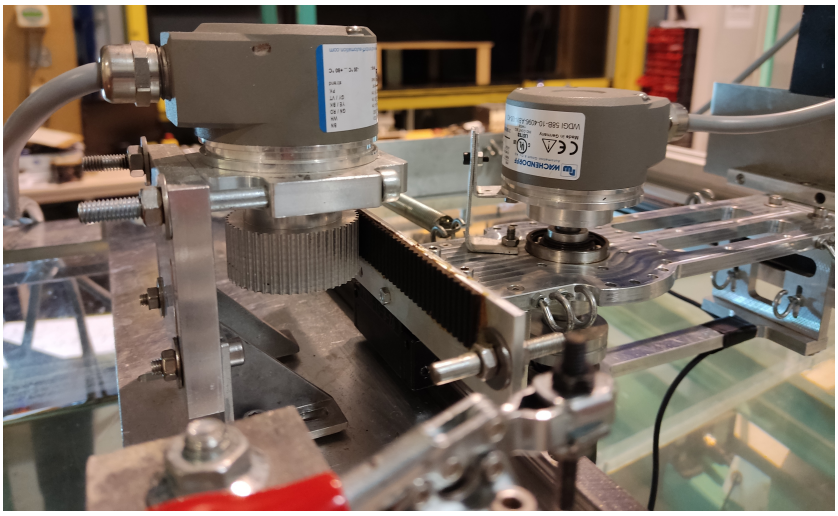

Figure 5.4: Timing belt used to transform the heaving encoder information into the heaving displacement.

Simultaneously to the foil kinematics, the $\tilde{x}'$ and $\tilde{y}'$ force components (see Figure 5.1 for the axis) and the $\tilde{z}$ torque component, $D'_p(\tilde{t})$, $L'_p(\tilde{t})$ and $M'_p(\tilde{t})$, respectively, are measured at the pivot axis by a six-axis force/torque transducer (ATI Nano17 IP68) placed below the pitch encoder, and then processed by the data-acquisition board and the LabVIEW code. The instantaneous force components in the streamwise ($\tilde{x}$) and transverse ($\tilde{y}$) directions are then obtained as

$$D_p = D'_p \cos\tilde{\alpha} + L'_p \sin\tilde{\alpha}, \quad L_p = -D'_p \sin\tilde{\alpha} + L'_p \cos\tilde{\alpha}. \tag{5.32}$$

In addition, the water temperature, as well as the temperature of the aluminum sliding plate of the eddy-current brake, are measured with a monitoring thermometer (Testo 110) and an infrared thermometer (Limit 94), respectively. The water temperature during a given test is used to determine its density and its dynamic viscosity by interpolating the tabulated data available in the book of Munson et al. [2013]. Regarding the temperature of the eddy-current brake's sliding plate, it is used to correct the values of the heave damping constant of the eddy-current brake (see Section D.2.5 of Appendix D).

All the experiments are conducted three times each in order to allow us to calculate the uncertainty of the experimental results through the standard deviation, which is given by

$$\Delta\overline{Z} = \sqrt{\frac{1}{n-1}\sum_{i=1}^{n}\left(\overline{Z}_i - \text{mean}(\overline{Z})\right)^2}, \tag{5.33}$$

where n represents the number of samples of the experiment ($n = 3$). Results are compared with the instrumental uncertainty, and the greater value is retained.

5.3.3 PIV measurements

To study the vortex dynamics associated with the pitching and heaving motion of the foil, in some of the reported configurations, we use a two-dimensional PIV (Particle Image Velocimetry) system to measure the flow field around the wing. A scheme of this PIV setup can be seen in Figure 5.5.

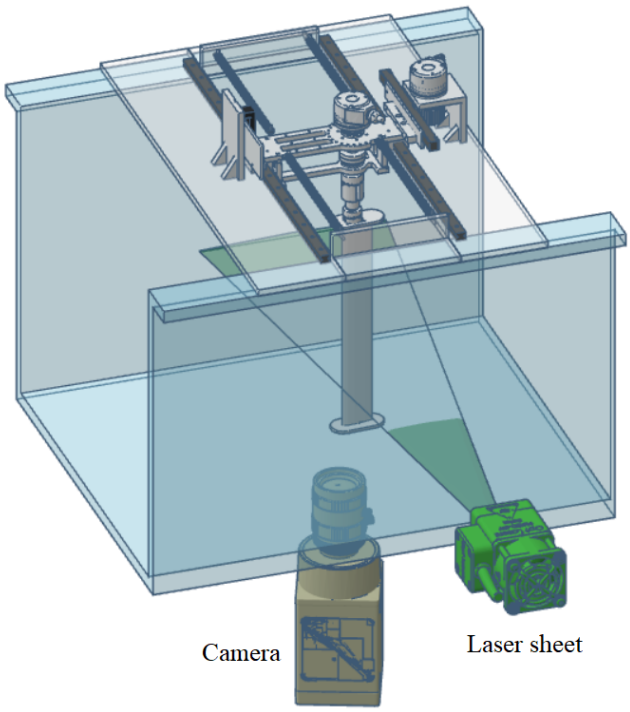

Figure 5.5: A 3D scheme of the PIV setup used to obtain the flow visualizations.

We seed the water with 10 μm diameter neutrally buoyant silver-coated spheres and illuminate the mid-span plane using a double-pulse Nd:YAG laser (532 nm, 1W, Panatec) with Microvec sheet optics. An sCMOS high-speed camera (Phantom v611) with a resolution of 1280×800 pixels is used to record PIV image pairs at 300 frames per second, with an external shutter (Nikon 32 mm). The recorded PIV images are processed through a Matlab code developed by the Fluid Mechanics Department of the University of Málaga, where the velocity fields are calculated using two passes of interrogation window size of 64×64 pixels, followed by two more passes of interrogation window size of 32×32 pixels, with an overlap of 50%. The time between the image pair was set such that an average of 16-pixel displacement per interrogation window is achieved in the streamwise direction. In general, about 3000 images are taken, which corresponds to approximately 10 s of flow recording. On the other hand, the vorticity field given by

$$\widetilde{w}_z = \frac{d\tilde{u}}{d\tilde{y}} - \frac{d\tilde{v}}{d\tilde{x}}, \tag{5.34}$$

is calculated through the circulation method depicted in Raffel et al. [2002], where $\tilde{u}$ and $\tilde{v}$ are the velocity in the $\tilde{x}$ and $\tilde{y}$ directions, respectively. The discrete scheme used to calculate the vorticity field with this method is the following

$$\widetilde{w}_{z,(i-2,j-2)} = \frac{\gamma_{i-2,j-2}}{4\Delta\tilde{x}\Delta\tilde{y}}, \tag{5.35}$$

where

$$\begin{aligned}\gamma_{i-2,j-2} = &\frac{\Delta\tilde{x}}{2}\left(\tilde{u}_{j-1,i-1} + 2\tilde{u}_{j-1,i} + \tilde{u}_{j-1,i+1}\right) + \frac{\Delta\tilde{y}}{2}\left(\tilde{v}_{j-1,i+1} + 2\tilde{v}_{j,i+1} + \tilde{v}_{j+1,i+1}\right)\\ &-\frac{\Delta\tilde{x}}{2}\left(\tilde{u}_{j+1,i+1} + 2\tilde{u}_{j+1,i} + \tilde{u}_{j+1,i-1}\right) - \frac{\Delta\tilde{y}}{2}\left(\tilde{v}_{j+1,i-1} + 2\tilde{v}_{j,i-1} + \tilde{v}_{j-1,i-1}\right),\\ &\text{with}\quad j = \{3,\cdots,N_{\tilde{y}}-2\}, \text{and}\quad i = \{3,\cdots,N_{\tilde{x}}-2\},\end{aligned} \tag{5.36}$$

being $\Delta\tilde{x} = 5.4$ mm and $\Delta\tilde{y} = 5.0$ mm the step size in the $\tilde{x}$ and $\tilde{y}$ directions, respectively, while $N_{\tilde{x}} = 80$ and $N_{\tilde{y}} = 50$ are the number of steps in those directions.

5.3.4 Springs and damper configurations

For the experimental analysis, we decided to study six different values of $\tilde{k}_h$ and eight of $\tilde{b}_{he}$, thus allowing for a total of 48 different experimental setups. The different spring configurations are shown in Table 5.1, where the corresponding values of each spring are previously obtained and shown in Section D.2.1 of Appendix D. Notice that the non-dimensional values on the right side of the table are shown in averaged quantities, this is because each of those non-dimensional values depends on the density of the water, and it differs for each experimental setup as its temperature varies. The same happens for the rest of the non-dimensional variables that depend on density, so their values will also be shown in their averaged quantities.

On the other hand, the different damper configurations are shown in Table 5.2, where the new values of $\tilde{b}_{he}$ are obtained considering the temperature at which the experiments are carried out, following

$$\tilde{b}_{he} = \frac{(1+\alpha_{B_0}\Delta T)^2}{(1+\alpha_{\rho_e}\Delta T)}\tilde{b}_{he\ calib}, \quad \text{with} \quad \Delta T = T - T_{calib}. \tag{5.37}$$

See Section D.2.5 of Appendix D for more information about this procedure. Therefore, with the new values of $\tilde{b}_{he}$, we can obtain the final viscous heave damping $\tilde{b}_h$, which are also shown in Table 5.2, through the simple equation

$$\tilde{b}_h = \tilde{b}_{he} + \tilde{b}_{hv}. \tag{5.38}$$

Spring configurations	$\tilde{k}_h$ **[N/m]**	$\bar{k}_h$
$\tilde{k}_{3,1} + \tilde{k}_{3,2}$	$\tilde{k}_{h1} = 80.30 \pm 0.85$	$\bar{k}_{h1} = 1.50 \pm 0.17$
$\tilde{k}_{8,1} + \tilde{k}_{8,2}$	$\tilde{k}_{h2} = 124.91 \pm 0.79$	$\bar{k}_{h2} = 2.33 \pm 0.26$
$\tilde{k}_{3,1} + \tilde{k}_{3,2} + \tilde{k}_{4,1} + \tilde{k}_{4,2}$	$\tilde{k}_{h3} = 173.08 \pm 1.64$	$\bar{k}_{h3} = 3.22 \pm 0.37$
$\tilde{k}_{3,1} + \tilde{k}_{3,2} + \tilde{k}_{8,1} + \tilde{k}_{8,2}$	$\tilde{k}_{h4} = 205.21 \pm 1.64$	$\bar{k}_{h4} = 3.82 \pm 0.43$
$\tilde{k}_{3,1} + \tilde{k}_{3,2} + \tilde{k}_{4,1} + \tilde{k}_{4,2} + \tilde{k}_{6,1} + \tilde{k}_{6,2}$	$\tilde{k}_{h5} = 268.50 \pm 2.42$	$\bar{k}_{h5} = 5.00 \pm 0.57$
$\tilde{k}_{1,1} + \tilde{k}_{1,2}$	$\tilde{k}_{h6} = 312.86 \pm 0.85$	$\bar{k}_{h6} = 5.83 \pm 0.63$

Table 5.1: The six different heave stiffness configurations used in the experimental campaign and the corresponding non-dimensional values for $U_\infty = 0.37 \pm 0.02$ m/s.

$\boldsymbol{l_m}$ **[mm]**	$\tilde{b}_{he}$ [Ns/m]	$\bar{b}_{he}$	$\tilde{b}_h$ [Ns/m]	$\bar{b}_h$
$\boldsymbol{l_{m1} = \nexists}$	$\tilde{b}_{he1} = 0.00 \pm 0.00$	$\bar{b}_{he1} = 0.00 \pm 0.00$	$\tilde{b}_{h1} = 6.46 \pm 0.06$	$\bar{b}_{h1} = 1.82 \pm 0.12$
$\boldsymbol{l_{m2} = 0.00 \pm 0.01}$	$\tilde{b}_{he2} = 0.94 \pm 0.12$	$\bar{b}_{he2} = 0.26 \pm 0.05$	$\tilde{b}_{h2} = 7.40 \pm 0.17$	$\bar{b}_{h2} = 2.08 \pm 0.17$
$\boldsymbol{l_{m3} = 5.00 \pm 0.01}$	$\tilde{b}_{he3} = 2.36 \pm 0.13$	$\bar{b}_{he3} = 0.67 \pm 0.07$	$\tilde{b}_{h3} = 8.82 \pm 0.19$	$\bar{b}_{h3} = 2.49 \pm 0.19$
$\boldsymbol{l_{m4} = 7.50 \pm 0.01}$	$\tilde{b}_{he4} = 3.66 \pm 0.14$	$\bar{b}_{he4} = 1.03 \pm 0.10$	$\tilde{b}_{h4} = 10.12 \pm 0.20$	$\bar{b}_{h4} = 2.85 \pm 0.21$
$\boldsymbol{l_{m5} = 10.00 \pm 0.01}$	$\tilde{b}_{he5} = 5.22 \pm 0.14$	$\bar{b}_{he5} = 1.47 \pm 0.12$	$\tilde{b}_{h5} = 11.68 \pm 0.20$	$\bar{b}_{h5} = 3.29 \pm 0.24$
$\boldsymbol{l_{m6} = 12.50 \pm 0.01}$	$\tilde{b}_{he6} = 6.41 \pm 0.16$	$\bar{b}_{he6} = 1.81 \pm 0.14$	$\tilde{b}_{h6} = 12.87 \pm 0.22$	$\bar{b}_{h6} = 3.63 \pm 0.26$
$\boldsymbol{l_{m7} = 17.50 \pm 0.01}$	$\tilde{b}_{he7} = 7.64 \pm 0.17$	$\bar{b}_{he7} = 2.15 \pm 0.17$	$\tilde{b}_{h7} = 14.10 \pm 0.23$	$\bar{b}_{h7} = 3.97 \pm 0.28$
$\boldsymbol{l_{m8} = 25.00 \pm 0.01}$	$\tilde{b}_{he8} = 8.53 \pm 0.18$	$\bar{b}_{he8} = 2.40 \pm 0.18$	$\tilde{b}_{h8} = 14.99 \pm 0.24$	$\bar{b}_{h8} = 4.22 \pm 0.30$

Table 5.2: The eight different heave damping configurations for the eddy-current brake used in the experimental campaign and the corresponding non-dimensional values for $U_\infty = 0.37 \pm 0.02$ m/s.

5.4 Experimental results

Before going into any experimental results, it is essential to make a proper characterization of the parameters involved in the governing equations, i.e., Equations (5.8) to (5.10). This parameter characterization is well conducted in Appendix D, but a summary of these parameters is presented in Table 5.3 together with their corresponding non-dimensional values for the velocity used in the whole experimental campaign ($U_\infty = 0.37 \pm 0.02$ m/s).

Parameter	**Value**	**Non-dim. paramet**	**Average Value**
U_∞ [m/s]	0.37 ± 0.02	$\overline{Re}$	22200 ± 170
$\widetilde{m}_h$ [kg]	2.16 ± 0.01	$\overline{m}_h$	9.22 ± 0.10
$\tilde{I}_a$ [kgm^2/rad]	$(1.24 \pm 0.01) \cdot 10^{-6}$	$\bar{I}_a$	0.86 ± 0.01
$\widetilde{\Omega}$ [kgm]	$(1.7 \pm 0.1) \cdot 10^{-3}$	$\overline{\Omega}$	0.29 ± 0.02
$\tilde{b}_{hv}$ [Ns/m]	6.46 ± 0.06	$\bar{b}_{hv}$	1.82 ± 0.12
$\tilde{b}_{\alpha v}$ [Nms/rad]	$(3.96 \pm 0.04) \cdot 10^{-4}$	$\bar{b}_{\alpha v}$	0.09 ± 0.01
$\tilde{k}_\alpha$ [Nm/rad]	0 ± 0	$\bar{k}_\alpha$	0 ± 0
$\tilde{f}_C$ [N]	1.19 ± 0.03	$\bar{f}_C$	0.90 ± 0.12
$\widetilde{m}_C$ [Nm]	$(2.04 \pm 0.02) \cdot 10^{-3}$	$\overline{m}_C$	0.030 ± 0.004
$\tilde{a}$ [mm]	-9.900 ± 0.002	a	-0.4000 ± 0.0002

Table 5.3: Parameter characterization of the flapping-foil turbine.

Following a preliminary series of tests, a case achieving a high efficiency based on the fluid power (η_f) has been selected as the baseline case. It is important to remark that the highest efficiency η_e is not obtained for the highest η_f, as we will see later in the chapter. However, the baseline case has been selected by taking into consideration some damping from the eddy-current brake. Then, we have selected $\bar{k}_{h1} = 1.50 \pm 0.17$ and $l_{m2} = 0 \pm 0.01$ mm, which is related with the damping constants $\bar{b}_{he2} = 0.26 \pm 0.05$ and $\bar{b}_{h2} = 2.08 \pm 0.17$. The performance metrics for the baseline case are presented in Table 5.4.

Perf. metric	**Value**	**Perf. metric**	**Value**
$\bar{f}$	0.070 ± 0.004	$\overline{C_L}$	3.75 ± 0.41
$\bar{k}$	0.438 ± 0.023	$\overline{C_D}$	3.00 ± 0.38
$\bar{\phi}$ [deg.]	-72.76 ± 1.53	$\overline{C_M}$	0.051 ± 0.003
$\bar{h}$	-0.010 ± 0.006	$\overline{C_{P_e}}$	0.049 ± 0.008
$\bar{\alpha}$ [deg.]	1.871 ± 0.006	$\overline{C_P}$	1.63 ± 0.28
$\bar{h}_0$	1.29 ± 0.01	$\bar{\eta}_e$ [%]	1.94 ± 0.02
$\bar{\alpha}_0$ [deg.]	87.47 ± 0.45	$\bar{\eta}_f$ [%]	64.98 ± 0.61

Table 5.4: Averaged values and standard deviations of the performance metrics characterizing the baseline case computed from 90 blade cycles.

5.4.1 Data treatment

Once the parameter characterization is done, we also need to treat the data before performing any analysis. Especially for the force/torque measurements since they typically present a high noise. Furthermore, an additional problem appears when we look at the Coulomb friction data C_{L_C} and C_{M_C} because they are intermittent signals that depend on the sign of $\dot{h}$ and $\dot{\alpha}$, respectively. Therefore, they are going to cause problems when analyzing the final filtered values. Our approach to this issue is to mix the force/torque and the Coulomb signals, so after applying the filter, the final resulting data will be smooth, and we will be able to analyze it properly. Then, we define two new parameters

$$C_{L_{pC}} = C_{L_p} + C_{L_C}, \quad C_{M_{pC}} = C_{M_p} + C_{M_C}, \tag{5.39}$$

so Equations (5.8) to (5.10) will be now

$$m_h\ddot{h} + \Omega\left(\dot{\alpha}^2 \sin\alpha - \ddot{\alpha}\cos\alpha\right) = C_L - b_h\dot{h} - k_h h - C_{L_{pC}}, \tag{5.40}$$

$$\Omega\left(\ddot{\alpha}\sin\alpha + \dot{\alpha}^2\cos\alpha\right) = C_D - C_{D_p}, \tag{5.41}$$

$$\Omega\ddot{h}\cos\alpha - I_a\ddot{\alpha} = 2\left(C_M + b_\alpha\dot{\alpha} + k_\alpha\alpha - C_{M_{pC}}\right). \tag{5.42}$$

Equations (5.21) and (5.22) will be combined into

$$C_{P_{hpC}} = \dot{h}C_{L_{pC}}, \quad C_{P_{\alpha pC}} = -2\dot{\alpha}C_{M_{pC}}, \quad C_{P_{pC}} = C_{P_{hpC}} + C_{P_{\alpha pC}}, \tag{5.43}$$

and Equation (5.23) will be

$$C_P = C_{P_R} + C_{P_b} + C_{P_k} + C_{P_{pC}}, \tag{5.44}$$

making the same change in Equation (5.30).

Filter procedure

Once the formulation of the problem is adjusted, we can analyze the amplitude spectrum of the different experimental data and find the dominant frequencies. In Figure 5.6, we can see the single-sided amplitude spectrum for the variable L_{pC}, where the dominant frequencies are mainly below 4 Hz. The rest of the data presents a similar trend, so in this case, we can use a low pass Butterworth digital filter of seventh order with a cut-off frequency of $\tilde{f}_c = 4$ Hz, where its transfer function can be written as

$$H(z) = \frac{b_1 + b_2 \cdot z^{-1} + \cdots + b_{n+1} \cdot z^{-n}}{a_1 + a_2 \cdot z^{-1} + \cdots + a_{n+1} \cdot z^{-n}}, \tag{5.45}$$

with the coefficients a_n and b_n given by the Table 5.5. The filtered signal is sufficiently smooth and shows the main features of the physical interaction of the system.

$\boldsymbol{n}$	1	2	3	4	5	6	7	8
$\boldsymbol{b_n \cdot 10^{-15}}$	0.063	0.438	1.315	2.192	2.192	1.315	0.438	0.063
$\boldsymbol{a_n}$	1	-6.977	20.865	-34.662	34.551	-20.664	6.866	-0.978

Table 5.5: Low pass Butterworth digital filter coefficients of 7th order with a $\tilde{f}_c = 4$ Hz.

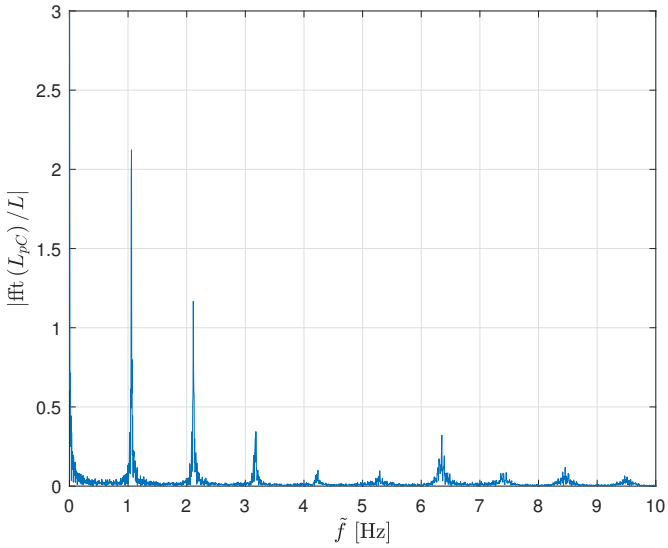

Figure 5.6: Single-sided amplitude spectrum of the variable L_{pC} for the case $k_h = 1.50$ and $b_{he} = 0.26$ (baseline case), being fft the Fast Fourier Transform and L the length of the signal.

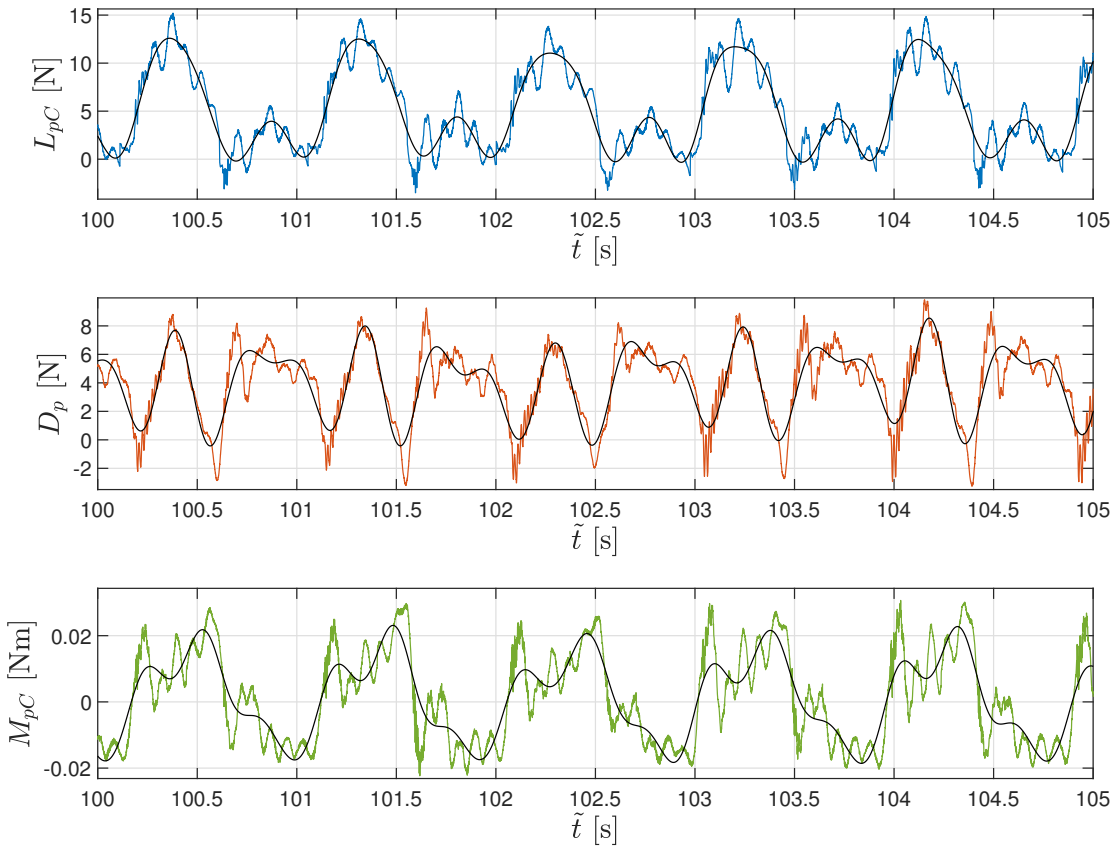

Figure 5.7: Some of the signals and the applied low pass Butterworth digital filter (black lines) for the case $k_h = 1.50$ and $b_{he} = 0.26$ (baseline case).

This low-pass Butterworth filter with a cut-off frequency of 4 Hz has been applied not only to the force/torque signals but also to the velocity and acceleration data in heave and pitch. These last signals, which are computed using second-order central difference schemes, present a high noise so the Butterworth filter is also necessary. To sum up, the same Butterworth filter has been applied to the following signals in their dimensional form

$$L_{pC} \qquad D_p \qquad M_{pC} \qquad \dot{\tilde{h}} \qquad \dot{\tilde{\alpha}} \qquad \ddot{\tilde{h}} \qquad \ddot{\tilde{\alpha}}.$$

In Figure 5.7, it is shown the original data and the applied Butterworth filter of the signals L_{pC}, D_p, and M_{pC} for the baseline case. A different filter could be applied but the results should be similar since we need to eliminate the noise of the signal.

Averaging treatment procedure

For the average treatment of the data, we obtain the average value for each cycle as it is depicted in Equations (5.24) to (5.26) during the last $N = 90$ cycles. To do that, we find the last 91 upper and lower peaks thanks to the Matlab function *findpeaks*, and then the mean value of each cycle is obtained with the *mean* command. The upper and lower peaks will also be used to calculate the mean of the amplitude signal through

$$\overline{Z}_0 = \frac{1}{N}\sum_{j=1}^{N}\left(Z_{\max,j} - Z_{\min,j}\right). \tag{5.46}$$

In Figure 5.8(a), we can see an example of this data treatment for the signal $h(t)$. In addition, a comparison between the heaving and pitching motions is shown in Figure 5.8(b), where the phase lag between the two signals can be observed.

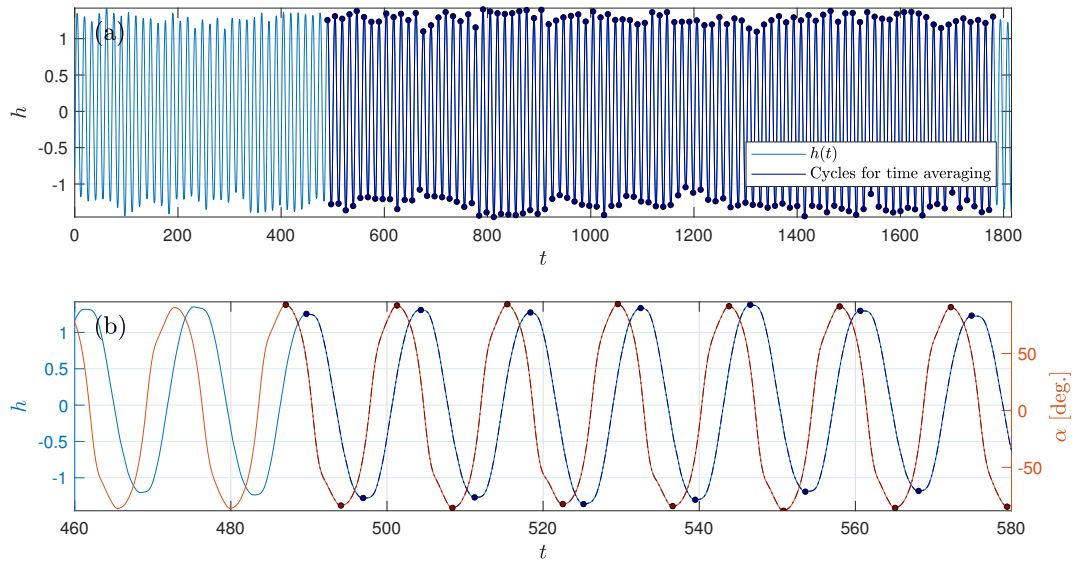

Figure 5.8: An example of the data treatment and how the averaged values are obtained for the $h(t)$ signal (a). A comparison between the $h(t)$ and $\alpha(t)$ signals is also shown (b), where the phase lag between both can be seen. Those figures correspond to the case $k_h = 1.50$ and $b_{he} = 0.26$ (baseline case).

5.4.2 Analysis of the temporal terms in the model equations

Terms in the governing equations

Defining the inertial terms of the model Equations (5.40) to (5.42) as

$$\begin{aligned} C_{L_R} &= m_h \ddot{h} + \Omega \left(\dot{\alpha}^2 \sin\alpha - \ddot{\alpha} \cos\alpha \right), \\ C_{D_R} &= \Omega \left(\ddot{\alpha} \sin\alpha + \dot{\alpha}^2 \cos\alpha \right), \\ C_{M_R} &= \Omega \ddot{h} \cos\alpha - I_a \ddot{\alpha}, \end{aligned} \tag{5.47}$$

the temporal evolution of the different terms involved in the model equations for the baseline case can be seen in Figure 5.9. Notice that the average contributions of the inertial terms are negligible. Something similar happens for the springs and dampers-associated terms, as the heaving and pitching motions are approximately harmonic.

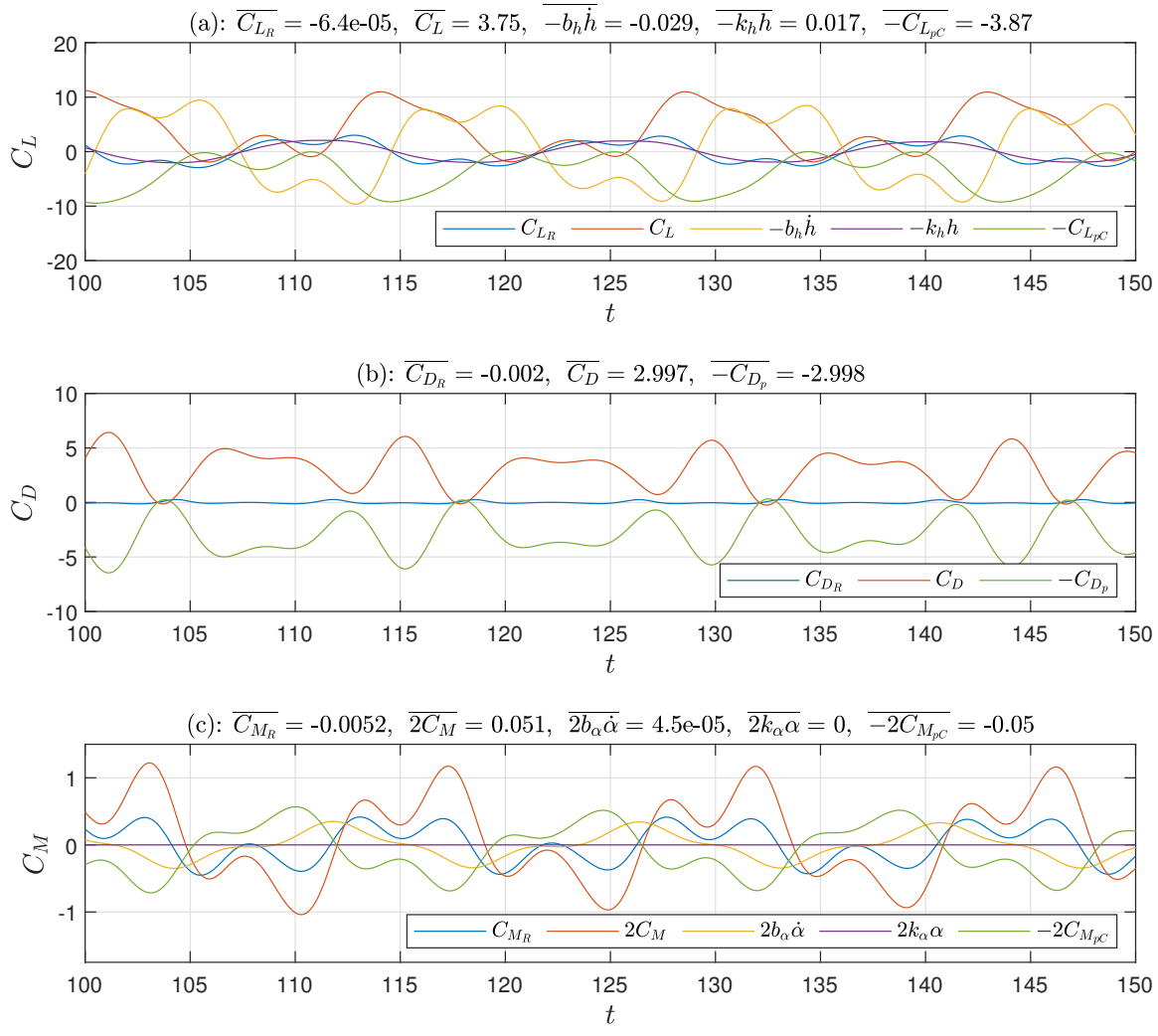

Figure 5.9: Temporal evolution of the different terms involved in the governing Equations (5.40) to (5.42) and their corresponding averaged values for the baseline case $k_h = 1.50$ and $b_{he} = 0.26$.

Therefore, we can conclude that, in order to have the system in balance, the measured terms with the force/torque transducer in the pivot axis have to be pretty close to the actual lift, drag, and moment coefficients, just with a minor correction for the lift and moment that comes from the springs and dampers-associated terms, since they are not purely harmonic. Being this difference, in this case, more critical in the lift equation because we are not using any spring in pitch. As a consequence, we could have relatively accurate measurements of the lift, drag, and moment coefficients by measuring the force and torque values around the pivot axis of the flapping-foil turbine.

Power terms derived from the governing equations

In Figure 5.10, we can see the temporal evolution of the different power terms derived from the model equations for the baseline case.

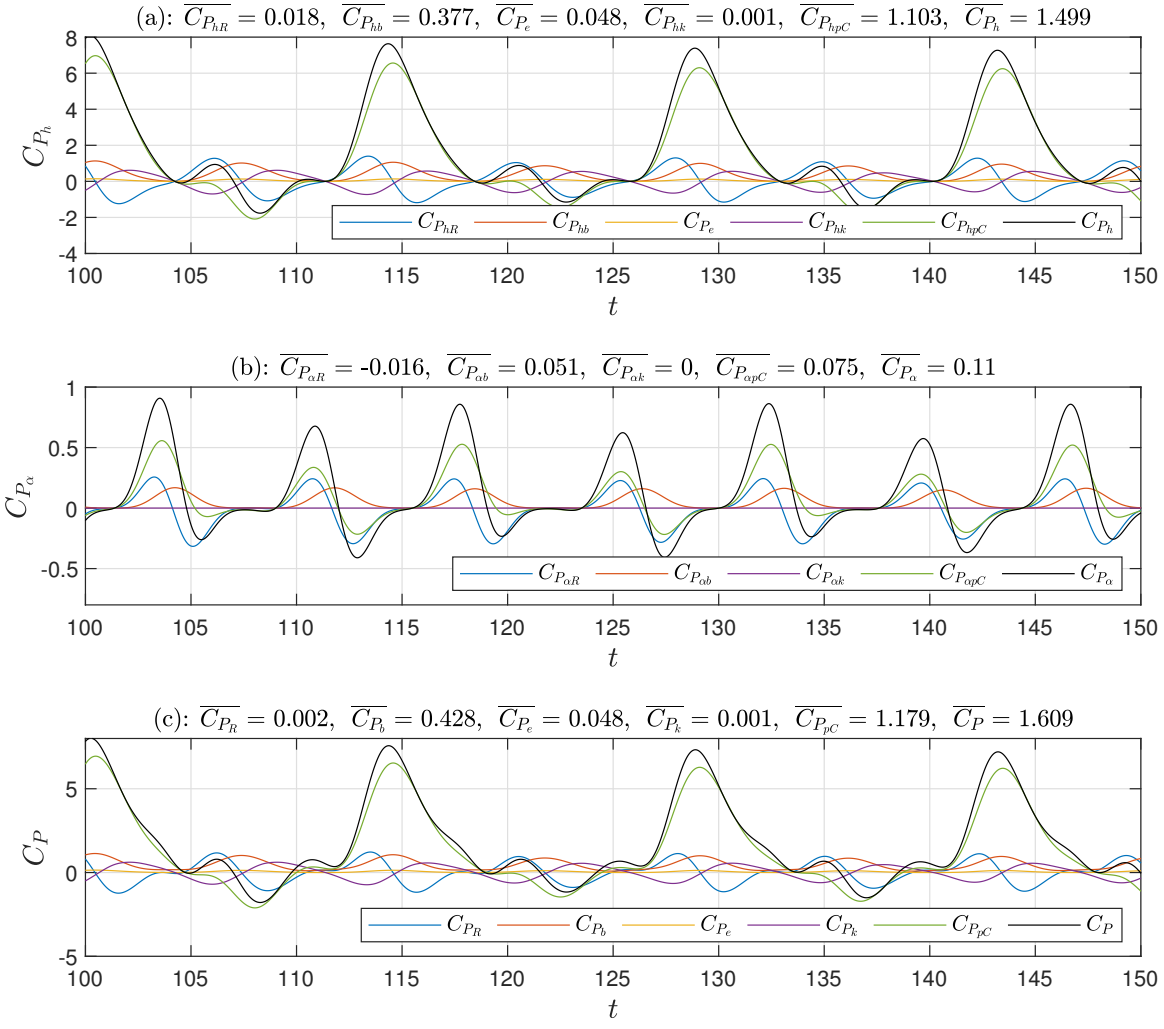

Figure 5.10: Temporal evolution of the different power coefficients derived from the governing Equations (5.40) to (5.42) and their corresponding averaged values for the baseline case $k_h = 1.50$ and $b_{he} = 0.26$.

It is observed that the contribution of the power coefficients associated with the inertial terms is again roughly negligible. The same happens for the one associated with the spring's power terms in both heaving and pitching motions. Therefore, the main contribution to the power that the fluid transferred to the flapping-foil turbine is made through the damping terms and the terms associated with the force and moment on the pivot axis of the foil plus the Coulomb contributions that are included in that signal, i.e., the power terms C_{P_b} and $C_{P_{pC}}$. However, the power that can be extracted from the flapping-foil turbine is obtained through the C_{P_e} term, which is just a fraction of the total power that the fluid transferred to the foil. For the baseline case, this ratio is around 3%, but it can be greater if we maximize the energy harvesting performance instead of the maximum power that the fluid transmits to the foil.

5.4.3 Analysis of the mean values in the magnitudes of interest

Once the temporal terms have been analyzed, we are interested in studying the mean values and the amplitudes of some of these primary magnitudes. Thus, we analyze the 6×8 different experimental setups with the data treatment presented before to find some trends in the results. Firstly, we analyze the mean values of the heaving and pitching motions as shown in Figure 5.11. We can see that in both cases, there is a little deviation from the equilibrium position at rest, especially when the damping constant is low and the spring constant is high. It seems that a greater damper and not-so-stiff springs can help to make the oscillations of the device more stable.

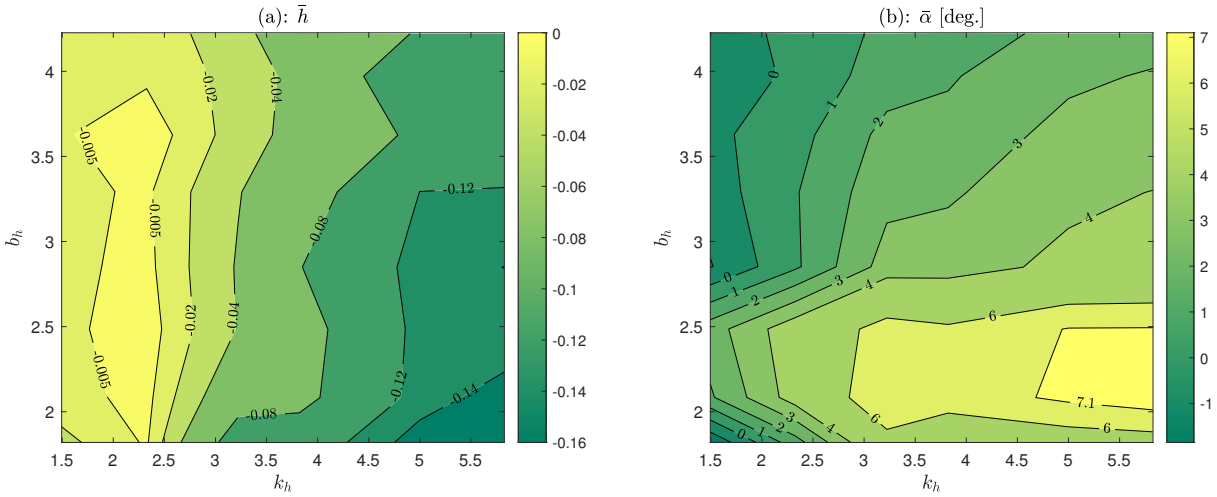

Figure 5.11: Contour plots in the $k_h - b_h$ plane of $\bar{h}$ (a) and $\bar{\alpha}$ (b) for the experiments carried out at $U_\infty = 0.37 \pm 0.02$ ($\overline{Re} = 22200 \pm 170$).

Working now with the mean values of the amplitudes for $h(t)$ and $\alpha(t)$ (see Figure 5.12), we can observe that larger amplitudes in heave and pitch are related with lower values of both damper and springs constants. The amplitude of the heaving motion rapidly decreases when either k_h or b_h increases. However, the amplitude of the pitching motion is mainly affected by the variation of k_h, being decreased when k_h is increased. Notice that the more

efficient configurations, where the flow transferred the maximum amount of power to the foil, are reached for the greater amplitudes in both heaving and pitching motions. Therefore, these regions of low k_h and b_h will be the ones where the best performance (based on the power transmitted from the fluid to the foil) is obtained, as we will see later.

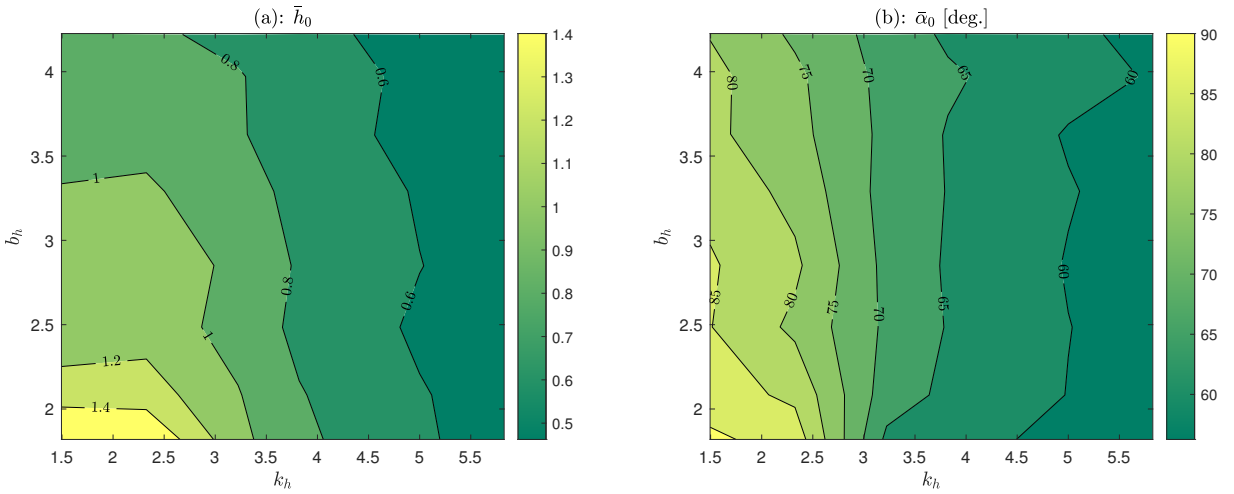

Figure 5.12: As in Figure 5.11 but for the contours of $\bar{h}_0$ (a), and $\bar{\alpha}_0$ (b).

Analyzing the mean values of the frequency and the phase lag between the heaving and pitching motions, as it is done in Figure 5.13, we can see some trends. For the frequency, we can observe that it is practically constant for all the ranges studied and so the reduced frequency k.[1] For the phase lag, it is remarkable that it is not affected by the damper configuration but for the spring selection, being this phase lag difference reduced as the springs become stiffer.

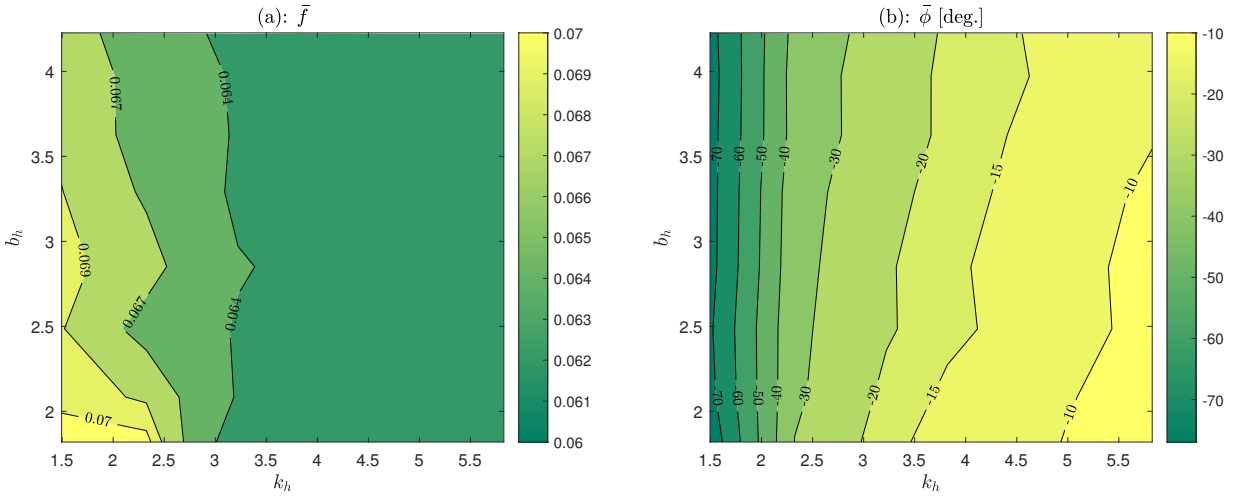

Figure 5.13: As in Figure 5.11 but for the contours of $\bar{f}$ (a), and $\bar{\phi}$ (b).

[1]This working frequency cannot be predicted from a flutter instability analysis (e.g., Fernandez-Feria and Alaminos-Quesada [2022]) because the present configuration is adapted to work by taking advantage of a non-linear divergence instability (Boudreau et al. [2018]).

Looking now at the mean values of the lift, drag, and moment coefficients (shown in Figure 5.14), we can observe that the lift and the drag are greater in the region where the fluid transfers the maximum power to the foil. The lift coefficient is especially relevant since stronger forces in the lift direction are associated with larger movements in that direction and, consequently, with more power and efficiency. The drag coefficient is not so significant in this scenario simply because the flapping-foil prototype can not move in the y direction. Stiffer springs also reduce the mean values of both the lift and drag coefficients. On the other hand, we can see that the mean values of the moment coefficient are much lower than their lift or drag counterparts.

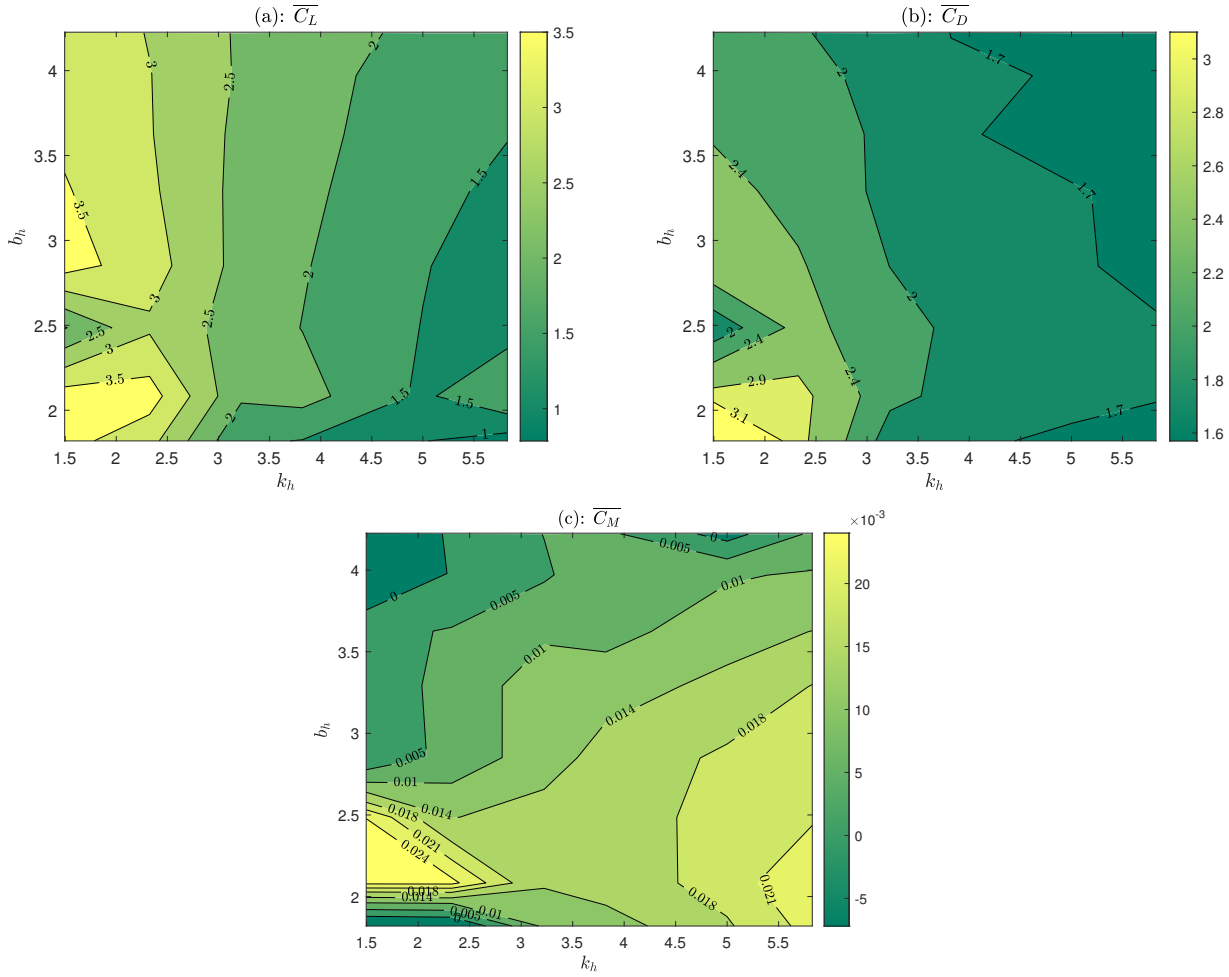

Figure 5.14: As in Figure 5.11 but for the contours of $\overline{C_L}$ (a), $\overline{C_D}$ (b), and $\overline{C_M}$ (c).

Studying the mean values of the power coefficients (see Figure 5.15), we can observe that the power extracted from the flapping-foil turbine (effective power) grows with the damping constant. It is clear since the energy is extracted directly through the eddy current brake and the damping associated with that, which is a considerable fraction of the total damping of the system. Therefore, the greater the damper, the more power will be obtained with this prototype. However, as we increase the damping, the power that the fluid transmits to the

foil is reduced and so we should find a maximum where increasing the value of b_h is no longer helpful. Unfortunately, our linear damper is not powerful enough to reach that point, so we can not see that in the figure. In addition, we can see that the best performance is achieved for not-so-rigid springs, and this is due to the greater amplitudes in heave and pitch that are associated with softer spring configurations, as already mentioned.

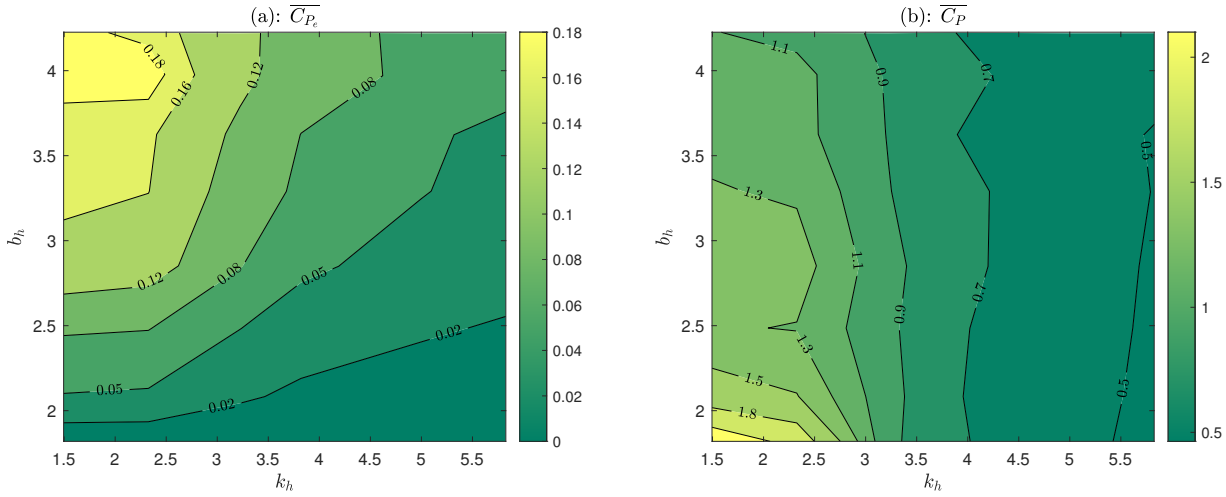

Figure 5.15: As in Figure 5.11 but for the contours of $\overline{C_{P_e}}$ (a), and $\overline{C_P}$ (b).

On the other hand, the power transmitted from the flow to the foil is directly related to the amplitude of the oscillations of the foil, so the best performance is found for the softer configuration of the damper and the springs where the amplitudes in heave and pitch are maximum. Also, this quantity seems to be more affected by the spring stiffness than the damping power, especially when we work far from the best-performance region.

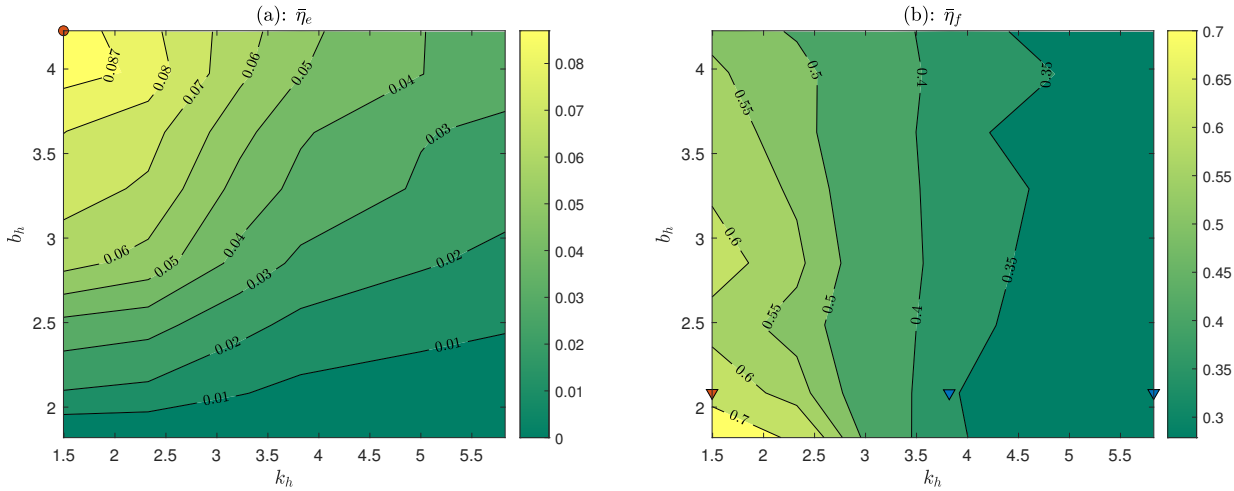

Figure 5.16: As in Figure 5.11 but for the contours of $\bar{\eta}_e$ (a), and $\bar{\eta}_f$ (b). The markers in the $\bar{\eta}_f$ plot correspond to the baseline case (red one) and to the other two points of interest (blue ones), which are analyzed with the PIV technique. The red point in the $\bar{\eta}_e$ plot corresponds to the best efficient configuration for energy harvesting.

Finally, in Figure 5.16, we can see the isocontours for both energy efficiencies, η_e, which is based on the effective power extracted from the flapping-foil turbine through the linear damper, and η_f, which is based on the power transmitted from the flow to the foil. It can be observed that they follow the same trend as the power coefficients since they are related to them through Equation (5.28). Remarkably, the efficiency η_e is much lower than its counterpart η_f. However, as we mentioned above for the power coefficient analysis, greater efficiencies can be found for η_e if a stronger magnetic brake is used. For the different configurations that we studied with our prototype, the best efficiency for energy harvesting is found for the highest b_h and the lowest k_h ($\bar{b}_{he8} = 2.40 \pm 0.18$ and $\bar{k}_{h1} = 1.50 \pm 0.17$). In contrast, the best efficiency based on the flow power is found for the lowest values of b_h and k_h (baseline case). In Table 5.6, we have presented the performance metrics for the best energy harvesting configuration, with the average values and their associated standard deviation for the 90 blade cycles.

Perf. metric	**Value**	**Perf. metric**	**Value**
$\bar{f}$	0.068 ± 0.004	$\overline{C_L}$	3.34 ± 0.38
$\bar{k}$	0.430 ± 0.022	$\overline{C_D}$	2.27 ± 0.25
$\bar{\phi}$ [deg.]	-73.32 ± 0.23	$\overline{C_M}$	-0.005 ± 0.001
$\bar{h}$	-0.017 ± 0.005	$\overline{C_{P_e}}$	0.19 ± 0.03
$\bar{\alpha}$ [deg.]	-0.44 ± 0.09	$\overline{C_P}$	1.11 ± 0.18
$\bar{h}_0$	0.832 ± 0.002	$\bar{\eta}_e$ [%]	9.05 ± 0.04
$\bar{\alpha}_0$ [deg.]	79.72 ± 0.19	$\bar{\eta}_f$ [%]	54.06 ± 0.08

Table 5.6: Averaged values and standard deviations of the performance metrics characterizing the best efficient configuration for energy harvesting, which is obtained for the case $k_h = 1.50$ and $b_{he} = 2.40$.

5.4.4 PIV results

In order to understand the flow structures developed around the foil, some of the experiments were conducted while applying the PIV technique. Particularly, we have analyzed three different cases: the baseline case and two more ones for the same damping constant but stiffer spring constants ($\bar{k}_{h3} = 3.22 \pm 0.37$ and $\bar{k}_{h6} = 5.83 \pm 0.63$), which are shown in Figures 5.17 to 5.19, respectively. The PIV images were recorded at the mid-span plane in the wake of the foil and the normalized spanwise vorticity field, defined as

$$w_z = \frac{\widetilde{w}_z c}{2U_\infty}, \tag{5.48}$$

is presented in the results, as well as the velocity field arrows that indicate the direction of the flow, at different time snapshots during a complete cycle of the foil's motion. The position of the foil is shown directly in the results. Paying attention to the PIV results in Figure 5.17, we can see the effect of the dynamic stall during the motion of the foil for a

complete cycle oscillation, and particularly in the transitions from the downstroke to the upstroke and vice versa. The first stalling event, corresponding to the transition between the upstroke to the downstroke, can be visualized at the $t/T = \{0.1, 0.2\}$ time snapshots. The second stalling event, corresponding to the transition between the downstroke to the upstroke, can be observed at $t/T = \{0.5, 0.6\}$. It is important to remark that the interaction of the shed vortex with the foil is crucial during the deep dynamic stall events.

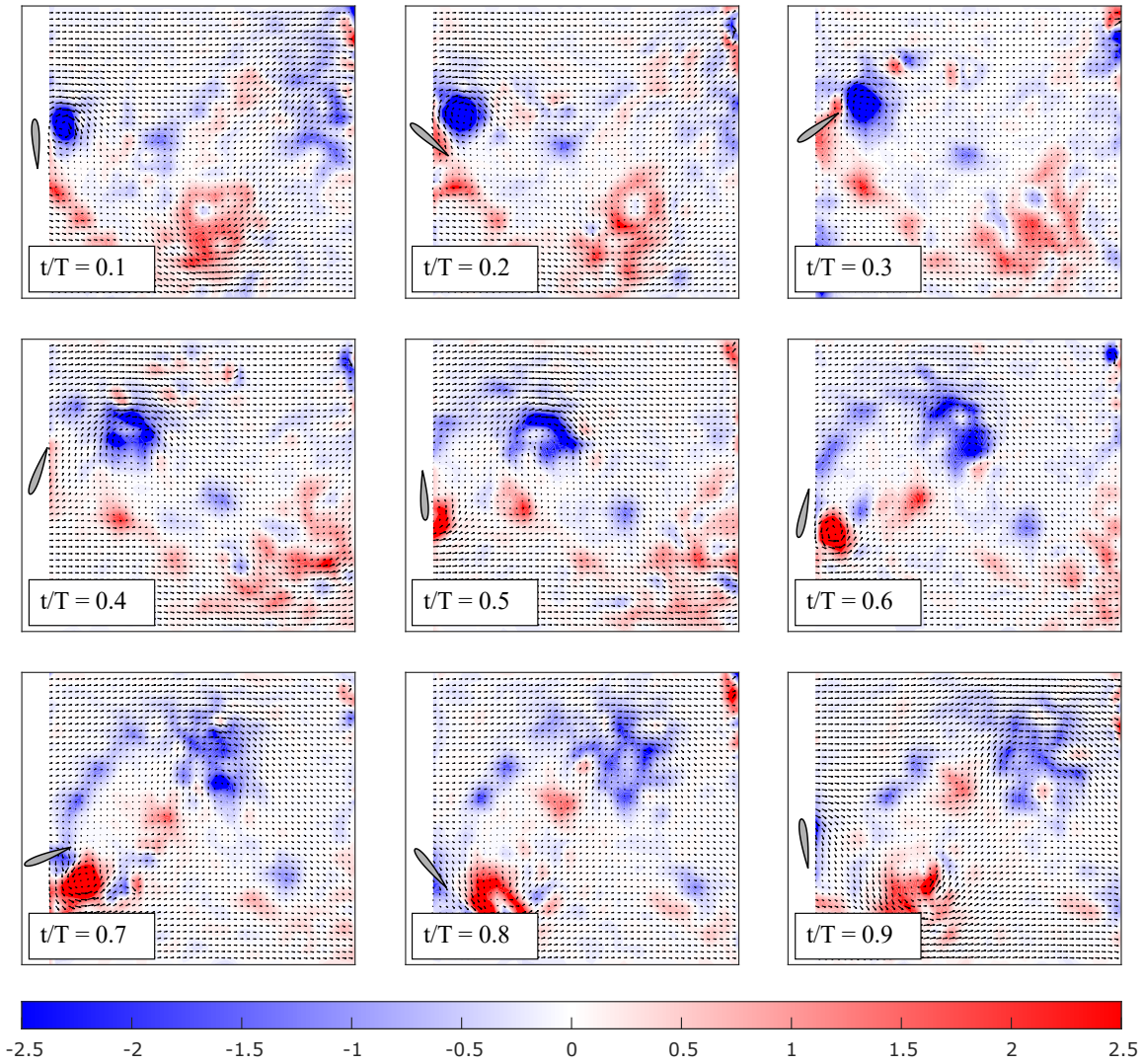

Figure 5.17: Snapshots of the normalized spanwise vorticity field measured by PIV at different instants during one representative blade cycle. The images correspond to the case $k_h = 1.50$ and $b_{he} = 0.26$ (baseline case).

The overall process that the foil experienced is the following. The foil starts its movement because of the fluid-structure interaction with the incoming flow. Once it reaches one of the extremes and the springs in heave (on the opposite side) generate too much force, the foil's

speed is reduced, and its angle of attack starts to change. At this precise moment, the vortex is created, thus generating a relatively intense low pressure on one side of the foil. As a result, the arm of the forces generated by the eddy on the foil increases, so it generates a relatively large moment that helps to rotate the foil. Then, as the foil continues its movement in the heave direction, a large leading-edge vortex is shed, which happens every half cycle for the baseline and the two extra-studied cases. When the foil is close to the new final position in the other extreme of the channel, and the angle of attack starts to change again, the same process that was explained above is repeated.

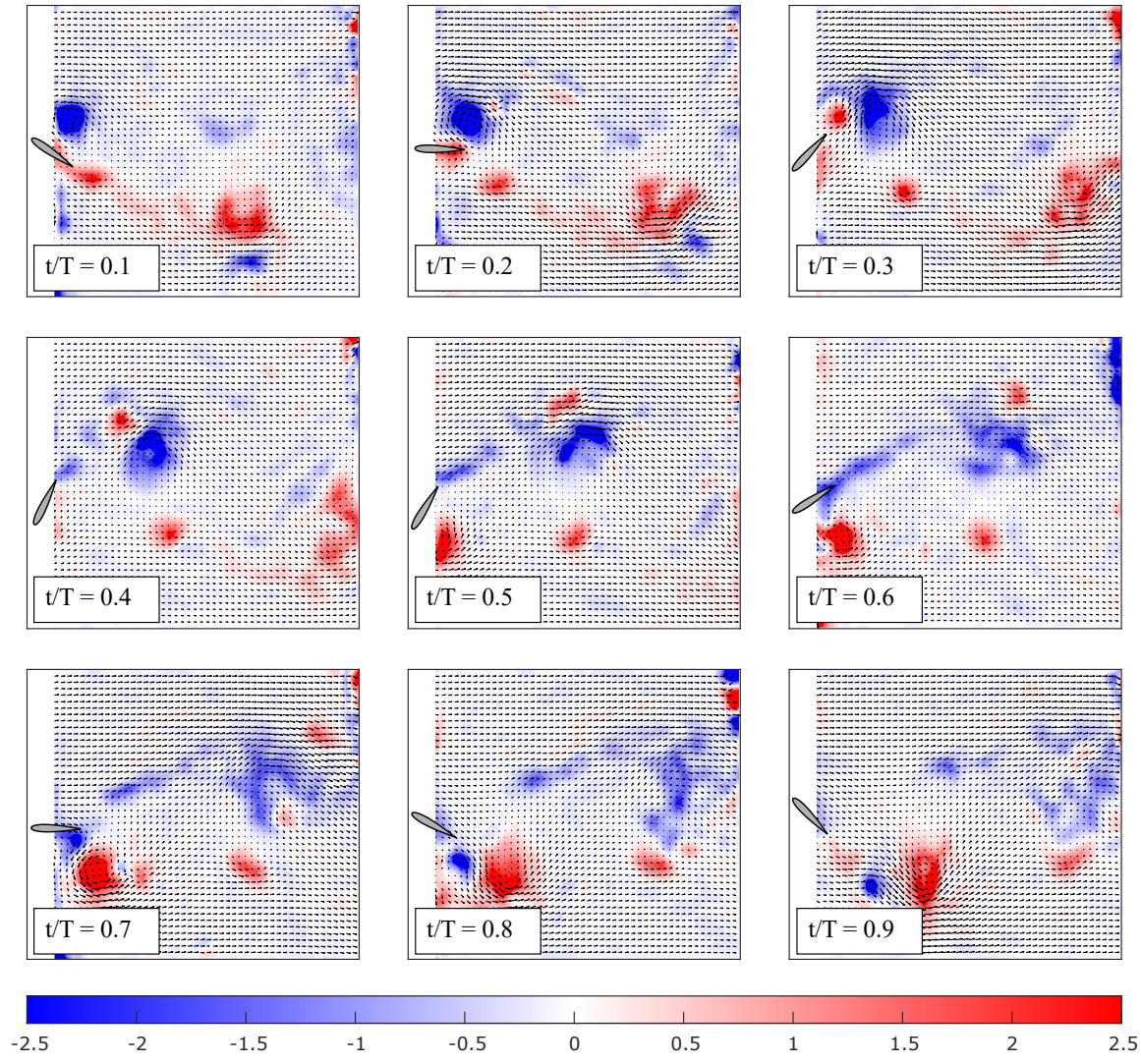

Figure 5.18: The same as Figure 5.17 but for the case $k_h = 3.82$ and $b_{he} = 0.26$.

As it is well explained in the work performed by Veilleux and Dumas [2017], this strong interaction between the foil and the vortex is the result of an adequate synchronization between the pitching and the heaving motions. Also, it is clear, as we are not using any springs

in pitch, that the vortex shedding is the physical mechanism through which the amplitude of motion of the foil is limited, thus leading to the periodic motion. It is also found that the results here obtained with the PIV technique are in good agreement with the ones presented by Boudreau et al. [2018].

Analyzing now the PIV results presented in Figures 5.18 and 5.19, it can be observed a very similar behavior in the motion of the foil as well as in the shedding and vortex formation. The main difference is found in the amplitudes described by the foil. They are smaller than in the baseline case, which is a reasonable consequence of the stronger springs that have been used in these experiments.

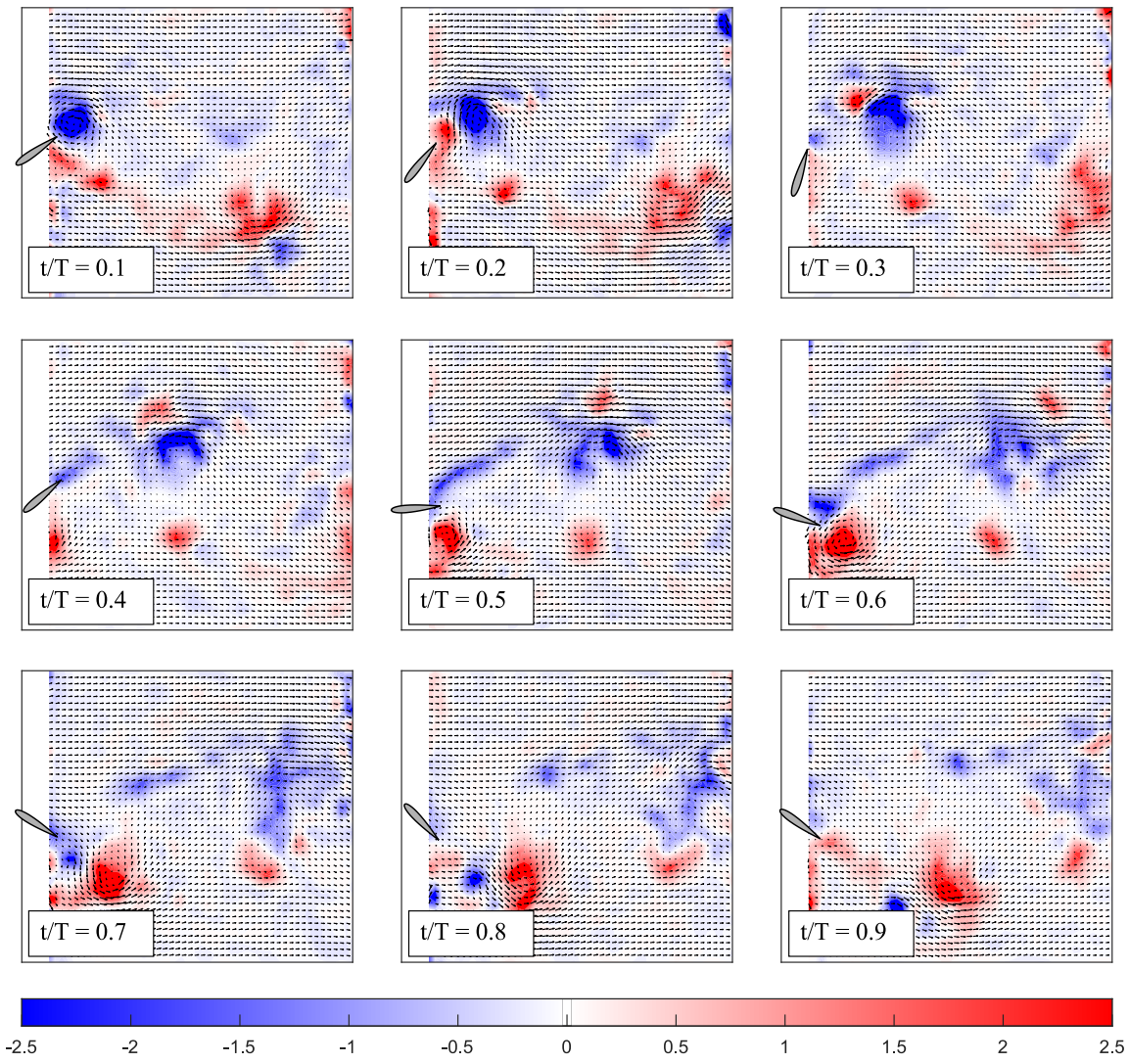

Figure 5.19: The same as Figure 5.17 but for the case $k_h = 5.83$ and $b_{he} = 0.26$.

5.5 Concluding remarks

In this chapter, we have explored the harvesting performance of a fully-passive flapping-foil turbine prototype, thus enriching the previous chapters of the thesis that were focused on the propulsion capacities of this flapping-foil technology. The prototype, based on the work performed by Boudreau et al. [2018], consists of a rigid foil elastically supported by springs in heave and pitch, as well as a damper in heave. This damper is used to model the energy conversion into electricity that would result from an electric generator. The foil is free to move in both pitching and heaving motions.

This work is primary focused on the performance characterization of the prototype for a wide range of different operating conditions. These conditions have been modified by selecting different spring configurations in heave and by changing the power of the magnetic damper. Particularly, 6×8 different operating conditions have been studied. For all of them, the temporal signals of the heave and pitch motions are recorded using two rotatory encoders. In addition, the forces and the momentum acted on the axis of the foil are also recorded with a force/torque transducer, which were not possible to measure with the Boudreau et al. [2018] experimental set up. Then, we have analyzed the mean values of several performance metrics, and the corresponding maps are presented. Thanks to the force and torque measurements, the power extracted from the turbine, as well as the efficiency of the prototype, can be studied. We have found that the best performance of the prototype is achieved for the baseline case (obtained with the softest spring and damper configuration) since it is associated with larger amplitudes in the foil's motion. The efficiency based on the power transmitted from the fluid to the foil is $\eta_f = 65\%$ for this configuration. However, the efficiency based on the effective power, i.e., obtained through the magnetic damper, is much lower $\eta_e = 2\%$. As it is explained in the chapter, this is because the power of the magnetic damper is very low for the baseline configuration. In contrast, the best harvesting performance is obtained by selecting the strongest damper and the softest spring configuration, with efficiencies of $\eta_f = 54\%$ and $\eta_e = 9\%$. Higher harvesting efficiency may be reached with stronger damper configurations, but unfortunately, our linear damper is not powerful enough.

Finally, to have a greater understanding of the flow structures involved in the foil's motion, some experiments have been conducted with the PIV technique. We have analyzed three different operating conditions for a fixed damping constant, which are the baseline case and two more cases with stronger spring configurations. The normalized spanwise vorticity field is presented in the results, and the effect of the dynamic stall is analyzed.

Chapter 6

Closure

6.1 Contribution of this thesis

To conclude, the main contributions of this thesis are summarized below.

Firstly, we have studied the self-propelled locomotion of a two-dimensional pitching foil. This study has been performed with an isolated foil, so the unsteady viscous friction needed to be modeled. To that end, high-resolution numerical simulations have been conducted for a wide range of frequency-based Reynolds numbers ($10^3 \lesssim Re_\omega \lesssim 10^4$). Then, two simplified models based on a combination of these simulations and the linear potential-flow theory for the Fluid-Structure Interaction (FSI) have been obtained. Particularly, two models for the unsteady thrust developed from the potential theory have been used, one from the results obtained by Theodorsen [1935] and Garrick [1936], and another one from the results obtained by Fernandez-Feria [2016]. The resulting Ordinary Differential Equation (ODE) for the swimming velocity has been solved numerically, and simple analytical expressions have been provided for small velocities. The two-scaled perturbation method was used for that purpose. The results were in good agreement with the simulations for small pitching amplitudes. Moreover, it has been found that the swimming velocity predicted by the two thrust models is quantitatively similar within their common validity range. However, the power-law dependencies on α_0 and Re_ω are also qualitatively different in each model. Additionally, the simplified model for the swimming velocity obtained with Fernandez-Feria's thrust has been found to work slightly better for very small α_0 over the whole Re_ω range and in the band closer to $Re_\omega = 10^3$ as α_0 increases. In contrast, the model with Garrick's thrust works better in the band closer to $Re_\omega = 10^4$ for increasing α_0.

The numerical simulations for this study have been performed with the Ansys Fluent solver for a thin flat plate. The FSI is mimicked by a User Defined Function (UDF) in a C program compiled in Fluent. Furthermore, the mesh is designed with two different regions: a background mesh and a moving mesh, which contains the plate. In order to keep the size of the initial domain constant, the layering algorithm is used as a dynamic mesh to destroy and build up the background mesh with the velocity of the center of mass of the plate. So the plate could continue its locomotion without collapsing with the wall. Therefore, this preliminary study results in a good starting point for this thesis because it explains and analyses

the physics involved in the flapping-foil propulsion with a prescribed pitching motion. It is also considered the unsteady viscous drag since the foil is not attached to the swimmer's body.

Secondly, we have investigated a theoretical model for an aquatic vehicle self-propelled by a rigid foil elastically mounted on the vehicle hull with translational and torsional springs and dampers that allow for passive heaving and pitching motions. The foil is actuated by a torque of small amplitude, which models the motor of the vehicle. The theoretical model has been based on the linear potential-flow theory, providing the lift, thrust, and moment coefficients on the foil, in combination with the dynamic equations to model the FSI of the passive flapping foil. A constant drag coefficient and an independent mass are used to model the vehicle. The three resulting ODEs (for heave, pitch, and swimming velocity) have been solved both numerically and analytically. The analytical approach has also been conducted through the two-scaled perturbation method, and simple expressions have been found for the heaving and pitching motions, the swimming velocity, the input power coefficient, the cost of transport, the efficiency, and the Strouhal number, all of them for small amplitudes. Additionally, a comparison with the high-resolution numerical simulations developed in the first study has been done. To that end, a simple modification in the UDF is required, so the new thrust equation is implemented. For that comparison, a specific α_0 value has been selected in order to match the same pitching amplitude, and a high frequency-based Reynolds number has been used since viscous effects are not considered in the flapping foil model.

The analytical solutions of the equations have been found to work fine far from the resonance of the system, however close to that region, they are not valid. It is through the numerical solution of the model equations that we obtain the adequate results in that region. Nevertheless, this analytical solution predicts really well the resonance of the system, which is proven to significantly enhance not only the swimming velocity but also the efficiency of the system. Then, thanks to the analytical approach, a simple expression for the resonant values of the heave and pitch springs has been proposed. It could be used to select the optimal frequencies of the input torque for a defined set of structural and geometric parameters. Notably, for a dimensionless torque intensity $\epsilon = 0.05$, the highest efficiency found is near 31%, with the highest non-dimensional swimming velocity close to 0.3, achieved in absence of dampers ($b_h \simeq b_\alpha \simeq 0$), negligible heaving motion ($k_h \gg 1$), i.e., for an almost pure pitching motion of the foil, and for the corresponding resonant value of the torsional spring constant ($k_\alpha \simeq 0.6$). Larger values of efficiency and non-dimensional swimming velocity could be found for a greater ϵ, but it have to remain small for the linear potential theory. In contrast, the minimum cost of transport near 0.007 is also observed for negligible b_h, but for b_α of order unity or larger (for which the value of k_α is larger than the one associated with the resonance), and k_h of order unity. Thus, the motion of the foil is more related to a pure heaving motion in that case. Therefore, this second study can be used as a guide for the design of an efficient bio-inspired aquatic vehicle. In fact, we have made a patent proposal for a water vehicle propulsion system based on these results.

Thirdly, we have studied the effect that flexibility on the foil roles for the theoretical model of the aquatic vehicle self-propelled by a foil that is proposed in the previous study. The theoretical model is similar to the one described above: the foil is also elastically mounted

on the vehicle hull with translational and torsional springs and dampers, and actuated by a torque of small amplitude to generate the pitch and heave motions. However, the passive flexural motion in the foil has been considered in this new approach. As a consequence, the new theoretical model considers the FSI through the Euler-Bernouilli beam equation in combination with the linear potential-flow theory, which now provides the lift, thrust, moment, and flexural moment coefficients on the foil. Also, with a constant drag coefficient and independent mass to model the aquatic vehicle. This Euler-Bernouilli equation models the self-propelled dynamics of the flapping foil, incorporating the flexibility of the propeller through a constant value, which is the stiffness ratio S. As before, the model is only valid for small amplitudes. The four resulting ODEs (for heave, pitch, flexural deflection, and swimming velocity) have been solved numerically and analytically. The two-scaled perturbation method has been used again for that purpose, and simple expressions are found for the heaving, pitching, and flexural deflection motions, the swimming velocity, the input power coefficient, the cost of transport, the efficiency, and the Strouhal number.

As in the previous model, the analytical solutions are found to work well far from the resonance of the system, while near that region, they are not valid. The proper results in that region are obtained again through the numerical solution of the model equations. This analytical solution also predicts accurately the resonant conditions for optimal performance. Furthermore, it has been found that the resonance is achieved for the same spring and damper configuration as in the rigid foil case, thus yielding the same simple expression obtained in the previous study. Additionally, the relation between the Strouhal and the Lighthill number has been widely analyzed, and the results have been compared favorably with experimental data for the most efficient swimming fishes in sustained cruise (Eloy [2012]). The maximum swimming velocity has been obtained for the pivot point location $a = -1$ when k_h is sufficiently large and k_α is close to the resonant value. These maxima of the swimming velocity have also been associated with the maxima of the cost of transport. However, the highest propulsive efficiencies, which are also reached for k_α close to its resonant value, have been found to increase as the stiffness S decreases, this being the main beneficial effect of the foil flexibility. These results for optimal efficiency have been observed for the Lighthill number range of most fishes whose primary mechanism for producing thrust is a prominent oscillatory caudal fin, $0.02 \lesssim Li \lesssim 0.2$, almost independently of the remaining parameters. As Li decreases, it has been observed that swimming velocity and efficiency are increased, and the cost of transport is decreased. Remarkably, for a dimensionless torque intensity $\epsilon = 0.05$ and a $Li \simeq 0.02$, the propulsive efficiency found is close to 45%. Below this Li, the swimming velocity may become slightly larger for a flexible foil than for its rigid counterpart, and the efficiency predicted by the model becomes larger than 50%. However, so low values of Li are not reached even by the most efficient fishes in sustained cruise. For a more reasonable value of the Lighthill number ($Li \simeq 0.1$), the maximum cruising speed, but with a higher associated cost of transport, has been achieved with a rigid foil ($S \simeq 10^3$), while maximum cruising efficiency has been obtained with a more flexible one ($S \simeq 10^2$). Specifically, efficiencies of 36% and 30% are found for those cases, respectively. Therefore, this third study can be considered an improved guide for the design of an efficient bio-inspired aquatic vehicle that takes into account the flexibility of the foil, which may improve the efficiency and cost of transport with almost no effect in the optimal thrust and swimming velocity.

Finally, an experimental investigation has been conducted on a novel fully-passive flapping-foil turbine. This prototype has been based on the work performed by Boudreau et al. [2018], which consists of a rigid foil elastically supported by springs in heave and in pitch as well as a magnetic damper in heave. The magnetic damper is used to model the energy-harvesting performance of the device, and the foil is free to move in both pitching and heaving directions. In this work, the performance characterization of the prototype has been analyzed for a wide range of different operating conditions with a fixed Reynolds number sufficiently high ($Re \simeq 22200$). Particularly, 6×8 different configurations have been studied. The heave, pitch, forces, and moment on the axis of the foil have been measured with two rotary encoders and a force/torque transducer. Average values over 90 cycles of the resulting temporal signals have been studied. Specifically, the averaged maps of the following magnitudes have been presented: the mean values of the heaving and pitching motions as well as their corresponding amplitudes, the frequency and the phase lag, the lift, drag, and moment coefficients, the power coefficients associated to the energy harvested from the magnetic damper (effective power) and the energy transmitted from the fluid to the foil, and their corresponding efficiencies. All of those maps have been presented and adequately analyzed. It has been found that the best performance of the prototype is achieved for the baseline case (obtained with the softest spring and damper configuration) with an efficiency based on the power transmitted from the fluid to the foil of $\eta_f = 65\%$. However, the efficiency based on the effective power is much lower $\eta_e = 2\%$ since the power of the damper is also very low for that configuration. In contrast, the best harvesting performance has been found with the strongest damper configuration while maintaining the softest springs in heave, yielding efficiencies of $\eta_f = 54\%$ and $\eta_e = 9\%$. Higher η_e efficiency may be reached, but unfortunately, our magnetic damper is not powerful enough. Additionally, three different operating conditions (including the baseline case) have been analyzed with the Particle Image Velocimetry (PIV) technique. The normalized spanwise vorticity field has been presented in the results, and the effect of the dynamic stall has been adequately studied. Being the results in good agreement with the ones obtained by Veilleux and Dumas [2017] and Boudreau et al. [2018]. The main contribution of this work, apart from the wide range of experimental data that has been analyzed, is the force and moment experimental analysis that allows the power and efficiency study of the device. These results, in combination with Appendix D, could be used as a guide to build and characterize better fully-passive flapping-foil turbines in future projects.

6.2 Future projects related to this thesis

During the work of this thesis, some new questions have appeared that we did not consider initially and can be the seed for future projects:

- Since we have developed the theoretical models for the bio-inspired aquatic vehicle, it would be interesting to build an experimental robotic prototype similar to the one developed by Sanchez-Rodriguez et al. [2021]. Thus, the theory could be experimentally checked for both rigid and flexible foils. Furthermore, different amplitudes of the foil's motion and different Reynolds numbers could be tested so that a more accurate range of validity for the models would be established. For the rigid foil, a standard NACA

profile could be used, while for the flexible one, a thin plate attached to a micro-NACA profile at the leading edge would be better. In this case, the stiffness ratio would be controlled through the thickness of the plate.

- Another exciting issue that we have not investigated yet is the effect that flexibility roles in the fully-passive flapping-foil turbine. It would be worthwhile to perform a work similar to the one developed for the turbine prototype but substituting the NACA0015 profile for a flexible thin plate configuration similar to the one mentioned above. Several thicknesses could be investigated, i.e., different stiffness ratios, and some maps could be presented for the best operating points obtained in this thesis. Moreover, it would provide helpful information about the efficiency of the device and how it could be modified just by adding some flexibility to the foil.

- On the other hand, all of our studies are focused on a single swimmer, and it has been well-studied that fish schooling can optimize the hydrodynamic interaction and save much energy (Weihs [1973]). For that reason, it would be interesting to investigate the influence and performance of several swimmers for both cases, the aquatic vehicle prototype and the flapping-foil turbine. Also, the theory could be modified to take into account that effect, and so it could be compared with the experiments. At first, we are content to understand the interaction within the smallest possible group, that is, between two aquatic vehicles or two flapping-foil turbines. Different sets of amplitudes, frequencies, and distances could be tested in both prototypes.

Appendices

Appendix A

Vortical impulse theory, coefficients, and parameters

In this first appendix, we will briefly revisit the linearized vortical impulse theory as it is depicted in Fernandez-Feria [2016] to understand better where the main equations and coefficients come from. We will cover both rigid and flexible formulations. So, we consider a two-dimensional, incompressible, and inviscid flow over a flapping thin foil of chord c that translates with speed $\tilde{u}$ along the $\tilde{x}$-axis (see Figure A.1 for more clarity). The vertical amplitudes of the heaving, pitching, and flexural motions are all very small compared to the chord length so that the foil and every point of the trail of vortices that it leaves behind can be considered to be upon the $\tilde{x}$ axis.

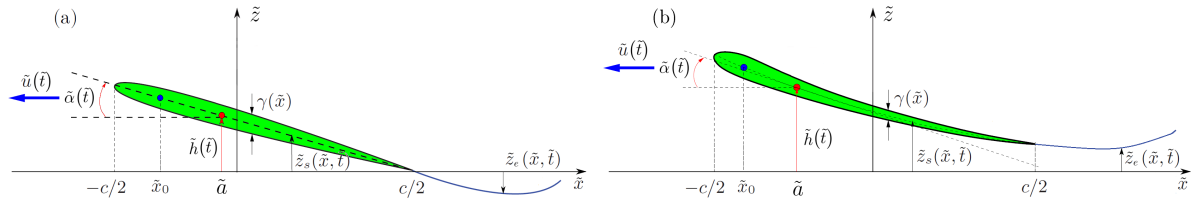

Figure A.1: Schematic of a self-propel flapping foil and its wake for (a) a pitching and heaving rigid case and (b) a pitching and heaving flexible case.

A.1 Linearized vortical impulse theory for a rigid foil

Considering first the rigid case, which is easier to understand, the motion of the foil is given by the vertical displacement

$$\tilde{z}_s\left(\tilde{x},\tilde{t}\right) = \tilde{h}(\tilde{t}) - (\tilde{x}-\tilde{a})\,\tilde{\alpha}(\tilde{t}), \quad \text{with } -c/2 \le \tilde{x} \le c/2, \tag{A.1}$$

where

$$\tilde{h}(\tilde{t}) = \Re\left[\tilde{h}_0 e^{i\omega\tilde{t}}\right], \quad \tilde{\alpha}(\tilde{t}) = \Re\left[\tilde{\alpha}_0 e^{i\omega\tilde{t}}\right], \tag{A.2}$$

being ω the frequency of the oscillations of both heaving motion $\tilde{h}(\tilde{t})$ and pitching rotation $\tilde{\alpha}(\tilde{t})$ around the pivot point $\tilde{x} = \tilde{a}$, and $\Re$ denotes real part. The amplitudes $\tilde{h}_0$ and $\tilde{\alpha}_0$ are complex constants that satisfy $|\tilde{h}_0| \ll c$ and $|\tilde{\alpha}_0| \ll 1$ since the linearized theory is considered. Notice that we use a *tilde* to remark that the variable is in the dimensional form to distinguish it from its dimensionless counterpart. On the other hand, the vertical velocity of the foil is

$$\tilde{v}_0\left(\tilde{x},\tilde{t}\right) = \dot{\tilde{h}} - \left(\tilde{x}-\tilde{a}\right)\dot{\tilde{\alpha}} - \tilde{u}\tilde{\alpha}, \tag{A.3}$$

where a dot denotes the time derivative. Now, the vortical impulse theory for an incompressible and unbounded flow can be used to obtain the forces and moment on the foil (Wu [1981]). Neglecting the volume (section) of the foil, one may obtain

$$\mathbf{F} = D\mathbf{e}_{\tilde{\mathbf{x}}} + L\mathbf{e}_{\tilde{\mathbf{z}}} = -\rho\frac{d\mathbf{I}}{d\tilde{t}}, \tag{A.4}$$

where D is the drag force (or minus the thrust), L the lift force, both per unit span, ρ the fluid density, and $\mathbf{I}$ the vortical impulse (or vorticity moment), defined as

$$\mathbf{I} = \int_{\mathcal{V}} \tilde{\mathbf{x}} \wedge \tilde{\boldsymbol{\omega}} d\mathcal{V}, \tag{A.5}$$

being $\tilde{\boldsymbol{\omega}} = \nabla \wedge \tilde{\mathbf{v}}$ the vorticity field and $\mathcal{V}$ the entire volume, or section, occupied by the fluid and the foil. This volume is considered to be unbounded, and that the flow is potential far from the foil. In the thin foil theory, it is assumed that the vorticity, which is directed along the normal $\mathbf{e}_{\tilde{\mathbf{y}}}$ to the plane of the fluid motion, is concentrated at the foil surface and the trailing wake, and both are considered as vortex sheets. So

$$\mathbf{I} \simeq \int_{-c/2}^{c/2} \left(-\tilde{z}_s\tilde{\omega}_s\boldsymbol{e}_{\tilde{\boldsymbol{x}}} + \tilde{x}\tilde{\omega}_s\boldsymbol{e}_{\tilde{\boldsymbol{z}}}\right) d\tilde{x} + \int_{c/2}^{\infty} \left(-\tilde{z}_e\tilde{\omega}_e\boldsymbol{e}_{\tilde{\boldsymbol{x}}} + \tilde{x}\tilde{\omega}_e\boldsymbol{e}_{\tilde{\boldsymbol{z}}}\right) d\tilde{x}, \tag{A.6}$$

being $\tilde{\omega}_s\left(\tilde{x},\tilde{t}\right)$, with $-c/2 \le \tilde{x} \le c/2$, the vorticity density distribution on the foil, $\tilde{\omega}_e\left(\tilde{x},\tilde{t}\right)$ the vorticity density distribution in the trailing wake, and $\tilde{z}_e\left(\tilde{x},\tilde{t}\right)$ the vertical position of each point in that vortex wake. It is considered the large-time behavior in which the vortex wake sheet extends many chord lengths downstream of the foil so that, in first approximation, $c/2 \le \tilde{x} \le \infty$ for $\tilde{\omega}_e\left(\tilde{x},\tilde{t}\right)$ and for $\tilde{z}_e\left(\tilde{x},\tilde{t}\right)$, with $|\tilde{z}_e| \ll c$ because of linearized theory. Thus, under these assumptions, the drag and lift forces on the foil are given by

$$D = \rho\frac{d}{d\tilde{t}}\int_{-c/2}^{c/2} \tilde{z}_s\tilde{\omega}_s d\tilde{x} + \rho\frac{d}{d\tilde{t}}\int_{c/2}^{\infty} \tilde{z}_e\tilde{\omega}_e d\tilde{x}, \tag{A.7}$$

$$L = -\rho\frac{d}{d\tilde{t}}\int_{-c/2}^{c/2} \tilde{x}\tilde{\omega}_s d\tilde{x} - \rho\frac{d}{d\tilde{t}}\int_{c/2}^{\infty} \tilde{x}\tilde{\omega}_e d\tilde{x}. \tag{A.8}$$

The vortical impulse theory also provides the moment on the foil

$$\mathbf{M} = M\mathbf{e}_{\tilde{\mathbf{y}}} = -\rho\frac{d\mathbf{A}}{d\tilde{t}}, \tag{A.9}$$

being $\mathbf{A}$ the angular impulse, which is defined as

$$\mathbf{A} = -\frac{1}{2}\int_{\mathcal{V}} |\tilde{\mathbf{x}}|^2 \tilde{\boldsymbol{\omega}} d\mathcal{V} \simeq -\frac{1}{2}\mathbf{e}_{\tilde{\mathbf{y}}} \left(\int_{-c/2}^{c/2} \tilde{x}^2 \tilde{\omega}_s d\tilde{x} + \int_{c/2}^{\infty} \tilde{x}^2 \tilde{\omega}_e d\tilde{x} \right). \tag{A.10}$$

The lift and moment were obtained for an oscillating thin foil from this vortical impulse theory by von Kármán and Sears [1938], reproducing previous results by Theodorsen [1935] from standard potential-flow theory. Thus, taking into consideration the modification made by Greeberg [1947] with additional terms proportional to $\dot{u}$ to account for the pulsating stream, the final non-dimensional coefficients obtained for the rigid flapping foil case (adapted for the self-propulsion)[1] are the followings (see Fernandez-Feria [2016] for more details)

$$\hat{C}_L = \frac{8L}{\pi\rho c^3\omega^2} = -\dot{v} - a\ddot{\alpha} + u\dot{\alpha} + \dot{u}\alpha + \Re[C(k)]u\Gamma_0(t), \tag{A.11}$$

$$\begin{aligned}\hat{C}_M = \frac{8M}{\pi\rho c^4\omega^2} = \frac{1}{2}\left[a\dot{v} + \left(a^2 + \frac{1}{8}\right)\ddot{\alpha} + \left(\frac{1}{2} - a\right)u\dot{\alpha} - a\dot{u}\alpha\right] \\ - \frac{1}{2}\left(\frac{1}{2} + a\right)\Re[C(k)]u\Gamma_0(t),\end{aligned} \tag{A.12}$$

$$\begin{aligned}\hat{C}_T = \frac{8T}{\pi\rho c^3\omega^2} = -\alpha\hat{C}_L + \dot{\alpha}\left[v + a\dot{\alpha} - u\alpha\right] + \Gamma_0(t)\Bigg\{\Re\left[\frac{2iC_1(k)}{\pi}\right] \\ \cdot\left[-v + 2\alpha u + (1-a)\dot{\alpha}\right] - \Re[C(k)]u\alpha\Bigg\},\end{aligned} \tag{A.13}$$

with Theodorsen's function $C(k)$ appearing in the circulatory terms evaluated at variable $k(t) = 1/u(t)$, and where

$$\Gamma_0(t) = -2\left[v + \left(a - \frac{1}{2}\right)\dot{\alpha} - u\alpha\right], \tag{A.14}$$

$$C(k) = \frac{H_1^{(2)}(k)}{iH_0^{(2)}(k) + H_1^{(2)}(k)} = \mathcal{F}(k) + i\mathcal{G}(k), \tag{A.15}$$

$$C_1(k) = \frac{\frac{1}{k}e^{-ik}}{iH_0^{(2)}(k) + H_1^{(2)}(k)} = \mathcal{F}_1(k) + i\mathcal{G}_1(k), \tag{A.16}$$

being $H_n^{(2)}(z) = J_n(z) - iY_n(z)$, with $n = \{0, 1\}$ the Hankel's function of the second kind and order n, related to the Bessel functions of the first and second kind $J_n(z)$ and $Y_n(z)$. Also, notice that all the parameters that appear in the coefficients are in their non-dimensional form scaled with ω, $c/2$, and ρ.

[1]Note that for self-propulsion we non-dimensionalize the force and moment with $\pi\rho c^3\omega^3/8$ and $\pi\rho c^4\omega^2/8$, respectively, instead of $\rho U_\infty^2 c/2$ and $\rho U_\infty^2 c^2/2$, because u is not constant. For that reason, we distinguish the coefficients with a *hat*. In addition, there are new terms related to $\dot{u}$.

A.2 Linearized vortical impulse theory for a flexible foil

Considering now a flexible flapping foil, a quartic approximation can be assumed for the vertical displacement of the foil, as it is well conducted in Fernandez-Feria and Alaminos-Quesada [2021a]. Thus, it can be defined as

$$\begin{aligned}\tilde{z}_s\left(\tilde{x},\tilde{t}\right) = \tilde{h}(\tilde{t}) - \left(\tilde{x}-\tilde{a}\right)\tilde{\alpha}(\tilde{t}) + \left(\tilde{x}-\tilde{a}\right)^2\tilde{d}(\tilde{t}) - \left(\tilde{x}-\tilde{a}\right)^3\frac{2\tilde{d}(\tilde{t})}{3\left(c/2-\tilde{a}\right)} \\ + \left(\tilde{x}-\tilde{a}\right)^4\frac{\tilde{d}(\tilde{t})}{6\left(c/2-\tilde{a}\right)^2}, \quad \text{with } -c/2\le\tilde{x}\le c/2,\end{aligned} \tag{A.17}$$

which accounts for the heaving and pitching motions, $\tilde{h}(\tilde{t})$ and $\tilde{\alpha}(\tilde{t})$, respectively, at $\tilde{x}=\tilde{a}$, and for a free trailing edge, $\partial^2\tilde{z}_s/\partial\tilde{x}^2 = \partial^3\tilde{z}_s/\partial\tilde{x}^3 = 0$ at $\tilde{x}=c/2$. On the other hand, $\tilde{d}(\tilde{t})$ is the flexural motion of the foil. As in the previous case, it is assumed that

$$\tilde{h}(\tilde{t}) = \Re\left[\tilde{h}_0 e^{i\omega\tilde{t}}\right], \quad \tilde{\alpha}(\tilde{t}) = \Re\left[\tilde{\alpha}_0 e^{i\omega\tilde{t}}\right], \quad \tilde{d}(\tilde{t}) = \Re\left[\tilde{d}_0 e^{i\omega\tilde{t}}\right], \tag{A.18}$$

being the amplitude $\tilde{d}_0$ another complex constant that, again, satisfy $|\tilde{d}_0| \ll c$ due to the linearized theory. The vertical velocity of the foil will be

$$\begin{aligned}\tilde{v}_0\left(\tilde{x},\tilde{t}\right) = \dot{\tilde{h}} - \left(\tilde{x}-\tilde{a}\right)\dot{\tilde{\alpha}} - \tilde{u}\tilde{\alpha} + \left(\tilde{x}-\tilde{a}\right)^2\dot{\tilde{d}} + 2\left(\tilde{x}-\tilde{a}\right)\tilde{u}\tilde{d} - \left(\tilde{x}-\tilde{a}\right)^3\frac{2\dot{\tilde{d}}}{3\left(c/2-\tilde{a}\right)} \\ - 2\left(\tilde{x}-\tilde{a}\right)^2\frac{\tilde{u}\tilde{d}}{\left(c/2-\tilde{a}\right)} + \left(\tilde{x}-\tilde{a}\right)^4\frac{\dot{\tilde{d}}}{6\left(c/2-\tilde{a}\right)^2} + 2\left(\tilde{x}-\tilde{a}\right)^3\frac{\tilde{u}\tilde{d}}{3\left(c/2-\tilde{a}\right)^2}.\end{aligned} \tag{A.19}$$

Thus, following the same procedure as that of the rigid case, one may obtain the new coefficients corresponding to a flexible flapping foil adapted for the self-propulsion in non-dimensional format (for details, see Fernandez-Feria and Alaminos-Quesada [2021a]).

$$\hat{C}_L = \frac{8L}{\pi\rho c^3\omega^2} = -\dot{v} - a\ddot{\alpha} + u\dot{\alpha} + \dot{u}\alpha + A_{l2}(a)\ddot{d} + A_{l1}(a)(u\dot{d}+\dot{u}d) + \Re[C(k)]u\Gamma_0(t), \tag{A.20}$$

$$\begin{aligned}\hat{C}_M = \frac{8M}{\pi\rho c^4\omega^2} = \frac{1}{2}\Bigg[a\dot{v} + \left(a^2+\frac{1}{8}\right)\ddot{\alpha} + \left(\frac{1}{2}-a\right)u\dot{\alpha} - a\dot{u}\alpha + A_{m2}(a)\ddot{d} + A_{m1}(a)u\dot{d} \\ + A_{m0}(a)u^2 d\Bigg] - \frac{1}{2}\left(\frac{1}{2}+a\right)\Re[C(k)]u\Gamma_0(t),\end{aligned} \tag{A.21}$$

$$\begin{aligned}\hat{C}_F = \frac{32F}{\pi\rho c^5\omega^2} = -\left(a^2+\frac{1}{4}\right)\dot{v} - a\left(a^2+\frac{1}{2}\right)\ddot{\alpha} + a(a-1)u\dot{\alpha} + A_{f2}(a)\ddot{d} + A_{f1}(a)u\dot{d} \\ + A_{f0}(a)u^2 d + \left(\frac{1}{2}+a+a^2\right)\Re[C(k)]u\Gamma_0(t),\end{aligned} \tag{A.22}$$

$$\begin{aligned}\hat{C}_T = \frac{8T}{\pi\rho c^3\omega^2} = &-(\alpha+2ad)\hat{C}_L + \frac{d}{2}\left(\frac{\ddot{\alpha}}{2} + a\ddot{d} - u\dot{d}\right) + \frac{\dot{d}}{2}\left(\frac{\dot{\alpha}}{2} + a\dot{d} - ud\right) + (\dot{\alpha}+2a\dot{d}) \\ &\cdot\left\{v + a\dot{\alpha} + \left(a^2+\frac{1}{4}\right)\dot{d} - u(\alpha+2ad) + \Gamma_0(t)\Re\left[\frac{i}{k}C(k) + \left(\frac{1+ik}{k}\right)\frac{2}{\pi}C_1(k)\right]\right\} \\ &- \left[v + a\dot{\alpha} - u(\alpha+2ad) + a^2\dot{d}\right]\Gamma_0(t)\Re\left[\frac{2i}{\pi}C_1(k)\right] \\ &- d\Gamma_0(t)\Re\left[iC_2(k) + 2\left(\frac{1+ik}{k}\right)\frac{2}{\pi}C_1(k)\right] \\ &+ \dot{d}\Gamma_0(t)\Re\left[\left(\frac{2i}{k^2} - \frac{2+ik}{k}\right)\frac{2}{\pi}C_1(k) - \frac{C_2(k)}{k}\right],\end{aligned} \tag{A.23}$$

with a new and extended-expression for $\Gamma_0(t)$

$$\Gamma_0(t) = -2\left[v + \left(a - \frac{1}{2}\right)\dot{\alpha} - u\alpha + A_{g1}(a)\dot{d} + A_{g0}(a)ud\right]. \tag{A.24}$$

The functions $C(k)$ and $C_1(k)$ remain the same as the rigid case, but a new function $C_2(k)$ appears, which is defined by

$$C_2(k) = \frac{H_2^{(2)}(k)}{iH_0^{(2)}(k) + H_1^{(2)}(k)} = \mathcal{F}_2(k) + i\mathcal{G}_2(k). \tag{A.25}$$

Again, with all the parameters in non-dimensional form and a new coefficient $\hat{C}_F$ related to the *flexural moment* of the foil. On the other hand, the constants involved in the above coefficients are the following

$$A_{l2} = -\frac{13+48a^2-64a^3+24a^4}{48(1-a)^2}, \quad A_{l1} = \frac{3+12a-12a^2+4a^3}{6(1-a)^2}, \tag{A.26}$$

$$A_{m2} = \frac{2+25a-12a^2+52a^3-64a^4+24a^5}{48(1-a)^2}, \tag{A.27}$$

$$A_{m1} = \frac{-9+12a-72a^2+56a^3-16a^4}{24(1-a)^2}, \quad A_{m0} = \frac{3}{4(1-a)^2}, \tag{A.28}$$

$$A_{f2} = -\frac{35+32a+392a^2-320a^3+496a^4-512a^5+192a^6}{384(1-a)^2}, \tag{A.29}$$

$$A_{f1} = \frac{1+8a-18a^2+48a^3-32a^4+8a^5}{12(1-a)^2}, \quad A_{f0} = \frac{7+18a}{12(1-a)^2}, \tag{A.30}$$

$$A_{g1} = \frac{15-48a+96a^2-80a^3+24a^4}{48(1-a)^2}, \quad A_{g0} = \frac{3-24a+24a^2-8a^3}{12(1-a)^2}. \tag{A.31}$$

A.3 Definition of some other parameters appearing in the main text

Taking into account the flexible formulation developed in Chapter 4, one may obtain the following parameters (in dimensional form) that appear during the several integrations of the Euler-Bernoulli beam equation

$$m = \int_{-c/2}^{c/2} \rho_s \gamma d\tilde{x}, \quad m\tilde{x}_0 = \int_{-c/2}^{c/2} \tilde{x}\rho_s \gamma d\tilde{x}, \tag{A.32}$$

$$\tilde{J}_a = \int_{-c/2}^{c/2} \left[(\tilde{x}-\tilde{a})^2 - \frac{2}{3}\frac{(\tilde{x}-\tilde{a})^3}{c/2-\tilde{a}} + \frac{(\tilde{x}-\tilde{a})^4}{6\,(c/2-\tilde{a})^2} \right] \rho_s \gamma d\tilde{x}, \tag{A.33}$$

$$\tilde{I}_a = \int_{-c/2}^{c/2} (\tilde{x}-\tilde{a})^2 \,\rho_s \gamma d\tilde{x}, \;\; \tilde{J}_d = \int_{-c/2}^{c/2} \left[(\tilde{x}-\tilde{a})^3 - \frac{2}{3}\frac{(\tilde{x}-\tilde{a})^4}{c/2-\tilde{a}} + \frac{(\tilde{x}-\tilde{a})^5}{6\,(c/2-\tilde{a})^2} \right] \rho_s \gamma d\tilde{x}, \tag{A.34}$$

$$\tilde{I}_d = \int_{-c/2}^{c/2} (\tilde{x}-\tilde{a})^3 \,\rho_s \gamma d\tilde{x}, \;\; \tilde{K}_d = \int_{-c/2}^{c/2} \left[(\tilde{x}-\tilde{a})^4 - \frac{2}{3}\frac{(\tilde{x}-\tilde{a})^5}{c/2-\tilde{a}} + \frac{(\tilde{x}-\tilde{a})^6}{6\,(c/2-\tilde{a})^2} \right] \rho_s \gamma d\tilde{x}, \tag{A.35}$$

where ρ_s is the density of the foil, γ its thickness, m its mass per unit span, $\tilde{x}_0$ its center of mass, and $\tilde{I}_a$ its moment of inertia. Working now with the non-dimensional form of these parameters (see Chapter 4), and assuming that the product $\rho_s \gamma c/m = \mathcal{M}$ is a constant, one may obtain

$$x_0 = \frac{1}{2}\int_{-1}^{1} x\mathcal{M}dx, \;\; J_a = \frac{1}{2}\int_{-1}^{1} \left[(x-a)^2 - \frac{2}{3}\frac{(x-a)^3}{1-a} + \frac{(x-a)^4}{6(1-a)^2} \right] \mathcal{M}dx, \tag{A.36}$$

$$I_a = \frac{1}{2}\int_{-1}^{1} (x-a)^2\mathcal{M}dx, \;\; J_d = \frac{1}{2}\int_{-1}^{1} \left[(x-a)^3 - \frac{2}{3}\frac{(x-a)^4}{c/2-a} + \frac{(x-a)^5}{6(c/2-a)^2} \right] \mathcal{M}dx, \tag{A.37}$$

$$I_d = \frac{1}{2}\int_{-1}^{1} (x-a)^3\mathcal{M}dx, \;\; K_d = \frac{1}{2}\int_{-1}^{1} \left[(x-a)^4 - \frac{2}{3}\frac{(x-a)^5}{c/2-a} + \frac{(x-a)^6}{6(c/2-a)^2} \right] \mathcal{M}dx. \tag{A.38}$$

Finally, taking $\mathcal{M} = 1$ and $x_0 = 0$, the integrals can be solved

$$J_a = \frac{1}{2}\left[a^2 - \frac{2}{3}a - \frac{1}{3} + \frac{16}{15(1-a)^2} \right], \tag{A.39}$$

$$I_a = a^2 + \frac{1}{3}, \;\; J_d = \frac{-12 - 93a + 60a^2 - 110a^3 + 120a^4 - 45a^5}{90(1-a)^2}, \tag{A.40}$$

$$I_d = -a\left(1+a^2\right), \;\; K_d = \frac{141 + 168a + 1281a^2 - 1120a^3 + 1015a^4 - 840a^5 + 315a^6}{630(1-a)^2}. \tag{A.41}$$

Appendix B

Perturbation Methods: Multiple-Scale Method

In this second appendix, we will briefly cover the perturbation methods, particularly the multiple-scale method, since they constitute the basis of the analytical work developed in this thesis, especially in Chapter 3 and Chapter 4.

So, as an introduction to the matter, it is well known that engineers, physicists, and mathematicians have to face many equations and do not always have an exact analytical solution, e.g., nonlinearities, variable coefficients, complex boundary shapes, nonlinear boundary conditions, or even unknown boundaries can cause it. However, some methods can be used to find an approximate solution for those problems. The perturbation (asymptotic) methods are some of the most relevant ones that are commonly used by the scientific community. These methods can be used when there are some small parameters in the mathematical description of the problem, of course, written in non-dimensional form. Thus, following this spirit, one may assume a straightforward expansion of an asymptotic solution to solve the governing equation, which can be developed in a power series of the desired variable, $x(t)$ in this case

$$x(t) = x_0(t) + \epsilon x_1(t) + \epsilon^2 x_2(t) + \cdots = \sum_{i=0}^{\infty} \epsilon^i x_i(t), \tag{B.1}$$

being ϵ the small parameter mentioned above. This expansion assumes that the zeroth-order power constitutes the first and simplest solution to the problem (without perturbation). If more terms are added, the approximation is refined and more accurate. However, these added terms tend to be smaller and smaller as the power is increased, so the main contribution to the approximate solution is generally made by the two first terms of the expansion. This asymptotic method can be very useful to solve some governing equations but utterly fails in other systems when different time scales are involved. The prototypical example where this kind of expansion does not work is the harmonic oscillator with small damping, which we are going to briefly revisit (see Nayfeh [2008] for a deeper analysis and explanation). The ordinary differential equation (ODE) is the following

$$\ddot{x} + 2\epsilon\dot{x} + x = 0, \quad \text{with } x(0) = 0,\ \dot{x}(0) = 1, \tag{B.2}$$

where a *dot* denotes a derivative with respect to time. This ODE has an exact solution that, in general form, is

$$x(t) = e^{-\epsilon t}\left(Ce^{i\sqrt{1-\epsilon^2}t} + C^* e^{-i\sqrt{1-\epsilon^2}t}\right), \tag{B.3}$$

where C is an arbitrary complex constant and C^* its conjugate form. By taking into consideration the initial conditions, the solution yields to

$$x(t) = \frac{1}{\sqrt{1-\epsilon^2}} e^{-\epsilon t}\sin(\sqrt{1-\epsilon^2}\ t). \tag{B.4}$$

Performing a straightforward expansion (as it is shown in Equation (B.1)), substituting that into the general Equation (B.2) and separating the terms in function of the ϵ order, one may find

$$\begin{aligned} \ddot{x}_0 + x_0 &= 0, \\ \ddot{x}_1 + x_1 &= -2\dot{x}_0, \end{aligned} \tag{B.5}$$

for the first two terms of the expansion. By solving these equations, it is found

$$\begin{aligned} x_0(t) &= C_0 e^{it} + C_0^* e^{-it}, \\ x_1(t) &= C_1 e^{it} + C_1^* e^{-it} - C_0 t e^{it} - C_0^* t e^{-it}, \\ x(t) &= \left(C_0 e^{it} + C_0^* e^{-it}\right) + \epsilon\left(C_1 e^{it} + C_1^* e^{-it} - C_0 t e^{it} - C_0^* t e^{-it}\right) + \cdots, \end{aligned} \tag{B.6}$$

and applying the initial conditions, the solution simplifies to

$$x(t) = \sin(t) - \epsilon t\sin(t) + O\left(\epsilon^2\right). \tag{B.7}$$

It is evident that the obtained expression is a bad approximation for x as t becomes large because the second term is not small compared to x_0 (it contains secular terms). Hence, the assumption made at the beginning is no longer valid. The failure of the straightforward expansion can be seen by investigating the exact solution. It is clear that $\exp(\epsilon t)$ can be approximated by a finite number of terms only if the combination ϵt is small, and when t becomes large, the approximation breaks down. Therefore, in order to determine a truncated expansion valid for all t up to $O(\epsilon^{-M})$, where M is a positive integer, we must determine the dependence of x on the $M+1$ different time scales $t_0, t_1, \ldots, t_M$, where

$$t_i = \epsilon^i t, \tag{B.8}$$

being time scale t_n always slower than t_{n-1}. Thus, it can be assumed that

$$x(t;\epsilon) = \tilde{x}(t_0, t_1, \ldots, t_M; \epsilon) = \sum_{i=0}^{M-1} \epsilon^i x_i(t_0, t_1, \ldots, t_M) + O(\epsilon t_M). \tag{B.9}$$

This expansion is only valid for times up to $O(\epsilon^{-M})$, and beyond these times, we must use other time scales to keep the expansion uniformly valid. Now, the original problem has been transformed from an ODE to a partial differential equation (PDE). So, by using the chain rule, the time derivatives are transformed according to

$$\frac{d}{dt} = \frac{\partial}{\partial t_0} + \epsilon\frac{\partial}{\partial t_1} + \epsilon^2\frac{\partial}{\partial t_2} + \cdots. \tag{B.10}$$

Substituting these new definitions in the general equation and equating coefficients of like powers of ϵ, equations can be obtained for determining $x_0, x_1, \ldots, x_M$. The solutions of these equations contain arbitrary functions of the time scales $t_1, t_2, \ldots, t_M$. In order to determine these functions, additional conditions need to be imposed, i.e., the higher approximations need to be no more singular than the first term, which means we need to eliminate the secular terms (compatibility condition). Thus, applying the multiple-scale method to our example, we have

$$x(t) = x(t_0, t_1), \quad \text{with } t_0 = t,\ t_1 = \epsilon t. \tag{B.11}$$

So Equation (B.2) turns to

$$\left(\frac{\partial^2 x}{\partial t_0^2} + 2\epsilon\frac{\partial^2 x}{\partial t_0 \partial t_1} + \epsilon^2\frac{\partial^2 x}{\partial t_1^2}\right) + 2\epsilon\left(\frac{\partial x}{\partial t_0} + \epsilon\frac{\partial x}{\partial t_1}\right) + x = 0, \tag{B.12}$$

with initial conditions $x(0,0) = 0$ and $\partial x(0,0)/\partial t_0 + \epsilon \partial x(0,0)/\partial t_1 = 1$. Thus, proceeding in the same manner as in the straightforward expansion, one may find the next PDEs for the two first ϵ orders

$$\begin{aligned} \frac{\partial^2 x_0}{\partial t_0^2} + x_0 &= 0, \\ \frac{\partial^2 x_1}{\partial t_0^2} + x_1 &= -2\frac{\partial x_0}{\partial t_0} - 2\frac{\partial^2 x_0}{\partial t_0 \partial t_1}. \end{aligned} \tag{B.13}$$

The general solution for the first order is

$$x_0(t_0, t_1) = C_0(t_1)e^{it_0} + C_0^*(t_1)e^{-it_0}. \tag{B.14}$$

So, the second-order equations become

$$\frac{\partial^2 x_1}{\partial t_0^2} + x_1 = -2i\left(C_0(t_1)e^{it_0} - C_0^*(t_1)e^{-it_0}\right) - 2i\left(\frac{dC_0}{dt_1}e^{it_0} - \frac{dC_0^*}{dt_1}e^{-it_0}\right). \tag{B.15}$$

Here, we need to apply the additional condition to avoid secular terms, which is

$$\begin{aligned} -2iC_0(t_1)e^{it_0} - 2i\frac{dC_0}{dt_1}e^{it_0} &= 0, \\ 2iC_0^*(t_1)e^{-it_0} + 2i\frac{dC_0^*}{dt_1}e^{-it_0} &= 0. \end{aligned} \tag{B.16}$$

Notice that to obtain the complete solution for the first order, we need to analyze the second order since we do not know the dependence of $C_0(t_1)$ and $C_0^*(t_1)$, and it is provided by the compatibility condition. This compatibility process has to be repeated for each order of the expansion. Thus, one may obtain the general approximate solution

$$\begin{aligned} x_0(t_0, t_1) &= e^{-t_1}\left(K_0 e^{it_0} + K_0^* e^{-it_0}\right), \\ x_1(t_0, t_1) &= C_1(t_1)e^{it_0} + C_1^*(t_1)e^{-it_0}, \\ x(t_0, t_1) &= e^{-t_1}\left(K_0 e^{it_0} + K_0^* e^{-it_0}\right) + \cdots. \end{aligned} \tag{B.17}$$

By taking into account the initial conditions, the solution simplifies to

$$x(t) = e^{-\epsilon t}\left(\frac{1}{2i}e^{it} - \frac{1}{2i}e^{-it}\right) + O(\epsilon) = e^{-\epsilon t}\sin(t) + O(\epsilon). \tag{B.18}$$

In Figure B.1, we can see a comparison between the different approximations (the straightforward expansion and the multiple-scale method) and the exact analytical solution for the harmonic damped oscillator here presented considering $\epsilon = 0.1$ and the initial conditions proposed. It shows how the straightforward expansion utterly fails when t begins to be large. The multiple-scale method fixes the two-time scale problem, providing an excellent approximation to the real solution.

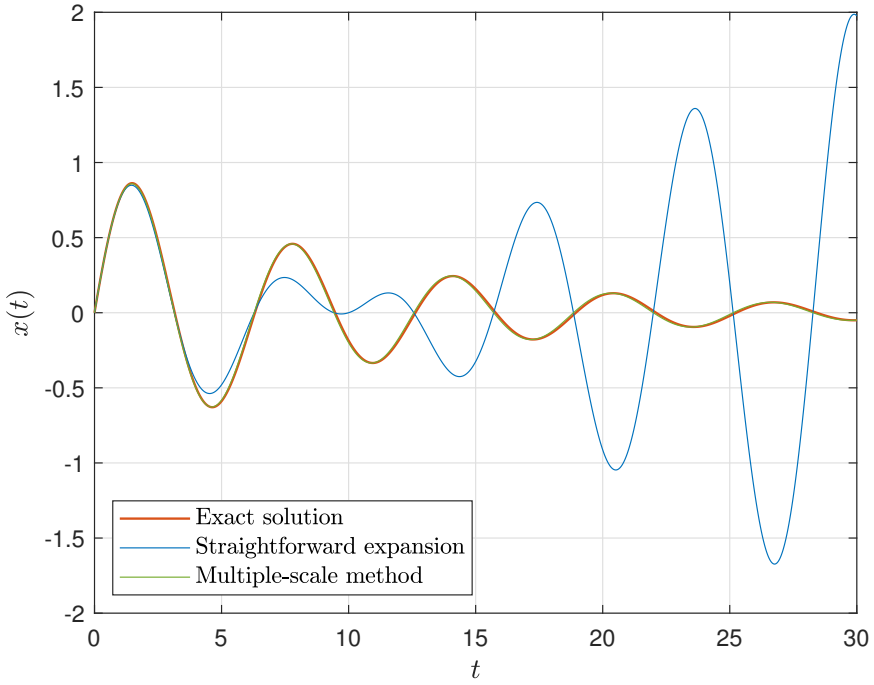

Figure B.1: Comparison of the analytical solution of Equation B.2 with the approximations made by the straightforward expansion and the multiple-scale method, for $\epsilon = 0.1$ and with initial conditions $x(0) = 0$ and $\dot{x}(0) = 1$.

This procedure presented for the asymptotic method applied to the harmonic damped oscillator problem will serve as a guide to understand better how to implement that and an example of the powerful tools that are the perturbation methods. In Chapter 3 and Chapter 4, we use this exact process, but more elaborated since the governing equations are more complex. However, the basis of the method is the same. In search of clarity, we have shown this prototypical example so the mathematical process developed in the manuscript will be easier to follow.

Appendix C

Solving the system of ordinary differential equations

In this third appendix, we will explain the technique employed in Chapter 3 and Chapter 4 to solve numerically the system of ordinary differential equations through the commercial solver Matlab. This solver has a very complete and practical set of tools to solve differential equations. One of them is the *odeset* package, and particularly, the *mass matrix* function is really helpful when solving huge ODE systems. This ode solver can solve problems containing a mass matrix of the form

$$M(t,y)\dot{y} = f(t,y), \tag{C.1}$$

where $M(t,y)$ is the mass matrix, t the time evolution, y a vector containing all the unknown variables, and $f(t,y)$ a vector with the remaining terms of the equations. The *odeset* environment is used to select the mass matrix system for solving the differential equations, and then regular ode solvers can be used to obtain the solution. In this thesis, we have selected *ode45* for all cases (except otherwise specified). By following this procedure, one can solve the large ODE system with just two simple code lines

```
options = odeset('Mass',@mass);
[t,y] = ode45(@f,t,y0,options);
```

being `mass` an independent Matlab function that contains the mass matrix $M(t,y)$, `f` a second Matlab function with the vector $f(t,y)$, and `y0` a vector containing the initial conditions of the vector y necessary to initiate the simulation.

To exemplify this technique, the case of the self-propelled locomotion with passive deflection developed in Chapter 4 is shown here for a better understanding. For that case, the mass matrix will be an 8×8 matrix containing the terms that multiply the variables present on $\dot{y}$ as follows

$$M(t,y) = \begin{pmatrix} -\alpha - A_{l1}d & R+1 & R(a-x_0)+a & RJ_a - A_{l2} & 0 & 0 & 0 & 0 \\ a\alpha & R(x_0-a) - a & -RI_a - a^2 - 1/8 & RJ_d - A_{m2} & 0 & 0 & 0 & 0 \\ 0 & RI_a + a^2 + 1/4 & -RI_d + a\left(a^2+1/2\right) & RK_d - A_{f2} & 0 & 0 & 0 & 0 \\ R' + \alpha(\alpha+2ad) & -(\alpha+2ad) & -a(\alpha+2ad) - d/4 & A_{l2}(\alpha+2ad) - ad/2 & 0 & 0 & 0 & 0 \\ 0 & 0 & 0 & 0 & 1 & 0 & 0 & 0 \\ 0 & 0 & 0 & 0 & 0 & 1 & 0 & 0 \\ 0 & 0 & 0 & 0 & 0 & 0 & 1 & 0 \\ 0 & 0 & 0 & 0 & 0 & 0 & 0 & 1 \end{pmatrix}. \tag{C.2}$$

The vector $\dot{y}$ will be of 1×8 size and contain the time derivative of the unknown variables, which will be obtained after applying the *ode45* command line. Finally, the vector $f(t,y)$ will also be of 1×8 size and contain the coefficients presented in Appendix A but modified, since some terms are now in the mass matrix, and also some remaining terms appears from the main equations.

$$\dot{y} = \frac{d}{dt}\begin{pmatrix} u \\ v \\ \dot{\alpha} \\ \dot{d} \\ x \\ h \\ \alpha \\ d \end{pmatrix} = \begin{pmatrix} \dot{u} \\ \ddot{h} \\ \ddot{\alpha} \\ \ddot{d} \\ u \\ \dot{h} \\ \dot{\alpha} \\ \dot{d} \end{pmatrix}, \qquad f(t,y) = \begin{pmatrix} \hat{C}_{L,mod} - \hat{C}_{Lo} \\ 2(\hat{C}_{M,mod} + \hat{C}_{Mi} - \hat{C}_{Mo}) \\ \hat{C}_{F,mod} - \frac{a^2+1/3}{3(1-a)^2}Sd \\ \hat{C}_{T,mod} - Liu^2 \\ u \\ \dot{h} \\ \dot{\alpha} \\ \dot{d} \end{pmatrix}, \tag{C.3}$$

where these modified coefficients are

$$\hat{C}_{L,mod} = u\dot{\alpha} + A_{l1}u\dot{d} + F_1 u\Gamma_0, \tag{C.4}$$

$$\hat{C}_{M,mod} = \frac{1}{2}\left[\left(\frac{1}{2}-a\right)u\dot{\alpha} + A_{m1}u\dot{d} + A_{m0}u^2 d\right] - \frac{1}{2}\left(\frac{1}{2}+a\right)F_1 u\Gamma_0, \tag{C.5}$$

$$\hat{C}_{F,mod} = a(a-1)u\dot{\alpha} + A_{f1}u\dot{d} + A_{f0}u^2 d + \left(\frac{1}{2}+a+a^2\right)F_1 u\Gamma_0, \tag{C.6}$$

$$\begin{aligned}\hat{C}_{T,mod} = &-(\alpha+2ad)\hat{C}_{L,mod} - \frac{d}{2}u\dot{d} + \frac{\dot{d}}{2}\left(\frac{\dot{\alpha}}{2} + a\dot{d} - ud\right) \\ &+ \left(\dot{\alpha}+2a\dot{d}\right)\left[v + a\dot{\alpha} + \left(a^2+\frac{1}{4}\right)\dot{d} - u(\alpha+2ad) + \Gamma_0 F_2\right] \\ &- \left(v + a\dot{\alpha} - u(\alpha+2ad) + a^2\dot{d}\right)\Gamma_0 F_3 - d\Gamma_0 F_4 + \dot{d}\Gamma_0 F_5,\end{aligned} \tag{C.7}$$

being

$$F_1 = \Re[C(k)], \tag{C.8}$$

$$F_2 = \Re\left[\frac{i}{k}C(k) + \left(\frac{1+ik}{k}\right)\frac{2}{\pi}C_1(k)\right], \tag{C.9}$$

$$F_3 = \Re\left[\frac{2i}{\pi}C_1(k)\right], \tag{C.10}$$

$$F_4 = \Re\left[iC_2(k) + 2\left(\frac{1+ik}{k}\right)\frac{2}{\pi}C_1(k)\right], \tag{C.11}$$

$$F_5 = \Re\left[\left(\frac{2i}{k^2} - \frac{2+ik}{k}\right)\frac{2}{\pi}C_1(k) - \frac{C_2(k)}{k}\right], \tag{C.12}$$

where $C(k)$, $C_1(k)$, and $C_2(k)$ are the functions of the reduced frequency presented in Appendix A. All the parameters and variables shown here are properly introduced in their respective chapters (see Chapter 3 and Chapter 4 for a better understanding of the equations involved). For the case of the self-propelled locomotion with a rigid foil (presented in Chapter 3), these matrix and vectors have the same format but much simpler since all the terms that depend on the deflection d (and its derivatives) disappear, as well as rows three and eight in $M(t,y)$ and $f(t,y)$, and column four in $M(t,y)$. Thus, it results in a 6×6 mass matrix, and 1×6 $\dot{y}$ and $f(t,y)$ vectors.

Appendix D

Parameters characterization of the flapping-foil turbine

D.1 Structural parameters

D.1.1 Elastic supports

The fixed structure of the turbine prototype is attached to the heaving carriage with extension springs. The number of these springs varies from zero to eight, and they are placed in pairs (one against the other) to maintain the heaving carriage properly oscillating in the water channel. In Figure 5.3, which is shown in Section 5.3.1 of Chapter 5, can be seen one of the tests performed where only one pair of springs is used. On the other hand, the number of springs in pitch that can be used is limited to either zero or two. These springs have one of their ends fixed to the carriage and the other one attached to a cable that is fastened to the shaft holding the blade, thereby undergoing the pitching motion, as shown in Figure D.1.

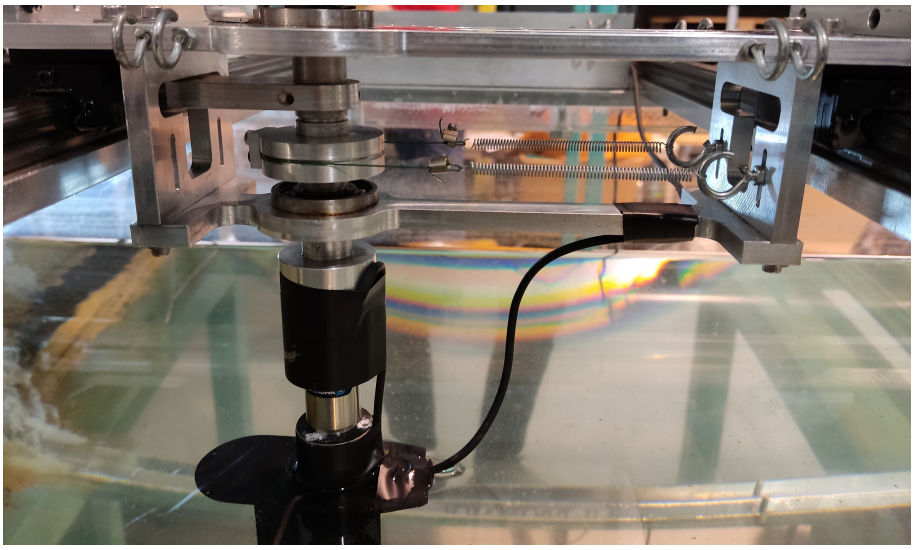

Figure D.1: Pitch springs attached to the shaft holding the turbine blade.

D.1.2 Damper designing process

A linear damper is used as an energy sink in heave. This damper consists of a thin aluminum sliding plate attached to the carriage and, therefore, undergoing the heaving motion that passes, without making contact, between two magnets yoked together with 1020 carbon steel to form an eddy-current brake. A picture of this damper, together with the rest of the main components, is shown in Figure D.2.

This damper is similar to the one designed by Boudreau et al. [2018]. For the designing process, it was first necessary to perform a theoretical study in order to select the proper values of the magnets and the rest of the parameters involved. In theory, the resistive force F_{damper} acting on the sliding plate of an eddy-current brake is given by Wouterse [1991]:

$$F_{damper} = \left(\frac{\pi D_m^2 t B_0^2 K}{4\rho_e} \right) \dot{\tilde{h}}, \tag{D.1}$$

where ρ_e is the electrical resistivity of the sliding plate material, D_m is the magnet diameter, t is the sliding plate thickness, B_0 is the magnetic field in the middle of the gap (e) between the magnets when the plate is not moving, $\dot{\tilde{h}}$ is the heave velocity and K is a constant given by

$$K = \frac{1}{2} \left[1 - \frac{\pi^2 D_m}{24\delta} \right], \tag{D.2}$$

being δ the width of the plate.

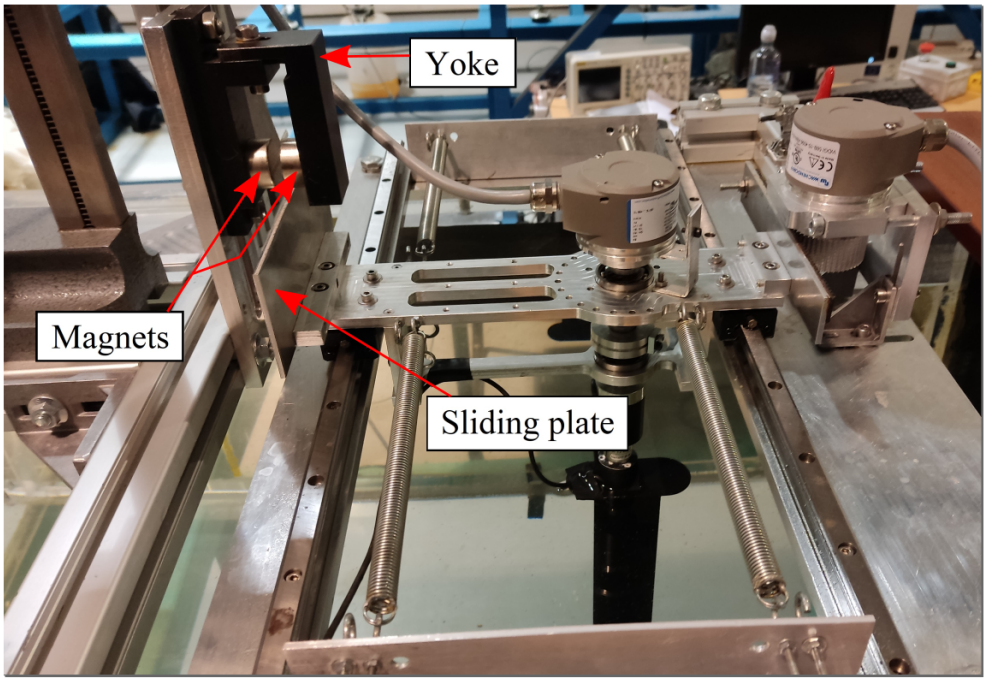

Figure D.2: Eddy-current brake used as the heave damper and the rest of the components involved.

Thus, the theoretical heave damping constant of the eddy-current brake is obtained by dividing the resistive force by the heave velocity

$$\tilde{b}_{he,theory} = \frac{\pi D_m^2 t B_0^2 K}{4\rho_e}. \tag{D.3}$$

For this application and by taking reference of Boudreau et al. [2018], we have selected magnets made of Neodymium (N48) with a diameter of 25.4 mm and a thickness of 12 mm. The width of the aluminum plate is set to 60 mm, the gap between the magnets to 5.3 mm, and the sliding plate thickness to 3 mm. On the other hand, we can vary the distance between the center of the magnets and the edge of the sliding plate by moving the yoke (see l_m in Figure D.3). So, we can reduce the magnetic field passing through the plate and, at the same time, the heave damping constant of the eddy-current brake.

Note that the theory presented above has only been used to design the damper. The actual heave damping constant of the prototype has been determined following a calibration process, as will be explained later.

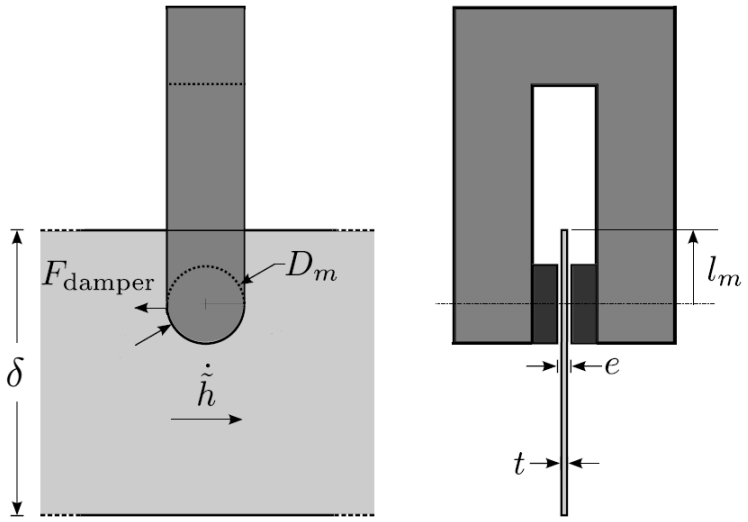

Figure D.3: Schematic of the eddy-current brake, showing the aluminum sliding plate, the yoke, and the magnets.

D.2 Calibrations

D.2.1 Springs

In order to determine the stiffness of the springs used for the heave and pitch control, we build a structure that allows us to measure the elongation of the springs by attaching one end of the spring to a Multi-Axis Force/Torque Sensor system (specifically, we use the Gamma IP68 model), and the other end to the mobile tool that measures the elongation. In Figure D.4, the calibration process for one of the analyzed springs is shown.

Figure D.4: Springs calibration process.

By prescribing different vertical positions of the tool and performing a linear regression analysis, the relation between the force measured with the Force/Torque sensor and the spring elongation can be found

$$F_z = \tilde{k}\Delta\tilde{z} + F_{z0}, \tag{D.4}$$

being $\tilde{k}$ the spring stiffness, $\Delta\tilde{z}$ the spring elongation, i.e., the distance between the position of the moving end of the spring and its initial position, F_{z0} is the tension force in the spring when the moving end is at its initial position and F_z is the tension force in the spring for a given elongation. In Figure D.5, we can see one of the springs analyzed showing the linear relation between the force and its elongation.

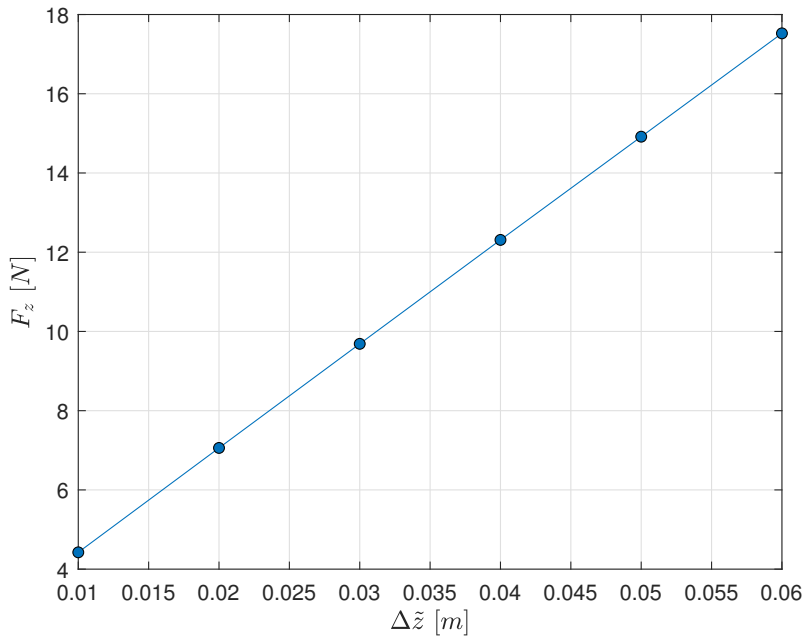

Figure D.5: Measurements of the force F_z as a function of the elongation $\Delta\tilde{z}$ for a given spring along with the linear regression curve. For this case, the spring stiffness found is $\tilde{k} = 261.98 \pm 0.42$ N/m. The error bars are not plotted since they are smaller than the marker points.

Notice that the uncertainty of the points is obtained through the standard deviation of the measures taken in the experiment. At the same time, the spring constant is calculated as the difference between the greatest and the lowest slope divided by two, taking into account the uncertainty of the extreme data points. Thus, as was mentioned earlier, several heave springs can be used in parallel to attach the carriage to the structure of the turbine, so the resultant heave stiffness $\tilde{k}_h$ in N/m is given by

$$\tilde{k}_h = \sum_{i=1}^{N_h} \tilde{k}_i, \tag{D.5}$$

where N_h is the number of heave springs used for a given case and $\tilde{k}_i$ is the stiffness of the ith heave spring. On the other hand, the resultant pitch stiffness in Nm/rad is given by

$$\tilde{k}_\alpha = \left(\tilde{k}_1 + \tilde{k}_2\right) \frac{D^2}{4}, \tag{D.6}$$

where $\tilde{k}_1$ and $\tilde{k}_2$ are the stiffness constants of the two springs used in pitch, and D is the diameter of the groove in the component around which the cable linking both pitch springs is rotating (see Figure D.1), being $D = 38.6$ mm in our turbine prototype.

Consequently, ten pairs of springs were built and analyzed (eight pairs for the heave control of the carriage and two of them for the pitch control of the blade), obtaining their respective stiffness constants and their associated uncertainties, which are shown in Table D.1.

Springs in heave [N/m]	
$\tilde{k}_{1,1} = 158.39 \pm 0.40$	$\tilde{k}_{1,2} = 157.61 \pm 0.45$
$\tilde{k}_{2,1} = 154.47 \pm 0.43$	$\tilde{k}_{2,2} = 154.95 \pm 0.43$
$\tilde{k}_{3,1} = 261.98 \pm 0.42$	$\tilde{k}_{3,2} = 263.05 \pm 0.41$
$\tilde{k}_{4,1} = 271.84 \pm 0.53$	$\tilde{k}_{4,2} = 272.60 \pm 0.43$
$\tilde{k}_{5,1} = 39.76 \pm 0.42$	$\tilde{k}_{5,2} = 40.54 \pm 0.43$
$\tilde{k}_{6,1} = 45.75 \pm 0.39$	$\tilde{k}_{6,2} = 47.03 \pm 0.40$
$\tilde{k}_{7,1} = 48.14 \pm 0.39$	$\tilde{k}_{7,2} = 47.28 \pm 0.39$
$\tilde{k}_{8,1} = 62.02 \pm 0.39$	$\tilde{k}_{8,2} = 62.89 \pm 0.40$
Springs in pitch [N/m]	
$\tilde{k}_{9,1} = 55.64 \pm 0.54$	$\tilde{k}_{9,2} = 55.25 \pm 0.55$
$\tilde{k}_{10,1} = 184.23 \pm 0.93$	$\tilde{k}_{10,2} = 184.80 \pm 1.36$

Table D.1: Stiffness constants and the associated uncertainties of the ten pairs of springs used in the whole experimental campaign.

D.2.2 Free vibration test in heave

In order to determine the heaving mass $\widetilde{m}_h$, the Coulomb friction force L_C, and the friction in the bearings $\tilde{b}_{hv}$, i.e., the total linear damping when the eddy-current brake is removed from the setup, a free vibration test in heave needs to be done. This test is performed at a sampling frequency of 5000 Hz in ambient air so that the fluid forces are negligible compared to the friction in the bearings. The blade and the pitching components have to be fastened and fixed to the shaft, eliminating that degree of freedom during the test. The reason for not simply weighing all the components undergoing the heaving motion is that free vibration tests are a simple method to evaluate the equivalent mass stemming from the rotation of some components, such as the linear guided roller bearings and that of the heave springs, which are not moving as rigid bodies with the carriage since one of their ends is attached to the fixed turbine structure. Taking that into account, the governing equation during a free vibration test in heave becomes

$$\widetilde{m}_h \ddot{\tilde{h}} = -\tilde{b}_h \dot{\tilde{h}} - \tilde{k}_h \tilde{h} - L_C. \tag{D.7}$$

This equation will be solved numerically later using the 4th-order Runge-Kutta method to assess the validity of the parameters experimentally obtained here. The experimental procedure to get the values of m_h, L_C, and $\tilde{b}_{hv}$ was described in the work of Feeny and Liang [1996], the first step consists of determining the parameter β, given by

$$\beta_i = -\frac{1}{\pi} \ln \left(-\frac{X_{i+1} - X_{i-1}}{X_i - X_{i-2}} \right), \quad \text{with} \;\; 3 \leq i \leq N_X - 1, \tag{D.8}$$

where X_i is the ith peak value (considering both positive and negative peaks) in heave of the free vibration test, then the mean value of β is obtained according to

$$\beta = \frac{1}{N_X} \sum_{i=3}^{N_X-1} \beta_i, \tag{D.9}$$

being N_X the number of peak values registered in the free vibration test. This parameter is then used to compute the damping ratio ζ of a given degree of freedom

$$\zeta = \frac{\beta}{\sqrt{1+\beta^2}}. \tag{D.10}$$

The heaving mass is then computed using the equation

$$\widetilde{m}_h = \frac{\tilde{k}_h T_h^2 \left(1-\zeta_h^2\right)}{4\pi^2}, \tag{D.11}$$

where T_h is the oscillation period in the free vibration test and ζ_h is referred to as the damping ratio in heave. Note that in order to obtain the peak values X_i, ten tests have been performed to ensure the validity of the results. On the other hand, the Coulomb friction force is evaluated using the following equation

$$C_i = \frac{(X_{i+1} - X_i) + e^{-\beta\pi}\left(X_i - X_{i-1}\right)}{2\left(1+e^{-\beta\pi}\right)}, \quad \text{with} \;\; 2 \leq i \leq N_X - 1, \tag{D.12}$$

then the mean value of C is obtained

$$C = \frac{1}{N_X} \sum_{i=2}^{N_X-1} |C_i|, \tag{D.13}$$

where C is the so-called Coulomb friction parameter, thus the constant friction force $\tilde{f}_C$ is given by

$$\tilde{f}_C = C_h \tilde{k}_h, \tag{D.14}$$

where C_h is referred to as the Coulomb friction parameter in heave. And so, the Coulomb friction force is

$$L_C = \tilde{f}_C \cdot \operatorname{sign}\left(\dot{\tilde{h}}\right). \tag{D.15}$$

Finally, the friction in the bearings can be evaluated as the total linear damping constant in heave since the eddy-current brake is removed from the setup, so

$$\tilde{b}_h = 2\zeta_h \sqrt{\tilde{k}_h \widetilde{m}_h}, \qquad \tilde{b}_{hv} = \tilde{b}_h. \tag{D.16}$$

Once the above parameters have been defined, we can perform the free vibration test in heave. To that end, we study three different spring configurations in heave with the springs previously presented, which are shown in Table D.2.

Spring configurations in heave	$\tilde{k}_h$ **[N/m]**
$\tilde{k}_{1,1} + \tilde{k}_{1,2} + \tilde{k}_{2,1} + \tilde{k}_{2,2} + \tilde{k}_{3,1} + \tilde{k}_{3,2}$	$\tilde{k}_{h1} = 1150.45 \pm 2.54$
$\tilde{k}_{1,1} + \tilde{k}_{1,2} + \tilde{k}_{3,1} + \tilde{k}_{3,2} + \tilde{k}_{4,1} + \tilde{k}_{4,2}$	$\tilde{k}_{h2} = 1385.47 \pm 2.64$
$\tilde{k}_{1,1} + \tilde{k}_{1,2} + \tilde{k}_{2,1} + \tilde{k}_{2,2} + \tilde{k}_{3,1} + \tilde{k}_{3,2} + \tilde{k}_{4,1} + \tilde{k}_{4,2}$	$\tilde{k}_{h3} = 1694.89 \pm 3.50$

Table D.2: The three different spring configurations used in the free vibration test in heave.

With these three configurations and the above-presented expressions, we obtain the results shown in Table D.3 and Figure D.6. We can see that the experimentally collected data and the numerical resolution of Equation (D.7) with the obtained parameters ($\widetilde{m}_h$, L_C, and $\tilde{b}_{hv}$) are in close agreement in all cases. The final values of these parameters will be selected later when determining the static moment, since heave and pitch equations are involved, and the characterization is more precise.

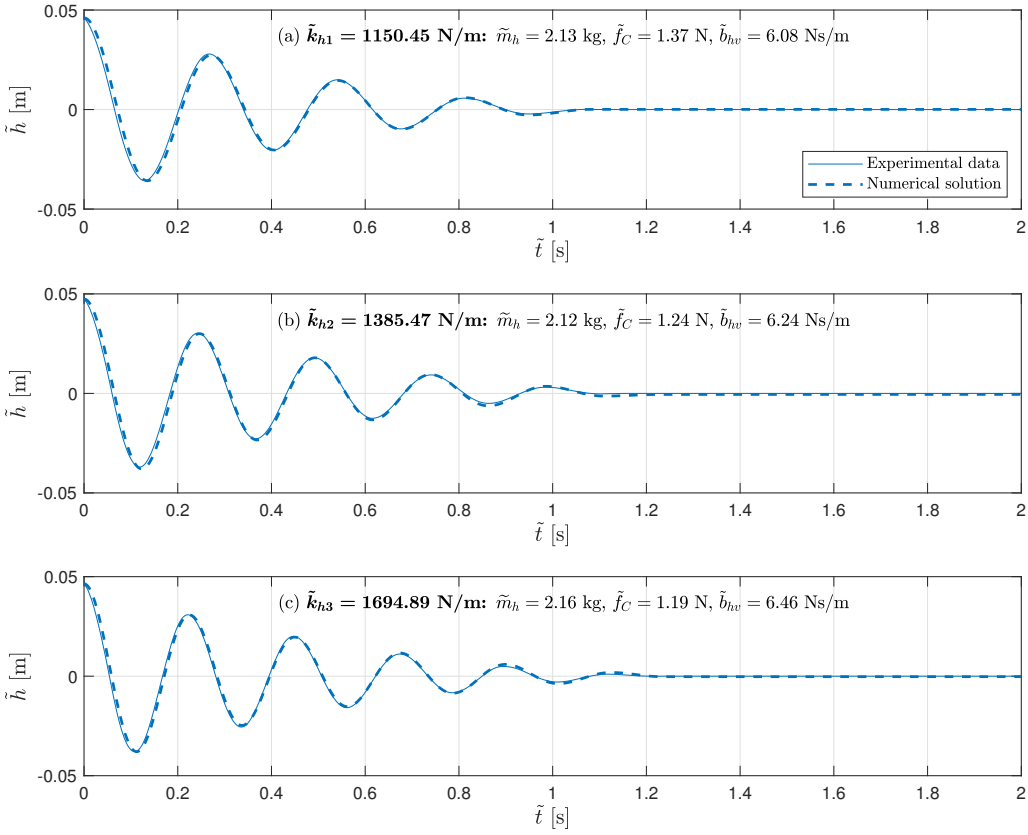

Figure D.6: Free vibration test in heave conducted for the three different spring configurations (only one of the ten tests carried out is shown for each case, thick line) and the numerical resolution (4th-order Runge-Kutta method, dotted line) of Equation D.7 with the parameters obtained for each one.

$\tilde{k}_h$ [N/m]	$\widetilde{m}_h$ [kg]	$\tilde{f}_C$ [N]	$\tilde{b}_{hv}$ [Ns/m]
$\tilde{k}_{h1} = 1150.45 \pm 2.54$	2.13 ± 0.01	1.37 ± 0.02	6.08 ± 0.04
$\tilde{k}_{h2} = 1385.47 \pm 2.64$	2.12 ± 0.01	1.24 ± 0.02	6.24 ± 0.05
$\tilde{k}_{h3} = 1694.89 \pm 3.50$	2.16 ± 0.01	1.19 ± 0.03	6.46 ± 0.06

Table D.3: Results from the free vibration test in heave for the different spring configurations.

D.2.3 Free vibration test in pitch

In order to determine the moment of inertia $\tilde{I}_a$, the Coulomb friction moment M_C, and the linear damping constant in the pitch bearings $\tilde{b}_{\alpha v}$, which corresponds to the total linear damping in pitch (no more damping elements in pitch are presented in the present set up, $\tilde{b}_{\alpha v} = \tilde{b}_\alpha$), we must follow the same idea as before and conduct a free vibration test in the other degree of freedom, i.e., a free vibration test in pitch. This test is also performed at a sampling frequency of 5000 Hz in ambient air to minimize the fluid forces. The heave motion of the carriage is inhibited in order to guarantee only the free degree of motion in pitch. Taking that into account, the governing equation during a free vibration test in pitch, which again will be solved later with the 4th-order Runge-Kutta method for the validation of the results, becomes

$$-\tilde{I}_a \ddot{\tilde{\alpha}} = \tilde{b}_\alpha \dot{\tilde{\alpha}} + \tilde{k}_\alpha \tilde{\alpha} - M_C. \tag{D.17}$$

The same procedure has been used to obtain these parameters. For the moment of inertia, the equation results in

$$\tilde{I}_a = \frac{\tilde{k}_\alpha T_\alpha^2 \left(1 - \zeta_\alpha^2\right)}{4\pi^2}. \tag{D.18}$$

On the other hand, the constant friction moment $\widetilde{m}_C$ is given by

$$\widetilde{m}_C = C_\alpha \tilde{k}_\alpha, \tag{D.19}$$

so, the Coulomb friction moment is

$$M_C = -\widetilde{m}_C \cdot \text{sign}\left(\dot{\tilde{\alpha}}\right). \tag{D.20}$$

Finally, the friction in the pitch bearings, i.e., the total linear damping in pitch, can be evaluated as

$$\tilde{b}_\alpha = 2\zeta_\alpha \sqrt{\tilde{k}_\alpha \tilde{I}_a}, \qquad \tilde{b}_{\alpha v} = \tilde{b}_\alpha. \tag{D.21}$$

Note that in all the above expressions, the subscript α is used to remark that now the parameters are referred to as the free vibration test in pitch.

To perform the free vibration test in pitch, we select two spring configurations as shown in Table D.4.

Spring configurations in pitch	$\tilde{k}_\alpha$ **[Nm/rad]**
$\left(\tilde{k}_{9,1} + \tilde{k}_{9,2}\right) \cdot D^2/4$	$\tilde{k}_{\alpha 1} = (4.13 \pm 0.04) \cdot 10^{-2}$
$\left(\tilde{k}_{10,1} + \tilde{k}_{10,2}\right) \cdot D^2/4$	$\tilde{k}_{\alpha 2} = (13.70 \pm 0.09) \cdot 10^{-2}$

Table D.4: The two different spring configurations used in the free vibration test in pitch. Note that $D = 38.6$ mm.

With the new expressions above developed and the two spring configurations, we obtain the results of Table D.5 and Figure D.7 with a good agreement between the experimental data and the numerical resolution of Equation (D.17), which is solved using the values obtained for $\tilde{I}_a$, M_C, and $\tilde{b}_{\alpha v}$. It can be observed that the results for the second spring configuration are more accurate, so we adopt them for the parameter characterization of the experiment.

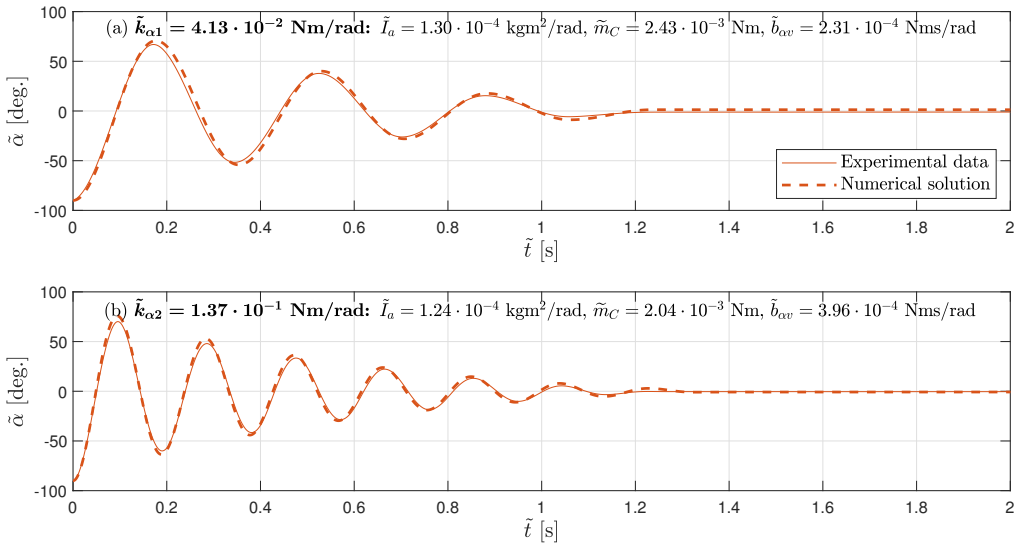

Figure D.7: Free vibration test in pitch conducted for the two different spring configurations (only one of the ten tests carried out is shown for each case, thick line) and the numerical resolution (4th-order Runge-Kutta method, dotted line) of Equation D.17 with the parameters obtained for each one.

$\tilde{k}_\alpha$ **[Nm/rad]**	$\tilde{I}_a$ [kgm^2/rad]	$\widetilde{m}_C$ [Nm]	$\tilde{b}_{\alpha v}$ [Nms/rad]
$\tilde{k}_{\alpha 1} = (4.13 \pm 0.04) \cdot 10^{-2}$	$(1.30 \pm 0.02) \cdot 10^{-4}$	$(2.43 \pm 0.03) \cdot 10^{-3}$	$(2.31 \pm 0.03) \cdot 10^{-4}$
$\tilde{k}_{\alpha 2} = (13.70 \pm 0.09) \cdot 10^{-2}$	$(1.24 \pm 0.01) \cdot 10^{-4}$	$(2.04 \pm 0.02) \cdot 10^{-3}$	$(3.96 \pm 0.04) \cdot 10^{-4}$

Table D.5: Results from the free vibration test in pitch for the different spring configurations.

D.2.4 Free vibration test in both degrees of freedom

To determine the static moment $\widetilde{\Omega}$, we have to perform another free vibration test, but now with the two degrees of freedom (heave and pitch) working. The test is conducted in ambient air to minimize the fluid forces at a sampling frequency of 5000 Hz, just like the previous ones. The idea is to adjust the value of the static moment in the resultant governing equations for this free vibration test until its numerical solution and the experimental data match. The governing equations, solved with the 4th-order Runge-Kutta method, are

$$\widetilde{m}_h\ddot{\tilde{h}} + \widetilde{\Omega}\left(\dot{\tilde{\alpha}}^2\sin\tilde{\alpha} - \ddot{\tilde{\alpha}}\cos\tilde{\alpha}\right) = -\tilde{b}_h\dot{\tilde{h}} - \tilde{k}_h\tilde{h} - L_C, \tag{D.22}$$

$$\widetilde{\Omega}\ddot{\tilde{h}}\cos\tilde{\alpha} - \tilde{I}_a\ddot{\tilde{\alpha}} = \tilde{b}_\alpha\dot{\tilde{\alpha}} + \tilde{k}_\alpha\tilde{\alpha} - M_C. \tag{D.23}$$

To that end, we analyze three different scenarios mixing the three spring configurations in heave with the last spring configuration in pitch. The reason for that is to reduce the uncertainties through various samples and check that the results from the previous test are right. We have selected only the last spring configuration in pitch since that was clearly more precise than the first one. The results from these comparisons are shown in Figure D.8.

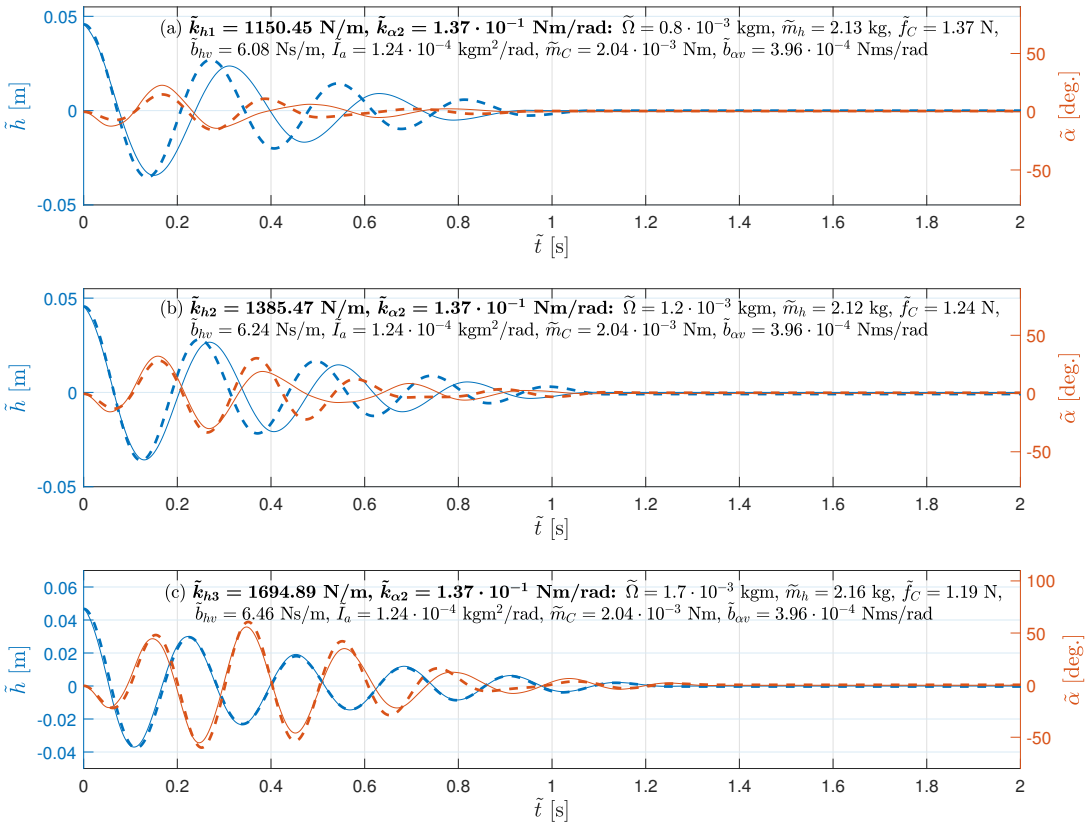

Figure D.8: Free vibration test (thick lines) in both degrees of freedom (heave and pitch) conducted for three different scenarios mixing the three spring configurations in heave with the last spring configuration in pitch. The numerical resolution (dotted lines) of Equations (D.22) and (D.23) is made through the 4th-order Runge-Kutta method with the parameters obtained in each case.

It can be observed that only in the last case do the numerical solutions and the experimental data match well. It is due to the cumulative minor errors in the parameter calculation. When we use more rigid springs in the setup, the number of peaks in the free vibration tests increases, so the parameters are better captured. Consequently, taking into account all the free vibration tests performed in the experimental campaign, we obtain the final parameter characterization shown in Table D.6.

Parameter	**Value**	**Parameter**	**Value**
$\widetilde{m}_h$ [kg]	2.16 ± 0.01	$\tilde{I}_a$ [kgm^2/rad]	$(1.24 \pm 0.01) \cdot 10^{-4}$
$\tilde{f}_C$ [N]	1.19 ± 0.03	$\widetilde{m}_C$ [Nm]	$(2.04 \pm 0.02) \cdot 10^{-3}$
$\tilde{b}_{hv}$ [Ns/m]	6.46 ± 0.06	$\tilde{b}_{\alpha v}$ [Nms/rad]	$(3.96 \pm 0.04) \cdot 10^{-4}$
$\widetilde{\Omega}$ [kgm]	$(1.7 \pm 0.1) \cdot 10^{-3}$		

Table D.6: The final parameter characterization obtained for the flapping-foil turbine.

D.2.5 Eddy-current brake calibration

In order to determine the eddy-current brake contribution, we perform several free vibration tests in heave with the damper, i.e., the two magnets yoked together with the carbon steel, acting on different heights during these tests. Consequently, we obtain several values of the total linear damping constant in heave thanks to Equation (D.16), which will be named as $\tilde{b}_{h\ calib}$. Thus, once we have the calibration values of the linear damping constant and since we know the friction in the bearings $\tilde{b}_{hv}$ from the first free vibration test in heave performed, we can obtain the eddy-current brake contribution in the calibration $\tilde{b}_{he\ calib}$ just simply by subtracting both values.

$$\tilde{b}_{he\ calib} = \tilde{b}_{h\ calib} - \tilde{b}_{hv}. \tag{D.24}$$

The different positions of the magnets tested during the calibration of the eddy-current brake have been chosen to match those used during the tests conducted in the water channel. On the other hand, one can notice that the eddy-current brake damping varies with temperature since the magnetic field B_0 and the electrical resistivity of aluminum ρ_e are temperature dependent. Consequently, the eddy-current brake damping needs to be corrected to take into account the temperature difference ΔT of the aluminum sliding plate between the time at which a given test is conducted and the time at which the calibration has been carried out. The eddy-current brake damping constant value for a given test is therefore given by

$$\tilde{b}_{he} = \frac{(1 + \alpha_{B_0} \Delta T)^2}{(1 + \alpha_{\rho_e} \Delta T)} \tilde{b}_{he\ calib}, \quad \text{with} \quad \Delta T = T - T_{calib}, \tag{D.25}$$

where T is the temperature of the aluminum sliding plate during a given test, T_{calib} its temperature during the calibration process, α_{B_0} the temperature coefficient of the magnetic field given by Pyrhonen et al. [2014], and α_{ρ_e} the temperature coefficient of the electrical resistivity given by Haynes [2015]. The values adopted for these two last coefficients are

$$\alpha_{B_0} = -0.0012^o C^{-1} \qquad \text{and} \qquad \alpha_{\rho_e} = 0.0044^o C^{-1}. \tag{D.26}$$

The results from the calibration can be seen in Figure D.9 and Table D.7.

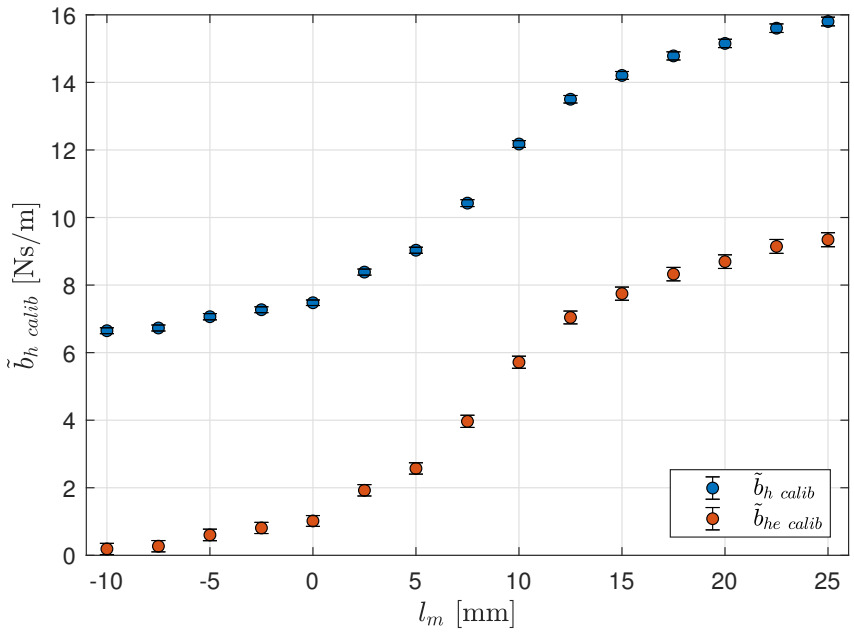

Figure D.9: Total linear damping constant and contribution of the eddy-current brake as a function of the distance l_m obtained in the calibration process. Note that ten free vibration tests have been performed for each case to ensure the validity of the results, all of them with the last spring configuration in heave $\tilde{k}_{h3}$ and being $\tilde{b}_{hv} = 6.46 \pm 0.06$ Ns/m.

$\boldsymbol{l_m}$ **[mm]**	T_{calib} [°C]	$\tilde{b}_{h\ calib}$ [Ns/m]	$\tilde{b}_{he\ calib}$ [Ns/m]
$\mathbf{-10 \pm 0.01}$	19.8 ± 0.1	6.65 ± 0.07	0.19 ± 0.13
$\mathbf{-7.5 \pm 0.01}$	19.4 ± 0.1	6.73 ± 0.07	0.27 ± 0.13
$\mathbf{-5 \pm 0.01}$	19.3 ± 0.1	7.06 ± 0.07	0.60 ± 0.13
$\mathbf{-2.5 \pm 0.01}$	19.6 ± 0.1	7.27 ± 0.07	0.81 ± 0.13
$\mathbf{0 \pm 0.01}$	19.5 ± 0.1	7.48 ± 0.06	1.02 ± 0.12
$\mathbf{2.5 \pm 0.01}$	19.2 ± 0.1	8.38 ± 0.07	1.92 ± 0.13
$\mathbf{5 \pm 0.01}$	19.6 ± 0.1	9.03 ± 0.06	2.57 ± 0.12
$\mathbf{7.5 \pm 0.01}$	19.2 ± 0.1	10.43 ± 0.07	3.97 ± 0.13
$\mathbf{10 \pm 0.01}$	18.2 ± 0.1	12.18 ± 0.07	5.72 ± 0.13
$\mathbf{12.5 \pm 0.01}$	18.7 ± 0.1	13.50 ± 0.07	7.04 ± 0.13
$\mathbf{15 \pm 0.01}$	18.3 ± 0.1	14.21 ± 0.08	7.75 ± 0.14
$\mathbf{17.5 \pm 0.01}$	18.6 ± 0.1	14.78 ± 0.08	8.32 ± 0.14
$\mathbf{20 \pm 0.01}$	18.2 ± 0.1	15.15 ± 0.08	8.69 ± 0.14
$\mathbf{22.5 \pm 0.01}$	18.4 ± 0.1	15.60 ± 0.08	9.14 ± 0.14
$\mathbf{25 \pm 0.01}$	18.3 ± 0.1	15.80 ± 0.08	9.34 ± 0.14

Table D.7: Results from the eddy-current brake calibration as a function of the distance l_m with the registered temperature for each case.

D.2.6 Angular correction from the static analysis

Once the parameters of the flapping-foil turbine prototype have been characterized, it is always a good practice to check if the center of the foil has some deviation in comparison with the force and moment acting on the static profile. If this is the case, the pitching motion must be corrected by that amount, and the final calibration can be considered complete.

For this calibration, we have analyzed the force and moment on the static profile for different angles of attack at the velocity that will be used in the experiments of Chapter 5, which is $U_\infty = 0.37 \pm 0.02$ m/s ($Re \simeq 20800$).[1] The results for the forces and moment acting on the force/torque transducer can be seen in Figure D.10, where L'_p and D'_p are the forces measured on the transducer (i.e., on the pivot axis) in the directions $\tilde{y}'$ and $\tilde{x}'$ of the axis of the foil, respectively; and M_p is the moment measured on the pivot axis. Notice that these $\tilde{y}'$ and $\tilde{x}'$ directions are not the same as the global $\tilde{y}$ and $\tilde{x}$ axes, which are not related to the motion of the foil.

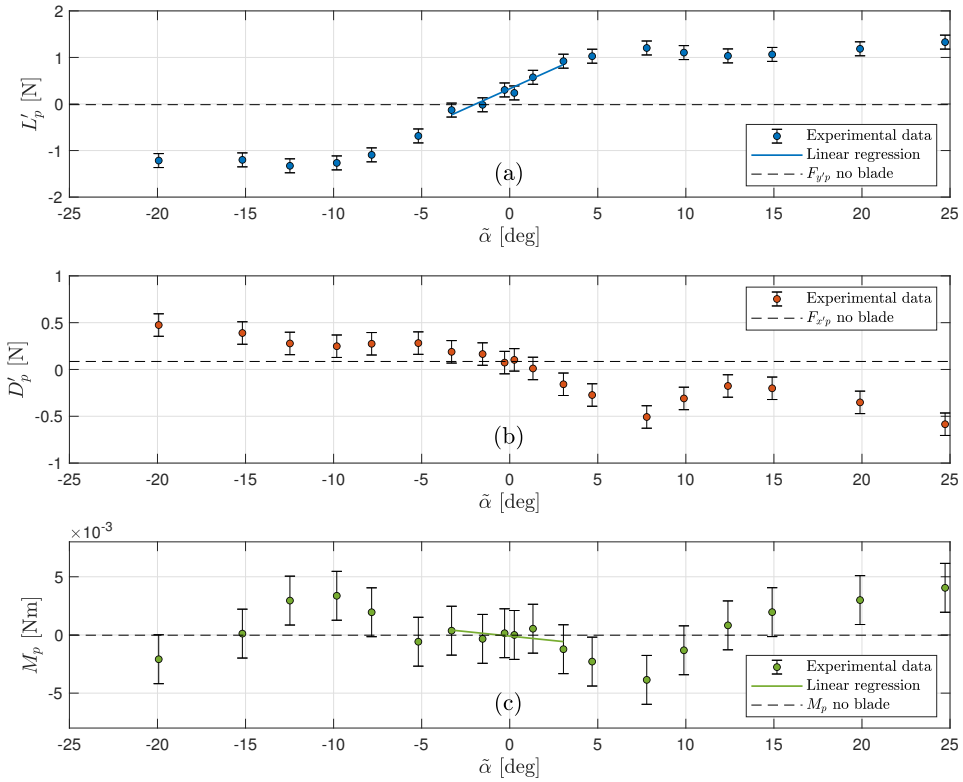

Figure D.10: Analysis of the forces and moment on the static profile varying the angle of attack for $Re = 20800$. A linear regression for the six centered points is used to obtain the deviation of the pitching motion. The forces and the moment acting on the transducer with no blade are also shown in dashed lines.

[1] Notice that the Reynolds number associated with this velocity is different from the one presented in Chapter 5 ($Re \simeq 22200$), which is due to the fact that the experiments are conducted at different seasons of the year, and consequently, the viscosity of the water is different in both scenarios.

Through the comparison with the linear regression of the six more centered points in the L'_p and M_p curves, we have found that the mean deviation for the pitching motion is

Pitching deviation [deg.]
$\phi_c = 1.9303$

Table D.8: Pitching deviation in degrees found through the static analysis of the forces and the moment acting on the static profile while varying the angle of attack.

Therefore, the quantity $\phi_c = 1.9303$ deg must be added to correct the pitch angle

$$\tilde{\alpha}_c = \tilde{\alpha} + \phi_c. \tag{D.27}$$

For simplicity, in Chapter 5, we will rename $\tilde{\alpha}_c$ as $\tilde{\alpha}$ but considering that ϕ_c added for the correction of the pitching motion. On the other hand, the instantaneous force components in the streamwise ($\tilde{x}$) and transverse ($\tilde{y}$) directions can be obtained as

$$D_p = D'_p \cos\tilde{\alpha}_c + L'_p \sin\tilde{\alpha}_c, \qquad L_p = -D'_p \sin\tilde{\alpha}_c + L'_p \cos\tilde{\alpha}_c. \tag{D.28}$$

Thus, one may obtain the static lift, drag, and moment coefficients acting on the pivot axis (see Chapter 5 for more details), which are shown in Figure D.11.

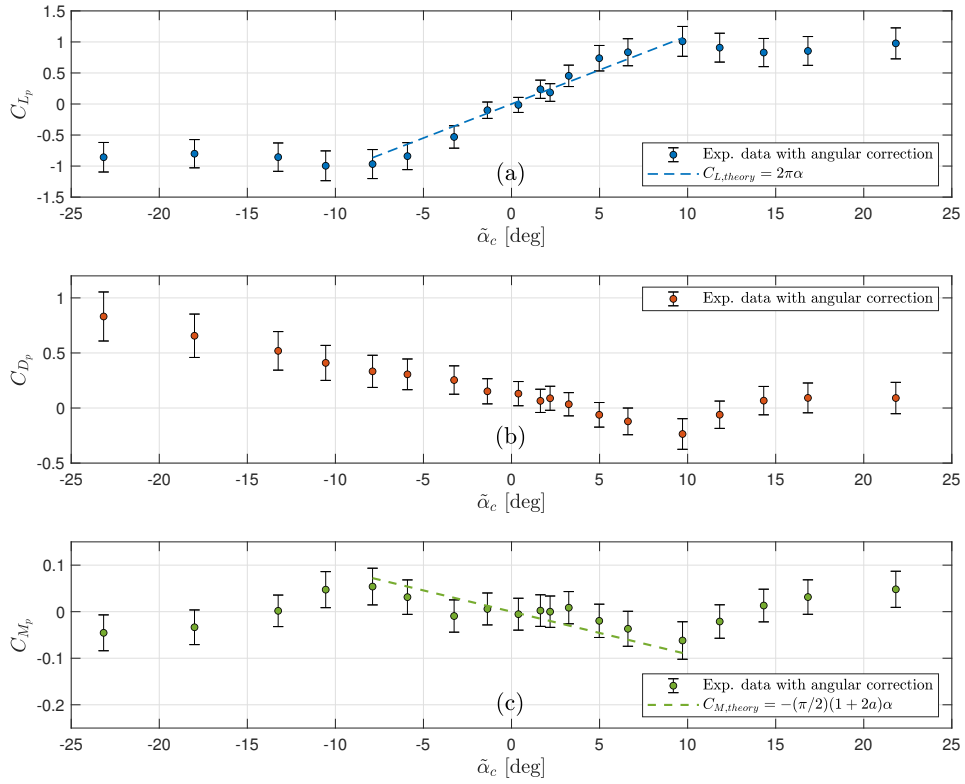

Figure D.11: Static lift (a), drag (b), and moment (c) coefficients for $Re = 20800$. The dashed straight lines correspond to the theoretical results from the 2D linear potential-flow theory for small α.

In addition, by adjusting the experimental results of C_M for small α to a straight line and comparing it with the linearized potential-flow theory result, $C_M = -(\pi/2)(1 + 2a)\alpha$, one would obtain a non-dimensional pivot point location of $a \simeq -0.4$, close to the design value $a = -1/3$.

Bibliography

H. Abiru and A. Yoshitake. Study on a flapping wing hydroelectric power generation system. *J. Envir. Eng. 6 (1)*, pp. 178-186. DOI: 10.1299/jee.6.178, 2011.

H. Abiru and A. Yoshitake. Experimental study on a cascade flapping wing hydroelectric power generator. *J. Energy Power Eng. 6 (9)*, pp. 1429-1436. DOI: 10.1115/POWER2011-55364, 2012.

E. Akoz and K.W. Moored. Unsteady propulsion by an intermittent swimming gait. *J. Fluid Mech. 834*, pp. 149-172. DOI: 10.1017/jfm.2017.731, 2018.

J. Alaminos-Quesada. Limit of the two-dimensional linear potential theories on the propulsion of a flapping airfoil in forward flight in terms of the reynolds and strouhal number. *Phys. Rev. Fluids 6 (12), 123101.* DOI: 10.1103/PhysRevFluids.6.123101, 2021.

J. Alaminos-Quesada and R. Fernandez-Feria. Propulsion of a foil undergoing a flapping undulatory motion from the impulse theory in the linear potential limit. *J. Fluid Mech. 883 A19*, pp. 1-24. DOI: 10.1017/jfm.2019.870, 2020.

S. Alben. Optimal flexibility of a flapping appendage in an inviscid fluid. *J. Fluid Mech. 614*, pp. 355–380. DOI: 10.1017/S0022112008003297, 2008.

S. Alben and M. Shelley. Coherent locomotion as an attracting state for a free flapping body. *Proc. Nat. Acad. Sci. USA 102 (32)*, pp. 11163-11166. DOI: 10.1073/pnas.0505064102, 2005.

S. Alben, C. Witt, T.V. Baker, E. Anderson, and G.V. Lauder. Dynamics of freely swimming flexible foils. *Phys. Fluids 24 (5)*, pp. 109–133. DOI: 10.1063/1.4709477, 2012.

A. Andersen, T. Bohr, T. Schnipper, and J.H. Walther. Wake structure and thrust generation of a flapping foil in two-dimensional flow. *J. Fluid Mech. 812, R4.* DOI: 10.1017/jfm.2016.808, 2017.

J.M. Anderson, K. Streitlien, D.S. Barrett, and M.S. Triantafyllou. Oscillating foils of high propulsive efficiency. *J. Fluid Mech. 360*, pp. 41–72. DOI: 10.1017/S0022112097008392, 1998.

D.E. Anevlavi, E.S. Filippas, A.E. Karperaki, and K.A. Belibassakis. A non-linear bem-fem coupled scheme for the performance of flexible flapping-foil thrusters. *J. Mar. Sci. Eng. 8, 56.* DOI: 10.3390/jmse8010056, 2020.

G. Arranz, A. Gonzalo, M. Uhlmann, O. Flores, and M. Garcia-Villalba. A numerical study of the flow around a model winged seed in auto-rotation. *Flow Turbulence Combust. 101*, pp. 477-497. DOI: 10.1007/s10494-018-9945-z, 2018.

D. Asselin and C.H.K. Williamson. 'addition of passive dynamics to a heaving airfoil to improve performance' in the report by c.h.k. williamson 'fluid-structure interactions employing cyber-physical fluid dynamics'. *Technical Report AFRL-AFOSR-VA-TR-2019-0114, Air Force Research Laboratory*, 2019.

B. Augier, J. Yan, A. Korobenko, J. Czarnowski, G. Ketterman, and Y. Bazilevs. Experimental and numerical fsi study of compliant hydrofoils. *Comput. Mech. 55*, pp. 1079-1090. DOI: 10.1007/s00466-014-1090-5, 2015.

Y.S. Baik, L.P. Bernal, K. Granlund, and M.V. Ol. Unsteady force generation and vortex dynamics of pitching and plunging aerofoils. *J. Fluid Mech. 709*, pp. 37-68. DOI: 10.1017/jfm.2012.318, 2012.

S. Bansmer, R. Radespiel, R. Unger, M. Haupt, and P. Horst. Experimental and numerical fluid-structure analysis of rigid and flexible flapping airfoils. *AIAA J. 48 (9)*, pp. 1959-1974. DOI: 10.2514/1.J050158, 2010.

O. Barannyk, B.K Buckham, and P. Oshkai. On performance of an oscillating plate underwater propulsion system with variable chordwise flexibility at different depths of submergence. *J. Fluids Struct. 28*, pp. 152–166. DOI: 10.1016/j.jfluidstructs.2011.10.005, 2012.

D.N. Beal, M.S. Hover, M.S. Triantafyllou, J.C. Liao, and G.V. Lauder. Passive propulsion in vortex wakes. *J. Fluid Mech. 549*, pp. 385-402. DOI: 10.1017/S0022112005007925, 2006.

O. Boiron, C. Guivier-Curien, and E. Bertrand. Study of the hydrodynamic of a flapping foil at moderate angle of attack. *Comput. Fluid 59*, pp 117–124. DOI: 10.1016/j.compfluid.2012.01.010, 2012.

M. Boudreau, G. Dumas, M. Rahimpour, and P. Oshkai. Experimental investigation of the energy extraction by a fully-passive flapping-foil hydrokinetic turbine prototype. *J. Fluids Struct. 82*, pp. 446-472. DOI: 10.1016/j.jfluidstructs.2018.07.014, 2018.

D.J. Cleaver, I. Gursul, D.E. Calderon, and Z. Wang. Thrust enhancement due to flexible trailing-edge of plunging foils. *J. Fluids Structures 51*, pp. 401-412. DOI: 10.1016/j.jfluidstructs.2014.09.006, 2014.

D.J. Cleaver, D.E. Calderon, Z. Wang, and I. Gursul. Lift enhancement through flexibility of plunging wings at low reynolds numbers. *J. Fluids Struct. 64*, pp. 27-45. DOI: 10.1016/j.jfluidstructs.2016.04.004, 2016.

J. D'Adamo, M. Collaud, R. Sosa, and R. Godoy-Diana. Wake and aeroelasticity of a flexible pitching foil. *Bioinspir. Biomim. 17, 045002.* DOI: 10.1088/1748-3190/ac6d96, 2022.

P. Dagenais and C.M. Aegerter. How shape and flapping rate affect the distribution of fluid forces on flexible hydrofoils. *J. Fluid Mech. 901, A1.* DOI: 10.1017/jfm.2020.489, 2020.

H. Dai, H. Luo, P.J.S.A.F. de Sousa, and J.F. Doyle. Thrust performance of a flexible low-aspect-ratio pitching plate. *Phys. Fluids 24 (10), 101903.* DOI: 10.1063/1.4764047, 2012.

A. Das, R.K. Shukla, and R.N. Govardhan. Existence of a sharp transition in the peak propulsive efficiency of a low-re pitching foil. *J. Fluid Mech. 800*, pp. 307-326. DOI: 10.1017/jfm.2016.399, 2016.

A. Das, R.K. Shukla, and R.N. Govardhan. Contrasting thrust generation mechanics and energetics of flapping foil locomotory states characterized by a unified st-re scaling. *J. Fluid Mech. 930 (A27).* DOI: 10.1017/jfm.2021.910, 2022.

S.M. Dash, K.B. Lua, T.T. Lim, and K.S. Yeo. Enhanced thrust performance of a two dimensional elliptic airfoil at high flapping frequency in a forward flight. *J. Fluids Struct. 76*, pp. 37-59. DOI: 10.1016/j.jfluidstructs.2017.08.008, 2018.

M. Jimreeves David, R.N. Govardhan, and J.H. Arakeri. Thrust generation from pitching foils with flexible trailing edge flaps. *J. Fluid Mech. 828*, pp. 70-103. DOI: 10.1017/jfm.2017.491, 2017.

E. Demirer, Y.-C. Wang, A. Erturk, and A. Alexeev. Effect of actuation method on hydrodynamics of elastic plates oscillating at resonance. *J. Fluid Mech. 910, A4.* DOI: 10.1017/jfm.2020.915, 2021.

J. Deng, L. Teng, D. Pan, and X. Shao. Inertial effects of the semi-passive flapping foil on its energy extraction efficiency. *Phys. Fluids 27 (5), 053103*, (17 pp.). DOI: 10.1063/1.4921384, 2015.

J. Derakhshandeh, M. Arjomandi, B. Dally, and B. Cazzolato. Flow-induced vibration of an elastically mounted airfoil under the influence of the wake of a circular cylinder. *Exp. Therm Fluid Sci. 74*, pp. 58-72. DOI: 10.1016/j.expthermflusci.2015.12.003, 2016.

P.A. Dewey, B.M. Boschitsch, K.W. Moored, H.A. Stone, and A.J. Smits. Scaling laws for the thrust production of flexible pitching panels. *J. Fluid Mech. 732*, pp. 29–46. DOI: 10.1017/jfm.2013.384, 2013.

L. Duarte, N. Dellinger, G. Dellinger, A. Ghenaim, and A. Terfous. Experimental investigation of the dynamic behaviour of a fully passive flapping foil hydrokinetic turbine. *J. Fluids Struct. 88*, pp. 1-12. DOI: 10.1016/j.jfluidstructs.2019.04.012, 2019.

L. Duarte, G. Dellinger, N. Dellinger, A. Ghenaim, and A. Terfous. Implementation and validation of a strongly coupled numerical model of a fully passive flapping foil turbine. *J. Fluids Struct. 102, 103248.* DOI: 10.1016/j.jfluidstructs.2021.103248, 2021a.

L. Duarte, N. Dellinger, G. Dellinger, A. Ghenaim, and A. Terfous. Experimental optimisation of the pitching structural parameters of a fully passive flapping foil turbine. *Renew. Energy 171*, pp. 1436-1444. DOI: 10.1016/j.renene.2021.02.014, 2021b.

U. Ehrenstein and C. Eloy. Skin friction on a moving wall and its implication for swimming animals. *J. Fluid Mech. 718*, pp. 321-346. DOI: 10.1017/jfm.2012.613, 2013.

U. Ehrenstein, M. Marquillie, and C. Eloy. Skin friction on a flapping plate in uniform flow. *Phil. Trans. R. Soc. A 372, 20130345.* DOI: 10.1098/rsta.2013.0345, 2014.

C. Eloy. Optimal strouhal number for swimming animals. *J. Fluids Struct. 30*, pp. 205-218. DOI: 10.1016/j.jfluidstructs.2012.02.008, 2012.

B. Feeny and J. Liang. A decrement method for the simultaneous estimation of coulomb and viscous friction. *J. Sound Vib. 195 (1)*, pp. 149-154. DOI: 10.1006/jsvi.1996.0411, 1996.

R. Fernandez-Feria. Linearized propulsion theory of flapping airfoils revisited. *Physical Review Fluids 1, 084502*, pp. 379–390. DOI: 10.1103/PhysRevFluids.1.084502, 2016.

R. Fernandez-Feria. Note on optimum propulsion of heaving and pitching airfoils from linear potential theory. *Journal of Fluid Mechanics 826*, pp. 781–796. DOI: 10.1017/jfm.2017.500, 2017.

R. Fernandez-Feria. Effects of inertia on the time-averaged propulsive performance of a pitching and heaving foil. *J. Fluids Structures 120, 103907.* DOI: 10.1016/j.jfluidstructs.2023.103907, 2023.

R. Fernandez-Feria and J. Alaminos-Quesada. Analytical results for the propulsion performance of a flexible foil with prescribed pitching and heaving motions and passive small deflection. *J. Fluid Mech. 910, A43.* DOI: 10.1017/jfm.2020.1015, 2021a.

R. Fernandez-Feria and J. Alaminos-Quesada. Propulsion and energy harvesting performances of a flexible thin airfoil undergoing forced heaving motion with passive pitching and deformation of small amplitude. *J. Fluids Struct. 102, 103255.* DOI: 10.1016/j.jfluidstructs.2021.103255, 2021b.

R. Fernandez-Feria and J. Alaminos-Quesada. Energy harvesting and propulsion of pitching airfoils with passive heave and deformation. *AIAA J. 60 (2)*, pp. 783-797. DOI: 10.2514/1.J060738, 2022.

R. Fernandez-Feria and E. Sanmiguel-Rojas. Comparison of aerodynamic models for two-dimensional pitching foils with experimental data. *Phys. Fluids 31, 057104.* DOI: 10.1063/1.5096337, 2019.

D. Floryan and C. W. Rowley. Distributed flexibility in inertial swimmers. *J. Fluid Mech. 888, A24*, pp. 1-37. DOI: 10.1017/jfm.2020.49, 2020.

D. Floryan and C.W. Rowley. Clarifying the relationship between efficiency and resonance for flexible inertial swimmers. *J. Fluid Mech. 853*, pp. 271–300. DOI: 10.1017/jfm.2018.581, 2018.

D. Floryan, T. Van Buren, C.W. Rowley, and A.J. Smits. Scaling the propulsive performance of heaving and pitching foils. *J. Fluid Mech. 822*, pp. 386-397. DOI: 10.1017/jfm.2017.302, 2017.

G. Gabrielli and T. von Kármán. What price speed? specific power required for propulsion. *J. Am. Soc. Naval Eng. 63*, pp. 188-200., 1951.

I.E. Garrick. Propulsion of a flapping and oscillating airfoil. *Report National Advisory Committee for Aeronautics, NACA Report 567*, pp. 419–427., 1936.

M. Gazzola, M. Argentina, and L. Mahadevan. Scaling macroscopic aquatic locomotion. *Nature Physics vol. 10 no. 10*, pp. 758-761. DOI: 10.1038/nphys3078, 2014.

F. Gibouin, C. Raufaste, Y. Bouret, and M. Argentina. Study of the thrust-drag balance with a swimming robotic fish. *Phys. Fluids 30 (9), 091901.* DOI: 10.1063/1.5043137, 2018.

A. Gonzalo, G. Arranz, M. Moriche, M. Garcia-Villalba, and O. Flores. From flapping to heaving: A numerical study of wings in forward flight. *J. Fluids Struct. 83*, pp. 293-309. DOI: 10.1016/j.jfluidstructs.2018.09.006, 2018.

A. Goza, D. Floryan, and C. Rowley. Connections between resonance and nonlinearity in swimming performance of a flexible heaving plate. *J. Fluid Mech. 888, A30.* DOI: 10.1017/jfm.2020.60, 2020.

J.M. Greeberg. Airfoil in sinusoidal motion in a pulsating stream. *Tech. Rep. TR 1326, NACA*, 1947.

M.D. Griffith, D.L Jacono, J. Sheridan, and J.S. Leontini. Passive heaving of elliptical cylinders with active pitching from cylinders towards flapping foils. *J. Fluids Struct. 67*, pp. 124-141. DOI: 10.1016/j.jfluidstructs.2016.09.005, 2016.

D. Gross, Y. Roux, C. Raufaste, and M. Argentina. Drag analysis with a self-propelled flexible swimmer. *Phys. Rev. Fluids 6, 053101.* DOI: 10.1103/PhysRevFluids.6.053101, 2021.

R.L. Halfman. Experimental aerodynamic derivatives of a sinusoidally oscillating airfoil in two-dimensional flow. *Tech. Rep. TR 1108, NACA*, 1952.

W. Haynes. *CRC Handbook of Chemistry and Physics, ninety sixth ed.* CRC Press, Boca Raton, FL, USA, 2015.

S. Heathcote and I. Gursul. Flexible flapping airfoil propulsion at low reynolds numbers. *AIAA J. 45 (5)*, pp. 1066–1079. DOI: 10.2514/1.25431, 2007.

S. Heathcote, D. Martin, and I. Gursul. Flexible flapping airfoil propulsion at zero freestream velocity. *AIAA J. 42 (11)*, pp. 2196–2204. DOI: 10.2514/1.5299, 2004.

S. Heathcote, Z. Wang, and I. Gursul. Effect of spanwise flexibility on flapping wing propulsion. *J. Fluids Struct. 24 (2)*, pp. 183-199. DOI: 10.1016/j.jfluidstructs.2007.08.003, 2008.

A.P. Hoover, R. Cortez, E.D. Tytell, and L.J. Fauci. Swimming performance, resonance and shape evolution in heaving flexible panels. *J. Fluid Mech. 847, 386.* DOI: 10.1017/jfm.2018.305, 2018.

F.S. Hover, O. Haugsdal, and M.S. Triantafyllou. Effect of angle of attack profiles in flapping foil propulsion. *J. Fluids Struct. 19 (1)*, pp 37–47. DOI: 10.1016/j.jfluidstructs.2003.10.003, 2004.

R.N. Hua, L. Zhu, and X.Y. Lu. Locomotion of a flapping flexible plate. *Phys. Fluids 25, 121901.* DOI: 10.1063/1.4832857, 2013.

G.H. Huxham, S. Cochard, and J. Patterson. Experimental parametric investigation of an oscillating hydrofoil tidal stream energy converter. *In: Proceedings of the 18th Australasian Fluid Mechanics Conference. Launceston, Australia*, 2012.

Idealsimulations. Courant number in cfd simulations. Consulting date: 13-03-2023. URL: https://www.idealsimulations.com/resources/courant-number-cfd/, 2020.

G. Jeanmonod and M. Olivier. Effects of chordwise flexibility on 2d flapping foils used as an energy extraction device. *J. Fluids Structures 70*, pp. 327-345. DOI: 10.1016/j.jfluidstructs.2017.01.009, 2017.

C.K. Kang, H. Aono, C.E.S. Cesnik, and W. Shyy. Effects of flexibility on the aerodynamic performance of flapping wings. *J. Fluid Mech. 689*, pp. 32-74. DOI: 10.1017/jfm.2011.428, 2011.

J. Katz and D. Weihs. Hydrodynamic propulsion by large amplitude oscillation of an aerofoil with chordwise flexibility. *J. Fluid Mech, 88*, pp. 485-497. DOI: 10.1017/S0022112078002220, 1978.

J. Kevorkian and J.D. Cole. *Perturbation methods in applied mathematics.* Springer-Verlag, New York, 1981.

D. Kim, B. Strom, S. Mandre, and K. Breuer. Energy harvesting performance and flow structure of an oscillating hydrofoil with finite span. *J. Fluids Struct. 70*, pp. 314-326. DOI: 10.1016/j.jfluidstructs.2017.02.004, 2017.

T. Kinsey and G. Dumas. Parametric study of an oscillating airfoil in a power-extraction regime. *AIAA J. 46 (6)*, pp. 1318-1330. DOI: 10.2514/1.26253, 2008.

T. Kinsey and G. Dumas. Computational fluid dynamics analysis of a hydrokinetic turbine based on oscillating hydrofoils. *J. Fluids Eng. 134 (2), 021104*, (16 pp.). DOI: 10.1115/1.4005841, 2012.

T. Kinsey and G. Dumas. Optimal operating parameters for an oscillating foil turbine at reynolds number 500,000. *AIAA J. 52 (9)*, pp. 1885-1895. DOI: 10.2514/1.J052700, 2014.

T. Kinsey, G. Dumas, G. Lalande, J. Ruel, A. Mehut, P. Viarouge, J. Lemay, and Y. Jean. Prototype testing of a hydrokinetic turbine based on oscillating hydrofoils. *Renew. Energy 36 (6)*, pp. 1710-1718. DOI: 10.1016/j.renene.2010.11.037, 2011.

R. Kumar and H. Shin. Thrust estimation of a flapping foil attached to an elastic plate using multiple regression analysis. *Int. J. Nav. Archit. Ocean Eng. 11 (2)*, pp. 828–834. DOI: 10.1016/j.ijnaoe.2019.02.006, 2019.

J. Labasse, U. Ehrenstein, and P. Meliga. Numerical exploration of the pitching plate parameter space with application to thrust scaling. *Appl. Ocean Res. 101, 102278.* DOI: 10.1016/j.apor.2020.102278, 2020.

G. V. Lauder. Fish locomotion: Recent advances and new directions. *Annu. Rev. Mar. Sci. 7, 521.* DOI: 10.1146/annurev-marine-010814-015614, 2015.

G.V. Lauder, E.J. Anderson, J. Tangorra, and P.G.A. Madden. Fish biorobotics: Kinematics and hydrodynamics of self-propulsion. *J. Exp. Biol 210*, pp. 2767–2780. DOI: 10.1242/jeb.000265, 2007.

T. Quang Le and J. Hwan Ko. Effect of hydrofoil flexibility on the power extraction of a flapping tidal generator via two- and three-dimensional flow simulations. *Renew. Energy 80*, pp. 275-285. DOI: 10.1016/j.energy.2021.122940, 2015.

M.J. Lighthill. Hydromechanics of aquatic animal propulsion. *Annu. Rev. Fluid Mech. 1*, pp. 413-446. DOI: 10.1146/annurev.fl.01.010169.002213, 1969.

M.J. Lighthill. Aquatic animal propulsion of high hydromechanical efficiency. *Journal of Fluid Mechanics 44.2*, pp. 265–301. DOI: 10.1017/S0022112070001830, 1970.

M.J. Lighthill. Large-amplitude elongated-body theory of fish locomotion. *Proc. R. Soc. Lond. B 179 (1055)*, pp. 125-138. DOI: 10.1098/rspb.1971.0085, 1971.

X. Lin, J. Wu, and T. Zhang. Self-directed propulsion of an unconstrained flapping swimmer at low reynolds number: hydrodynamic behaviour and scaling laws. *J. Fluid Mech. 907 (R3).* DOI: 10.1017/jfm.2020.955, 2021.

W. Liu, Q. Xiao, and F. Cheng. A bio-inspired study on tidal energy extraction with flexible flapping wings. *Bioinspiration Biomimetics 8(3), 036011.* DOI: 10.1088/1748-3182/8/3/036011, 2013.

W. Liu, Q. Xiao, and Q. Zhu. Passive flexibility effect on oscillating foil energy harvester. *AIAA J. 54(4)*, pp. 1172-1187. DOI: 10.2514/1.J054205, 2016.

K.B. Lua, S.M. Dash, and T.T. Limand K.S. Yeo. On the thrust performance of a flapping two-dimensional elliptic airfoil in a forward flight. *J. Fluids Struct. 66*, pp. 91–109. DOI: 10.1016/j.jfluidstructs.2016.07.012, 2016.

P. Ma, G. Liu, Y. Wang, Y. Zhang, and Y. Xie. Numerical study on the hydrodynamic performance of a semi-passive oscillating hydrofoil. *Ocean Eng. 223, 108649.* DOI: 10.1016/j.oceaneng.2021.108649, 2021.

A.W. Mackowski and C.H.K. Williamson. Direct measurement of thrust and efficiency of an airfoil undergoing pure pitching. *J. Fluid Mech. 765*, pp. 524-543. DOI: 10.1017/jfm.2014.748, 2015.

A.W. Mackowski and C.H.K. Williamson. Effect of pivot point location and passive heave on propulsion from a pitching airfoil. *Phys. Rev. Fluids 2, 013101*, pp. 915-926. DOI: 10.1103/PhysRevFluids.2.013101, 2017.

S.A. Manjunathan and R. Bhardwaj. Thrust generation by pitching and heaving of an elastic plate at low reynolds number. *Phys. Fluids 32, 073601.* DOI: 10.1063/5.0010873, 2020.

C. Marais, B. Thiria, J.E. Wesfreid, and R. Godoy-Diana. Stabilizing effect of flexibility in the wake of a flapping foil. *J. Fluid Mech. 710*, pp. 659–669. DOI: 10.1017/jfm.2012.390, 2012.

W. McKinney and J. DeLaurier. Wingmill: An oscillating-wing windmill. *J. Energy 5 (2)*, pp. 109-115. DOI: 10.2514/3.62510, 1981.

W. Medjroubi, B. Stoevesandt, B. Carmo, and J. Peinke. High-order numerical simulations of the flow around a heaving airfoil. *Comput. Fluid 51 (1)*, pp. 68–84. DOI: 10.1016/j.compfluid.2011.07.015, 2011.

W. Medjroubi, B. Stoevesandt, and J. Peinke. Wake classification of heaving airfoils using the spectral/hp element method. *Comput. Appl. Math. 236 (15)*, pp. 3774–3782. DOI: 10.1016/j.cam.2011.11.004, 2012.

S. Michelin and S. G. Llewellyn Smith. An unsteady point vortex method for coupled fluid-solid problems. *Theor. Comput. Fluid Dyn. 23*, pp. 127-153. DOI: 10.1007/s00162-009-0096-7, 2009.

B. Monnier, A.M. Naguib, and M.M Koochesfahani. Influence of structural flexibility on the wake vortex pattern of airfoils undergoing harmonic pitch oscillation. *Exp. Fluid 56 (4).* DOI: 10.1007/s00348-015-1946-2, 2015.

M.N.J. Moore. Analytical results on the role of flexibility in flapping propulsion. *J. Fluid Mech. 757, 599.* DOI: 10.1017/jfm.2014.533, 2014.

M.N.J. Moore. Torsional spring is the optimal flexibility arrangement for thrust production of a flapping wing. *Phys. Fluids 27, 091701.* DOI: 10.1063/1.4930235, 2015.

M. Moriche, A. Gonzalo, O. Flores, and M. Garcia-Villalba. Fast transverse maneuvers at low reynolds numbers. *AIAA SciTech 2019 Forum.* DOI: 10.2514/6.2019-0640, 2019.

B.R. Munson, T.H. Okiishi, W.W. Huebsch, and A.P. Rothmayer. *Fundamentals of Fluid Mechanics*. Seventh ed. John Wiley & Sons, Hoboken, NJ, USA, 2013.

M.M. Murray and L.E. Howle. Spring stiffness influence on an oscillating propulsor. *J. Fluids Structures 17*, pp. 915-926. DOI: 10.1016/S0889-9746(03)00026-4, 2003.

A. H. Nayfeh. *Perturbation methods*. John Wiley & Sons, 2008.

M. Olivier and G. Dumas. Effects of mass and chordwise flexibility on 2d self-propelled flapping wings. *J. Fluids Struct. 64, 46.* DOI: 10.1016/j.jfluidstructs.2016.04.002, 2016.

F.W.J. Olver, D.W. Lozier, R.F. Boisvert, and C.W. Clark. *NIST Handbook of Mathematical Functions*. Cambridge University Press, Cambridge, (UK), 2010.

D. Paniccia, L. Padovani, G. Graziani, and R. Piva. The performance of a flapping foil for a self-propelled fishlike body. *Sci. Rep. 11, 22297.* DOI: 10.1038/s41598-021-01730-4, 2021.

F. Paraz, L. Schouvelier, and C. Eloy. Thrust generation by a heaving foil: Resonance, nonlinearities, and optimality. *Phys. Fluids 28, 011903.* DOI: 10.1063/1.4939499, 2016.

Z. Peng and Q. Zhu. Energy harvesting through flow-induced oscillations of a foil. *Phys. Fluids 21 (12)*, pp. 174-191. DOI: 10.1063/1.3275852, 2009.

M. Picard-Deland, M. Olivier, G. Dumas, and T. Kinsey. Oscillating-foil turbine operating at large heaving amplitudes. *AIAA J. 57*, pp. 5104-5113. DOI: 10.2514/1.J058505, 2019.

M. Platzer, K. Jones, J. Young, and J. Lai. Flapping wing aerodynamics: progress and challenges. *AIAA J. 46*, pp. 2136-2149. DOI: 10.2514/1.29263, 2008.

P. Prempraneerach, F.S. Hoover, and M.S. Triantafyllou. The effect of chordwise flexibility on the thrust and efficiency of a flapping foil. *In: Proceedings of 13th International Symposium Unmanned Untethered Submersible Technology*, pp. 1-10, 2003.

J. Pyrhonen, T. Jokinen, and V. Hrabovcová. *Design of rotating electrical machines, second ed.* Wiley, Chichester, West Sussex, United Kingdom, 2014.

D.B. Quinn, G.V. Lauder, and A.J. Smits. Scaling the propulsive performance of heaving flexible panels. *J. Fluid Mech. 738*, pp. 250–267. DOI: 10.1017/jfm.2013.597, 2014.

M. Raffel, C.E. Willert, S.T. Wereley, and J. Kompenhans. *Particle Image Velocimetry. A Practical Guide.* Springer-Verlag. DOI: 10.1007/978-3-540-72308-0, 2002.

S. Ramananarivo, R. Godoy-Diana, and B. Thiria. Rather than resonance, flapping wings flyers may play on aerodynamics to improve performance. *Proc. Natl. Acad. Sci. USA 108*, pp. 5964–5969. DOI: 10.1073/pnas.1017910108, 2011.

L.B. Ramos, O. Marquet, M. Bergmann, and A. Iollo. Fluid-solid floquet stability analysis of self-propelled heaving foils. *J. Fluid Mech. 910, A28.* DOI: 10.1017/jfm.2020.1021, 2021.

D.A. Read, F.S. Hover, and M.S. Triantafyllou. Forces on oscillating foils for propulsion and maneuvering. *J. Fluids Struct. 17 (1)*, pp. 163–183. DOI: 10.1016/S0889-9746(02)00115-9, 2003.

K.V. Rozhdestvensky and V.A. Ryzov. Aerohydrodynamics of flapping-wing propulsors. *Prog. Aero. Sci. 39*, pp. 585-633. DOI: 10.1016/S0376-0421(03)00077-0, 2003.

M. Saadat, F. E. Fish, A. Domel, V. Di Santo, G. Lauder, and H. Haj-Hariri. On the rules for aquatic locomotion. *Physical Review Fluids 2, 083102.* DOI: 10.1103/PhysRevFluids.2.083102, 2017.

J. Sanchez-Rodriguez, C. Raufaste, and M. Argentina. A minimal model of self propelled locomotion. *J. Fluids Struct. 97, 103071.* DOI: 10.1016/j.jfluidstructs.2020.103071, 2020.

J. Sanchez-Rodriguez, F. Celestini, C. Raufaste, and M. Argentina. Proprioceptive mechanism for bioinspired fish swimming. *Phys. Rev. Lett. 126, 234501.* DOI: 10.1103/PhysRevLett.126.234501, 2021.

E. Sanmiguel-Rojas and R. Fernandez-Feria. Propulsion enhancement of flexible plunging foils: Comparing linear theory predictions with high-fidelity cfd results. *Ocean Eng. 235, 109331.* DOI: 10.1016/j.oceaneng.2021.109331, 2021.

E. Sanmiguel-Rojas and R. Fernandez-Feria. Numerical study of the propulsive performance of two-dimensional pitching foils at very high frequencies: Scaling laws and turbulence effects. *Int. J. Numer. Methods Heat Fluid Flow 32*, pp. 1602–1617. DOI: 10.1108/HFF-02-2021-0152, 2022.

T. Schnipper, A. Andersen, and T. Bohr. Vortex wakes of a flapping foil. *J. Fluid Mech. 633, 411.* DOI: 10.1017/S0022112009007964, 2009.

L. Schouveiler, F.S. Hover, and M.S. Triantafyllou. Performance of flapping foil propulsion. *J. Fluids Struct. 20 (7)*, pp. 949–959. DOI: 10.1016/j.jfluidstructs.2005.05.009, 2005.

E. Shimizu, K. Isogai, and S. Obayashi. Multiobjective design study of a flapping wing power generator. *J. Fluids Eng. 130 (2), 021104*, (8 pp.). DOI: 10.1115/1.2829580, 2008.

P.E. Sitorus, T.Q. Le, J.H. Ko, T.Q. Truong, and H.C. Park. Design, implementation, and power estimation of a lab-scale flapping-type turbine. *J. Mar. Sci. Technol. 21*, pp. 115-128. DOI: 10.1007/s00773-015-0336-z, 2016.

A. J. Smits. Undulatory and oscillatory swimming. *J. Fluid Mech., 874*, pp. 1-70. DOI: 10.1017/jfm.2019.284, 2019.

Y. Su and K. Breuer. Resonant response and optimal energy harvesting of an elastically mounted pitching and heaving hydrofoil. *Phys. Rev. Fluids 4, 064701.* DOI: 10.1103/PhysRevFluids.4.064701, 2019.

G. K. Taylor, R. L. Nudds, and A. L. Thomas. Flying and swimming animals cruise at a strouhal number tuned for high power efficiency. *Nature vol. 425 no. 6959*, pp. 707-711. DOI: 10.1038/nature02000, 2003.

L. Teng, J. Deng, D. Pan, and X. Shao. Effects of non-sinusoidal pitching motion on energy extraction performance of a semi-active flapping foil. *Renew. Energy 85*, pp. 810-818. DOI: 10.1016/j.renene.2015.07.037, 2016.

T. Theodorsen. General theory of aerodynamic instability and the mechanism of flutter. *Tech. rep. No. 496, p. 24*, pp. 521–544. DOI: 10.1017/CBO9781107415324.004, 1935.

R. Tian, R. Mitchell, L. Martin-Alarcon, and F. Shu. Experimental investigation of 2d flexible plunging hydrofoil. *J. Flow Vis. Image Process. 20 (4)*, pp. 243–260. DOI: 10.1615/JFlowVisImageProc.2015013527, 2013.

G. S. Triantafyllou, M. S. Triantafyllou, and M. A. Grosenbaugh. Optimal thrust development in oscillating foils with application to fish propulsion. *J. Fluid Structures, 7*, pp. 205-224. DOI: 10.1006/jfls.1993.1012, 1993.

M. S. Triantafyllou, G. S. Triantafyllou, and D. K. P. Yue. Hydrodynamics of fishlike swimming. *Ann. Rev. Fluid Mech., 32*, pp. 33-53. DOI: 10.1146/annurev.fluid.32.1.33, 2000.

M.S. Triantafyllou and G.S. Triantafyllou. An efficient swimming machine. *Sci. Am.*, pp. 64-70. DOI: 10.1038/scientificamerican0395-64, 1995.

M.S. Triantafyllou, G.S. Triantafyllou, and R. Gopalkrishnan. Wake mechanics for thrust generation in oscillating foils. *Phys. Fluids A 3*, pp. 2835–2837. DOI: 10.1063/1.858173, 1991.

M.S. Triantafyllou, A.H. Techet, and F.S. Hover. Review of experimental work in biomimetic foils. *IEEE J. Oceanic Enf. 29(3)*, pp. 585-594. DOI: 10.1109/JOE.2004.833216, 2004.

M.S. Triantafyllou, F.S. Hover, A.H. Techet, and D.K.P. Yue. Review of hydrodynamic scaling laws in aquatic locomotion and fishlike swimming. *Appl. Mech. Rev. 7*, pp. 226-237. DOI: 10.1115/1.1943433, 2005.

I.H. Tuncer and M. Kaya. Optimization of flapping airfoils for maximum thrust and propulsive efficiency. *AIAA J. 43*, pp. 2329-2336. DOI: 10.2514/1.816, 2005.

T. Van Buren, D. Floryan, N. Wei, and A.J. Smits. Flow speed has little impact on propulsive characteristics of oscillating foils. *Phys. Rev. Fluids 3, 013103.* DOI: 10.1103/PhysRevFluids.3.013103, 2018.

J.-C. Veilleux and G. Dumas. Numerical optimization of a fully-passive flapping-airfoil turbine. *J. Fluids Struct. 70*, pp. 102-130. DOI: 10.1016/j.jfluidstructs.2017.01.019, 2017.

Th.H. von Kármán and R. William Sears. Airfoil theory for non-uniform motion. *Journal of the Aeronautical Sciences 5.10*, pp. 379–390. DOI: 10.2514/8.674, 1938.

W. Wang, H. Huang, and X.-Y. Lu. Optimal chordwise stiffness distribution for self-propelled heaving flexible plates. *Phys. Fluids 32, 11905.* DOI: 10.1063/5.0029806, 2020.

P.W. Webb. *Hydrodynamics and energetics of fish propulsion.* Bull. Fish. Res. Board Can. 1–158, 1975.

D. Weihs. Hydromechanics of fish schooling. *Nature, vol. 241, no. 5387*, pp. 290-291. DOI: 10.1038/241290a0, 1973.

L. Wen, T.M. Wang, G.H. Wu, and J.H. Liang. Hydrodynamic investigation of a self-propelled robotic fish based on a force-feedback control method. *Bioinsp. Biomimetics 7, 032012.* DOI: 10.1088/1748-3182/7/3/036012, 2012.

M.W. Westneat and S.A. Wainwright. Mechanical design for swimming: Muscle, tendon, and bone. *Fish Physiol. 19*, pp. 271-311. DOI: 10.1016/S1546-5098(01)19008-4, 2001.

Wikimedia. Law of the wall, horizontal velocity near the wall with mixing length model. URL: https://commons.wikimedia.org/w/index.php?curid=15672321, 2011.

J. Wouterse. Critical torque and speed of eddy current brake with widely separated soft iron poles. *IEE Proc. B 138 (4)*, pp. 153-158. DOI: 10.1049/ip-b.1991.0019, 1991.

J. Wu, Y.L. Qiu, C. Shu, and N. Zhao. Pitching-motion-activated flapping foil near solid walls for power extraction: a numerical investigation. *Phys. Fluids 26 (8), 083601.* DOI: 10.1063/1.4892006, 2014.

J. Wu, C. Shu, N. Zhao, and F.B. Tian. Numerical study on the power extraction performance of a flapping foil with a flexible tail. *Phys. Fluids 27 (1), 013602.* DOI: 10.1063/1.4905537, 2015.

J.C. Wu. Theory for aerodynamic force and moment in viscous flows. *AIAA J. 19 (4)*, pp. 432-441. DOI: 10.2514/3.50966, 1981.

T.Y. Wu. Swimming of a waving plate. *Journal of Fluid Mechanics 10.3*, pp. 321–344. DOI: 10.1017/S0022112061000949, 1961.

T.Y. Wu. Hydromechanics of swimming propulsion. part 1. swimming of a two-dimensional flexible plate at variable forward speeds in an inviscid fluid. *Journal of Fluid Mechanics 46.2*, pp. 337–355. DOI: 10.1017/S0022112071000570, 1971a.

T.Y. Wu. Hydromechanics of swimming propulsion. part 2. some optimum shape problems. *Journal of Fluid Mechanics 46.3*, pp. 521–544. DOI: 10.1017/S0022112071000685, 1971b.

X. Wu, X. Zhang, X. Tian, X. Li, and W. Lu. A review on fluid dynamics of flapping foils. *Ocean Eng. 195, 106712.* DOI: 10.1016/j.oceaneng.2019.106712, 2020.

Q. Xiao and Q. Zhu. A review of energy harvesters based on flapping foils. *J. Fluids Struct. 46*, pp. 174-191. DOI: 10.1016/j.jfluidstructs.2014.01.002, 2014.

G. Xu, W. Xu, and J. Dai. Numerical and experimental study of a flapping foil generator. *Appl. Ocean Res. 63*, pp. 242-250. DOI: 10.1016/j.apor.2017.01.020, 2017.

I. Yamamoto, Y. Terada, T. Nagamatu, and Y. Imaizumi. Propulsion system with flexible/rigid oscillating fin. *IEEE J. Oceanic Eng., 20(1)*, pp. 23-30. DOI: 10.1109/48.380249, 1995.

P.D. Yeh and A. Alexeev. Free swimming of an elastic plate plunging at low reynolds number. *Phys. Fluids 26, 053604.* DOI: 10.1063/1.4876231, 2014.

P.D. Yeh, Y. Li, and A. Alexeev. Efficient swimming using flexible fins with tapered thickness. *Phys. Rev. Fluids 2, 102101(R).* DOI: 10.1103/PhysRevFluids.2.102101, 2017.

J. Young, J.C. Lai, and M.F Platzer. A review of progress and challenges in flapping foil power generation. *Prog. Aerosp. Sci. 67*, pp. 2-28. DOI: 10.1016/j.paerosci.2013.11.001, 2014.

D. Yu, X. Sun, X. Bian, D. Huang, and Z. Zheng. Numerical study of the effect of motion parameters on propulsive efficiency for an oscillating airfoil. *J. Fluids Struct. 68*, pp. 245–263. DOI: 10.1016/j.jfluidstructs.2016.10.009, 2017.

M.L. Yu, H. Hu, and Z.J. Wang. Experimental and numerical investigations on the asymmetric wake vortex structures around an oscillating airfoil. *Tech. Report Ieice Sdm 108 (236)*, pp. 1-6. DOI: 10.2514/6.2012-299, 2012.

M.L. Yu, Z.J. Wang, and H. Hu. High fidelity numerical simulation of airfoil thickness and kinematics effects on flapping airfoil propulsion. *J. Fluids Struct. 42*, pp. 166–186. DOI: 10.1016/j.jfluidstructs.2013.06.001, 2013.

J. Zhan, B. Xu, J. Wu, and J. Wu. Power extraction performance of a semi-activated flapping foil in gusty flow. *J. Bionic Eng. 14 (1)*, pp. 99-110. DOI: 10.1016/S1672-6529(16)60381-5, 2017.

Y. Zhang, C. Zhou, and H. Luo. Effect of mass ratio on thrust production of an elastic panel pitching or heaving near resonance. *J. Fluids Structures 74*, pp. 385-400. DOI: 10.1016/j.jfluidstructs.2017.07.003, 2017.

B. Zhu, P. Xia, Y. Huang, and W. Zhang. Energy extraction properties of a flapping wing with an arc-deformable airfoil. *J. Renewable Sustainable Energy 11, 023302.* DOI: 10.1063/1.5079864, 2019a.

J. Zhu, C. White, D. K. Wainwright, V. Di Santo, G. V. Lauder, and H. Bart-Smith. Tuna robotics: A high-frequency experimental platform exploring the performance space of swimming fishes. *Sci. Rob. 4 (34).* DOI: 10.1126/scirobotics.aax4615, 2019b.

Q. Zhu and Z. Peng. Mode coupling and flow energy harvesting by a flapping foil. *Phys. Fluids 21 (3), 033601*, (10 pp.). DOI: 10.1063/1.3092484, 2009.

Q. Zhu, M. Haase, and C.H. Wu. Modeling the capacity of a novel flow-energy harvester. *Appl. Math. Model. 33 (5)*, pp. 2207-2217. DOI: 10.1016/j.apm.2008.05.027, 2009.

X. Zhu, G. He, and X. Zhang. Numerical study on hydrodynamic effect of flexibility in a self-propelled plunging foil. *Comput. Fluids 97, 1.* DOI: 10.1016/j.compfluid.2014.03.031, 2014.